2014-01-06

Calibration of Multi-Sensor Laser Scanning Systems

Hassan, Essam

UNIVERSITY OF CALGARY

Calibration of Multi-Sensor Laser Scanning Systems

by

Essam Hassan Hamza Hassan

A THESIS

SUBMITTED TO THE FACULTY OF GRADUATE STUDIES

IN PARTIAL FULFILMENT OF THE REQUIREMENTS FOR THE

DEGREE OF DOCTOR OF PHILOSOPHY

DEPARTMENT OF GEOMATICS ENGINEERING

AND

DEPARTMENT OF ELECTRICAL AND COMPUTER ENGINEERING

CALGARY, ALBERTA

JANUARY, 2014

Abstract

Over the past few years, LiDAR or laser scanning systems (airborne, static and terrestrial mobile mapping systems) are considered as well-accepted technologies that can quickly acquire precise 3D point clouds of the terrain surfaces. On the functional level, any mobile system could be defined as an integration of several subsystems such as: Global Positioning System (GPS), an Inertial Navigation System (INS), and the laser scanner. To ensure the geometric quality of the collected point cloud, LiDAR systems should undergo a rigorous calibration procedure. LiDAR system calibration comprises individual sensor calibration (i.e., laser ranging and scanning unit) and mounting parameters calibration (i.e., lever arm offset and boresight angles) relating the system components such as the GPS, INS, and laser scanner. In this research work, a new method for automatic selection of suitable overlapping strip pairs/regions for optimized LiDAR system calibration is introduced. The experimental results have shown that the quality of the estimated parameters using the automatic selection is quite similar to the estimated parameters using the manual selection while the processing time of automatic selection is 3 times faster than the manual selection.

In the field of surveying and mapping in recent years, the development of airborne LiDAR systems is characterized by the use of multiple laser scanners for accurate and efficient capture of 3D data along ground and above ground features. In this research, new calibration procedure for dealing with airborne multi-laser scanning systems is presented. The experimental results have shown that accurate estimation of the calibration parameters of each laser scanner can be obtained using the proposed method.

Terrestrial mobile laser scanning (TMLS) is the latest approach towards fast and cost-effective acquisition of 3-dimensional spatial data. Accurately evaluating the intrinsic and mounting parameters of TMLS systems is an obvious necessity. However, available systems on the market may lack suitable and efficient practical workflows on how to perform this calibration. This research introduces an innovative method for accurately determining the intrinsic and mounting parameters of multi-TMLS systems. The proposed calibration method investigates a two-step (indoor followed by outdoor) calibration procedure for calibrating terrestrial mobile multi-laser scanning systems. In this research work, a simulation program is developed for generating 3D LiDAR data such as a Velodyne-based Mobile laser scanning system (HDL-32E). The experimental results are performed using a simulated dataset for investigating the one-step and two-step calibration procedures. The experimental results have shown that the estimated parameters using the two-step calibration procedure are better than the estimated parameters derived from the one-step calibration procedure.

Acknowledgements

First, thanks to God, the most beneficent and the most merciful

I would like to express my great indebtedness to my supervisor Dr. Ayman Habib for the valuable guidance and advice. Dr. Habib inspired me greatly to work in this thesis. His willingness to motivate me contributed tremendously to this work. To him, I am sincerely grateful for offering much of his precious time revising and correcting many of shortcomings of this study. Really, I was honored to work under his supervision.

Many and special thanks to Dr. Michel Fattouche for his kind supervision, professional teaching and valuable discussion.

I would like to extend my appreciation to my supervising committee Dr. Naser El-Sheimy, Dr. Jonathan Li, Dr. Ruisheng Wang and Dr. Mohamed Helaoui for carefully reading and providing valuable comments on this dissertation.

I would also like to thank the past and present members of the Digital Photogrammetry Research Group (DPRG) for all their wonderful friendship, support and valuable discussion: Ana, Mohannad, Zahra, Kaleel, Abdullah, Ivan, Hossein, Hussein and Fang. It was my pleasure to work with them in this wonderful working environment.

I can't find words to express my gratitude to my MTC colleagues, Dr. Hassan Elhifnawy, Dr. Ahmed Mohsen, Dr. Ahmed Shawky and Dr. Bassem Sheta for their wonderful friendship and

great time we spent together with ourselves and with our families, I really enjoyed each and every moment.

I also give a great thanks to my wife Marwa, my two sons Ahmed and Hamza and my daughter Nour. You are the best thing happen in my life, may ALLAH bless you all.

I would like to acknowledge my dept to my father, my mother. Please keep praying for me. I love you and thank you for everything.

Dear brothers, Mohamed and Mahmoud thanks for your support, encouragement and help along the way.

Finally I would like thank my country, Egypt, for funding and supporting my research, specially the Egyptian Armed Forces, my sponsor, for the unwavering support.

Dedication

To my wife Marwa, my sons Ahmed and Hamza, my daughter Nour, and my family in Egypt.

Table of Contents

List of Tables

List of Figures and Illustrations

Coordinate System

Laser unit coordinate system: 3D Cartesian coordinate system associated with the laser unit.

Laser beam coordinate system: 3D Cartesian coordinate system associated with the laser beam, with the z-axis defined along the laser beam.

IMU coordinate system (b): 3D Cartesian coordinate system associated with the IMU body frame. In this dissertation, it is assumed that the position and orientation information from the GPS/INS integration process is defined relative to the IMU body frame (i.e., the GPS/INS integration process is performed while considering the lever arm offset between the IMU body frame and the phase center of the GPS antenna).

Mapping Frame (m): In this dissertation, the mapping frame (i.e., the coordinate system associated with the object space) is assumed to be a 3D Cartesian coordinate system.

List of Abbreviations

2D	Two Dimensional
3D	Three Dimensional
AGL	Above Ground Level
ALS	Airborne Laser Scanner
CW	Continuous Wave
DGPS	Differential Global positioning System
DTM	Digital Terrain Model
GCP	Ground Control point
GPS	Global positioning System
IMU	Inertial Measurement unit
INS	Inertial Navigation System
LASER	Light Amplification by Stimulated Emission of Radiation
LiDAR	Light Detection And Ranging
LSA	Least Square Adjustment
NASA	National Aeronautics and Space Administration
PRF	Pulse Repetition Frequency
SW	swath width
TIN	Triangular Irregular Network
TLS	Terrestrial Laser scanner
TMLS	Terrestrial Mobile Laser scanners
TOF	Time of Flight

Chapter One: **INTRODUCTION**

1.1 Motivation

Over the past few years, there are several methods, tools, and techniques that can be used to collect spatial data for topographic mapping and other surveying applications. These methods include conventional ground surveys, photogrammetry, and different types of remote sensing techniques including laser scanning. Light Detection And Ranging (LiDAR) or airborne laser scanning (ALS), static terrestrial laser scanning (TLS) and terrestrial mobile laser scanning (TMLS) systems have been established as a leading technologies for the acquisition of high density 3D spatial data. The availability of 3D surface data is very important for several applications such as environmental monitoring, military simulation, contour mapping, transportation planning, oil and gas exploration, mining, shoreline management, 3D city modeling, and forest mapping. The ability of the LiDAR system to determine 3D points on the ground is the result of multiple components integrated to work together. A typical LiDAR system consists of one or multiple laser scanners, together with a Global Positioning System (GPS) and an Inertial Navigation System (INS). The laser scanner records the scan angle relative to the sensor platform in addition to estimating the distance from the sensor to the ground point by measuring the time delay between a laser pulse transmission and its detection, while the GPS/INS component provides the position and orientation of the platform. The above information allows for the determination of the location of the points along the mapped surface.

The advancement in navigation and GPS technology stimulated the emergence of the concept of mobile LiDAR (i.e., ALS and TMLS system) as a cost-effective technology for the collection of geo-spatial information. As well, the development in GPS/INS technology is enabling highly accurate determination of position and orientation of the moving platform. TMLS is a term

extensively used for one or multiple laser scanners distributed on any moving platform such as a van, boat or even a 4 × 4 vehicle, and TMLS would never imply airborne system. However, the general principles of operation are the same for ALS and TMLS systems and the data processing workflows are very similar or almost identical in both cases.

The calibration of ALS and TMLS is very important task to ensure the achievement of the expected accuracy and is also the most complex task. Laser system calibration comprises individual sensor calibration (i.e., laser ranging and scanning unit) and mounting parameters calibration (i.e., lever arm offset and boresight angles) relating the system components such as the GPS, INS, and laser scanners. The lever arm offset is usually measured using traditional surveying techniques, while approximate values for the boresight angles are known from the sensors' mechanical alignment, but these initial mounting parameters might be biased. The whole process of calibrating a laser scanning system includes several steps such as the calibration of the individual system components in a laboratory, which is performed by the system manufacturer, in addition to a platform calibration to determine the system mounting parameters (Schenk, 2001). An in-flight system calibration is usually required to refine the parameters determined in the laboratory and the platform calibrations. Without adequate laser scanning system calibration, the quality of the final product cannot be guaranteed. ALS and TMLS calibration is a more challenging task due to the irregular nature of the LiDAR point cloud, which demands appropriate primitives and mechanism for using them, compared to the photogrammetric system calibration.

Over the last few years, many research efforts have been performed on ALS system calibration (Burman, 2000; Filin, 2001; Morin, 2002; Toth, 2002; Skaloud and Lichti, 2006; Friess, 2006; Habib et al. 2010b; Bang, 2010; Kersting, 2011). Some of the current techniques either depend

on primitives, which are not appropriate to deal with the irregular nature of LiDAR surfaces (Morin, 2002), or deal with appropriate primitives while demanding specific features in the calibration site (e.g., planar or linear features) and/or pre-processing of the LiDAR point cloud, i.e., classification of LiDAR data into terrain/off-terrain features or segmentation of planar patches (Skaloud and Lichti, 2006; Friess, 2006) or even the requirement for control surfaces (Filin, 2001). In terms of data requirement, current methods require the system's raw measurements (Filin, 2001; Skaloud and Lichti, 2006; Friess, 2006) or at least the trajectory and time-tagged point cloud (Burman, 2000; Toth, 2002; Morin, 2002) for the estimation of biases in the system parameters with the help of the LiDAR point positioning equation. Recently, two calibration approaches that overcome the limitation in terms of data requirements for the ALS system calibration faced by most users have been proposed in (Habib et al., 2010b and Bang, 2010). One of the methods, denoted as "Simplified Calibration", only required the LiDAR point cloud coordinates. This relaxed data requirement is enabled by the use of a simplified LiDAR point positioning equation. The underlying assumptions to simplify the LiDAR point positioning equation and to derive the calibration mathematical model limit its use to datasets following a strict flight configuration and terrain characteristics, i.e., parallel flight lines acquired by fixed wing platforms (small pitch and roll angles) over an area with moderately varying elevation (minor terrain elevation variations compared to the flying height above ground). On the other hand, the second method proposed in (Habib et al., 2010a and Bang, 2010), denoted as "Quasi-Rigorous Calibration", is more flexible in terms of the required flight configuration (i.e., it can be used in datasets consisting of non-parallel flight lines) and has no restriction in terms of the terrain characteristics. However, this method is only suitable for datasets acquired by steady platforms (small pitch and roll angles) and requires time-tagged point cloud and the trajectory

position. Recently, the current calibration method proposed in (Kersting, 2011), denoted as "Rigorous Calibration", is a more flexible calibration procedure that can be executed without strict requirements (e.g., flight, terrain coverage, control, and pre-processing requirements such as classification of the LiDAR point cloud into terrain/off-terrain features or segmentation of planar features). However, in this approach, manually-selected regions between the overlapping LiDAR strips are used in LiDAR system calibration, where some problems could take place when using these manually-selected pairs/regions (i.e., non-uniform balance of the distribution of the slope and aspect values within the selected regions, redundant slope and aspect values, and reliance on the experience of the operator). In addition, this method deals only with one laser unit in ALS system.

A reliable system calibration procedure requires the identification of appropriate primitives in overlapping LiDAR strips as well as control data. Distinct points have been used as a primitive in photogrammetric data for a long time. However, it is well-known that distinct points cannot be directly captured by a LiDAR system as the system produces irregular point data unlike photogrammetric systems (Ackermann, 1999). Planar patches can be indirectly identified and used as conjugate surface elements in overlapping LiDAR strips (Skaloud and Lichti, 2006; Habib et al., 2007; Lee et al., 2007; Skaloud and Schaer, 2007; Habib et al., 2009b). Planar patches such as gable roofs can be extracted by a plane segmentation process. These planar patches can be used as suitable primitives in overlapping LiDAR strips. Also, these planar patches should have varying slope and aspect angles to be beneficial in the LiDAR system calibration. The implementation of procedure with high level of automation for selecting overlapping pairs/regions among LiDAR strips used in the calibration procedure would be

essential. An automatic methodology for selecting appropriate overlapping strip pairs/regions among LiDAR strips is one of the goals of this research.

In recent years, in the field of mapping and surveying, the evolution of airborne LiDAR systems is characterized by the use of multiple laser scanners for accurate and efficient capture of 3D data of ground and above ground. RIEGL BP-560 and OPTECH ALTM Pegasus systems are examples of ALS systems that consist of multiple laser scanners. These systems require reliable calibration. The implementation of calibration procedure to deal with multi-ALS system is one of the objectives of this research work.

Over the past few years, Terrestrial Mobile Laser Scanning (TMLS) is an emerging technology that uses laser scanner technology in combination with GPS/INS and other sensors to produce accurate and precise geospatial data from a moving vehicle. In contrast to ALS systems, the calibration of TMLS has been introduced in few research work such as (Rieger et al., 2010; Glennie and Lichti (2010, 2011); Chan, 2011; Gerardo et al., 2011). Some approaches depend on scanning objects of known size and position from different driving and scanning directions. Most of the calibration procedures of TMLS system are usually conducted by the system manufacturer, are not flexible and require significant efforts for preparing special calibration sites. The estimation of the mounting parameters (i.e., lever arm offset and boresight angles) relating the laser sensor in a TMLS system and the IMU body frame as well as the quality of the navigation data (i.e., GPS/INS information) play an important role in the overall point cloud quality. This is true especially when objects are scanned with multiple drive lines and scanners. As a result, poor mounting parameters estimation and deterioration in the quality of the navigation data in urban canyons will seriously affect the quality of the estimated system parameters. Therefore rigorous, but also cost-effective, calibration methodologies are always

desired. The implementation of a calibration procedure to deal with multi-TMLS systems is one of the objectives of this research work.

1.2 Research Objective

The main objectives of this research can be summarized in the following list:

1. Investigate an existing airborne LiDAR system calibration technique, which is based on the manual selection of overlapping pairs/regions among LiDAR strips and how to increase the efficiency of this technique as follows:

- Automatic selection of suitable overlapping strip pairs, which should achieve the minimum optimal flight configuration that maximizes the impact of the discrepancies among conjugate surface elements in overlapping LiDAR strips.
- Automatic selection of regions (planar patches) within the appropriate overlapping strip pairs. The main criteria for the selection of these regions are as follows:
  - The selected regions should have good variations in the topography (i.e., surfaces with varying slope and aspect values),
  - The selected regions should be well-distributed within the overlapping area, and
  - The selected regions should have a balance between their sizes.

2. Propose calibration technique to deal with airborne multi-laser scanning systems. The proposed method aims at estimating the mounting parameters relating the individual scanners to the IMU body frame and the intrinsic parameters of each scanner.

3. Propose two-step calibration technique (indoor followed by outdoor) to deal with terrestrial mobile multi-laser scanning systems. The advantage of this approach is that the mounting parameters relating the different scanners to a reference one can be estimated through an indoor calibration procedure. While the mounting parameters relating the reference scanner to the IMU body frame can be estimated through an outdoor calibration procedure. In addition, a simulation program for generating 3D LiDAR data as a Velodyne Mobile laser scanning system (HDL-32E) is proposed to investigate the indoor and outdoor calibration techniques of TMLS system.

1.3 Thesis Outline

The structure of this thesis and brief explanations of the chapters can be summarized as follows:

- Chapter 2 provides an overview of the laser scanning principles, the difference between ALS and TMLS systems and also focuses on the review of existing methods for ALS and TMLS system calibration.

- Chapter 3 introduces a novel method for automated selection of suitable overlapping strip pairs/regions for optimized LiDAR system calibration. The main criteria for the selection of overlapping strip pairs/regions are as follows (i) the overlapping strip pairs should achieve the minimum optimal flight configuration (three overlapping strip pairs as follows: two flown in different heights in opposite directions and one flown in parallel direction) (ii) the selected regions should exhibit good variation in the topography (i.e., surfaces with varying slope, aspect and distribution).

- Chapter 4 presents a new calibration method for the estimation of the mounting parameters relating the individual scanners to the IMU body frame and the intrinsic parameters of each laser scanner involved in airborne multi-laser scanning systems.

- Chapter 5 discusses an innovative method for calibrating the terrestrial mobile multi-laser scanning systems. The concept of the proposed calibration method is that the mounting parameters relating the individual scanners to the reference frame of the navigation unit (IMU body frame) will be divided into two groups as follows (i) the mounting parameters relating the different scanners to a reference scanner, and (ii) the mounting parameters relating the reference scanner to the reference frame of the navigation unit. The advantage of this approach is that the first group can be determined through an indoor calibration test field, while the latter group can be determined in an open-sky environment (outdoor calibration).

- Chapter 6 describes the experimental results to demonstrate the feasibility of the proposed methodologies. In addition, a simulation program for generating 3D LiDAR data such as a Velodyne Mobile laser scanning system is demonstrated to verify the indoor and outdoor calibration techniques of TMLS system.

- Chapter 7 finally presents the conclusions of the presented research work and recommendations for future investigations.

Chapter Two: **Literature Review**

2.1 Introduction

In the past few years, several laser scanners that can be characterized become available, based on their intended application, as close range, and airborne systems. Close range means that laser scanning is performed over ranges between 0 and 200 meters and is typically conducted using tripod, other stationary mounts or a mobile vehicle. These systems are sometimes referred to as Terrestrial Laser Scanners (TLS) or Terrestrial Mobile Laser Scanners (TMLS). Airborne laser scanning systems (ALS) typically operate over ranges between several hundred meters up to several kilometers from helicopters or fixed-wing airplanes. The term LiDAR (Light Detection And Ranging) is sometimes used interchangeably with laser scanner, but is more often associated with the airborne systems. The basic principle of operation of laser scanner depends on range measurements, i.e., the determination of the distance between the laser firing point and the footprint on the object surface. Range measurements can be carried out using Continuous Wave (CW) laser systems or pulsed laser systems. In CW laser systems, the range (ρ) is determined by measuring the phase difference between the transmitted and the received signal. CW laser systems are usually used in terrestrial laser scanners (Faro, 2007; 3rdTech, 2007), as shown Figure 2.1. Most of available ALS systems in the market are pulsed lasers (Riegl, 2007; Optech, 2007; Leica, 2007; TopEye, 2007; TopoSys, 2007). In ALS and TLS systems, the range measurement is based on the time-of-flight (TOF) of the laser pulse (i.e., time delay between the emitted and received laser pulses). Equation 2.1 can be used for the computation of the laser range (Petrie and Toth, 2009).

$$\rho = \frac{Ct}{2} \tag{2.1}$$

Where:

ρ: the range;

C: the speed of light;

t: the measured time interval.

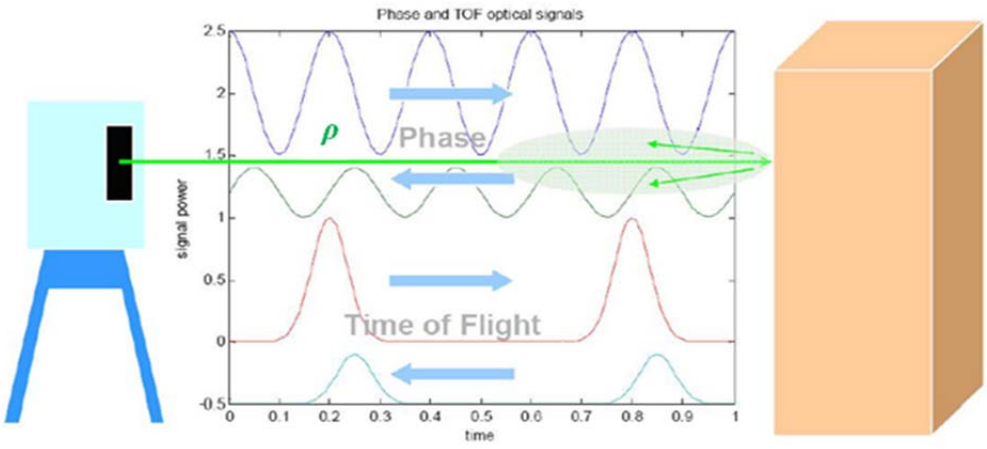

Figure 2.1. Principle of phase based terrestrial laser scanners (adapted from: http://www.ahmct.ucdavis.edu)

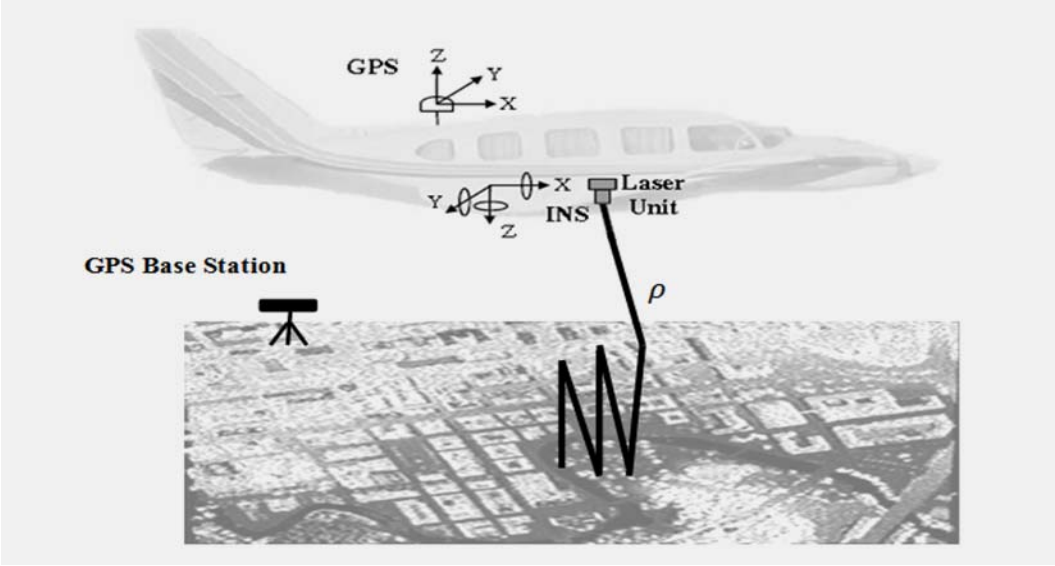

Figure 2.2. Basic components of LiDAR system and its operational principles

In addition to laser ranging unit, LiDAR systems also involve a scanning unit. The different scanning mechanisms which are in use in airborne and/or terrestrial laser scanner are: an oscillating mirror, palmer scan, rotating polygon, and fiber scanner (Vosselman, 2010). Figure 2.2 shows an example of scanning mechanisms (e.g., oscillating mirror which produces a zigzag pattern). The geo-referencing of the sensor platform, which is essential for deriving the coordinates of the points of the scanned object relative to the mapping frame, is performed using a GPS/INS unit onboard the platform. A GPS base station is used for differential GPS positioning (DGPS). The LiDAR system components and its operational principles are illustrated in Figure 2.2. In addition to the point positions (i.e., 3D coordinates of the scanned points), most modern laser systems can provide intensity information, which is the ratio between the strength of received and emitted light (laser beam), and is mainly influenced by the reflectance properties of the object surface, atmospheric parameters, and energy loss. The intensity data can be used for object extraction, change detection, and land-cover classification (Song et al., 2002; Clode et al., 2004; Wang and Tseng, 2004). Figure 2.3a shows an interpolated image using the elevation and intensity data. Figure 2.3b shows an interpolated range image using intensity information.

(a) (b)

Figure 2.3. Sample of interpolated LiDAR imagery: (a) range image and (b) intensity image (Bossler, 2010)

The specifications of typical airborne LiDAR systems are listed in Table 2.1. The typical wavelength of a LiDAR system is about 900-1550 nano-meters which falls in the infrared portion of the electromagnetic spectrum. The majority of objects on the ground have a reasonable reflectance at infrared wavelengths. Therefore they generate a return signal with sufficient intensity to be detected. Some types of objects such as water body, damp soil and dark surfaces have very low reflectance. Therefore it is difficult to detect a signal reflected from these types of objects (Harding, 2004).

Table 2.1. Specifications of typical LiDAR systems (Bossler, 2010)

Specification	**Typical values**
Laser wavelength	600-1550 nm, near-infrared
Pulse repetition frequency	25-167 kHz
Pulse energy	Up to 100s μJ
Pulse width	<10 ns
Beam divergence	0.25-2.0 mrad
Scan angle (or Field Of View)	40°-80°
Scan rate	25-90 Hz
GPS frequency	1-10 Hz
INS frequency	200-300 Hz
Operating altitude	80-3500 m (6000 m max)
Footprint size	0.25-2.0 m (at 1,000 m altitude AGL)
Number of returns	1-4 or full waveform
Ground spacing	0.5-2.0 m
Vertical accuracy	<15 cm at 1000 m AGL
Horizontal accuracy	<50 cm at 1000 m AGL

The pulse repetition frequency (PRF) indicates the number of emitted laser pulses per second. The scan rate refers to the number of completed full scans per second. The density of a point cloud depends on the system and on the balance between flying speed, pulse frequency rate, scan angle and flight altitude (Ackermann, 1999). Higher pulse and scan rates require a lower flight altitude because there is a limitation in the capacity of a laser scanner power (Fugro EarthData, Inc., 2009). Figure 2.4 shows the configuration parameters involved in the LiDAR mapping. The swath width (SW) of a LiDAR strip depends on the total scan angle (β_T) and flying height (H) above ground as shown in Equation 2.2. The diameter of the footprint will be mainly dependent on the beam divergence angle and flying height. Other factors such as the scan angle of the laser beam and the slope of the terrain will also have an influence on the shape and size of the footprint.

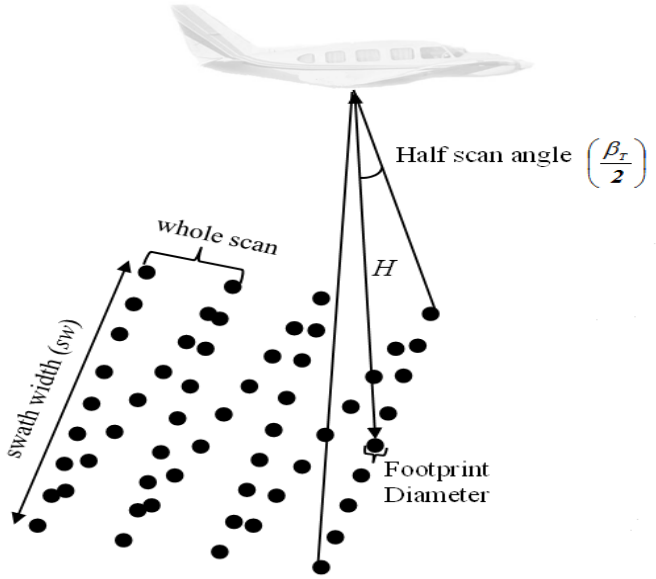

Figure 2.4. Configuration parameters involved in the LiDAR mapping

$$SW = 2H\ tan\left(\frac{\beta_T}{2}\right) \tag{2.2}$$

Four coordinate systems are used in the LiDAR geo-referencing equation, as shown in Figure 2.5.

1. Mapping frame (ground coordinate system),
2. Inertial Measurement Unit (IMU) body frame,
3. Laser unit coordinate system, and
4. Laser beam coordinate system.

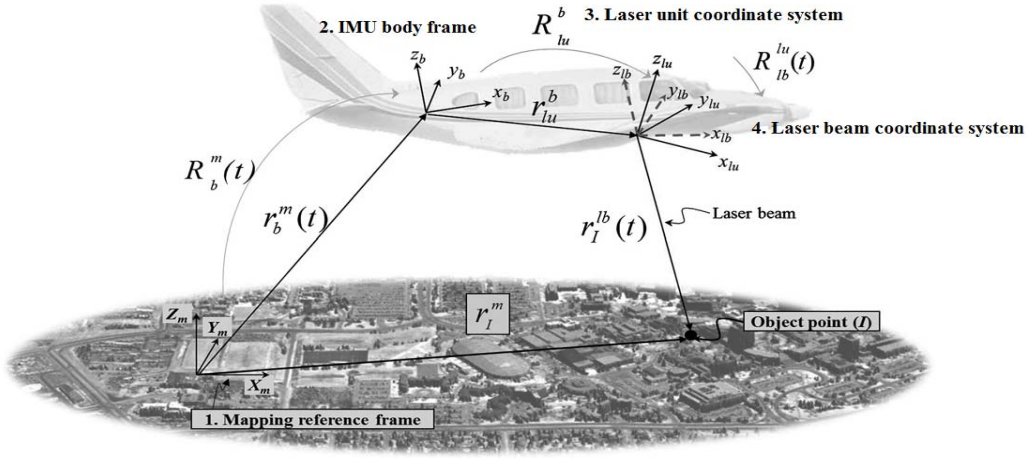

Figure 2.5. Coordinate systems and involved quantities in the LiDAR point positioning equation (Adapted from Habib, 2012)

The coordinates of the LiDAR points are calculated using the derived measurements from each of the system components, as well as the mounting parameters relating such components. The relationship between the LiDAR point coordinates, the system measurements, and parameters is expressed through the LiDAR point positioning equation represented in Equation 2.3 (Schenk, 2001; El-Sheimy et al., 2005; Habib et al., 2010).

$$r_I^m = r_b^m(t) + R_b^m(t) r_{lu}^b + R\,{}_b^m(t) R\,{}_{lu}^b R_{lb}^{lu}(t) r_I^{lb}(t) \tag{2.3}$$

As shown in Figure 2.5, the position of the laser point (r_I^m) is derived from the summation of three vectors, $r_b^m(t), r_{lu}^b$, and $r_I^{lb}(t)$, after applying the appropriate rotation matrices: $R_b^m(t), R_{lu}^b$, and $R_{lb}^{lu}(t)$. In this equation, $r_b^m(t)$ is the vector from the origin of the reference frame coordinate system to the origin of the IMU coordinate system, $r_{lu}^b(\Delta X, \Delta Y, \Delta Z)$ – lever arm offset – is the vector from the origin of the IMU coordinate system to the origin of the laser unit coordinate system (defined relative to the IMU body frame), and $r_I^{lb}(t)$ is the laser range vector whose magnitude (ρ) is equivalent to the distance between the laser firing point to its footprint. It should be noted that $r_b^m(t)$ is derived from the GPS/INS integration process while considering the lever arm offset between the IMU body frame and the phase center of the GPS antenna. The term $R_b^m(t)$ stands for the rotation matrix relating the ground and IMU coordinate systems, which is derived from the GPS/INS integration process. The term R_{lu}^b represents the rotation matrix relating the IMU and laser unit coordinate systems, which is defined by the boresight angles $(\Delta\omega, \Delta\varphi, \Delta\kappa)$. The term $R_{lb}^{lu}(t)$ refers to the rotation matrix relating the laser unit and laser beam coordinate systems, which is defined by the mirror scan angle (i.e., the spatial direction of the laser beam w.r.t. the laser unit coordinate system).

The accuracy of the derived point cloud coordinates from airborne laser scanning systems (ALS) and terrestrial mobile laser scanning systems (TMLS) is affected by inherent random and systematic errors. A detailed description of ALS random and systematic errors is discussed in (Huising and Pereira, 1998; Baltsavias, 1999; Schenk, 2001; Csanyi, 2008; Habib, 2009; and Bang, 2010). In general, the impact of random errors in ALS and TMLS systems depend on the precision of the system's measurements, which comprise the position and orientation information from the GPS/INS unit, mirror angles, and ranges. Moreover, systematic errors in ALS and

TMLS systems are mainly caused by biases in the mounting parameters (i.e., lever arm offset and boresight angles) relating the system components as well as biases in the system measurements (e.g., ranges and scale of mirror scanning angles). Although many similarities exist between ALS and TMLS, the most significant difference in their error sources is the GPS positioning error. The GPS error is much higher in the TMLS than the ALS since the environment surveyed with the TMLS will always contain dense architectures or vegetations which limit the GPS receiver's exposure to the GPS base stations or GPS satellites. On the contrary, the ALS usually flies over 80-3500 m and so it does not suffer from this problem (Chan, 2011).

2.2 Differences between Terrestrial Mobile Laser Scanning and Airborne Laser Scanning Systems

The TMLS is very similar to ALS in terms of the position modeling. In general, ALS cannot survey the façades of building while TMLS is capable of doing this, and therefore, it becomes the major surveying tool for 3D city model generation and many other applications such as national mapping and infrastructure deformation monitoring. Although, the basic model of TMLSs is very similar to ALSs, there are some differences between them that are worthwhile noting. These differences can be summarized as follows:

(1) Difference in laser measurement and point density: The time-of-fight measurement of the ALS is based on the pulse method. The idea is to record time difference between transmitted and reflected pulses to determine the distance for the round trip (Baltsavias, 1999a; Wehr and Lohr, 1999). The strength of the pulse decreases as the flying height increases while seriously attenuated returning pulses cannot be detected. Therefore, multiple pulse measurements have

been introduced to increase the point density to allow for the operation of ALS at higher altitudes. On the other hand, the time-of- fight measurement of TMLS can be based on the phase comparison method (Zhu et al., 2011). Instead of emitting a series of pulses, a continuous waveform from the laser is radiated in the phase comparison method. This method estimates the distance between the laser and the target by using the phase shift between the emitted and received laser waveform.

Typically, ALS is operated at altitude of 80-3500 meters while TMLS is operated at a distance not larger than several hundred meters from the object. Due to the difference in the range and also the laser time-of-fight measurement techniques, ALS point density is only several points per square meter while TMLS point density can reach several thousands per square meter. For ALS being operated at altitude of 1000-3000 m, the vertical accuracy varies from 5-30 cm and the horizontal accuracy is approximately 50-150 cm (Bang, 2010). On the contrary, the current TMLS accuracy is at the sub-decimeter level.

(2) GPS signal availability: ALS always operates at higher altitudes so that it is always exposed to good satellite geometry. As a result, the GPS signal received by ALS is relatively accurate and stable compared to TMLS. TMLS usually runs within urban areas for surveying. Tall buildings, bridges, and other infrastructure commonly exist in urban areas and they potentially block GPS receivers from receiving satellite signals. This extremely lowers the accuracy of GPS position and contributes to the lower overall system accuracy.

(3) IMU requirement: The ALS always requires a higher grade and a more costly IMU (navigation-grade IMU). The TMLS demands a lower grade IMU (tactical-grade IMU).

(4) Scanning geometry: The ALS is usually nadir-looking while the TMLS is able to scan in other directions (e.g. two sides, upward and downward scanning).

Figure 2.6 shows examples of the laser scanning systems that are commonly used by the mapping industry.

http://hds.leica-geosystems.com/en/Press-Releases_5604.htm?id=3277

(a)

http://www.geoinformatics.com/blog/latest-news/sanborn-using-optechs-state-of-the-art-lynx-mobile-mapper

(b)

http://www.rieglusa.com/products/airborne/lms-q680/index.shtml

(c)

Figure 2.6. Examples of different laser scanning systems: (a) Leica HDS 7000 (example of terrestrial laser system), (b) Optech Lynx Mobile Mapper V200 (example of terrestrial mobile laser system), and (c) RIEGL LMS-Q680i (example of airborne laser system)

2.3 Overview of Laser Scanning System Calibration

Calibration of laser scanning system is the process of determining the relative mounting parameters (i.e., lever arm offset and boresight angles) relating to the IMU body frame as well as the intrinsic parameters (i.e., laser ranging and scanning unit). The progress of calibration procedures for both airborne and terrestrial devices is one important development for the early steps of data processing. The system calibration is usually executed in several steps: (i) Laboratory calibration, (ii) Platform calibration, and (iii) In-flight calibration. In the laboratory calibration, which is performed by the system manufacturer, the individual system components are calibrated. In addition, the lever arm offset and boresight angles between the laser unit mirror and the IMU, as well as the lever arm offset between the IMU and the sensor reference point, are determined (Figure 2.7). In the platform calibration, the lever arm offset between the sensor reference point and the GPS antenna is determined (Figure 2.7).

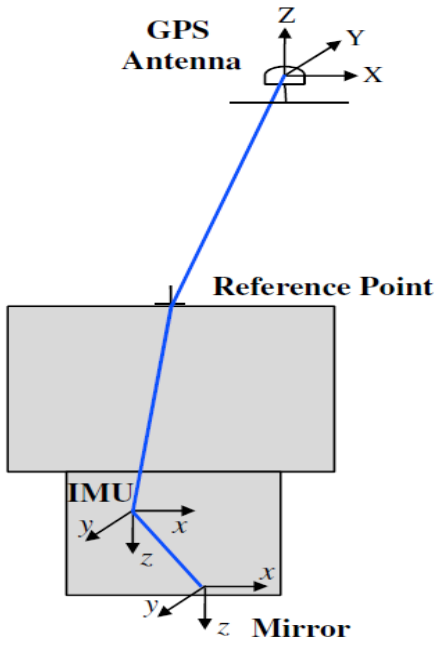

Figure 2.7. Determination of Lever arm offsets in the laboratory and platform calibration (Adapted from Kersting, 2011)

The parameters that are determined in laboratory and platform calibration might be biased and/or not stable over time. Therefore, an in-flight calibration should be carried out to refine such parameters. Since the different laser systems became commercially available and until very recently, the in-flight techniques which have been used by some of the data providers have several drawbacks such as: (i) the use of manual and experimental procedures, (ii) expensive and time consuming requirements, (iii) the use of complicated and sequential procedures, and (iv) strong dependence on control surfaces. Furthermore, until now there is no commonly accepted methodology since the calibration techniques are usually based on a manufacturer-provided software package and the expertise of the LiDAR data provider. As a result of the experimental calibration procedures, considerable systematic discrepancies between conjugate surface elements in overlapping LiDAR strips have been observed in the collected data. These discrepancies contaminate the similarity of the dataset. Furthermore, they significantly decrease the accuracy of the point cloud. A review of current techniques for the calibration of airborne and terrestrial laser scanning systems is introduced in the next section.

2.4 Calibration Techniques of Airborne and Terrestrial Laser Scanning Systems.

Over the past few years, extensive research has been carried out to develop techniques for the elimination of the impact of the systematic errors in the LiDAR system parameters on the derived point cloud. These existing approaches have been categorized into two classes depending on the nature of the utilized data: data-driven and system-driven methods. Data-driven methods utilize the LiDAR point cloud coordinates only. They are usually based on arbitrary coordinate transformation model between the laser strip coordinate system and the reference data coordinate system. On the other hand, system-driven methods utilize the system raw measurements or at

least the trajectory (i.e., position and orientation of the platform) and time-tagged point cloud coordinates. Then, such dataset is used in combination with the LiDAR geometric model (i.e., the LiDAR point positioning equation) to estimate the biases in the system parameters. Obviously, system-driven approaches are the most accurate way to eliminate the impact of systematic errors in the LiDAR system parameters on the derived point cloud. Due to the difficulty in accessing the system raw measurements, the development of data-driven methods (e.g., Kilian et al., 1996; Crombaghs et al., 2000; Kager and Krauss, 2001; Maas, 2002; Filin and Vosselman, 2004; Habib et al., 2010b) has been quite popular. Data-driven approaches are also known as strip adjustment procedures since they aim at improving the compatibility between overlapping strips by estimating local transformation parameters between the LiDAR strips coordinate system and the reference one. In (Kilian et al., 1996), an adjustment procedure similar to the photogrammetric strip adjustment was introduced for detecting discrepancies and improving the compatibility between overlapping strips. The drawback of this approach is depending on distinct points to relate overlapping LiDAR strips and control surfaces. Due to the irregular nature of the LiDAR points, the identification of distinct points (for example, building corners) is quite difficult and not reliable. More suitable primitives have been suggested by (Kager, 2004), where planar features are used in the strip adjustment procedure. In Maas, 2002 where a least-square matching procedure is proposed to derive the correspondence between discrete points in one LiDAR strip and TIN patches in the other one. The focus of the method proposed by (Maas, 2002) relies on detecting the discrepancies between conjugate surface elements rather than improving the compatibility between neighboring strips or analyzing the detected discrepancies. The limitation of this work is that simple shifts were used as the transformation function relating conjugate point-patch pairs. The main drawback of data-driven

approaches is that the utilized transformation function might not be appropriate depending on the nature of the inherent biases in the LiDAR system parameters and the adopted flight configuration. Recently, Habib et al., 2009 and Bang, 2010 have proposed a data-driven method based on a more appropriate mathematical model, which makes use of a simplified LiDAR equation. This method is different from the previous data-driven strip adjustment procedures. This method derives an estimate of biases in the system parameters. Therefore, this method can be categorized as a data-driven calibration procedure. The underlying assumptions to simplify the LiDAR equation limit its use to datasets following a strict flight configuration and terrain characteristics; i.e., parallel flight lines acquired by fixed wing platforms (small pitch and roll angles) over an area with moderately varying elevation (i.e., minor terrain elevation variations compared to the flying height above ground).

System-driven (or calibration) techniques can be classified as rigorous or quasi-rigorous approaches. Rigorous approaches utilize the system raw measurements (e.g., Filin, 2001; Skaloud and Lichti, 2006; Friess, 2006; Kersting, 2011, Lindenthal et al., 2011) while the quasi-rigorous approaches utilize the trajectory and time-tagged point cloud coordinates (Burman, 2000; Toth, 2002; Morin, 2002; Habib et al., 2010b; Bang, 2010) for the estimation of biases in the system parameters with the help of the LiDAR equation. Skaloud and Lichti, 2006 propose a method for estimating the calibration parameters by enforcing a group of points to lie on a common plane. The utilized planes are selected manually and its parameters are determined along with the calibration parameters. The drawback of this approach lies in depending on the availability of large planar patches with varying slopes and aspects, which can be only available in LiDAR data over urban areas. In addition, the number of unknowns changes with the number of used planes in the calibration procedure. In the proposed work by (Morin, 2002), point

primitives are utilized to establish the correspondence between overlapping strips. Due to the irregular nature of the LiDAR points, the identification of distinct points is quite difficult and not reliable. In addition, this method relies on the assumption that the average of the coordinates of tie points in overlapping strips corresponds approximately to the ground truth. In the calibration methods proposed by Burman, 2000 and Toth, 2002, only biases in the boresight angles are considered in the calibration procedure. The proposed method in Habib et al., 2010b and Bang, 2010 overcome such limitations in the quasi-rigorous method. This method assumes that one is dealing with a linear scanner and the laser unit is nearly vertical (i.e., small pitch and roll angles). These assumptions lead to a more relaxed data requirement in the sense that only the trajectory position and time-tagged point cloud coordinates are required. However, one should note that for datasets captured by unsteady platforms (e.g., helicopters), where significant pitch and roll angles take place, the quality of the estimated parameters using this procedure might be negatively affected. The current calibration method proposed by Kersting et al., 2012, denoted as "Rigorous Calibration", is more flexible calibration procedure that can be carried out without strict requirements (e.g., flight, terrain coverage, control, and pre-processing requirements such as classification of the LiDAR point cloud into terrain/off-terrain features or segmentation of planar features). However, in this method, manually-selected overlapping strip pairs and regions among the overlapping strip pairs are utilized in LiDAR system calibration, where some problems could arise when using these manually-selected pairs/regions (i.e., non-uniform balance of the distribution of the slope and aspect values within the selected regions, redundant slope and aspect values, and dependence on the experience of the operator). Also, this method deals only with one unit in ALS system.

In contrast to ALS systems, the calibration of TMLS systems has been presented by few authors in the past few years. Some methods of acquiring suitable data for estimating the boresight angles between IMU and laser scanner of a TMLS system are introduced (Rieger et al., 2010; Glennie and Lichti (2010, 2011); Chan, 2011; Gerardo et al., 2011). Other methods require a terrestrially surveyed test site providing accurate absolute coordinates for, e.g., retro-reflective targets of known shape and size (Leslar, 2009; Chow et al., 2010). Other procedures rely on scanning objects of known size and position from different driving directions and distances (Morgan, 2009; Kumari et al., 2011). All these approaches lack of flexibility and demand high efforts on preparing special test sites. Measurement errors possibly introduced by the terrestrial surveys of reference objects decrease the confidence in the accuracy of the estimated mounting parameters. The estimation of the mounting parameters by analyzing distances between one and the same object appearing in two scans is often not automated and based on manual trial-and-error algorithms. Most of the calibration procedures of TLS and TMLS are usually carried out by the system manufacturer. Moreover, until now there is no commonly accepted methodology for accurately determining the intrinsic and mounting parameters of multi-TMLS systems.

Due to the rapid advancement of LiDAR systems and efforts in developing standards for the delivery of the LiDAR data, one should note that access to the system raw measurements is not the only requirement to have a rigorous calibration, which can be easily carried out by the end-users. A precise analysis of the necessary flight and control configuration requirements for reliable estimation of the system parameters is vital for an accurate and flexible LiDAR system calibration. Few authors have looked into the necessary flight and control configuration for LiDAR system calibration. A review of some of the existing works in this area is presented in the following section.

2.5 Overview of Required Flight and Control Configuration for Airborne LiDAR System Calibration

The necessary flight and control configuration requirements have been discussed by few authors to perform the calibration of airborne LiDAR systems. Burman, 2000 has introduced an analytical analysis of the recoverability of the boresight angles, datum shifts, and the elevation and intensity values at the interpolated grid cells using different configurations. The following configurations were investigated: one LiDAR strip, two LiDAR strips flown in opposite directions, and three LiDAR strips (i.e., two strips in opposite directions and one strip perpendicular to them). The analysis is performed with and without elevation and intensity gradients and with control information. The possibility of estimating the investigated parameters is analyzed for each scenario. The final recommended flight configuration, to give enough redundancy, consists of four strips flown in opposite and cross direction (Figure 2.8) along with control information.

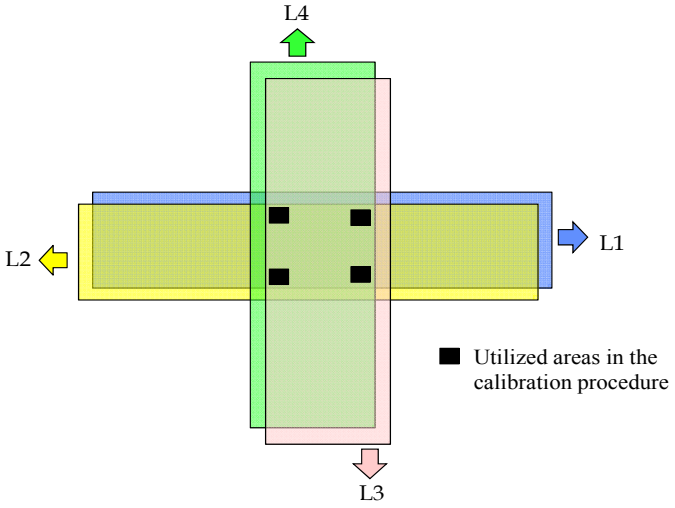

Figure 2.8. Recommended flight configuration for airborne LiDAR system calibration by Burman, 2000 (Adapted from Burman, 2000)

In Burman, 2000 the use of a calibration site with sloped terrain as well as the selection of regions close to the edges of the strips for the calibration procedure is suggested. In the performed analysis, high correlation among the parameters was still observed, e.g., the vertical datum shift and the elevation values at the grid cells, due to the nature of the proposed calibration procedure (the primitives are considered unknowns). The recoverability of the lever arm offset and systematic errors in the measured range and scan angle is not investigated.

The flight configuration proposed by (Morin, 2002) was devised for the recoverability of the boresight angles and the scale factor of mirror scanning angle while considering a flat calibration site. It is also based on the assumption that control points can be identified in overlapping strips. The recommended flight configuration is illustrated in Figure 2.9. The different flying heights were recommended to recover the boresight pitch angle. A bias in the boresight pitch angle ($\delta\Delta\omega$) cause a vertical discrepancy (Δh) between overlapping strips flown at different flying heights as shown in Equation 2.4 (Morin, 2002). One should note that for small values of $\delta\Delta\omega$, the vertical discrepancy will be very small, which might affect the reliability of the estimated parameter.

$$\Delta h = (H_1 - H_2)\left(\frac{1}{cos\delta\Delta\omega} - 1\right) \tag{2.4}$$

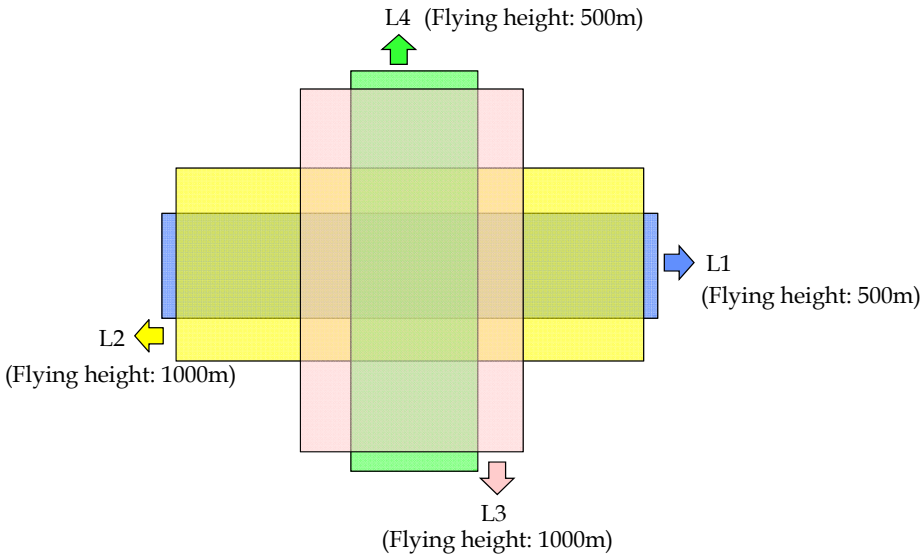

Figure 2.9. Recommended flight configuration for airborne LiDAR system calibration by Morin, 2002 (Adapted from Morin, 2002)

Kersting (2011) suggests that the optimum flight and control configuration for reliable estimation of the system parameters (i.e., the planimetric lever arm offset components, the boresight angles, the range bias, and the mirror angle scale) should consist of three side lap cases and one vertical control point as illustrated in Figure 2.10. As demonstrated in this figure, the optimum flight configuration consists of four LiDAR strips which are captured from two different flying heights in opposite directions with 100 % side lap, and two LiDAR strips, which are flown in the same direction with the least side lap possible (while having enough conjugate surface elements among the strips). However, in this method overlapping strip pairs/regions are manually selected for the calibration procedure. Some problems could arise when using these manually-selected pairs/regions (i.e., insufficient flight configuration, excessive slope and aspect values, and reliance on the experience of the operator). These problems might affect the reliability of the estimated parameters during the calibration procedure.

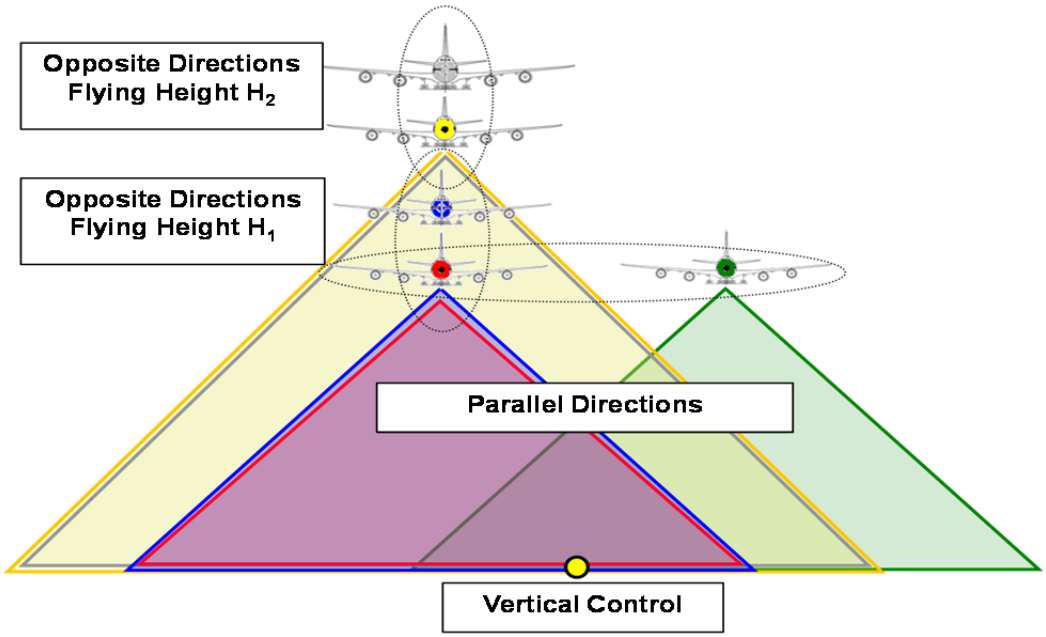

Figure 2.10. Recommended optimum flight and control configuration for airborne LiDAR system calibration by Kersting, 2011 (Adapted from Kersting, 2011)

Chapter Three: **AUTOMATIC SELECTION OF OVERLAPPING STRIP PAIRS/REGIONS**

3.1 Introduction

The development of the calibration procedure for LiDAR airborne devices is an important development for the early stages of LiDAR data processing (i.e., classification or segmentation of the point cloud). It is important to mention that in order to reliably estimate the system parameters through the calibration process, the calibration site should have topography with different slope and aspect, for instance, an area that has gable roof buildings with varying slope and aspect values. Figure 3.1 illustrates the calibration site utilized in this research, which covers an urban area with several gable roof buildings at different orientation.

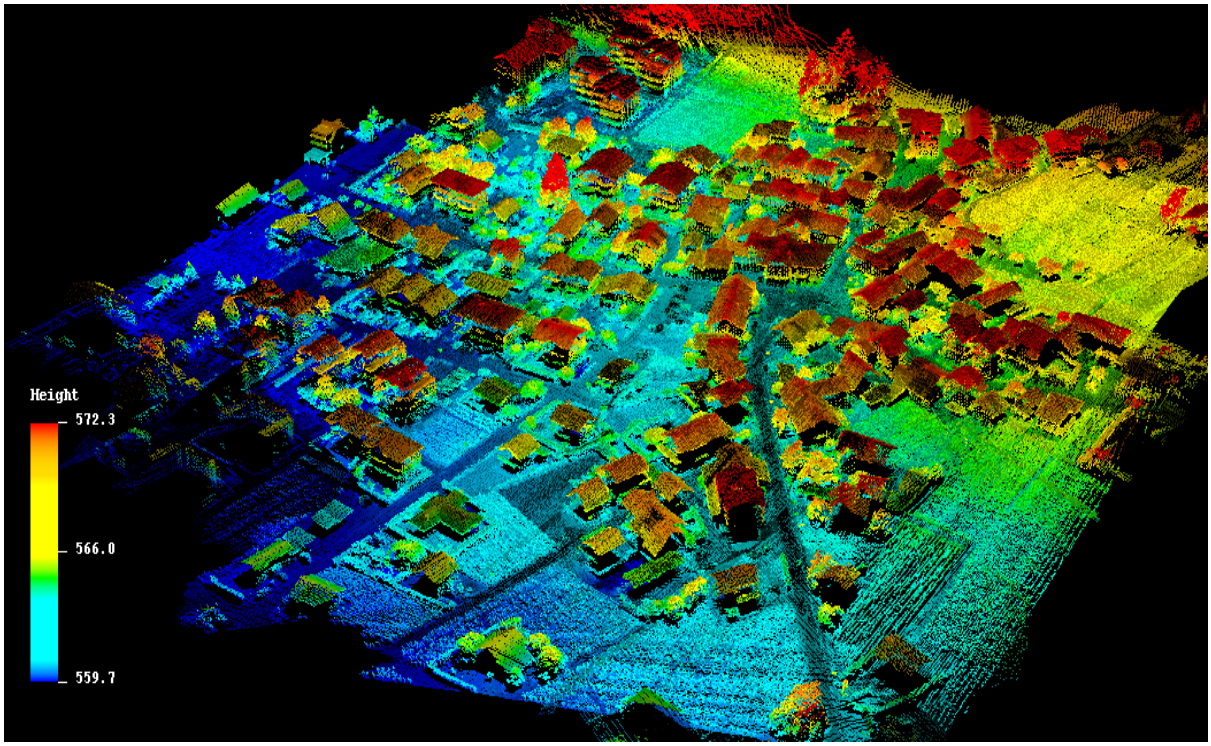

Figure 3.1. Perspective view of the calibration site over an area that includes gable roofs with varying slope and aspect (Source: Kersting, 2011)

The proposed method will be clarified with the help of a real dataset. The real dataset used to perform the experiments was captured by a compact LiDAR system built at École Polytechnique Fédérale de Lausanne (EPFL) (Skaloud et al., 2005). The system is operated from the side of a helicopter. The sensor head incorporates an LN200/A1 tactical grade IMU with 400 Hz measurement rate from Northtrop Grumann and a dual-frequency GPS receiver. The laser scanner is a short-range 2D scanner (Riegl LMS-Q240) with a scanning angle of 60° and maximal range of 450m at 80% reflectance (Skaloud and Lichti, 2006). The flight lines used in the calibration process and the available ground control points (10 signalized targets located along roads in the covered area) are illustrated in Figure 3.2.

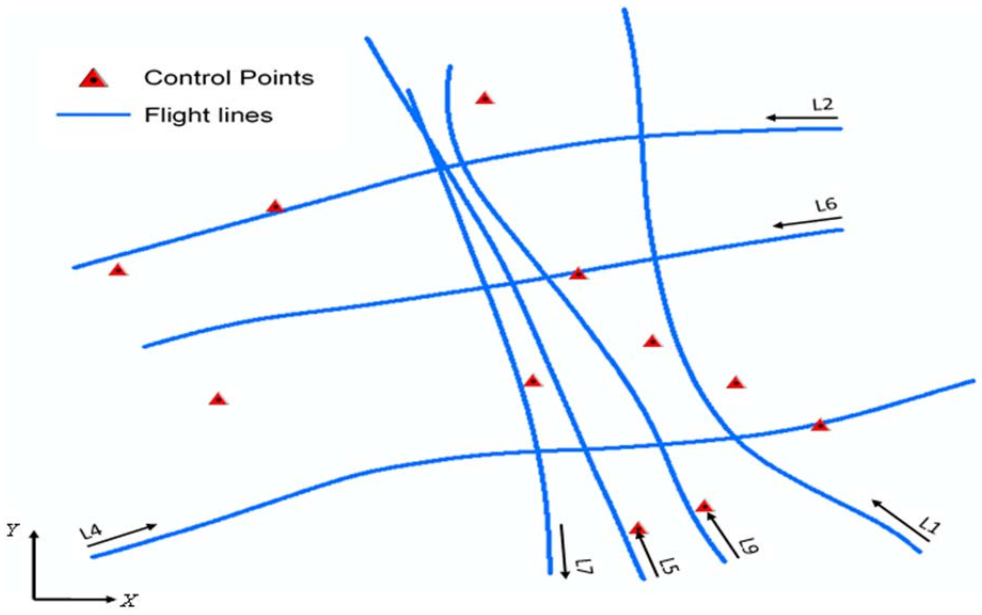

Figure 3.2. Flight and control configuration of the utilized real dataset

Typically, the undertaken steps during the current LiDAR system calibration procedure, which is proposed by (Kersting, 2011), include manual selection of overlapping strip pairs and regions with varying slope and aspect among the LiDAR strips as shown in Figure 3.3.

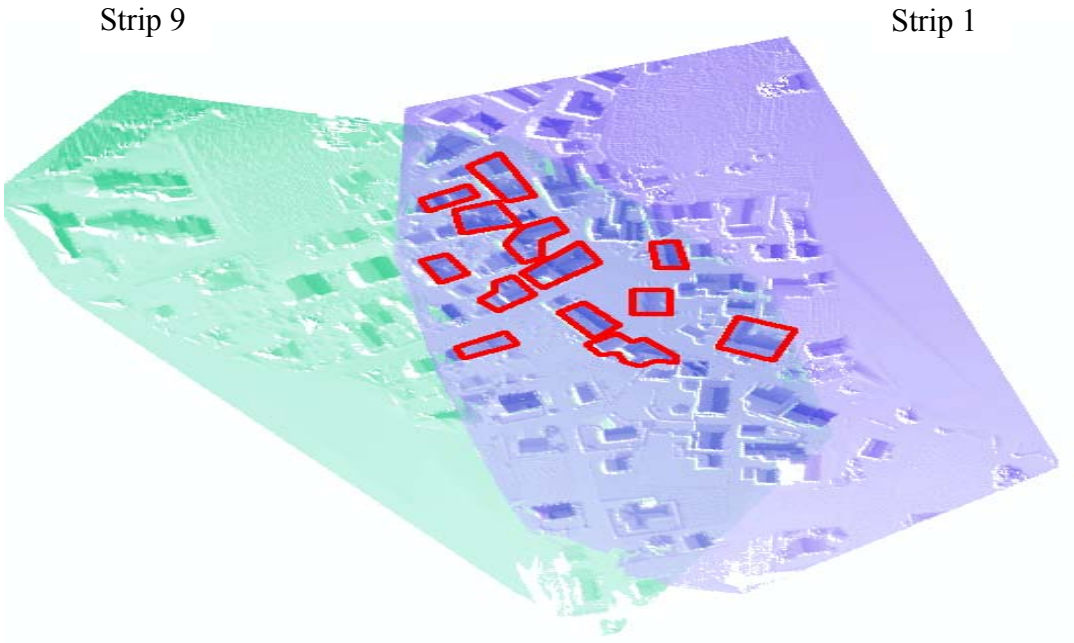

Figure 3.3. Sample of manually selected pairs/regions within the overlapping area between two LiDAR strips (1 and 9)

Some problems could arise when using these manually-selected pairs/regions as follows:

- Insufficient configuration will reduce the quality of the estimated parameters,
- Redundant slope and aspect will increase the execution time of the calibration procedure,
- The size of some regions might be larger than the others. This inhomogeneous distribution will cause overweighting for a specific slope and aspect values when compared to the other regions. As a result, such distribution will affect the quality of the estimated parameters, and
- The manual selection reliance on the experience of the operator.

These problems might affect the reliability of the estimated system parameters during the calibration procedure.

In this chapter, a novel method for automatic selection of suitable overlapping strip pairs/regions is introduced. The main objective of this method is to investigate the existing LiDAR system calibration technique which is proposed by (Kersting, 2011) and how to increase the efficiency of this technique as follows:

- Automatic selection of appropriate overlapping strip pairs, which should achieve the minimum optimal flight configuration that maximizes the impact of the discrepancies among conjugate surface elements in overlapping strips. As already mentioned in (Kersting, 2011), the recommended minimum optimal flight configuration consists of three overlapping strip pairs (two flown in different flying heights in opposite directions and one flown in parallel direction).

- Automatic selection of regions (planes) within the appropriate overlapping strip pairs. The main criteria for the selection of these regions are as follows:
  - The selected regions should exhibit good variation in the topography (i.e., surfaces with varying slope and aspect values should be utilized),
  - The selected regions should be well-distributed within the overlapping region, and
  - The selected regions should have a balance between their sizes (i.e, the regions with different slope and aspect should be of similar size).

Figure 3.4 shows the stages of the proposed methodology. A detailed description of this proposed methodology will be explained in the following sub-sections.

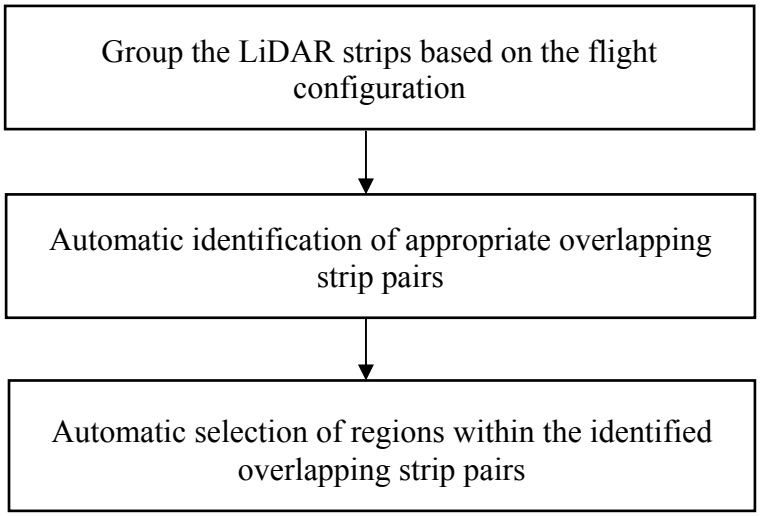

Figure 3.4. The flow chart for the automatic selection of overlapping strip pairs/regions.

3.2 Group the LiDAR Strips Based on the Flight Configuration

In this step, the average flying height and flight direction (heading angle) of each LiDAR strip (as shown in Figure 3.2) are computed. Table 3.1 presents examples of the average flying height and flight direction of each LiDAR strip. The LiDAR strips that have variations in the average flying heights within a predefined threshold (distance) are considered to be at the same flying height. Then, the LiDAR strips that have the same flying height are classified based on the flight direction into (parallel/cross/opposite) groups. Table 3.2 presents examples of different categories and groups of LiDAR strips based on the average flying heights and flight directions. From Tables 3.1 and 3.2 one can note that, strips (1, 2, 3, 4, and 9) have the same flying height, denoted as "Category 1", and strips (5, 6, 7, and 8) have a different flying height, denoted as "Category 2". In category 1, ten possible groups (parallel/cross/opposite) within the LiDAR strips are automatically identified. Also, in category 2, six possible groups within the LiDAR strips are automatically identified. Note, the ten and six possible pairs are the total number of combinations from the flight lines in each category taken two at a time regardless of their order.

Table 3.1. Average flying height and flight direction for the 9 strips in the involved dataset

Strip NO.	Average Flying Height (m)	Average Flight Direction (Heading Angle) (deg)
1	696	112
2	698	-155
3	693	-90
4	708	19
5	796	100
6	812	-172
7	795	-93
8	779	6
9	703	137

Table 3.2. Different categories and groups of LiDAR strips based on the flying heights and their relative flight directions

First strip	Second strip	Category based on the flying height	Flight Direction
1	9	Category 1	Parallel Direction
1	3		Opposite Direction
2	4		Opposite Direction
3	9		Opposite Direction
1	2		Cross Direction
1	4		Cross Direction
2	3		Cross Direction
2	9		Cross Direction
3	4		Cross Direction
4	9		Cross Direction
5	7	Category 2	Opposite Direction
6	8		Opposite Direction
5	6		Cross Direction
5	8		Cross Direction
6	7		Cross Direction
7	8		Cross Direction

3.3 Automatic Identification of Appropriate Overlapping Strip Pairs

The selection of suitable overlapping strip pairs will be achieved through the following two steps:

- Automatic extraction of the overlapping region between the grouped LiDAR strip pairs.
- Automatic identification of the appropriate overlapping strip pairs from each group to be used in the calibration procedure.

3.3.1 Automatic Extraction of the Overlapping Region between the Grouped LiDAR Strip Pairs

The idea of this method is to project the 3D LiDAR strip points for a given pair on a 2D grid. The cell dimension of the gird (x_dim, y_dim) should be greater than the average point spacing and expected voids in the LiDAR data (Lari and Habib, 2013). Figure 3.5 illustrates the flowchart of the proposed algorithm for deriving the overlapping region between two LiDAR strips. First, the maximum and minimum X and maximum and minimum Y of each LiDAR strip are computed as follows:

- $Xmax_1$, $Xmin_1$, $Ymax_1$, $Ymin_1$ – represent maximum and minimum X and maximum and minimum Y of the first strip respectively,
- $Xmax_2$, $Xmin_2$, $Ymax_2$, $Ymin_2$ – represent maximum and minimum X and maximum and minimum Y of the second strip respectively,

Then, the overall maximum and minimum X and maximum and minimum Y for both LiDAR strips are calculated as follows:

$$\text{Max\_X} = \max(Xmax_1, Xmax_2) \;\&\; \text{Min\_X} = \min(Xmin_1, Xmin_2)$$

$$\text{Max\_Y} = \max(Ymax_1, Ymax_2) \;\&\; \text{Min\_Y} = \min(Ymin_1, Ymin_2)$$

Second, empty three 2D grids, denoted as “Grid 1”, “Grid 2”, and “Grid 3” are created, where the cell size in each grid is (x_dim, y_dim). The extents X_range and Y_range of each grid are calculated as in Equation 3.1.

$$\text{X\_range} = \text{Max\_X} - \text{Min\_X} \quad \& \quad Y\_range = Max\_Y - Min\_Y \tag{3.1}$$

Third, Min_X and Min_Y are subtracted from each point in the first and second strips as in Equation 3.2.

$$i_1 = \frac{\text{Point\_1.X} - \text{Min\_X}}{\text{x\_dim}} \quad \& \quad j_1 = \frac{\text{Point\_1.Y} - \text{Min\_Y}}{\text{y\_dim}}$$

$$i_2 = \frac{\text{Point\_2.X} - \text{Min\_X}}{\text{x\_dim}} \quad \& \quad j_2 = \frac{\text{Point\_2.Y} - \text{Min\_Y}}{\text{y\_dim}} \tag{3.2}$$

Where:

- Point_1 represents the point in question in the first strip (for example, strip 1)
- Point _2 represents the point in question in the second strip (for example, strip 9)

Then, the cell index (i_1, j_1) for each point in strip1 is identified in Grid 1 as covered cell (√) and the cell index (i_2, j_2) for each point in strip 9 is identified in Grid 2 as covered cell (√). Finally, Grid 1 and 2 are re-scanned and the points within the covered cells by both strips are only included in Grid 3, which represents the common overlapping region between two LiDAR strips.

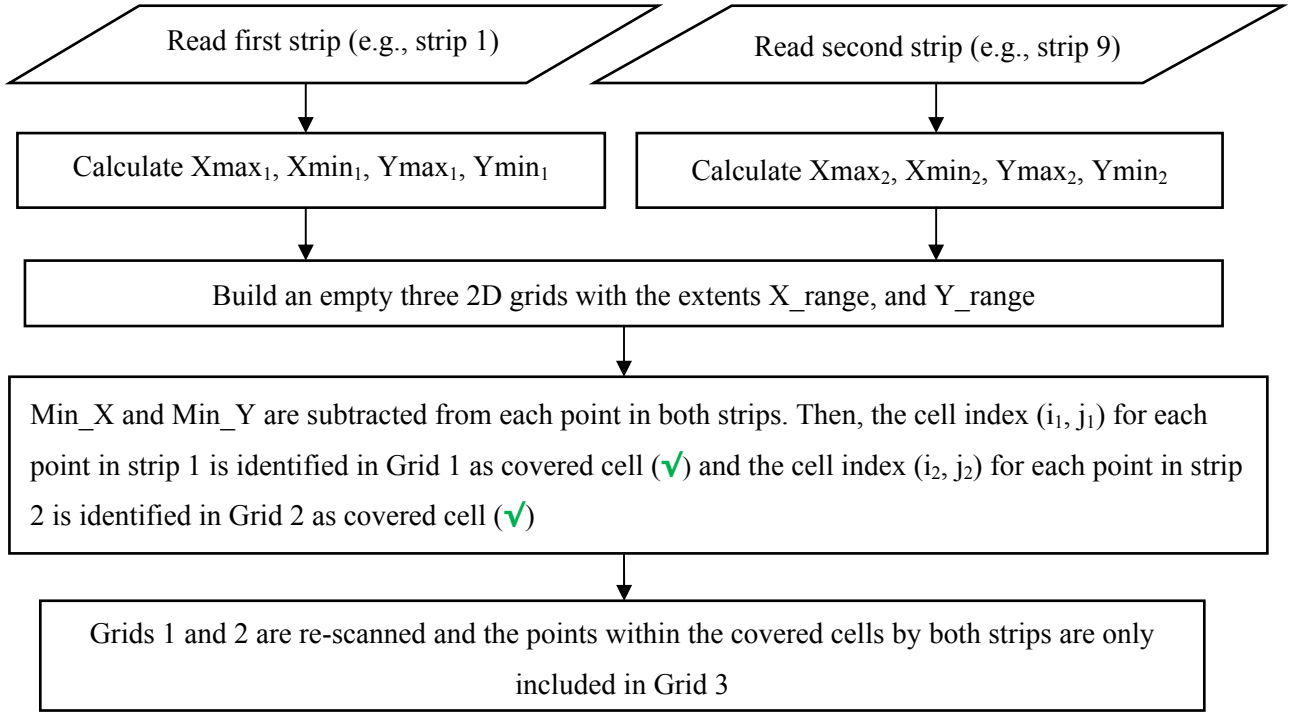

Figure 3.5. The flow chart for deriving the overlapping region between LiDAR Strips

Figure 3.6 shows a visualization of samples of LiDAR strips (strip 1 and strip 9). Figure 3.7 shows the selected overlapping region between two LiDAR strips (related to the illustrated strips in Figure 3.6), where the overlapping cells are labeled by (√) and the non-overlapping cells are labeled by (x). Figure 3.8 shows a visualization of the selected overlapping area between the two LiDAR strips in question (related to the illustrated strips in Figure 3.6).

Strip 9 Strip 1

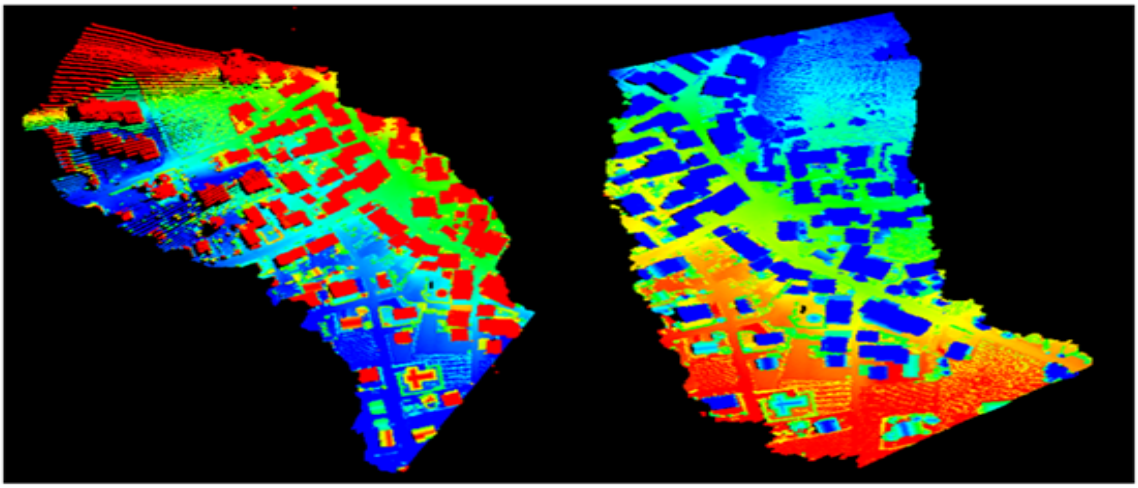

Figure 3.6. Visualization of samples of LiDAR strips

Figure 3.7. The selected overlapping region between two LiDAR strips (1&9) (√)

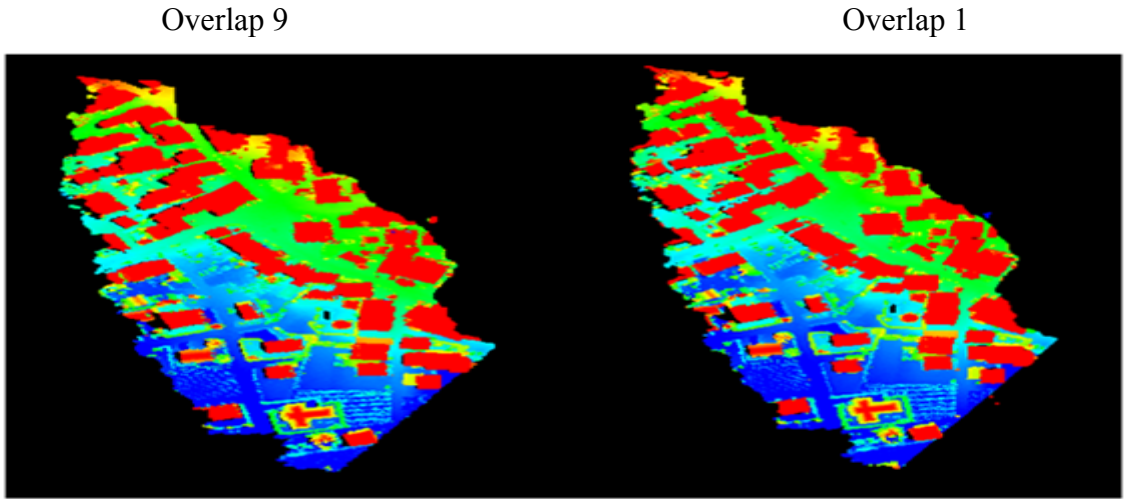

Figure 3.8. Visualization of the overlapping region between two LiDAR strips (1 and 9)

3.3.2 Automatic Identification of Appropriate Overlapping Strip Pairs from each Group

From the previous step, all possible overlapping regions between the LiDAR strip pairs in each category are identified. One might ask, what is the criteria to select the most suitable overlapping strip pairs which should achieve the minimum optimal flight configuration (two overlapping strip pairs flown in different flying heights in opposite directions and one overlapping strip pair flown in parallel direction) to be used in the calibration procedure?

The number of points in the overlapping area, as a measure or criteria to choose the suitable overlapping strip pairs, is not enough since some regions among the overlapping area that have the necessary slope and aspect angles and a balanced distribution might not be represented. Additionally, the number of regions among the overlapping area is also not sufficient as a measure or criteria to select the appropriate overlapping strip pairs because the slope and aspect angles of the available regions do not cover the required slope and aspect range for accurate calibration. As mentioned in section 2.1, regions with varying slope and aspect angles within the overlapping strips can be used as suitable regions to represent the LiDAR surfaces. In this step,

in each category, one of the overlapping strip pairs is segmented into homogenous clustered regions. The objective of the segmentation process is to cluster the points with similar attributes into homogenous regions and introduce some level of organization to the data before the extraction of useful information. In the past few years, several methods have been suggested for the segmentation of 3D laser data, which are generally divided into three classes: region growing, model fitting methods, and clustering of attributes (Lari and Habib, 2013). The segmentation method based on clustering of attributes is a robust approach for the identification of homogenous patterns in the data (Lari and Habib, 2013). The applied segmentation process in this research work is proposed by Lari and Habib, 2013. This method is categorized under the class of clustering of attributes. From this method, clustered segments or regions sharing similar properties can be obtained and will be used as suitable clustered regions for the selection of the most appropriate overlapping pairs and the calibration process. Figure 3.9 shows sample of segmented clusters within one strip from a given pair (related to the illustrated strips in Figure 3.8) that include gable roofs with varying slope and aspect angles. In this figure, different colors signify different segmented clusters.

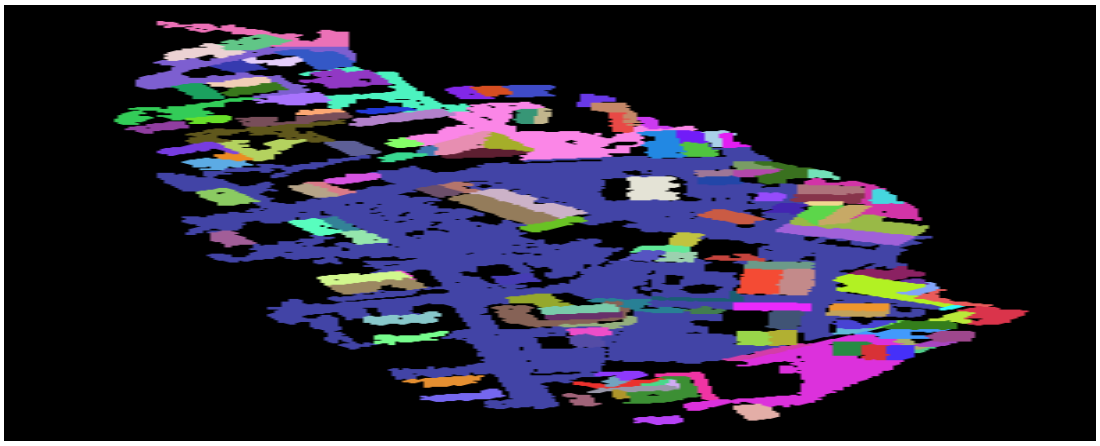

Figure 3.9. Visualization of segmented clusters within one overlapping strip from a given pair that include some gable roofs with varying slope and aspect

The proposed method in this research work establishes the variations in slope and aspect angles (angular coverage) of clustered regions within overlapping strip pairs as a suitable measure to select the appropriate overlapping strip pairs to be used in LiDAR system calibration. Figure 3.10 illustrates the flowchart for deriving an estimate of the angular coverage. First, an angular coverage grid is created with pre-defined cell dimensions (Slope_Step, Aspect_Step) to represent the covered slope and aspect angles of each clustered region in the overlapping area as shown in Figure 3.11. From the segmentation process, the surface normal component (n_x, n_y, n_z) of each clustered region is calculated. Second, the slope (α) and aspect (θ) for each given clustered region are computed as shown in Figure 3.12. Third, the corresponding angular coverage aspect and slope indices (C_i, C_ j) for each clustered region are calculated as in Equations 3.3 and 3.4. Then, the cell at (C_i, C_ j) is labeled as a covered cell (√) as shown in Figure 3.11. One can note that in Equation 3.3, π is added to θ because the outcome from the atan2 function will be within the range of $[-\pi, \pi]$. Also, in Equation 3.4, $\frac{\pi}{2}$ is added to α because the outcome from the arcsine function will be within the range of $[-\frac{\pi}{2}, \frac{\pi}{2}]$.

$$C\_i = (\theta + \pi) * 180 / (\pi * Aspect\_\text{Step}) \tag{3.3}$$

$$C\_j = (\alpha + \pi / 2) * 180 / (\pi * \text{S}lpoe\_\text{Step}) \tag{3.4}$$

The second and third steps are repeated until the all clustered regions are investigated. Finally, the angular coverage is calculated according to in Equation 3.5.

$$\text{angular coverage} = \frac{\text{Number of non - empty cells in the angular coverage grid}}{\text{Total number of cells in the angular coverage grid}} * 100 \tag{3.5}$$

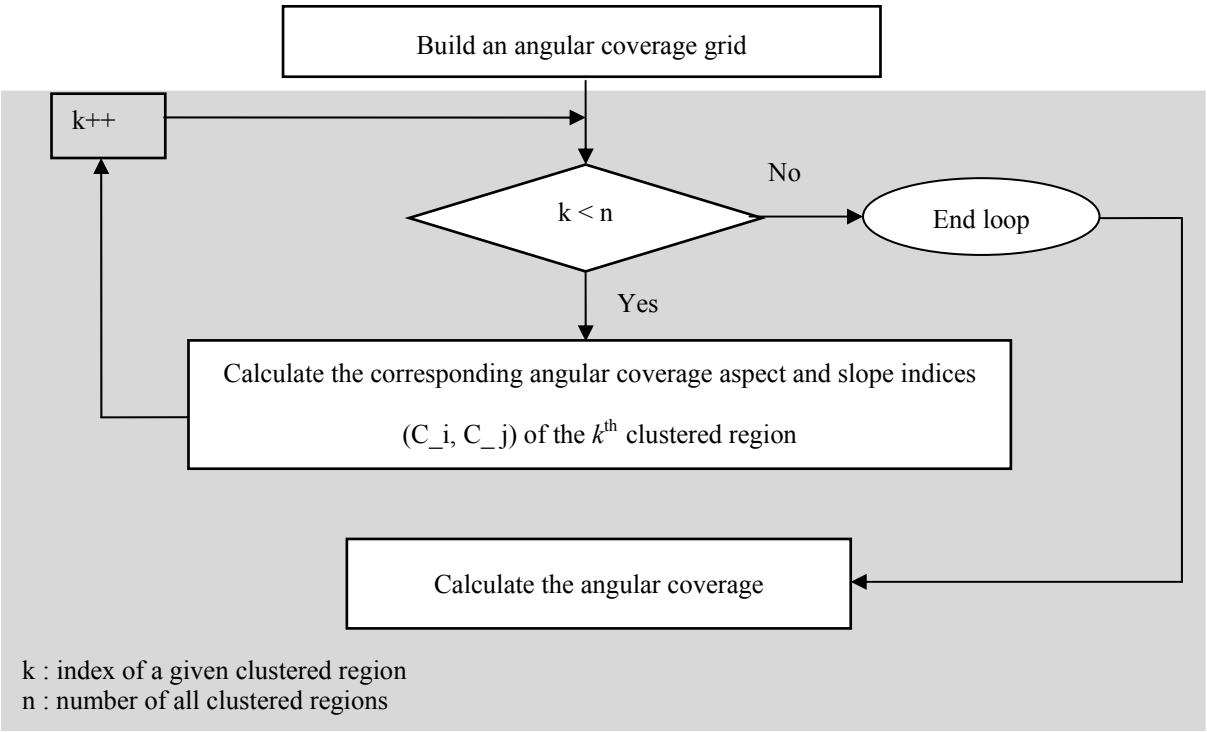

Figure 3.10. The flow chart for deriving an estimate of the angular coverage

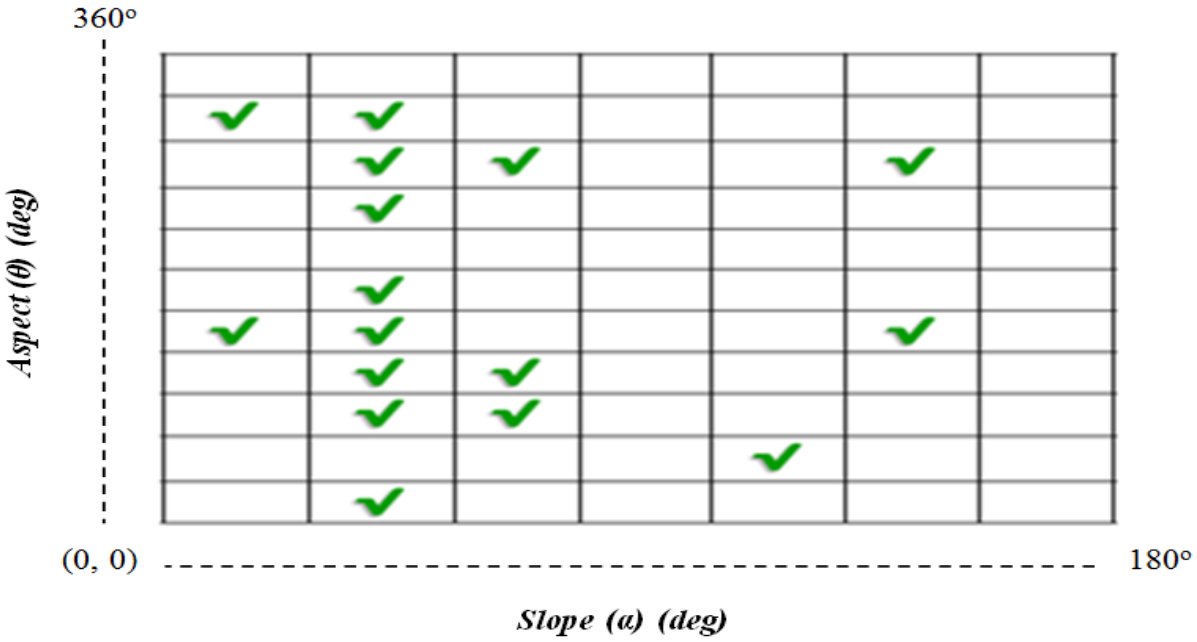

Figure 3.11. The grid representation of the covered slope/aspect angles by segmented clusters

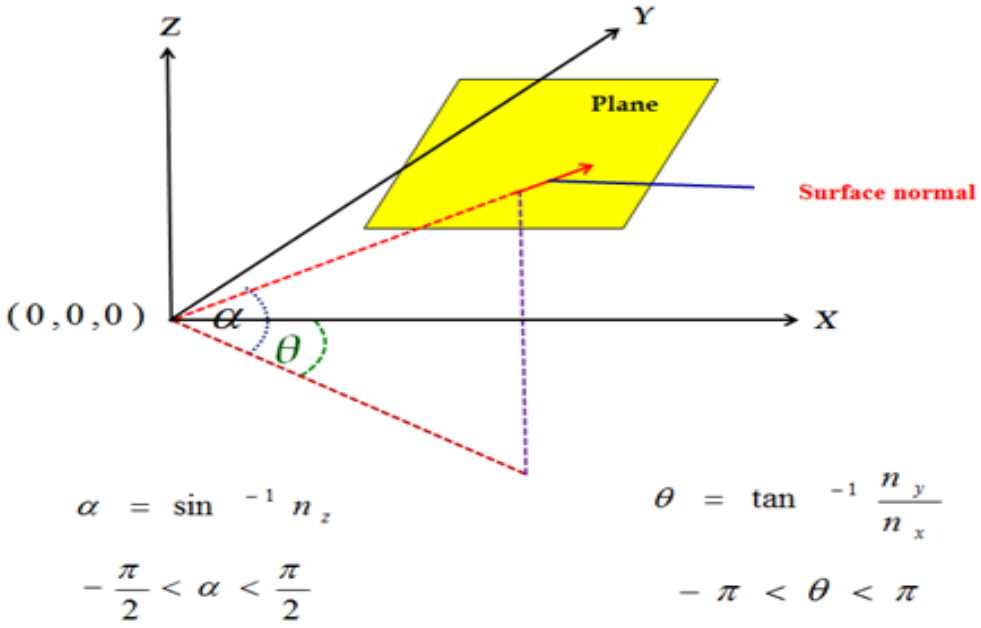

Figure 3.12. The evaluation of the slope (α) and aspect (θ) angles for a given cluster

The angular coverage percentages are calculated for all possible overlapping strip pairs in each category. As mentioned ealier, the minimum optimal flight configuration includes opposite and parallel groups of LiDAR strip pairs, therefore the cross groups in each category are excluded (as presented in Table 3.3). The answer of the pervious question (what is the criteria for selection the most suitable overlapping strip pairs which should achieve the minimum optimal flight configuration) is the overlapping strip pair with high angular coverage percentage in each group is selected for the calibration procedure. In case two or more overlapping strip pairs have similar angular coverage percentages (refer to overlapping strip pairs (2&4), and (3&9)), the overlapping strip pair with higher overlap percentage is selected for the calibration procedure. The overlap percentage is calculated as in Equation 3.6.

$$\text{overlap percentage} = \frac{\text{Number of points in the overlapping area}}{\text{Total number of points in the original LiDAR strip}} * 100 \quad (3.6)$$

From Table 3.3, one can deduce that the selected overlapping strip pairs form each group are (2&4), (1&9), and (5&7).

Table 3.3. Samples of overlapping strip pairs that have been based on angular coverage percentage

First strip	Second strip	Category based on flying height	Flight Direction	Overlap Percentage (%)	Angular coverage Percentage (%)
1	9		Parallel Direction	75%	13 %
1	3	Category 1	Opposite Direction	22%	5 %
2	4		Opposite Direction	42%	8%
3	9		Opposite Direction	40%	8 %
5	7	Category 2	Opposite Direction	64%	11 %
6	8		Opposite Direction	60%	8 %

3.4 Automatic Selection of Regions within the Selected Overlapping Strip Pairs

From the previous steps, the suitable overlapping strip pairs are selected. The objective of this step is to ensure the quality of the estimated parameters and increase the computational speed of the calibration process by reducing the number of clustered regions among the overlapping strip pairs, while maintaining the candidate clustered regions with good variations in slope, aspect, and covered range over the whole overlapping area as much as possible. The proposed technique is based on the following two steps:

- Selection of candidate clustered regions with good variations in slope and aspect angles,
- Selection of candidate clustered regions that are well-distributed within the whole overlapping area.

3.4.1 Selection of the Clustered Regions Based on their Slopes and Aspects

The purpose of this step is to minimize the number of clustered regions by removing the clustered regions with redundant slope and aspect angles while maintaining the clustered regions with large size (maximum number of points). The method of selecting the candidate clustered regions with good variations in slope and aspect angles can be summarized as follows:

- First, from the previous steps that were discussed in Figure 3.10, the covered slope and aspect angles of each clustered region in the overlapping area is represented in the angular coverage grid.
- Then, for each covered cell in the angular coverage grid, all clustered regions inside this cell are checked and the clustered region with the maximum size (maximum number of points) is selected as a candidate region. The selected region will be added to the possible candidate clusters that will be used in the calibration process.

Figure 3.13 shows sample of automatically selected clustered regions based on the slope and aspect criteria (related to the illustrated strip in Figure 3.9).

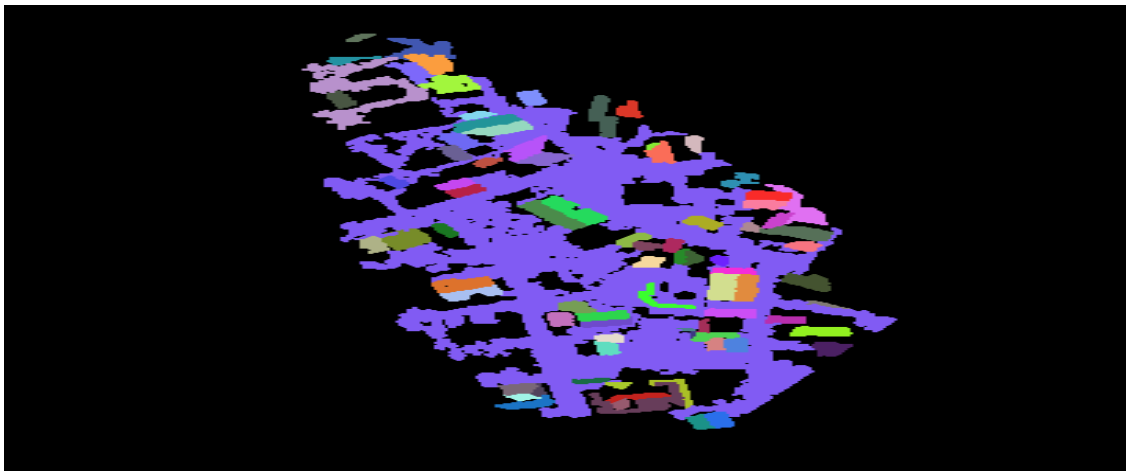

Figure 3.13. Visualization of automatically selected clustered regions based on the slope and aspect criteria

3.4.2 Selection of Appropriate Clustered Regions Based on Their Distribution in the Whole Overlapping Area.

The objective of this step is to ensure that all clustered regions are well-distributed over the whole overlapping area and these different clustered regions have a balance between their sizes. In other words, if one clustered region is excessively larger than the others, it will cause overweighting for specific slope and aspect values when compared to the other clustered regions. Hence, the quality of the estimated parameters in the calibration procedure will be affected. In this step, the new candidate clusters that are chosen by their distribution, and not chosen before by their slope and aspect angles, will be added to the possible candidate clusters used in the calibration process. The algorithm of selecting the candidate clustered regions based on their distribution over the whole overlapping area can be summarized as follows:

- First, an empty 2D grid is created to represent the extent of the overlapping area. This grid is divided into cells based on the dimensions of the overlapping area.
- Second, one can note from Figure 3.13 that the biggest clustered region is the ground and it is extended over the whole overlapping area. If the ground is showing good distribution of slope and aspect values, it should not be excluded. In the case that appears in Figure 3.13, the ground can be excluded as follows:
  - For each given cell in the gird, all clustered regions which have any points inside that cell are checked and for each given clustered region, if 50% or more of their points are inside that cell, this region is kept. One can note that this constraint will ensure the biggest clustered region (i.e., ground) is excluded because 50% or more of their points cannot completely be inside one cell in the grid.

- Then, all kept regions inside a given cell are checked and the region with the maximum ratio (number of points of a given region inside the cell divided by total number of points of a given region) is selected as a candidate region based on the distribution criteria.

- Finally; all candidate clusters that have been based on the slope and aspect criteria are checked. If the new candidate cluster that has been based on the distribution criteria is not chosen before by the slope and aspect criteria, then this cluster will be added to the possible candidate clusters.

At the end, the list of possible candidate clusters holds the candidate clusters that have been based on the slope and aspect criteria as well as the candidate clusters that have been based on the distribution criteria. Figure 3.14 shows sample of automatically selected clustered regions among overlapping strip pairs (related to the displayed clustered regions in Figure 3.13).

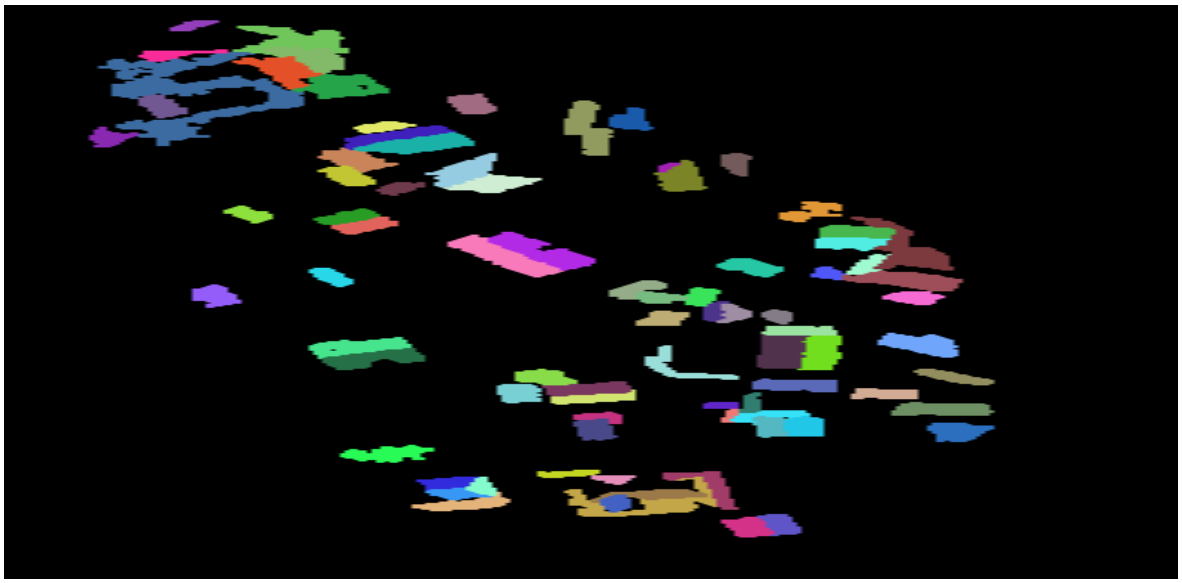

Figure 3.14. Visualization of automatically selected candidate clustered regions for one of the selected overlapping strip pairs

Table 3.4 presents samples of automatically selected candidate clustered regions with different slopes, aspects, and distribution among the selected overlapping strip pairs. From Table 3.4 one can deduce that the number of candidate clustered regions is reduced compared to the total number of clustered regions among the overlapping strip pairs while maintaining the representation of the candidate clustered regions with good variations in slope, aspect, and distribution.

Table 3.4. Samples of automatically selected clustered regions with different slopes, aspects, and distribution among the selected overlapping strip pairs

First strip	Second strip	Flight Direction	Total number of clustered regions	Number of utilized regions in the calibration
1	9	Parallel Direction	157	83
2	4	Opposite Direction	117	55
5	7	Opposite Direction	150	74

3.5 Summary

It is important to state that for reliable estimation of the system parameters using the calibration procedure, the calibration site should have topography with varying slope and aspect values. The current LiDAR system calibration procedure, which is proposed by (Kersting, 2011), based on manual selection of overlapping strip pairs and regions with varying slope and aspect among the LiDAR strips. Some problems could arise when using these manually-selected pairs/regions. In this chapter, a method for automatic selection of suitable overlapping strip pairs/regions has been introduced. The main objective of the proposed method is to look into the existing LiDAR system calibration technique proposed by (Kersting, 2011), and to study how to improve the efficiency of this technique as follows:

- Automatic selection of suitable overlapping strip pairs, which should achieve the minimum optimal flight configuration that maximizes the impact of the discrepancies among conjugate surface elements in overlapping LiDAR strips. The recommended minimum optimal flight configuration which is proposed by (Kersting, 2011), consists of three overlapping strip pairs (two flown in different flying heights in opposite directions and one flown in parallel direction).

- Automatic selection of regions within the suitable overlapping strip pairs. The main criteria for the selection of these regions are as follows:

  – The candidate regions should have good variation in the topography (i.e., surfaces with varying slope and aspect values).

  – The candidate regions should be well-distributed within the overlapping area.

  – The candidate regions should have a balance between their sizes.

The contributions of the proposed method can be summarized as follows:

- The proposed method is fully automated and does not rely on the operator, while the manual selection of overlapping pairs/regions relies on the experience of the operator,

- Appropriate overlapping strip pairs which should achieve the minimum optimum flight configuration are automatically selected. Also, regions which represent suitable LiDAR surfaces (regions with varying slope, aspect, and distribution among the overlapping strips) to be used in the calibration procedure are automatically selected compared to the manual selection of overlapping pairs/regions proposed by (Kersting, 2011),

The general hypotheses, which will be tested in the experimental results section, can be summarized as follows:

- The quality of the estimated parameters using the automatic selection are quite comparable to the estimated parameters using the manual selection,
- The processing time of automatic selection is faster than the manual selection,
- The proposed method leads to accurate estimation of the calibration parameters, and
- The proposed method is used for faster and reliable LiDAR system calibration.

Chapter Four: **CALIBRATION TECHNIQUE OF AIRBORNE MULTI LASER SCANNING SYSTEMS**

4.1 Introduction

In the field of surveying and mapping in recent years, the development of airborne LiDAR systems is characterized by the use of multiple laser scanners (for example, RIEGL BP-560 and OPTECH ALTM Pegasus, as shown in Figure 4.1) for accurate and efficient capture of 3D data of ground and above ground. The accuracy of the LiDAR point cloud from different sensors is very dependent on the calibration of the system. In order to fully attain the potential accuracy of the system and guarantee accurate multi-sensor integration, accurate system calibration should be carried out. System calibration for each laser scanner involves the following parameters:

- Calibration of the intrinsic parameters (i.e., laser ranging and scanning unit) and,
- Calibration of the mounting parameters (i.e., lever arm offset and boresight angles) relating to the IMU body frame.

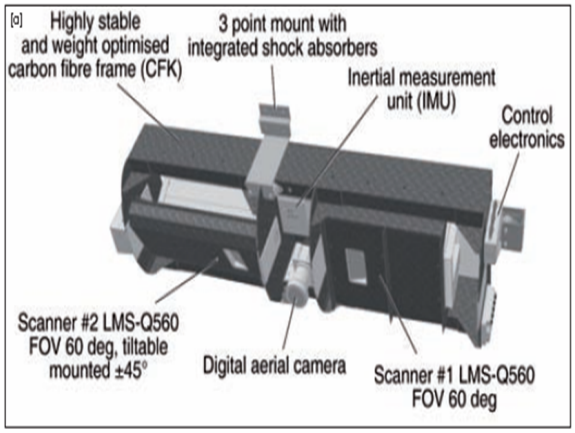

www.riegl.com/fileadmin/user_upload/Press/ Petrie_Airborne_Topographic_Laser_Scanners_GEO_1_2011.pdf

(a)

http://www.optech.ca/pegasus.htm

(b)

Figure 4.1. Examples of ALS multi-laser scanning systems: (a) RIEGL BP-560, (b) OPTECH ALTM Pegasus

Figure 4.2 shows the configuration of the mounting parameters relating the different laser scanners to the IMU body frame. The existing calibration technique proposed in Kersting, 2011 denoted as "Rigorous Calibration", assumes that all overlapping strips are imaged by the same scanner (i.e., only one laser scanner in the system). In this research work, new calibration procedure for dealing with multi-laser scanning systems is introduced. The main objective of the proposed calibration method is to estimate the system parameters (the mounting parameters relating the individual scanners to the IMU body frame and the intrinsic parameters of each scanner) that minimize the discrepancies between conjugate surface elements in overlapping LiDAR strips and overlapping LiDAR and control surfaces. The implementation of the new model of the calibration technique, which deals with multi-laser scanning systems, is explained in the following sub-sections.

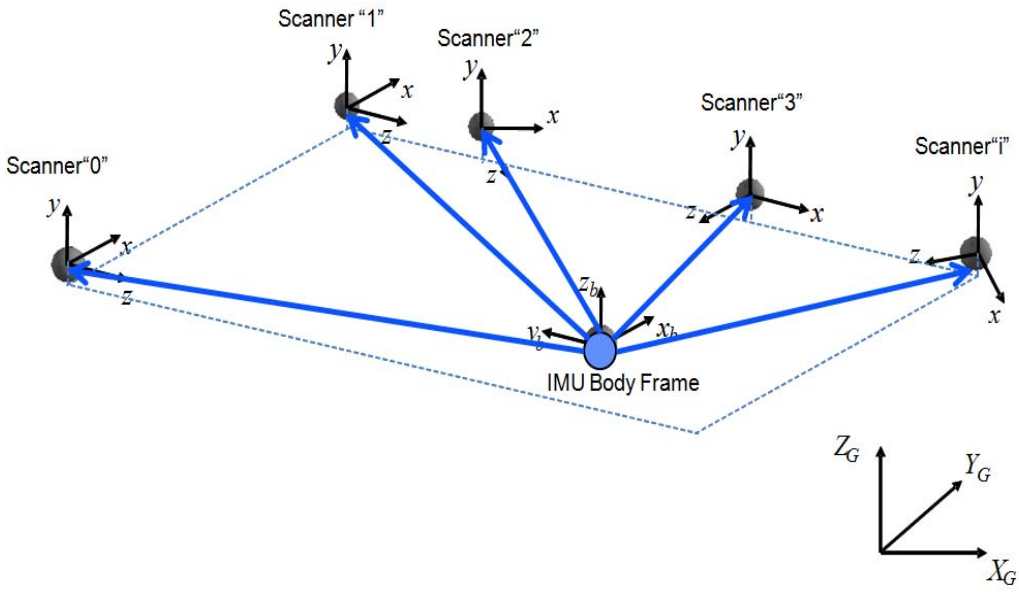

Figure 4.2. Configuration of the mounting parameters relating the different scanners to the IMU body frame.

4.2 The Proposed Mathematical Model

The relationship between the LiDAR point coordinates, the system measurements, and parameters associated with the i^{th} scanner are expressed through the LiDAR point positioning equation represented in Equation 4.1.

$$r_I^m = r_b^m(t) + R\,{}_b^m(t)\, r_{lu_i(\Delta X_i, \Delta Y_i, \Delta Z_i)}^b + R\,{}_b^m(t)\, R_{lu_i(\Delta\omega_i, \Delta\varphi_i, \Delta\kappa_i)}^b\, R_{lb_i}^{lu_i}(t)_{(S_{\alpha i}\alpha i, S_{\beta i}\beta i)}\, r_I^{lb_i}(t)_{(\rho_i + \Delta\rho_i)} \quad (4.1)$$

Where:

- r_I^m is the position of the laser point,
- $r_{lu_i}^b\ (\Delta X_i, \Delta Y_i, \Delta Z_i)$ lever arm offset – is the vector from the origin of the IMU coordinate system to the origin of the i^{th} scanner coordinate system,
- $R\,{}_{lu_i}^b\ (\Delta\omega_i, \Delta\varphi_i, \Delta\kappa_i)$ boresight matrix – is the rotation matrix relating the IMU and the i^{th} scanner coordinate systems,
- $r_I^{lb_i}(t)$ is the laser range vector associated with the i^{th} scanner, whose magnitude (ρ_i) is equivalent to the distance from the laser firing point to its footprint, and $\Delta\rho_i$ is a constant bias in the laser range measurements,
- $R_{lb_i}^{lu_i}(t)$ is the rotation matrix relating the laser unit and laser beam coordinate systems associated with the i^{th} scanner, which is defined by the mirror scan angle α_i and β_i, and
- $S_{\alpha i}$, $S_{\beta i}$ are scale factors for the mirror scan angles.

The LiDAR point positioning equation in Equation 4.1 can be represented in a symbolic form by Equation 4.2. This equation indicates that the true coordinates of a given point I $\left(r_I^m(True)\right)$ are derived using the true values of the system parameters $(\vec{x}_i)$ and the noise-free measurements $(\vec{l}_{nfi})$ associated with the i^{th} scanner. The system parameters comprise the mounting parameters

($\Delta X_i, \Delta Y_i, \Delta Z_i, \Delta\omega_i, \Delta\varphi_i,$ and $\Delta\kappa_i$) relating i^{th} scanner to the reference frame of the navigation unit (IMU body frame) and the intrinsic parameters ($\Delta\rho_i$, $S_{\alpha i}$, and $S_{\beta i}$) of the i^{th} scanner.

The true values of the system parameters are unknown (i.e., they are determined in the calibration procedure) while the system measurements ($\vec{l}_{ni}$) are contaminated with noise ($\vec{e}_i$) whose magnitude depends on the system's measurements precision.

$$r_I^m(true) = f\left(\vec{x}_i, \vec{l}_{nfi}\right) \tag{4.2}$$

Where:

- $\vec{l}_{nfi} = \vec{l}_{ni} - \vec{e}_i,$

If one has two conjugate points in overlapping strips where these overlapping strips are imaged by different laser scanners, these conjugate points will be denoted by subscripts A and B. The difference between the true coordinates of these points (i.e., r_A^m(True) and r_B^m(True)) can be expressed by Equation 4.3. In a similar fashion, if one is dealing with conjugate points in a LiDAR strip and control surface, the difference between the coordinates of the control point and the true coordinates of the LiDAR point in the strip denoted by subscript B can be expressed as in Equation 4.4. Equations 4.3 and 4.4 represent the mathematical model (observation equations) when dealing with overlapping strips and control data, respectively.

$$r_A^m(True) - r_B^m(True) = f\left(\vec{x}_i, \vec{l}_{n_{iA}} - \vec{e}_{iA}\right) - f\left(\vec{x}_j, \vec{l}_{n_{jB}} - \vec{e}_{jB}\right) = 0 \tag{4.3}$$

$$(r_{control}^m - \vec{e}_{control}) - r_B^m(True) = (r_{control}^m - \vec{e}_{control}) - f\left(\vec{x}_j,\ \vec{l}_{n_{jB}} - \vec{e}_{jB}\right) = 0 \tag{4.4}$$

Where:

$\vec{x}_i$ refers to the unknown system parameters associated with the i^{th} scanner,

$\vec{x}_j$ refers to the unknown system parameters associated with the j^{th} scanner,

$\vec{l}_{n_{iA}}$ refers to the system measurements associated with the i^{th} scanner that captures strip A,

$\vec{l}_{n_{jB}}$ refers to the system measurements associated with the j^{th} scanner that captures strip B,

$\vec{e}_{iA}$ refers to the system measurement noise associated with the i^{th} scanner that captures strip A, and

$\vec{e}_{jB}$ refers to the system measurement noise associated with the j^{th} scanner that captures strip B.

Since these equations are not linear with respect to the unknown system parameters and measurement noise, a linearization process by Taylor series expansion is required for the Least Square Adjustment (LSA). The linearized equations when using overlapping strips and control information are presented in Equations 4.5 and 4.6, respectively. These equations are obtained using the noise-contaminated system measurements $(\vec{l}_{niA})$ and $(\vec{l}_{njB})$ as well as the initial approximations for the unknown system parameters $(\vec{x}_{oi})$ and $(\vec{x}_{oj})$ associated with i^{th} and j^{th} scanner as the point of expansion while ignoring second and higher order terms.

$$r_A^m(True) - r_B^m(True) \cong f(\vec{x}_{oi}, \vec{l}_{n_{iA}}) + \partial f/\partial \vec{x}|_{\vec{x}_{oi},\vec{l}_{n_{iA}}} \delta\vec{x}_i + \partial f/\partial \vec{l}\big|_{\vec{x}_{oi},\vec{l}_{n_{iA}}} (-\vec{e}_{iA})$$

$$-f(\vec{x}_{oj}, \vec{l}_{n_{jB}}) - \partial f/\partial \vec{x}|_{\vec{x}_{oj},\vec{l}_{n_{jB}}} \delta\vec{x}_j - \partial f/\partial \vec{l}\big|_{\vec{x}_{oj},\vec{l}_{n_{jB}}} (-\vec{e}_{jB}) = 0 \qquad (4.5)$$

$$(r_{control}^m - \vec{e}_{control}) - r_B^m(True) \cong (r_{control}^m - \vec{e}_{control}) - f(\vec{x}_{oj}, \vec{l}_{n_{jB}}) - \partial f/\partial \vec{x}|_{\vec{x}_{oj},\vec{l}_{n_{jB}}} \delta\vec{x}_j -$$

$$\partial f/\partial \vec{l}\big|_{\vec{x}_{oj},\vec{l}_{n_{jB}}} (-\vec{e}_{jB}) = 0 \qquad (4.6)$$

Where:

$\vec{x}_{oi}$ refers to the initial approximations for the unknown system parameters associated with the i^{th} scanner, and

$\vec{x}_{oj}$ refers to the approximations for the unknown system parameters associated with the j^{th} scanner.

Rearranging the terms in Equations 4.5 and 4.6, one can get the final form of the linearized observation equations (Equations 4.7 and 4.8) according to the traditional Gauss Markov stochastic model (Equation 4.9).

$$f(\vec{x}_{oi}, \vec{l}_{n_{iA}}) - f(\vec{x}_{oj}, \vec{l}_{n_{jB}})$$

$$= -\partial f/\partial \vec{x}|_{\vec{x}_{oi},\vec{l}_{n_{iA}}} \delta\vec{x}_i + \partial f/\partial \vec{x}|_{\vec{x}_{oj},\vec{l}_{n_{jB}}} \delta\vec{x}_j + \partial f/\partial \vec{l}\big|_{\vec{x}_{oi},\vec{l}_{n_{iA}}} \vec{e}_{iA} - \partial f/\partial \vec{l}\big|_{\vec{x}_{oj},\vec{l}_{n_{jB}}} \vec{e}_{jB} \quad (4.7)$$

$$r^m_{control} - f(\vec{x}_{oj}, \vec{l}_{n_{j_B}}) = \partial f/\partial \vec{x}|_{\vec{x}_{0j},\vec{l}_{n_{jB}}} \delta\vec{x}_j + \vec{e}_{control} - \partial f/\partial \vec{l}\big|_{\vec{x}_{oj},\vec{l}_{n_{jB}}} \vec{e}_{jB} \quad (4.8)$$

$$\vec{y}_{3\times1} = A_{i_{(3\times9)}}\, \delta\vec{x}_{i_{(9\times1)}} + A_{j_{(3\times9)}}\, \delta\vec{x}_{j_{(9\times1)}} + \vec{e}_{(3\times1)} \qquad \vec{e}\sim(0,\Sigma) \;\; where \;\; \Sigma = \sigma_o^2 P^{-1} \quad (4.9)$$

Where:

- $\vec{y}$ is the $K\times1$ vector of observations, where K is the number of observations (K=3):
  - When using overlapping LiDAR strips, the vector of observations corresponds to the discrepancy between the predicted coordinates of conjugate points in overlapping strips using the noise-contaminated system measurements and the approximate values of the system parameters associated with the i^{th} and j^{th} scanners. In this case the vector $\vec{y}$ will take the following form $\left\{ \vec{y} = f(\vec{x}_{oi}, \vec{l}_{n_{iA}}) - f(\vec{x}_{oj}, \vec{l}_{n_{jB}}) \right\}$;
  - When using overlapping LiDAR and control points, the vector of observations corresponds to the discrepancy between the control point coordinates and the predicted

LiDAR point coordinates using the noise-contaminated system measurements and the approximate values of the system parameters associated with the j^{th} scanner. In this case the vector $\vec{y}$ will take the following form $\left\{ \vec{y} = r^{m}_{control} - f(\vec{x}_{oj}, \vec{l}_{n_{jB}}) \right\}$;

- $\delta\vec{x}_i$ is an $E_i \times 1$ vector, which represents the vector of unknown corrections to the approximate values of the system parameters associated with the i^{th} scanner, where ($E_i = 9$) is the number of unknowns associated with the i^{th} scanner;
- $\delta\vec{x}_j$ is an $E_j \times 1$ vector, which represents the vector of unknown corrections to the approximate values of the system parameters associated with the j^{th} scanner, where ($E_j = 9$) is the number of unknowns associated with the j^{th} scanner;
- A_i is a $K \times E_i$ matrix, which represents the design matrix that corresponds to the unknowns associated with the i^{th} scanner;

  $A_i = \partial f / \partial \vec{x}|_{\vec{x}_{oi}, \vec{l}_{n_{iA}}}$, represents the partial derivatives of the discrepancy vector w.r.t. the unknown system parameters of the i^{th} scanner using the system measurements and the initial approximate values of the unknown system parameters.
- A_j is a $K \times E_j$ matrix, which represents the design matrix that corresponds to the unknowns associated with the j^{th} scanner,

  $A_j = \partial f / \partial \vec{x}|_{\vec{x}_{oj}, \vec{l}_{n_{jB}}}$, represent the partial derivatives of the discrepancy vector w.r.t. the unknown system parameters of the j^{th} scanner using the system measurements and the initial approximate values of the unknown system parameters.
- $\vec{e}$ is the $K \times 1$ combined vector of random noise (normally distributed with a zero mean and variance-covariance matrix $\Sigma = \sigma_o^2 P^{-1}$), which represents the random error in the

discrepancy vector among conjugate points as a function of the random error in the system measurements;

where:

- σ_o^2 is a-priori variance factor, and
- P is a weight matrix of the noise vector.

o $\vec{e} = \partial f/\partial \vec{l}\big|_{\vec{x}_{oi},\vec{l}_{ni_A}} \vec{e}_{iA} - \partial f/\partial \vec{l}\big|_{\vec{x}_{oj},\vec{l}_{nj_B}} \vec{e}_{jB}$ when using LiDAR strips imaged by the i^{th} and j^{th} scanners;

o $\vec{e} = \vec{e}_{control} - \partial f/\partial l|_{\vec{x}_{oj},\vec{l}_{n_B}} \vec{e}_B$ when using LiDAR strip imaged by j^{th} scanner and control points;

o Σ variance-covariance matrix of $\vec{e}$, which is derived through error propagation:

- when using overlapping LiDAR strips imaged by the i^{th} and j^{th} scanners:

$$\Sigma = \begin{bmatrix} \partial f/\partial \vec{l}\big|_{\vec{x}_{oi},\vec{l}_{n_{iA}}} & -\partial f/\partial \vec{l}\big|_{\vec{x}_{oj},\vec{l}_{n_{jB}}} \end{bmatrix} \begin{bmatrix} \Sigma_{\vec{e}_{iA}} & 0 \\ 0 & \Sigma_{\vec{e}_{jB}} \end{bmatrix} \begin{bmatrix} \left(\partial f/\partial \vec{l}\big|_{\vec{x}_{oi},\vec{l}_{ni_A}}\right)^T \\ \left(-\partial f/\partial \vec{l}\big|_{\vec{x}_{oj},\vec{l}_{n_{jB}}}\right)^T \end{bmatrix}$$

Where:

– $\Sigma_{\vec{e}_{iA}}$ and $\Sigma_{\vec{e}_{jB}}$ are the variance-covariance matrices of the system measurements utilized to derive the coordinates of points A and B, respectively.

- when using LiDAR strip imaged by the j^{th} scanner and control points:

$$\Sigma = \begin{bmatrix} I & -\partial f/\partial \vec{l}\big|_{\vec{x}_{oj},\vec{l}_{n_{jB}}} \end{bmatrix} \begin{bmatrix} \Sigma_{\vec{e}_{control}} & 0 \\ 0 & \Sigma_{\vec{e}_{jB}} \end{bmatrix} \begin{bmatrix} I \\ \left(-\partial f/\partial \vec{l}\big|_{\vec{x}_{oj},\vec{l}_{nj_B}}\right)^T \end{bmatrix}$$

Where:

- $\Sigma_{\vec{e}_{\text{control}}}$ is the variance - covariance matrix of the control points.

Considering all the conjugate points in all the overlapping strips, one can get the observations in Equation 4.10.

$$\vec{y}_{3m\times 1} = A_{3m\times 9n}\, \delta\vec{x}_{9n\times 1} + \vec{e}_{\,3m\times 1} \tag{4.10}$$

Where:

- m is the total number of conjugate points;
- n is the total number of involved scanners;
- $\delta\vec{x}$ is the $9n \times 1$ combined vector of unknown corrections to the approximate values of the system parameters;
- A is the $(3m \times 9n)$ combined design matrix.

Using the LSA target function, which minimizes the sum of squares of weighted residuals (Equation 4.11), the solution vector can be derived using the normal equation matrix (N) and the normal equation vector (C) in Equation 4.12.

$$\vec{e}^T P\vec{e} = min|_{\delta\vec{x}} \qquad \text{(LSA Target Function)} \tag{4.11}$$

$$\delta\hat{\vec{x}}_{(9n\times 1)} = \quad (N^{-1})_{(9n\times 9n)}(C)_{(9n\times 1)} \qquad \text{(General Solution Vector)} \tag{4.12}$$

Where:

$$N = A^T PA \;\; \& \;\; C = A^T P\vec{y}$$

Rather than completely building the observation equations in Equation 4.10 and then deriving the normal equations, one can use the observation equations in Equation 4.12 to sequentially update

the normal equations. The process starts by deriving the normal equations for a given conjugate pair of points in Equation 4.13.

$$\begin{bmatrix} A_i^T \\ A_j^T \end{bmatrix} P \begin{bmatrix} A_i & A_j \end{bmatrix} \begin{bmatrix} \delta\hat{\hat{x}}_i \\ \delta\hat{\hat{x}}_j \end{bmatrix} = \begin{bmatrix} A_i^T \\ A_j^T \end{bmatrix} P\, \vec{y} \tag{4.13}$$

After simplification, Equation 4.13 will take the form of Equation 4.14.

$$\begin{bmatrix} N_{ii} & N_{ij} \\ N_{ji} & N_{jj} \end{bmatrix} \begin{bmatrix} \delta\hat{\hat{x}}_i \\ \delta\hat{\hat{x}}_j \end{bmatrix} = \begin{bmatrix} C_i \\ C_j \end{bmatrix} \tag{4.14}$$

Where:

$$N_{ii_{(9\times9)}} = A_i{}^T P\, A_i \quad \& \quad N_{ij_{(9\times9)}} = A_i{}^T P\, A_j \quad \& \quad N_{ji_{(9\times9)}} = A_j{}^T P\, A_i$$

$$N_{jj_{(9\times9)}} = A_j{}^T P\, A_j \quad \& \quad C_{i_{(9\times1)}} = A_i{}^T P\, \vec{y} \quad \& \quad C_{j_{(9\times1)}} = A_j{}^T P\, \vec{y}$$

The above sub-matrices can be used to update the normal equation matrix and normal equation vector according to the illustrated structure in Equation 4.15.

	1	2	...	i	...	j	...	n	
1	$\sum N_{11}$	$\sum N_{12}$	...	$\sum N_{1i}$	...	$\sum N_{1j}$	...	$\sum N_{1n}$	$\sum C_1$
2	$\sum N_{21}$	$\sum N_{22}$	...	$\sum N_{2i}$	...	$\sum N_{2j}$	...	$\sum N_{2n}$	$\sum C_2$
⋮	⋮	⋮		⋮		⋮		⋮	⋮
i	$\sum N_{i1}$	$\sum N_{i2}$	...	$\sum N_{ii}$	...	$\sum N_{ij}$	...	$\sum N_{in}$	$\sum C_i$
⋮	⋮	⋮		⋮		⋮		⋮	⋮
j	$\sum N_{j1}$	$\sum N_{j2}$	...	$\sum N_{ji}$	...	$\sum N_{jj}$	...	$\sum N_{jn}$	$\sum C_j$
⋮				⋮		⋮		⋮	⋮
n	$\sum N_{n1}$	$\sum N_{n2}$	...	$\sum N_{ni}$	...	$\sum N_{nj}$	...	$\sum N_{nn}$	$\sum C_n$
				N – Matrix					**C – Vector**

(4.15)

Where:

- For $\sum N_{ii}$, the summation is carried out for all the conjugate points where the i^{th} scanner is used to capture either one or both of the overlapping strips where the points in question reside,
- For $\sum N_{jj}$, the summation is carried out for all the conjugate points where the j^{th} scanner is used to capture either one or both of the overlapping strips where the points in question reside,
- For $\sum \mathrm{N_{ij}}$, the summation is carried out for all the conjugate points where the i^{th} and j^{th} scanners are used to capture the overlapping strips where the points in question reside,
- One should note that $N_{ij} = {N_{ji}}^{T}$,
- For $\sum \mathrm{C_i}$, the summation is carried out for all the conjugate points where the i^{th} scanner is used to capture either one or both of the overlapping strips where the points in question reside,
- For $\sum \mathrm{C}_j$, the summation is carried out for all the conjugate points where the j^{th} scanner is used to capture either one or both of the overlapping strips where the points in question reside,

It should be noted that if $i = j$, the sub-matrices N_{ii}, N_{ij}, N_{ji} , and N_{jj} and the sub-vectors C_i and C_j will be summed in the same location in the normal equation matrix N and normal equation vector C, respectively.

In summary, the mathematical model that has been developed so far is based on the availability of conjugate points in overlapping LiDAR surfaces (Equation 4.7) or conjugate points in control

and LiDAR surfaces (Equation 4.8). Assuming that conjugate points in overlapping strips exist, observations representing the discrepancy between these points follow the traditional Gauss Markov stochastic model in Equation 4.10. The LSA procedure aims at estimating the correction to the approximate values of the unknown parameters (Equation 4.12), which would lead to the solution in Equations 4.16, 4.17, and 4.18.

$$\tilde{\vec{e}} = \vec{y} - A\delta\hat{\vec{x}} \qquad \text{(Predicted Residuals)} \qquad (4.16)$$

$$\Sigma\{\delta\hat{\vec{x}}\} = \hat{\sigma}_o^2(A^T P A)^{-1} = \hat{\sigma}_o^2 N^{-1} \qquad \text{(Variance-Covariance Matrix)} \qquad (4.17)$$

$$\hat{\sigma}_o^2 = (\tilde{\vec{e}}^T P \tilde{\vec{e}})/(K - E * n) \qquad \text{(A-posteriori Variance Factor)} \qquad (4.18)$$

Due to the irregular nature of the LiDAR data, there is no point-to-point correspondence among the point clouds in overlapping strips or between a given strip and a control surface. Therefore, the abovementioned LSA solution cannot be directly used to come up with an estimate of the system parameters. The appropriate conjugate primitives that could be identified in overlapping LiDAR strips have been discussed in more details in (Habib et al., 2011; Kersting, 2011; Habib et al., 2010b; Bang, 2010). In these research efforts, the point-to-patch correspondence is used as suitable primitives for the calibration procedure. The idea of this method is that one of the overlapping strip pairs, denoted by "S_1", is represented by a set of irregular points while the second strip, denoted by "S_2", is represented by triangular patches, which can be derived from a TIN generation procedure. When a control surface is used, it will be represented by the original points (due to its sparse nature) and the LiDAR strips will be represented by triangular patches. In this research work (as discussed in chapter 3), automatic selection of suitable regions among the overlapping strips to be used in the LiDAR system calibration is introduced. Therefore, the

used primitives in the proposed calibration procedure will be as follows: original points in strip "S_1" imaged by the i^{th} scanner, while triangular patches in strip "S_2" imaged by j^{th} scanner, which includes appropriate regions with good variations in slope, aspect, and distribution. Figure 4.3 illustrates the case where strip "S_1" is represented by a set of the original points while strip "S_2" is represented by a set of triangular patches. The Closest Patch procedure proposed by Habib et al., 2009 establishes the correspondence between a LiDAR point (q) in strip "S_1" and a triangular patch (defined by the vertices P_1, P_2, and P_3) in strip "S_2" (as shown in Figure 4.3).

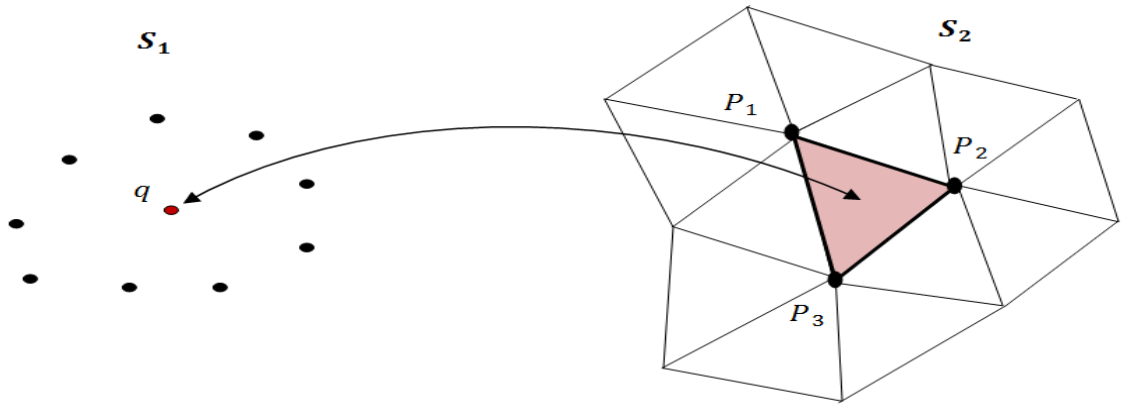

Figure 4.3. Conceptual basis of the utilized point-patch correspondence procedure

In the Closest Patch procedure, a TIN patch (defined by the vertices P_1, P_2, and P_3) is considered conjugate to a given point (q) if it is the closest patch to this point and the projection of the point (q') onto the patch should be inside the patch (as shown in Figure 4.4). As well, a pre-defined threshold for the point-patch separation (normal distance n, as shown in Figure 4.4 is achieved to avoid the matching of triangular patches and points corresponding to non-physical surfaces (i.e., points within vegetations and at building boundaries as shown in Figure 4.5a). Figure 4.5b shows the non-matched points among overlapping strips through the exclusion of instances where the TIN patches do not represent the physical surface (vegetation and building boundaries), which

indicates the robustness of the matching procedure in terms of avoiding the use of point-patch pairs corresponding to non-physical surfaces in the calibration procedure. For a given point-patch pair, it will be assumed that one of the vertices of the TIN patch (vertex P_1 which is arbitrarily selected from the triangular patch) is conjugate to the corresponding point (q). Therefore, the TIN vertex P_1 and the point q are denoted as pseudo-conjugate points (as shown in Figure 4.4).

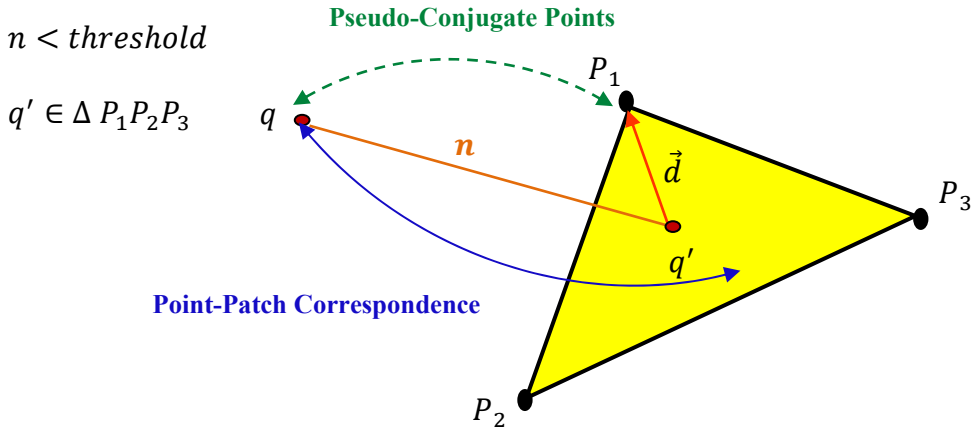

Figure 4.4. Point-patch correspondence and pseudo conjugate points (the vertex $\boldsymbol{P_1}$ which is arbitrarily selected from the triangular patch corresponds to the point $\boldsymbol{q}$)

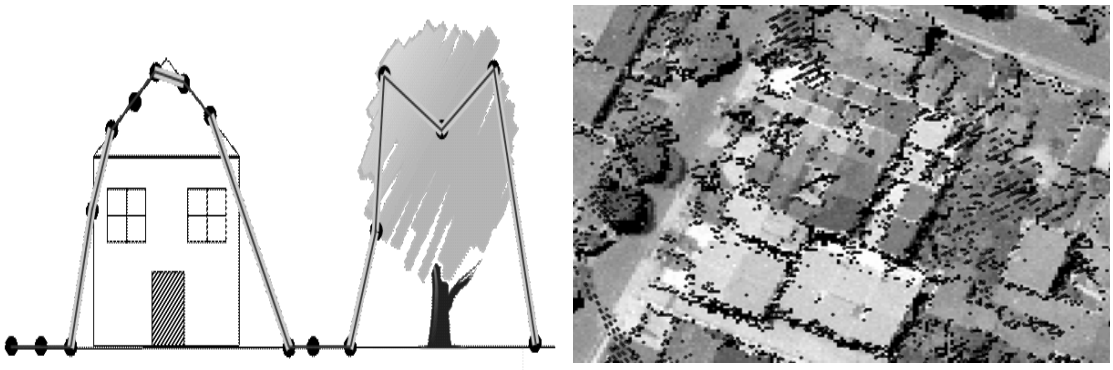

(a) (b)

Figure 4.5. Exceptions where the TIN patches do not represent the physical surface (highlighted in grey) (a) and non-matched points along edges of buildings and around areas with vegetation (b) (Kersting, 2011)

Starting from Equation 4.5, the mathematical model describing the discrepancy vector between pseudo-conjugate points in overlapping LiDAR strips will take the form in Equation 4.19. In a similar fashion, the mathematical model describing the discrepancy vector between pseudo-conjugate control and LiDAR points will take the form in Equation 4.20.

$$r_A^m(True) - r_B^m(True) \cong f(\vec{x}_{oi}, \vec{l}_{n_{iA}}) + \partial f/\partial \vec{x}|_{\vec{x}_{oi},\vec{l}_{ni_A}} \delta\vec{x}_i + \partial f/\partial \vec{l}|_{\vec{x}_{oi},\vec{l}_{n_{iA}}} (-\vec{e}_{iA})$$
$$-f(\vec{x}_{oj}, \vec{l}_{nj_B}) - \partial f/\partial \vec{x}|_{\vec{x}_{oj},\vec{l}_{nj_B}} \delta\vec{x}_j - \partial f/\partial \vec{l}|_{\vec{x}_{oj},\vec{l}_{nj_B}} (-\vec{e}_{jB}) = \vec{d} \quad (4.19)$$

$$(r_{control}^m - \vec{e}_{control}) - r_B^m(True) \cong (r_{control}^m - \vec{e}_{control}) - f(\vec{x}_{oj}, \vec{l}_{n_{jB}}) - \partial f/\partial \vec{x}|_{\vec{x}_{oj},\vec{l}_{n_{jB}}} \delta\vec{x}_j -$$
$$\partial f/\partial \vec{l}|_{\vec{x}_{oj},\vec{l}_{n_{jB}}} (-\vec{e}_{jB}) = \vec{d} \quad (4.20)$$

The stochastic model describing the discrepancies in Equations 4.19 and 4.20 can be represented by the Gauss Markov stochastic model in Equation 4.21. This model in Equation 4.21 can be represented in a general form by Equation 4.22. The difference between this model and the one in Equation 4.10 is the additional unknown vector $(\vec{d})$, which results from using non-conjugate points along a point-patch pair (as shown in Figure 4.4).

$$\vec{y} = A_i\, \delta\vec{x}_i + A_j\, \delta\vec{x}_j + \vec{d} + \vec{e} \qquad \vec{e} \sim (0, \Sigma) \qquad where\ \Sigma = \sigma_o^2 P^{-1} \quad (4.21)$$

$$\vec{y} = A\, \delta\vec{x} + \vec{d} + \vec{e} \qquad \vec{e} \sim (0, \Sigma) \qquad where\ \Sigma = \sigma_o^2 P^{-1} \quad (4.22)$$

To compensate for using non-corresponding problem, weight matrices for the pseudo-conjugate points are modified using surface normal vectors of the matched triangular patches. Specifically, for the vertex point P_1, a certain weight value determined by the precision of LiDAR data will be assigned along the surface normal, while zero weights will be assigned along the patch plane. By doing this, the non-corresponding problem of the point P_1 can be compensated. The modification

to the LSA and the weight matrix to deal with the model in Equation 4.22 is explained in more details in (Kersting, 2011). To explain the modification process, the stochastic properties of the random noise vector, as represented by Equation 4.23, will be changed first. The new weight matrix ($P^{`}$) of the noise vector is chosen such that $P^{`}\vec{d} = 0$ (i.e., the unknown discrepancy vector ($\vec{d}$) belongs to the null space of the weight matrix ($P^{`}$)). Such a condition indicates that the modified weight matrix is not positive-definite (i.e., the inverse matrix ($P^{`-1}$) does not exist). Therefore, the modified variance-covariance matrix will be represented as follows: $\Sigma^{`}\{e\} = \sigma_o^2\, P^{`+}$, where the plus sign indicates the Moore-Penrose pseudo-inverse (Koch, 1988).

$$\Sigma^{`}\{e\} = \sigma_o^2\, P^{`+} \text{ , where } P^{`}\vec{d} = 0 \tag{4.23}$$

By using the modified weight matrix, the LSA target function will take the form in Equation 4.24. Since the additional unknown vector ($\vec{d}$) belongs to the null space of the modified weight matrix, then the LSA target function in Equation 4.24 reduces to the form in Equation 4.25. Therefore, the general solution ($\delta\hat{\vec{x}}$) to the LSA target function is defined by Equation 4.26. Using the law of error propagation, the variance-covariance matrix of the solution vector ($\Sigma\{\delta\hat{\vec{x}}\}$) is shown in Equation 4.27.

$$\vec{e}^T P^{`} \vec{e} = \left(\vec{y} - A\,\delta\vec{x} - \vec{d}\right)^T P^{`} \left(\vec{y} - A\,\delta\vec{x} - \vec{d}\right) = min|_{\delta\vec{x},\vec{d}} \qquad \text{LSA Target Function} \tag{4.24}$$

$$\vec{e}^T P^{`} \vec{e} = (\vec{y} - A\,\delta\vec{x})^T P^{`} (\vec{y} - A\,\delta\vec{x}) = min|_{\delta\vec{x}} \qquad \text{LSA Target Function} \tag{4.25}$$

$$\delta\hat{\vec{x}} = (A^T P^{`} A)^{-1} A^T P^{`} \vec{y} = N^{-1} A^T P^{`} \vec{y} \qquad \text{Estimated Unknowns} \tag{4.26}$$

$$\Sigma\{\delta\hat{\vec{x}}\} = \sigma_o^2 N^{-1} \qquad \text{Variance-Covariance Matrix} \tag{4.27}$$

The last step is to estimate the a-posteriori variance factor ($\hat{\sigma}_o^2$) by deriving the expected value of the sum of squares of weighted predicted residuals. Starting from Equation 4.28, one can derive

an estimate for the a-posteriori variance factor according to Equation 4.29, where q is the rank of the modified weight matrix.

$$E\left(\tilde{\vec{e}}^T P` \tilde{\vec{e}}\right) = E\{(\vec{y} - A\,\delta\hat{\vec{x}} - \vec{d})^T P`\left(\vec{y} - A\,\delta\hat{\vec{x}} - \vec{d}\right)\} = E\left\{\left(\vec{y} - A\,\delta\hat{\vec{x}}\right)^T P`\left(\vec{y} - A\,\delta\hat{\vec{x}}\right)\right\}$$
$$= (q - m)\sigma_o^2 \tag{4.28}$$

$$\hat{\sigma}_o^2 = \left(\vec{y} - A\delta\hat{\vec{x}}\right)^T P`(\vec{y} - A\delta\hat{\vec{x}})/(q - E * n) \tag{4.29}$$

In summary, from an implementation point of view, the LSA solution to the stochastic model in Equation 4.30 can be derived from Equations 4.26, 4.27, and 4.29. This solution is similar to the one of the traditional Gauss Markov model (Equations 4.12, 4.17, and 4.18) with the exception that the redundancy is evaluated as the difference between the rank of the modified weight matrix and the number of unknowns for each scanner multiplied by the number of available scanners. In order to have a solution, one should note that, the rank of the modified weight matrix should be larger than the number of unknowns. This should not be a concern given the large number of point-patch pairs utilized in the calibration procedure. It is important to note that the proposed weight modification process will nullify the unknown vector ($\vec{d}$). The modified LSA will deal with pseudo-conjugate points, after the weight modification process, in the same way it would deal with true conjugate points, which makes the implementation much simpler.

$$\vec{y} = A\,\delta\vec{x} + \vec{d} + \vec{e} \quad \vec{e}\sim\left(0, \Sigma`\right) \quad where\ \Sigma` = \sigma_o^2 P`^{+}\ and\ P`\vec{d} = 0 \tag{4.30}$$

4.3 Workflow of the Calibration Procedure

Figure 4.6 illustrates the flowchart of the proposed calibration procedure to deal with multi-laser scanning systems. First, the overlapping strip pairs, which are captured by i^{th} and/or j^{th} scanner are selected for the calibration procedure. For each overlapping strip pair, one strip S_1 is

represented by points (with their associated raw measurements) and the second strip S_2 is represented by TIN patches (TIN indices, and the vertices coordinates together with their associated raw measurements). When using LiDAR strip and control surface pairs, the control surface S_1 is represented by points while the LiDAR surface S_2 is represented by TIN patches. Then, the predicted coordinates of the LiDAR point cloud are computed using the system raw measurements and the initial approximations for the system parameters ($\vec{x}_{oi}$) associated with the i^{th} laser scanner. The initial correspondence (matching) between points in S_1 and patches in S_2 is established using the Closest Patch procedure proposed in Habib et al., 2009. Using the established point-patch pairs, the modified LSA procedure can be performed to come up with an updated estimate for the system parameters of each individual scanner. Since the observation equations are non-linear, the LSA would follow an iterative procedure (this iterative procedure is denoted by the "inside loop" – *il* – in Figure 4.6). After estimating the system parameters of individual scanners, one can derive a better prediction of the point cloud coordinates in the different strips. Since the correspondence between point-patch pairs might change after updating the point/vertices coordinates, a new set of correspondences is established using the updated point cloud coordinates. Using these correspondences, one can iteratively proceed to derive better estimates of the system parameters of individual scanners (this iterative procedure is referred to as the "outside loop" – *ol* – in Figure 4.6). In summary, in the outside loop, an iterative matching and parameter estimation is conducted until the change in the estimated system parameters of individual scanners or the estimated a-posteriori variance factor $\left(\hat{\sigma}^2_{o_{ol}}\right)$ is below pre-defined thresholds.

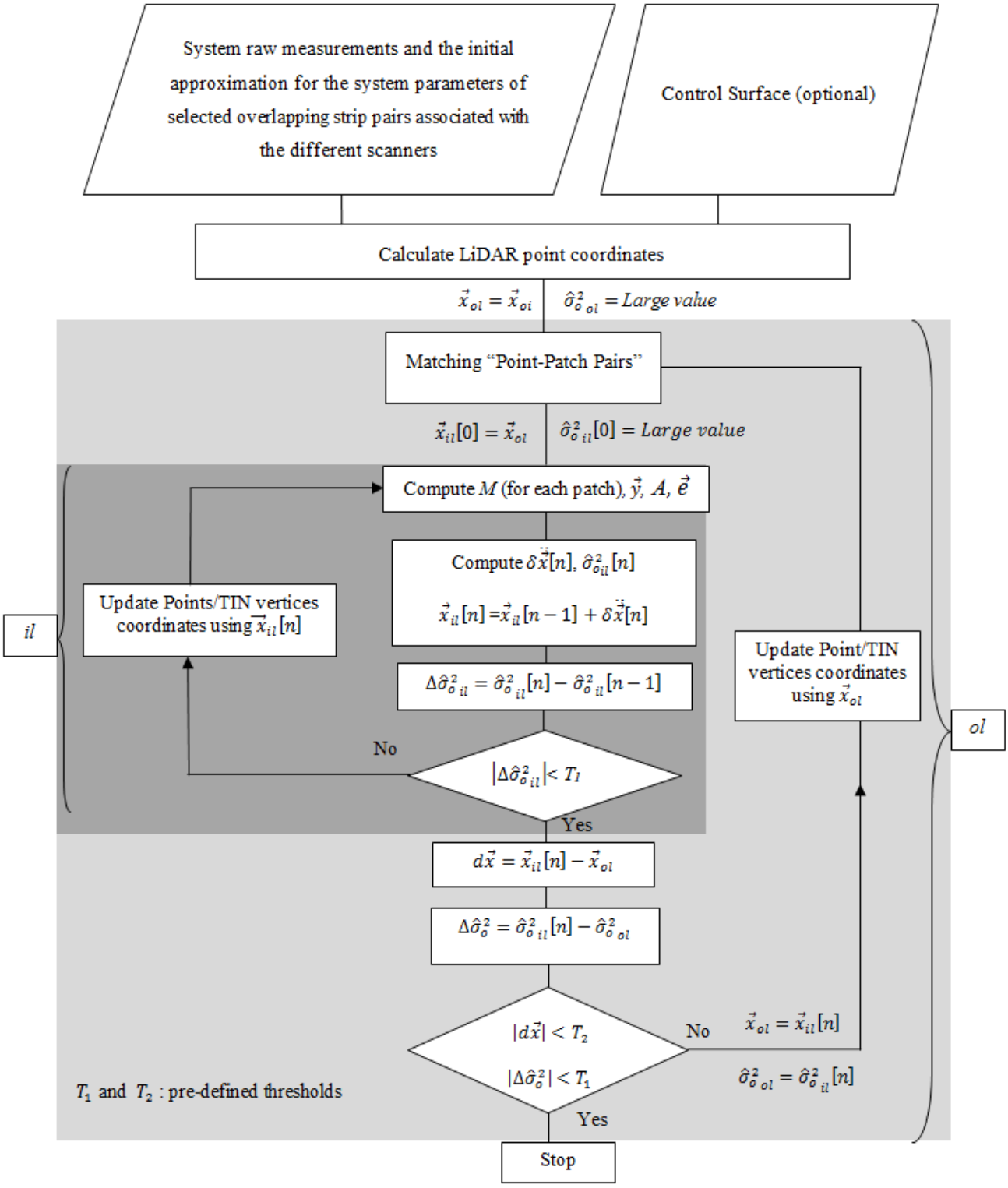

Figure 4.6. Flowchart for the proposed calibration procedure

4.4 Summary

In this chapter, new calibration procedure for dealing with multi- laser scanning systems is introduced. The main objective of the proposed calibration method is to estimate the system parameters (the mounting parameters relating the individual scanners to the IMU body frame and the intrinsic parameters of each scanner) that minimize the discrepancies between conjugate surface elements in overlapping LiDAR strips and overlapping LiDAR and control surfaces. The mathematical model of the proposed calibration technique has been demonstrated.

The contributions of the proposed method can be summarized as follows:

- The proposed method is fully automated,
- The utilized suitable primitives, which can deal with the irregular nature of the LiDAR point cloud, are implemented. The used primitives in the proposed calibration procedure will be as follows: one of the overlapping strip pairs imaged by the i^{th} scanner denoted by S_1, is represented by the original points. While the second strip imaged by j^{th} scanner (which includes suitable regions with good variations in slope, aspect, and distribution), denoted by S_2, is represented by triangular patches, which can be derived from a TIN generation procedure. It is important to note that the these primitives will make the proposed calibration procedure fast and reliable for the estimation of the system parameters,
- The correspondence between conjugate primitives (point-patch pair) is established within the proposed calibration process using the Closest Patch procedure that filters out instances where the TIN patches do not represent the physical surface, and
- The proposed calibration procedure can deal with control information.

The general hypotheses, which will be tested in the experimental results section, can be summarized as follows:

- The proposed method is capable of deriving an accurate estimate of the mounting and intrinsic parameters of each laser scanner in multi-laser scanning systems,
- The proposed approach can be used to test the stability of the system parameters with the flight as well as verify the quality of the navigation data within the data collection mission,
- The utilized primitive will lead to fast and reliable estimation of the system parameters using the proposed calibration technique, and
- Using the ground control points will help for estimation of the calibration system parameters.

Chapter Five: **INDOOR AND OUTDOOR CALIBRATION TECHNIQUES OF TERRESTRIAL MOBILE MULTI-LASER SCANNING SYSTEMS**

5.1 Introduction

Terrestrial mobile laser scanning (TMLS) is the latest approach towards fast and cost-efficient acquisition of 3-dimensional spatial data. Accurately evaluating the intrinsic and mounting parameters of TMLS systems is an obvious necessity. However, available systems on the market may lack suitable and efficient practical workflows on how to perform this calibration. This research discusses an innovative method for accurately determining the intrinsic and mounting parameters of multi-TMLS systems. The proposed calibration method investigates a two-step calibration procedure for calibrating terrestrial mobile multi-laser scanning systems. As mentioned in section 4.1, when the scanning unit has multiple scanners, the involved parameters in the system calibration procedure include the following:

1. The intrinsic parameters of the individual scanners comprise the following:
    - The range error ($\Delta\rho$) and,
    - Scale factors of the mirror scan angles (S_α, and S_β,).

    The number of the intrinsic parameters = 3 * number of scanners.
2. The mounting parameters relating the individual scanners to the reference frame of the navigation unit involve the following:
    - Three parameters for the lever arm (ΔX, ΔY, and ΔZ) and,
    - Three parameters for the boresight angles ($\Delta\omega$, $\Delta\varphi$, and $\Delta\kappa$)

    The number of the mounting parameters = 6 * number of scanners.

To reliably estimate these parameters, one needs to have good quality information regarding the position and orientation of the navigation frame (this usually refers to the position and orientation of the IMU body frame). Such quality can be ensured by conducting the data collection for the calibration process in an open-sky environment where one has good accessibility to the GPS satellite constellation. However, such requirement will have a negative impact on the geometric distribution of the calibration features. In other words, one will not have access to calibrating surfaces with different slope and aspect values. To circumvent such problem, the mounting parameters relating the individual scanners to the reference frame of the navigation unit will be divided into two groups as follows:

1. The mounting parameters relating the different scanners to a reference scanner (refer to group 1 as shown in Figure 5.1) and,
2. The mounting parameters relating the reference scanner to the reference frame of the navigation unit (refer to group 2 as shown in Figure 5.1).

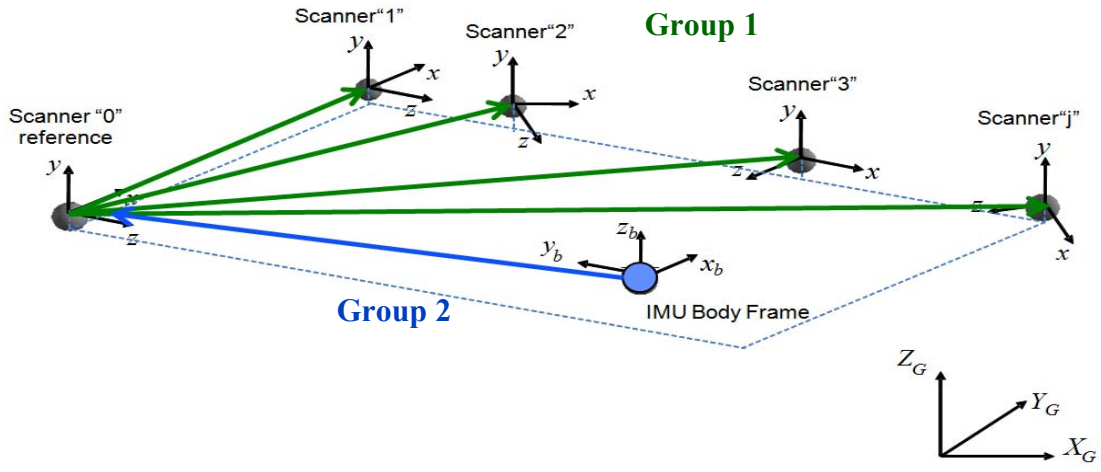

Figure 5.1. Configuration of the mounting parameters relating the different scanners to a reference scanner (group 1) and the mounting parameters relating the reference scanner to the reference frame of the navigation unit (IMU body frame) (group 2).

The advantage of this approach is that the first group of parameters (the mounting parameters relating the different laser scanners to the reference one) can be determined through an indoor calibration test field, where one has access to a favorable distribution of the calibration targets (e.g., good distribution of planar features with different slope and aspect values). During the indoor calibration stage, data will be collected from few locations in a static mode. The latter group (the mounting parameters relating the reference scanner to the reference frame of the navigation unit) can be determined in an open-sky environment (outdoor calibration) to ensure reliable derivation of the position and orientation of the navigation frame while having an unfavorable distribution of the calibration targets. The proposed mathematical model of the indoor and outdoor calibration is discussed in more details in the following sections.

5.2 The Proposed Mathematical Model for the Indoor Calibration

In the proposed methodology, the following unknown parameters are considered in the indoor calibration procedure:

- The position, denoted by (pos), and the orientation, denoted by (ort), of the navigation unit at specific data collection epochs (e.g., t_k and t_l): In this case, the number of unknown parameters denoted by ($x_{pos/ort_{t_k}}$ & $x_{pos/ort_{t_l}}$) will be (6 * number of epochs).

- The mounting parameters relating the different scanners (e.g., i^{th} and j^{th} scanners), denoted by lu_i and lu_j, to a reference scanner, denoted by lu_r: In this case, the number of unknown parameters, denoted by ($x_{mou_{lu_i}^{lu_r}}$ & $x_{mou_{lu_j}^{lu_r}}$), will be (6 * (number of scanners – 1).

- The mounting parameters relating the reference scanner, denoted by lu_r, to the reference frame of the navigation unit, denoted by b: In this case, the number of unknown parameters, denoted by $x_{mou^b_{lu_r}}$, will be 6.

- The intrinsic parameters of the individual scanners (e.g., i^{th} and j^{th} scanners), denoted by int_i and int_j: In this case, the number of unknown parameters, denoted by x_{int_i} and x_{int_j}, will be (3 * number of scanners).

The general mathematical model, which can be used for the indoor system calibration procedure, is represented in Equation 5.1:

$$r_l^m(i,t_k) = r_b^m(t_k) + R_b^m(t_k)r_{lu_r}^b + R_b^m(t_k)R_{lu_r}^b r_{lu_i}^{lu_r} + R_b^m(t_k)R_{lu_r}^b R_{lu_i}^{lu_r} R_{lb_i}^{lu_i}(t_k)r_l^{lb_i}(t_k) \quad (5.1)$$

This equation indicates that the true coordinates of a given point $r_l^m(i,t_k)$ are derived using the following parameters:

1. *P*osition & orientation of the navigation frame at time t_k

– $r_b^m(t_k)$ is the position of the navigation frame, and

– $R_b^m(t_k)$ is the orientation of the navigation frame.

2. Mounting parameters relating i^{th} scanner to the reference scanner

– $r_{lu_i}^{lu_r}$ $(\Delta X\_lu_i 2ref, \Delta Y\_lu_i 2ref, \Delta Z\_lu_i 2ref)$ – lever arm offset – is the vector from the origin of the reference scanner coordinate system to the origin of the i^{th} scanner coordinate system, and

– $R_{lu_i}^{lu_r}$ $(\Delta\omega\_lu_i2ref, \Delta\varphi\_lu_i2ref, \Delta\kappa\_lu_i2ref)$ is the rotation matrix relating the reference scanner and the i^{th} scanner coordinate systems.

3. Mounting parameters relating the reference scanner to the navigation frame.

– $r_{lu_r}^{b}$ *(ΔX_*lu_r*2b, ΔY_*lu_r*2b, ΔZ_*lu_r*2b)* – lever arm offset – is the vector from the origin of the navigation frame coordinate system to the origin of reference scanner coordinate system, and

– $R_{lu_r}^{b}$ $(\Delta\omega\_lu_r2b,\ \Delta\varphi\_lu_r2b,\ \Delta\kappa\_lu_r2b)$ is the rotation matrix relating the navigation frame and reference scanner coordinate systems.

4. Intrinsic parameters of the i^{th} scanner

– $r_I^{lb_i}(t_k)$ is the laser range vector, which involves the bias in the range vector ($\Delta\rho$) associated with the i^{th} scanner, and

– $R_{lb_i}^{lu_i}(t_k)$ is the rotation matrix relating the laser unit and laser beam coordinate systems of the i^{th} scanner, which includes the scale factors of the two mirror scan angles (S_α and S_β).

For the indoor system calibration, one needs to derive the discrepancy vector $(\vec{d})$ between the coordinates of two non-conjugate points (i.e., correspondence point-patch pairs as discussed in chapter 4) in overlapping strips that have been captured at the same time or different times by different scanners (these non-conjugate points will be denoted by subscripts A and B). The difference between the true coordinates of these points can be expressed by Equation 5.2. In a similar fashion, if one is dealing with non-conjugate points in a LiDAR strip and control surface, the difference between the coordinates of the control point $r_{control}^{m}$ and the true coordinates of

the LiDAR point in the strip denoted by the subscript B can be expressed as in Equation 5.3. Equations 5.2 and 5.3 represent the general observation equations corresponding to the discrepancy vector when dealing with overlapping strips and control data, respectively.

$$r_A^m(i,t_k) - r_B^m(j,t_l) \; =$$

$$\left[r_b^m(t_k) + R_b^m(t_k)r_{lu_r}^b + R_b^m(t_k)R_{lu_r}^b r_{lu_i}^{lu_r} + R_b^m(t_k)R_{lu_r}^b R_{lu_i}^{lu_r} R_{lb_i}^{lu_i}(t_k) r_A^{lb_i}(t_k)\right] -$$

$$\left[r_b^m(t_l) + R_b^m(t_l)r_{lu_r}^b + R_b^m(t_l)R_{lu_r}^b r_{lu_j}^{lu_r} + R_b^m(t_l)R_{lu_r}^b R_{lu_j}^{lu_r} R_{lb_j}^{lu_j}(t_l) r_B^{lb_j}(t_l)\right] = \vec{d} \quad (5.2)$$

$$r_{control}^m - r_B^m(j,t_l) =$$

$$r_{control}^m - \left[r_b^m(t_l) + R_b^m(t_l)r_{lu_r}^b + R_b^m(t_l)R_{lu_r}^b r_{lu_j}^{lu_r} + R_b^m(t_l)R_{lu_r}^b R_{lu_j}^{lu_r} R_{lb_j}^{lu_j}(t_l) r_B^{lb_j}(t_l)\right] = \vec{d} \quad (5.3)$$

Since these equations are not linear with respect to the unknown system parameters and measurement noise, a linearization process by Taylor series expansion is required for the Least Square Adjustment (LSA). The linearized equations when using overlapping strips and control information are presented in Equations 5.4 and 5.5, respectively. These equations are obtained using the initial approximations for the unknown system parameters associated with the i^{th} and j^{th} scanners at the same time or different times as the point of expansion while ignoring second and higher order terms.

$$y_t \; = \; A_{pos/ort}(t_k,i)x_{pos/ort_{t_k}} + A_{mou_{lu_r}^b}(t_k,i)x_{mou_{lu_r}^b} + A_{mou_{lu_i}^{lu_r}}(t_k,i)x_{mou_{lu_i}^{lu_r}} +$$

$$A_{int_i}(t_k,i)x_{int_i} + \; A_{pos/ort}(t_l,j)x_{pos/ort_{t_l}} + A_{mou_{lu_r}^b}(t_l,j)x_{mou_{lu_r}^b} + \; A_{mou_{lu_j}^{lu_r}}(t_l,j)x_{mou_{lu_j}^{lu_r}} +$$

$$A_{int_j}(t_l,j)x_{int_j} + \vec{d} + \vec{e} \quad (5.4)$$

$$y_c = A_{pos/ort}(t_l, j)x_{pos/ort_{t_l}} + A_{mou^b_{lu_r}}(t_l, j)x_{mou^b_{lu_r}} + A_{mou^{lu_r}_{lu_j}}(t_l, j)x_{mou^{lu_r}_{lu_j}} +$$

$$A_{int_j}(t_l, j)x_{int_j} + \vec{d} + \vec{e} \quad (5.5)$$

Rearranging the terms in Equations 5.4 and 5.5, one can get the final form of the linearized observations equations (Equations 5.6 and 5.7) according to the traditional Gauss Markov stochastic model (Equation 5.8).

$$y_t = A_{pos/ort}(t_k, i)x_{pos/ort_{t_k}} + A_{pos/ort}(t_l, j)x_{pos/ort_{t_l}} + A_{mou^{lu_r}_{lu_i}}(t_k, i)x_{mou^{lu_r}_{lu_i}} +$$

$$A_{mou^{lu_r}_{lu_j}}(t_l, j)x_{mou^{lu_r}_{lu_j}} + \left(A_{mou^b_{lu_r}}(t_k, i) + A_{mou^b_{lu_r}}(t_l, j)\right)x_{mou^b_{lu_r}} + A_{int_i}(t_k, i)x_{int_i} +$$

$$A_{int_j}(t_l, j)x_{int_j} + \vec{d} + \vec{e} \quad (5.6)$$

$$y_c = A_{pos/ort}(t_l, j)x_{pos/ort_{t_l}} + A_{mou^{lu_r}_{lu_j}}(t_l, j)x_{mou^{lu_r}_{lu_j}} + A_{mou^b_{lu_r}}(t_l, j)x_{mou^b_{lu_r}} +$$

$$A_{int_j}(t_l, j)x_{int_j} + \vec{d} + \vec{e} \quad (5.7)$$

$$\vec{y}_{3m\times 1} = A_{3m\times u}\,\delta\vec{x}_{u\times 1} + \vec{e}_{\,3m\times 1} + \vec{d}_{\,3m\times 1} \quad \vec{e}\sim(0, \Sigma^{`}) \; where \; \Sigma^{`} = \sigma_o^2 P^{`+} \; and \; P^{`}\vec{d} = 0 \quad (5.8)$$

Where:

- ***m*** is the number of conjugate points in overlapping strips as well as conjugates points among the overlapping strips and the control surface,
- ***u*** is the total number of the unknown parameters,

  $u = 6v + 6(n-1) + 6 + 3n$
- ***v*** is total number of epochs, and
- ***n*** is the total number of involved scanners,

- $\boldsymbol{\delta\vec{x}}$ is the $u \times 1$ combined vector of unknown corrections to the approximate values of the system parameters, and
- $\boldsymbol{A}$ is the $(3m \times u)$ combined design matrix.

Using the LSA target function, the solution vector can be derived using the normal equation matrix (N) and the normal equation vector (C) as in Equation 5.9.

$$(N)_{(u\times u)}\,\delta\hat{\vec{x}}_{(u\times 1)} = (C)_{(u\times 1)} \qquad \text{(General Solution Vector)} \qquad (5.9)$$

Where:

$N = A^T P` A \quad \& \quad C = A^T P` \vec{y}$

The structure of N, $\delta\vec{x}$ and C will be as follows:

$$\begin{bmatrix} N_{11_{(6v\times 6v)}} & N_{12_{(6v\times 6(n-1))}} & N_{13_{(6v\times 6)}} & N_{14_{(6v\times 3n)}} \\ N_{21_{(6(n-1)\times 6v)}} & N_{22_{(6(n-1)\times 6(n-1))}} & N_{23_{(6(n-1)\times 6)}} & N_{24_{(6(n-1)\times 3n)}} \\ N_{31_{(6\times 6v)}} & N_{32_{(6\times 6(n-1))}} & N_{33_{(6\times 6)}} & N_{34_{(6\times 3n)}} \\ N_{41_{(3n\times 6v)}} & N_{42_{(3n\times 6(n-1))}} & N_{43_{(3n\times 6)}} & N_{44_{(3n\times 3n)}} \end{bmatrix} \begin{bmatrix} \delta x_{1_{(6v\times 1)}} \\ \delta x_{2_{(6(n-1)\times 1)}} \\ \delta x_{3_{(6\times 1)}} \\ \delta x_{4_{(3n\times 1)}} \end{bmatrix} = \begin{bmatrix} C_{1_{(6v\times 1)}} \\ C_{2_{(6(n-1)\times 1)}} \\ C_{3_{(6\times 1)}} \\ C_{4_{(3n\times 1)}} \end{bmatrix} \qquad (5.10)$$

Where:

- $\boldsymbol{\delta\vec{x}_1}$ is the $6v \times 1$ vector of unknown corrections to the approximate values of the position and orientation of the platform at specific epochs,
- $\boldsymbol{\delta\vec{x}_2}$ is the $6(n-1) \times 1$ vector of unknown corrections to the approximate values of the mounting parameters relating the different scanners to the reference one,

- $\boldsymbol{\delta\vec{x}_3}$ is the 6×1 vector of unknown corrections to the approximate values of the mounting parameters relating the reference scanner to the navigation frame, and
- $\boldsymbol{\delta\vec{x}_4}$ is the $3n \times 1$ vector of unknown corrections to the approximate values of the intrinsic parameters of the individual scanners.

One can note that rather than completely building the design matrix A together with the misclosure vector $\vec{y}$ and then deriving the normal equation matrix (*N*) and normal equation vector (*C*), one can use the resulting observation equations for a specific set of non-conjugate points in the overlapping strips (Equation 5.6) as well as non-conjugate points among the overlapping strips and control surface (Equation 5.7).

First, when the observations for a specific set of non-conjugate points result from the overlapping strips only, the following contributions are computed to build the sub-normal equation matrices and sub-normal equation vectors (as in Equations 5.11 - 5.17).

$$N_{11}(t_k, t_k) = N_{11}(pos/ort_{t_k}, pos/ort_{t_k}) = A^T_{pos/ort}(t_k, i)\, P` A_{pos/ort}(t_k, i)$$

$$N_{11}(t_k, t_l) = N_{11}(pos/ort_{t_k}, pos/ort_{t_l}) = A^T_{pos/ort}(t_k, i)\, P` A_{pos/ort}(t_l, j)$$

$$N_{12}(t_k, lu_i) = N_{12}(pos/ort_{t_k}, mou^{lu_r}_{lu_i}) = A^T_{pos/ort}(t_k, i)\, P` A_{mou^{lur}_{lu_i}}(t_k, i)$$

$$N_{12}(t_k, lu_j) = N_{12}(pos/ort_{t_k}, mou^{lu_r}_{lu_j}) = A^T_{pos/ort}(t_k, i)\, P` A_{mou^{lur}_{lu_j}}(t_l, j) \qquad (5.11)$$

$$N_{13}(t_k, lu_r) = N_{13}(pos/ort_{t_k}, mou^b_{lu_r}) = A^T_{pos/ort}(t_k, i)\, P` [A_{mou^b_{lur}}(t_k, i) + A_{mou^b_{lur}}(t_l, j)]$$

$$N_{14}(t_k, lu_i) = N_{14}(pos/ort_{t_k}, int_i) = A^T_{pos/ort}(t_k, i)\, P` A_{int_i}(t_k, i)$$

$$N_{14}(t_k, lu_j) = N_{14}(pos/ort_{t_k}, int_j) = A^T_{pos/ort}(t_k, i)\, P` A_{int_j}(t_l, j)$$

$$C_1(t_k) = C_{x_{pos/ort_{t_k}}} = A^T_{pos/ort}(t_k, i)\, P` y_t$$

$$N_{11}(t_l, t_k) = N_{11}(pos/ort_{t_l}, pos/ort_{t_k}) = A^T_{pos/ort}(t_l, j)\ P`A_{pos/ort}(t_k, i)$$

$$N_{11}(t_l, t_l) = N_{11}(pos/ort_{t_l}, pos/ort_{t_l}) = A^T_{pos/ort}(t_l, j)\ P`A_{pos/ort}(t_l, j)$$

$$N_{12}(t_l, lu_i) = N_{12}(pos/ort_{t_l}, mou^{lu_r}_{lu_i}) = A^T_{pos/ort}(t_l, j)\ P`A_{mou^{lu_r}_{lu_i}}(t_k, i)$$

$$N_{12}(t_l, lu_j) = N_{12}(pos/ort_{t_l}, mou^{lu_r}_{lu_j}) = A^T_{pos/ort}(t_l, j)\ P`A_{mou^{lu_r}_{lu_j}}(t_l, j) \qquad (5.12)$$

$$N_{13}(t_l, lu_r) = N_{13}(pos/ort_{t_l}, mou^{b}_{lu_r}) = A^T_{pos/ort}(t_l, j)\ P`\ [A_{mou^{b}_{lu_r}}(t_k, i) + A_{mou^{b}_{lu_r}}(t_l, j)]$$

$$N_{14}(t_l, lu_i) = N_{14}(pos/ort_{t_l}, int_i) = A^T_{pos/ort}(t_l, j)\ P`A_{int_i}(t_k, i)$$

$$N_{14}(t_l, lu_j) = N_{14}(pos/ort_{t_l}, int_j) = A^T_{pos/ort}(t_l, j)\ P`A_{int_j}(t_l, j)$$

$$C_1(t_l) = C_{x_{pos/ort_{t_l}}} = A^T_{pos/ort}(t_l, j)\ P`y_t$$

$$N_{21}(lu_i, t_k) = N_{21}(mou^{lu_r}_{lu_i}, pos/ort_{t_k}) = A^T_{mou^{lu_r}_{lu_i}}(t_k, i)\ P`A_{pos/ort}(t_k, i)$$

$$N_{21}(lu_i, t_l) = N_{21}(mou^{lu_r}_{lu_i}, pos/ort_{t_l}) = A^T_{mou^{lu_r}_{lu_i}}(t_k, i)\ P`A_{pos/ort}(t_l, j)$$

$$N_{22}(lu_i, lu_i) = N_{22}\left(mou^{lu_r}_{lu_i}, mou^{lu_r}_{lu_i}\right) = A^T_{mou^{lu_r}_{lu_i}}(t_k, i)\ P`A_{mou^{lu_r}_{lu_i}}(t_k, i)$$

$$N_{22}(lu_i, lu_j) = N_{22}\left(mou^{lu_r}_{lu_i}, mou^{lu_r}_{lu_j}\right) = A^T_{mou^{lu_r}_{lu_i}}(t_k, i)\ P`A_{mou^{lu_r}_{lu_j}}(t_l, j) \qquad (5.13)$$

$$N_{23}(lu_i, lu_r) = N_{23}\left(mou^{lu_r}_{lu_i}, mou^{b}_{lu_r}\right) = A^T_{mou^{lu_r}_{lu_i}}(t_k, i)\ P`\ [A_{mou^{b}_{lu_r}}(t_k, i) + A_{mou^{b}_{lu_r}}(t_l, j)]$$

$$N_{24}(lu_i, lu_i) = N_{24}\left(mou^{lu_r}_{lu_i}, int_i\right) = A^T_{mou^{lu_r}_{lu_i}}(t_k, i)\ P`A_{int_i}(t_k, i)$$

$$N_{24}(lu_i, lu_j) = N_{24}\left(mou^{lu_r}_{lu_i}, int_j\right) = A^T_{mou^{lu_r}_{lu_i}}(t_k, i)\ P`A_{int_j}(t_l, j)$$

$$C_2(lu_i) = C_{x_{mou^{lu_r}_{lu_i}}} = A^T_{mou^{lu_r}_{lu_i}}(t_k, i)\ P`y_t$$

$$N_{21}(lu_j, t_k) = N_{21}(mou_{lu_j}^{lu_r}, pos/ort_{t_k}) = A^T_{mou_{lu_j}^{lu_r}}(t_l, j)\ P`A_{pos/ort}(t_k, i)$$

$$N_{21}(lu_j, t_l) = N_{21}(mou_{lu_j}^{lu_r}, pos/ort_{t_l}) = A^T_{mou_{lu_j}^{lu_r}}(t_l, j)\ P`A_{pos/ort}(t_l, j)$$

$$N_{22}(lu_j, lu_i) = N_{22}\left(mou_{lu_j}^{lu_r}, mou_{lu_i}^{lu_r}\right) = A^T_{mou_{lu_j}^{lu_r}}(t_l, j)\ P`A_{mou_{lu_i}^{lu_r}}(t_k, i)$$

$$N_{22}(lu_j, lu_j) = N_{22}\left(mou_{lu_j}^{lu_r}, mou_{lu_j}^{lu_r}\right) = A^T_{mou_{lu_j}^{lu_r}}(t_l, j)\ P`A_{mou_{lu_j}^{lu_r}}(t_l, j) \qquad (5.14)$$

$$N_{23}(lu_j, lu_r) = N_{23}\left(mou_{lu_j}^{lu_r}, mou_{lu_r}^{b}\right) = A^T_{mou_{lu_j}^{lu_r}}(t_l, j)\ P`\ [A_{mou_{lu_r}^{b}}(t_k, i) + A_{mou_{lu_r}^{b}}(t_l, j)]$$

$$N_{24}(lu_j, lu_i) = N_{24}\left(mou_{lu_j}^{lu_r}, int_i\right) = A^T_{mou_{lu_j}^{lu_r}}(t_l, j)\ P`A_{int_i}(t_k, i)$$

$$N_{24}(lu_j, lu_j) = N_{24}\left(mou_{lu_j}^{lu_r}, int_j\right) = A^T_{mou_{lu_j}^{lu_r}}(t_l, j)\ P`A_{int_j}(t_l, j)$$

$$C_2(lu_j) = C_{x_{mou_{lu_j}^{lu_r}}} = A^T_{mou_{lu_j}^{lu_r}}(t_l, j)\ P`y_t$$

$$N_{31}(lu_r, t_k) = N_{31}(mou_{lu_r}^{b}, pos/ort_{t_k}) = \ [A_{mou_{lu_r}^{b}}(t_k, i) + A_{mou_{lu_r}^{b}}(t_l, j)]^T P`A_{pos/ort}(t_k, i)$$

$$N_{31}(lu_r, t_l) = N_{31}(mou_{lu_r}^{b}, pos/ort_{t_l}) = \ [A_{mou_{lu_r}^{b}}(t_k, i) + A_{mou_{lu_r}^{b}}(t_l, j)]^T P`A_{pos/ort}(t_l, j)$$

$$N_{32}(lu_r, lu_i) = N_{32}\left(mou_{lu_r}^{b}, mou_{lu_i}^{lu_r}\right) = [A_{mou_{lu_r}^{b}}(t_k, i) + A_{mou_{lu_r}^{b}}(t_l, j)]^T P`A_{mou_{lu_i}^{lu_r}}(t_k, i)$$

$$N_{32}(lu_r, lu_j) = N_{32}\left(mou_{lu_r}^{b}, mou_{lu_j}^{lu_r}\right) = [A_{mou_{lu_r}^{b}}(t_k, i) + A_{mou_{lu_r}^{b}}(t_l, j)]^T P`A_{mou_{lu_j}^{lu_r}}(t_l, j)$$

$$N_{33}(lu_r, lu_r) = N_{33}(mou_{lu_r}^{b}, mou_{lu_r}^{b}) = [A_{mou_{lu_r}^{b}}(t_k, i) + A_{mou_{lu_r}^{b}}(t_l, j)]^T P`\ [A_{mou_{lu_r}^{b}}(t_k, i) +$$

$$A_{mou_{lu_r}^{b}}(t_l, j)] \qquad (5.15)$$

$$N_{34}(lu_r, lu_i) = N_{34}(mou_{lu_r}^{b}, int_i) = [A_{mou_{lu_r}^{b}}(t_k, i) + A_{mou_{lu_r}^{b}}(t_l, j)]^T P`A_{int_i}(t_k, i)$$

$$N_{34}(lu_r, lu_j) = N_{34}(mou_{lu_r}^{b}, int_j) = [A_{mou_{lu_r}^{b}}(t_k, i) + A_{mou_{lu_r}^{b}}(t_l, j)]^T P`A_{int_j}(t_l, j)$$

$$C_3(lu_r) = C_{x_{mou_{lu_r}^{b}}} = [A_{mou_{lu_r}^{b}}(t_k, i) + A_{mou_{lu_r}^{b}}(t_l, j)]^T\ P`y_t$$

$$N_{41}(lu_i, t_k) = N_{41}(int_i, pos/ort_{t_k}) = A^T_{int_i}(t_k, i)\ P` A_{pos/ort}(t_k, i)$$

$$N_{41}(lu_i, t_l) = N_{41}(int_i, pos/ort_{t_l}) = A^T_{int_i}(t_k, i)\ P` A_{pos/ort}(t_l, j)$$

$$N_{42}(lu_i, lu_i) = N_{42}\left(int_i, mou^{lu_r}_{lu_i}\right) = A^T_{int_i}(t_k, i)\ P` A_{mou^{lu_r}_{lu_i}}(t_k, i)$$

$$N_{42}(lu_i, lu_j) = N_{42}\left(int_i, mou^{lu_r}_{lu_j}\right) = A^T_{int_i}(t_k, i)\ P` A_{mou^{lu_r}_{lu_j}}(t_l, j) \qquad (5.16)$$

$$N_{43}(lu_i, lu_r) = N_{43}(int_i, mou^b_{lu_r}) = A^T_{int_i}(t_k, i)\ P` \left[A_{mou^b_{lu_r}}(t_k, i) + A_{mou^b_{lu_r}}(t_l, j)\right]$$

$$N_{44}(lu_i, lu_i) = N_{44}(int_i, int_i) = A^T_{int_i}(t_k, i)\ P` A_{int_i}(t_k, i)$$

$$N_{44}(lu_i, lu_j) = N_{44}(int_i, int_j) = A^T_{int_i}(t_k, i)\ P` A_{int_j}(t_l, j)$$

$$C_4(lu_i) = C_{x_{int_i}} = A^T_{int_i}(t_k, i)\ P` y_t$$

$$N_{41}(lu_j, t_k) = N_{41}(int_j, pos/ort_{t_k}) = A^T_{int_j}(t_l, j)\ P` A_{pos/ort}(t_k, i)$$

$$N_{41}(lu_j, t_l) = N_{41}(int_j, pos/ort_{t_l}) = A^T_{int_j}(t_l, j)\ P` A_{pos/ort}(t_l, j)$$

$$N_{42}(lu_j, lu_i) = N_{42}\left(int_j, mou^{lu_r}_{lu_i}\right) = A^T_{int_j}(t_l, j)\ P` A_{mou^{lu_r}_{lu_i}}(t_k, i)$$

$$N_{42}(lu_j, lu_j) = N_{42}\left(int_j, mou^{lu_r}_{lu_j}\right) = A^T_{int_j}(t_l, j)\ P` A_{mou^{lu_r}_{lu_j}}(t_l, j) \qquad (5.17)$$

$$N_{43}(lu_j, lu_r) = N_{43}(int_j, mou^b_{lu_r}) = A^T_{int_j}(t_l, j)\ P` \left[A_{mou^b_{lu_r}}(t_k, i) + A_{mou^b_{lu_r}}(t_l, j)\right]$$

$$N_{44}(lu_j, lu_i) = N_{44}(int_j, int_i) = A^T_{int_j}(t_l, j)\ P` A_{int_i}(t_k, i)$$

$$N_{44}(lu_j, lu_j) = N_{44}(int_j, int_j) = A^T_{int_j}(t_l, j)\ P` A_{int_j}(t_l, j)$$

$$C_4(lu_j) = C_{x_{int_j}} = A^T_{int_j}(t_l, j)\ P` y_t$$

Second, when the observations for a specific set of non-conjugate points result from the overlapping strips and control surface, the following contributions are computed to build the sub-normal equation matrices and sub-normal equation vectors (as in Equations 5.18 - 5.21).

$$
\begin{aligned}
N_{11}(t_l, t_l) &= N_{11}(pos/ort_{t_l}, pos/ort_{t_l}) = A^T_{pos/ort}(t_l, j)\, P` A_{pos/ort}(t_l, j) \\
N_{12}(t_l, lu_j) &= N_{12}(pos/ort_{t_l}, mou^{lu_r}_{lu_j}) = A^T_{pos/ort}(t_l, j)\, P` A_{mou^{lur}_{lu_j}}(t_l, j) \\
N_{13}(t_l, lu_r) &= N_{13}(pos/ort_{t_l}, mou^{b}_{lu_r}) = A^T_{pos/ort}(t_l, j)\, P` A_{mou^{b}_{lur}}(t_l, j) \\
N_{14}(t_l, lu_j) &= N_{14}(pos/ort_{t_l}, int_j) = A^T_{pos/ort}(t_l, j)\, P` A_{int_j}(t_l, j) \\
C_1(t_l) &= C_{x_{pos/ort_{t_l}}} = A^T_{pos/ort}(t_l, j)\, P` y_c
\end{aligned}
\tag{5.18}
$$

$$
\begin{aligned}
N_{21}(lu_j, t_l) &= N_{21}(mou^{lu_r}_{lu_j}, pos/ort_{t_l}) = A^T_{mou^{lur}_{lu_j}}(t_l, j)\, P` A_{pos/ort}(t_l, j) \\
N_{22}(lu_j, lu_j) &= N_{22}\left(mou^{lu_r}_{lu_j}, mou^{lu_r}_{lu_j}\right) = A^T_{mou^{lur}_{lu_j}}(t_l, j)\, P` A_{mou^{lur}_{lu_j}}(t_l, j) \\
N_{23}(lu_j, lu_r) &= N_{23}\left(mou^{lu_r}_{lu_j}, mou^{b}_{lu_r}\right) = A^T_{mou^{lur}_{lu_j}}(t_l, j)\, P` A_{mou^{b}_{lur}}(t_l, j) \\
N_{24}(lu_j, lu_j) &= N_{24}\left(mou^{lu_r}_{lu_j}, int_j\right) = A^T_{mou^{lur}_{lu_j}}(t_l, j)\, P` A_{int_j}(t_l, j) \\
C_2(lu_j) &= C_{x_{mou^{lur}_{lu_j}}} = A^T_{mou^{lur}_{lu_j}}(t_l, j)\, P` y_c
\end{aligned}
\tag{5.19}
$$

$$N_{31}(lu_r, t_l) = N_{31}(mou^b_{lu_r}, pos/ort_{t_l}) = [A_{mou^b_{lu_r}}(t_l, j)]^T P` A_{pos/ort}(t_l, j)$$

$$N_{32}(lu_r, lu_j) = N_{32}\left(mou^b_{lu_r}, mou^{lu_r}_{lu_j}\right) = [A_{mou^b_{lu_r}}(t_l, j)]^T P` A_{mou^{lu_r}_{lu_j}}(t_l, j)$$

$$N_{33}(lu_r, lu_r) = N_{33}\left(mou^b_{lu_r}, mou^b_{lu_r}\right) = [A_{mou^b_{lu_r}}(t_l, j)]^T P` A_{mou^b_{lu_r}}(t_l, j) \qquad (5.20)$$

$$N_{34}\left(lu_r, lu_j\right) = N_{34}\left(mou^b_{lu_r}, int_j\right) = [A_{mou^b_{lu_r}}(t_l, j)]^T P` A_{int_j}(t_l, j)$$

$$C_3(lu_r) = C_{x_{mou^b_{lu_r}}} = [A_{mou^b_{lu_r}}(t_l, j)]^T P` y_c$$

$$N_{41}\left(lu_j, t_l\right) = N_{41}(int_j, pos/ort_{t_l}) = A^T_{int_j}(t_l, j)\ P`\ A_{pos/ort}(t_l, j)$$

$$N_{42}\left(lu_j, lu_j\right) = N_{42}\left(int_j, mou^{lu_r}_{lu_j}\right) = A^T_{int_j}(t_l, j)\ P` A_{mou^{lu_r}_{lu_j}}(t_l, j)$$

$$N_{43}\left(lu_j, lu_r\right) = N_{43}\left(int_j, mou^b_{lu_r}\right) = A^T_{int_j}(t_l, j)\ P` A_{mou^b_{lu_r}}(t_l, j) \qquad (5.21)$$

$$N_{44}\left(lu_j, lu_j\right) = N_{44}\left(int_j, int_j\right) = A^T_{int_j}(t_l, j)\ P` A_{int_j}(t_l, j)$$

$$C_4\left(lu_j\right) = C_{x_{int_j}} = A^T_{int_j}(t_l, j)\ P`\ y_c$$

Then, the resulting sub-matrices/vectors can be used to update the full normal equation matrix/vector as follows:

<u>N_{11} (6v x 6v):</u>

$\Sigma N_{11}(t_1, t_1)$ $\Sigma N_{11}(t_1, t_2)$ .... $\Sigma N_{11}(t_1, t_k)$ .... $\Sigma N_{11}(t_1, t_l)$ .... $\Sigma N_{11}(t_1, t_v)$

$\Sigma N_{11}(t_2, t_1)$ $\Sigma N_{11}(t_2, t_2)$ .... $\Sigma N_{11}(t_2, t_k)$ .... $\Sigma N_{11}(t_2, t_l)$ .... $\Sigma N_{11}(t_2, t_v)$

.....

$\Sigma N_{11}(t_k, t_1)$ $\Sigma N_{11}(t_k, t_2)$ .... $\Sigma N_{11}(t_k, t_k)$ .... $\Sigma N_{11}(t_k, t_l)$ .... $\Sigma N_{11}(t_k, t_v)$

.....

$\Sigma N_{11}(t_l, t_1)$ $\Sigma N_{11}(t_l, t_2)$ .... $\Sigma N_{11}(t_l, t_k)$ .... $\Sigma N_{11}(t_l, t_l)$ .... $\Sigma N_{11}(t_l, t_v)$

.....

$\Sigma N_{11}(t_v, t_1)$ $\Sigma N_{11}(t_v, t_2)$ .... $\Sigma N_{11}(t_v, t_k)$ .... $\Sigma N_{11}(t_v, t_l)$ .... $\Sigma N_{11}(t_v, t_v)$

Where:

- For $\Sigma N_{11}(t_k, t_k)$, the summation of $N_{11}(t_k, t_k)$ is carried out for all the conjugate points, at least one of which has been captured at time t_k,
- For $\Sigma N_{11}(t_k, t_l)$, the summation of $N_{11}(t_k, t_l)$ is carried out for all the conjugate points which have been captured at time epochs t_k and t_l, and
- For $\Sigma N_{11}(t_l, t_l)$, the summation of $N_{11}(t_l, t_l)$ is carried out for all the conjugate points, at least one of which has been captured at time t_l.

NOTE: It is worth noting that if the set of conjugate points under consideration are captured at the same time epoch, the resulting N_{11} sub-blocks from that particular conjugate point pair will be added at the same location in N_{11} matrix. This location corresponds to the time epoch in question.

N_{12} (6v x 6 (n-1)):

$\Sigma N_{12}(t_1, lu_1)$ $\Sigma N_{12}(t_1, lu_2)$ ..... $\Sigma N_{12}(t_1, lu_i)$ ..... $\Sigma N_{12}(t_1, lu_j)$ ..... $\Sigma N_{12}(t_1, lu_{n-1})$

$\Sigma N_{12}(t_2, lu_1)$ $\Sigma N_{12}(t_2, lu_2)$..... $\Sigma N_{12}(t_2, lu_i)$ ..... $\Sigma N_{12}(t_2, lu_j)$ ..... $\Sigma N_{12}(t_2, lu_{n-1})$

……

$\Sigma N_{12}(t_k, lu_1)$ $\Sigma N_{12}(t_k, lu_2)$ ..... $\Sigma N_{12}(t_k, lu_i)$..... $\Sigma N_{12}(t_k, lu_j)$ ..... $\Sigma N_{12}(t_k, lu_{n-1})$

……

$\Sigma N_{12}(t_l, lu_1)$ $\Sigma N_{12}(t_l, lu_2)$ ..... $\Sigma N_{12}(t_l, lu_i)$ ..... $\Sigma N_{12}(t_l, lu_j)$ ..... $\Sigma N_{12}(t_l, lu_{n-1})$

……

$\Sigma N_{12}(t_v, lu_1)$ $\Sigma N12(t_v, lu_2)$ ..... $\Sigma N_{12}(t_v, lu_i)$..... $\Sigma N_{12}(t_v, lu_j)$ ..... $\Sigma N_{12}(t_v, lu_{n-1})$

Where:

- For $\Sigma N_{12}(t_k, lu_i)$, the summation of $N_{12}(t_k, lu_i)$ is carried out for all the conjugate points, at least one of which has been captured at time t_k and at least one of which is captured by the i^{th} scanner.

NOTE: It is worth noting that if the i^{th} or j^{th} scanner is the reference one, the corresponding N_{12} sub-block will be zero, since the terms $A_{mou_{lu_i}^{lu_r}}(t_k, i) = 0$ or $A_{mou_{lu_j}^{lu_r}}(t_l, j) = 0$. Also, It should be noted that $N_{21} = {N_{12}}^T$.

N_{13} (6v x 6):

$\Sigma N_{13}(t_1, lu_r)$

$\Sigma N_{13}(t_2, lu_r)$

……

$\Sigma N_{13}(t_k, lu_r)$

……

$\Sigma N_{13}(t_l, lu_r)$

……

$\Sigma N_{13}(t_v, lu_r)$

Where:

- For $\Sigma N_{13}(t_k, lu_r)$, the summation of $N_{13}(t_k, lu_r)$ is carried out for all the conjugate points, at least one of which has been captured at time t_k.

N_{14} (6v x 3n):

$\Sigma N_{14}(t_1, lu_1)$ $\Sigma N_{14}(t_1, lu_2)$ ..... $\Sigma N_{14}(t_1, lu_i)$ ..... $\Sigma N_{14}(t_1, lu_j)$ ..... $\Sigma N_{14}(t_1, lu_n)$

$\Sigma N_{14}(t_2, lu_1)$ $\Sigma N_{14}(t_2, lu_2)$..... $\Sigma N_{14}(t_2, lu_i)$ ..... $\Sigma N_{14}(t_2, lu_j)$ ..... $\Sigma N_{14}(t_2, lu_n)$

……

$\Sigma N_{14}(t_k, lu_1)$ $\Sigma N_{14}(t_k, lu_2)$..... $\Sigma N_{14}(t_k, lu_i)$ ..... $\Sigma N_{14}(t_k, lu_j)$ ..... $\Sigma N_{14}(t_k, lu_n)$

……

$\Sigma N_{14}(t_l, lu_1)$ $\Sigma N_{14}(t_l, lu_2)$..... $\Sigma N_{14}(t_l, lu_i)$ ..... $\Sigma N_{14}(t_l, lu_j)$ ..... $\Sigma N_{14}(t_l, lu_n)$

……

$\Sigma N_{14}(t_v, lu_1)$ $\Sigma N14(t_v, lu_2)$ ..... $\Sigma N_{14}(t_v, lu_i)$..... $\Sigma N_{14}(t_v, lu_j)$ ..... $\Sigma N_{14}(t_v, lu_n)$

Where:

- For $\Sigma N_{14}(t_k, lu_i)$, the summation of $N_{14}(t_k, lu_i)$ is carried out for all the conjugate points, at least one of which has been captured at time t_k and at least one of which is captured by the i^{th} scanner. It should also be noted that $N_{41} = {N_{14}}^T$.

C_1 (6v x1):

$\Sigma C_1(t_1)$

$\Sigma C_1(t_2)$

....

$\Sigma C_1(t_k)$

.....

$\Sigma C_1(t_l)$

.....

$\Sigma C_1(t_v)$

Where:

- For $\Sigma C_1 (t_k)$, the summation of $C_1 (t_k)$ is carried out for all the conjugate points, at least one of which has been captured at time t_k.

N_{22} (6(n-1) x 6(n-1)):

$\Sigma N_{22} (lu_1, lu_1)$ $\Sigma N_{22} (lu_1, lu_2)$..... $\Sigma N_{22} (lu_1, lu_i)$..... $\Sigma N_{22} (lu_1, lu_j)$..... $\Sigma N_{22} (lu_1, lu_{n-1})$

$\Sigma N_{22} (lu_2, lu_1)$ $\Sigma N_{22} (lu_2, lu_2)$..... $\Sigma N_{22} (lu_2, lu_i)$..... $\Sigma N_{22} (lu_2, lu_j)$..... $\Sigma N_{22} (lu_2, lu_{n-1})$

……

$\Sigma N_{22} (lu_i, lu_1)$ $\Sigma N_{22} (lu_i, lu_2)$..... $\Sigma N_{22} (lu_i, lu_i)$..... $\Sigma N_{22} (lu_i, lu_j)$..... $\Sigma N_{22} (lu_i, lu_{n-1})$

……

$\Sigma N_{22} (lu_j, lu_1)$ $\Sigma N_{22} (lu_j, lu_2)$..... $\Sigma N_{22} (lu_j, lu_i)$..... $\Sigma N_{22} (lu_j, lu_j)$..... $\Sigma N_{22} (lu_j, lu_{n-1})$

……

$\Sigma N_{22} (lu_{n-1}, lu_1)$ $\Sigma N_{22} (lu_{n-1}, lu_2)$.... $\Sigma N_{22} (lu_{n-1}, lu_i)$..... $\Sigma N_{22} (lu_{n-1}, lu_j)$.... $\Sigma N_{22} (lu_{n-1}, lu_{n-1})$

Where:

- For $\Sigma N_{22} (lu_i, lu_i)$, the summation of $N_{22} (lu_i, lu_i)$ is carried out for all the conjugate points, at least one of which has been captured by the i^{th} scanner,

- For $\Sigma N_{22} (lu_i, lu_j)$, the summation of $N_{22} (lu_i, lu_j)$ is carried out for all the conjugate points that have been captured by the i^{th} and j^{th} scanners, and

- For $\Sigma N_{22} (lu_j, lu_j)$, the summation of $N_{22} (lu_j, lu_j)$ is carried out for all the conjugate points, at least one of which has been captured by the j^{th} scanner.

NOTE: It should be noted that if the i^{th} or j^{th} scanner is the reference one, the corresponding N_{22} sub-block will be zero since the terms $A_{mou_{lu_i}^{lu_r}}(t_k, i) = 0$ or $A_{mou_{lu_j}^{lu_r}}(t_l, j) = 0$.

N_{23} (6(n-1) x 6):

ΣN_{23} (lu_1, lu_r)

ΣN_{23} (lu_2, lu_r)

……

ΣN_{23} (lu_i, lu_r)

……

ΣN_{23} (lu_j, lu_r)

……

ΣN_{23} (lu_{n-1}, lu_r)

Where:

- For ΣN_{23} (lu_i, lu_r), the summation of N_{23} (lu_i, lu_r) is carried out for all the conjugate points, at least one of which has been captured by the i^{th} scanner.

NOTE: It should be noted that if the i^{th} or j^{th} scanner is the reference one, the corresponding N_{23} sub-block will be zero, since the terms $A_{mou_{lu_i}^{lu_r}}(t_k, i) = 0$ or $A_{mou_{lu_j}^{lu_r}}(t_l, j) = 0$. Also, It should be noted that $N_{32} = {N_{23}}^T$.

N_{24} (6(n-1) x 3n):

ΣN_{24} (lu_1, lu_1) ΣN_{24} (lu_1, lu_2)..... ΣN_{24} (lu_1, lu_i)..... ΣN_{24} (lu_1, lu_j) ..... ΣN_{24} (lu_1, lu_n)

ΣN_{24} (lu_2, lu_1) ΣN_{24} (lu_2, lu_2) ..... ΣN_{24} (lu_2, lu_i) ..... ΣN_{24} (lu_2, lu_j)..... ΣN_{24} (lu_2, lu_n)

……

$\Sigma N_{24}(lu_i, lu_1)$ $\Sigma N_{24}(lu_i, lu_2)$ ..... $\Sigma N_{24}(lu_i, lu_i)$ ..... $\Sigma N_{24}(lu_i, lu_j)$..... $\Sigma N_{24}(lu_i, lu_n)$

....

$\Sigma N_{24}(lu_j, lu_1)$ $\Sigma N_{24}(lu_j, lu_2)$ ..... $\Sigma N_{24}(lu_j, lu_i)$ ..... $\Sigma N_{24}(lu_j, lu_j)$..... $\Sigma N_{24}(lu_j, lu_n)$

……

$\Sigma N_{24}(lu_{n-1}, lu_1)$ $\Sigma N_{24}(lu_{n-1}, lu_2)$ .....$\Sigma N_{24}(lu_{n-1}, lu_i)$ .....$\Sigma N_{24}(lu_{n-1}, lu_j)$..... $\Sigma N_{24}(lu_{n-1}, lu_n)$

Where:

- For $\Sigma N_{24}(lu_i, lu_i)$, the summation of $N_{24}(lu_i, lu_i)$ is carried out for all the conjugate points, at least one of which has been captured by the i^{th} scanner,
- For $\Sigma N_{24}(lu_i, lu_j)$, the summation of $N_{24}(lu_i, lu_j)$ is carried out for all the conjugate points that have been captured by the i^{th} and j^{th} scanners, and
- For $\Sigma N_{24}(lu_j, lu_j)$, the summation of $N_{24}(lu_j, lu_j)$ is carried out for all the conjugate points, at least one of which has been captured by the j^{th} scanner.

NOTE: It should be noted that if the i^{th} or j^{th} scanner is the reference one, the corresponding N_{24} sub-block will be zero, since the terms $A_{mou_{lu_i}^{lu_r}}(t_k, i) = 0$ or $A_{mou_{lu_j}^{lu_r}}(t_l, j) = 0$. It should also be noted that $N_{42} = {N_{24}}^T$.

<u>C_2 (6(n-1) x 1):</u>

$\Sigma C_2(lu_1)$

$\Sigma C_2(lu_2)$

....

$\Sigma C_2(lu_i)$

.....

$\Sigma C_2\ (lu_j)$

.....

$\Sigma C_2\ (lu_{n-1})$

Where:

- For $\Sigma C_2\ (lu_i)$, the summation of $C_2\ (lu_i)$ is carried out for all the conjugate points, at least one of which has been captured by the i^{th} scanner.

NOTE: It should be noted that if the i^{th} or j^{th} scanner is the reference one, the corresponding C_2 sub-vector will be zero, since the terms $A_{mou_{lu_i}^{lu_r}}(t_k, i) = 0$ or $A_{mou_{lu_j}^{lu_r}}(t_l, j) = 0$.

N_{33} (6 x 6):

$\Sigma N_{33}\ (lu_r)$

Where for $\Sigma N_{33}\ (lu_r)$, the summation of $N_{33}\ (lu_r)$ is carried out for all the conjugate points.

N_{34} (6 x 6n):

$\Sigma N_{34}\ (lu_r, lu_1)\ \Sigma N_{34}\ (lu_r, lu_2)\ ....\ \ \Sigma N_{34}\ (lu_r, lu_i)\ ...\ \Sigma N_{34}\ (lu_r, lu_j)\ ...\ \Sigma N_{34}\ (lu_r, lu_n)$

Where for $\Sigma N_{34}\ (lu_r, lu_i)$, the summation of $N_{34}\ (lu_r, lu_i)$ is carried out for all the conjugate points, at least one of which has been captured by the i^{th} scanner.

NOTE: It should be noted that $N_{43} = {N_{34}}^T$.

C_3 (6 x1):

$\Sigma C_3\ (lu_r)$

Where for $\Sigma C_3\ (lu_r)$, the summation of $C_3\ (lu_r)$ is carried out for all the conjugate points.

N_{44} (6nx6n):

$\Sigma N_{44}(lu_1, lu_1)$ $\Sigma N_{44}(lu_1, lu_2)$..... $\Sigma N_{44}(lu_1, lu_i)$ ... $\Sigma N44(lu_1, lu_j)$ ... $\Sigma N_{44}(lu_1, lu_n)$

$\Sigma N_{44}(lu_2, lu_1)$ $\Sigma N_{44}(lu_2, lu_2)$..... $\Sigma N_{44}(lu_2, lu_i)$ ... $\Sigma N44(lu_2, lu_j)$ ... $\Sigma N_{44}(lu_2, lu_n)$

...

$\Sigma N_{44}(lu_i, lu_1)$ $\Sigma N_{44}(lu_i, lu_2)$..... $\Sigma N_{44}(lu_i, lu_i)$ ... $\Sigma N44(lu_i, lu_j)$ ... $\Sigma N_{44}(lu_i, lu_n)$

...

$\Sigma N_{44}(lu_j, lu_1)$ $\Sigma N_{44}(lu_j, lu_2)$..... $\Sigma N_{44}(lu_j, lu_i)$ ... $\Sigma N44(lu_j, lu_j)$ ... $\Sigma N_{44}(lu_j, lu_n)$

...

$\Sigma N_{44}(lu_n, lu1)$ $\Sigma N44(lu_n, lu_2)$ ... $\Sigma N_{44}(lu_n, lu_i)$ ... $\Sigma N_{44}(lu_n, lu_j)$ ... $\Sigma N_{44}(lu_n, lu_n)$

Where:

- For $\Sigma N_{44}(lu_i, lu_i)$, the summation of $N_{44}(lu_i, lu_i)$ is carried for all the conjugate points, at least one of which has been captured by the i^{th} scanner,
- For $\Sigma N_{44}(lu_i, lu_j)$, the summation of $N_{44}(lu_i, lu_j)$ is carried for all the conjugate points that have been captured by the i^{th} and j^{th} scanners, and
- For $\Sigma N_{44}(lu_j, lu_j)$, the summation of $N_{44}(lu_j, lu_j)$ is carried for all the conjugate points, at least one of which has been captured by the j^{th} scanner.

C_4 (6n x 1):

$\Sigma C_4(lu_1)$

$\Sigma C_4(lu_2)$

...

$\Sigma C_4\ (lu_i)$

...

$\Sigma C_4\ (lu_j)$

...

$\Sigma C_4\ (lu_n)$

Where for $\Sigma C_4\ (lu_i)$, the summation of $C_4\ (lu_i)$ is carried out for all the conjugate points, at least one of which has been captured by the i^{th} scanner.

In summary, the mathematical model of the indoor calibration technique that has been developed so far is based on the availability of a specific set of non-conjugate points in the overlapping LiDAR strips (Equation 5.6) and control surface (Equation 5.7) that have been captured at the same time or different times by different scanners. Assuming that non-conjugate points in the overlapping strips exist, observations representing the discrepancy between these points follow the modified Gauss Markov stochastic model in Equation 5.8. The modified LSA procedure aims at estimating the correction to the approximate values of the unknown parameters, which would lead to the solution in Equations 5.22, 5.23, and 5.24

$$\delta\hat{\vec{x}} = (A^T P` A)^{-1} A^T P` \vec{y} = N^{-1} A^T P` \vec{y} \qquad \text{Estimated Unknowns} \qquad (5.22)$$

$$\Sigma\{\delta\hat{\vec{x}}\} = \sigma_o^2 N^{-1} \qquad \text{Variance - Covariance Matrix} \qquad (5.23)$$

$$\hat{\sigma}_o^2 = \left(\vec{y} - A\delta\hat{\vec{x}}\right)^T P` (\vec{y} - A\delta\hat{\vec{x}})/(q-u) \qquad (5.24)$$

Where $\boldsymbol{u}$ is the total number of the unknown parameters and $\boldsymbol{q}$ is the rank of the modified weight matrix ($\boldsymbol{P}$`). The modification to the LSA and the weight matrix is discussed in more details in (Kersting, 2011).

One should note that the observation equations and the normal equations matrices are manipulated to achieve the following cases:

1. If the same point is captured by two scanners at the same time (i.e., $t_k = t_l = t$). In this case, Equation 5.2 will take the following form:

$$r_A^m(i,t) - r_B^m(j,t) = \left[r_b^m(t) + R_b^m(t) r_{lu_r}^b + R_b^m(t) R_{lu_r}^b r_{lu_i}^{lu_r} + R_b^m(t) R_{lu_r}^b R_{lu_i}^{lu_r} R_{lb_i}^{lu_i}(t) r_A^{lb_i}(t)\right] -$$

$$\left[r_b^m(t) + R_b^m(t) r_{lu_r}^b + R_b^m(t) R_{lu_r}^b r_{lu_j}^{lu_r} + R_b^m(t) R_{lu_r}^b R_{lu_j}^{lu_r} R_{lb_j}^{lu_j}(t) r_B^{lb_j}(t)\right] = \vec{d} \quad (5.25)$$

After linearization of this equation, the observation equations will take the following form:

$$\mathrm{y} = A_{pos/ort}(t,i)\, x_{pos/ort_{\mathrm{t}}} + A_{pos/ort}(t,j)\, x_{pos/ort_{\mathrm{t}}} + A_{mou_{lu_i}^{lu_r}}(t,i)\, x_{mou_{lu_i}^{lu_r}} + A_{mou_{lu_j}^{lu_r}}(t,j)\, x_{mou_{lu_j}^{lu_r}} +$$

$$\left(A_{mou_{lu_r}^b}(t,i) + A_{mou_{lu_r}^b}(t,j)\right) x_{mou_{lu_r}^b} + A_{int_i}(t,i)\, x_{int_i} + A_{int_j}(t,j)\, x_{int_j} + \vec{d} + \vec{e} \quad (5.26)$$

Rearranging the terms in Equation 5.26, this equation will take the following form:

$$y = \left(A_{pos/ort}(t,i) + A_{pos/ort}(t,j)\right) x_{pos/ort_{\mathrm{t}}} + A_{mou_{lu_i}^{lu_r}}(t,i)\, x_{mou_{lu_i}^{lu_r}} + A_{mou_{lu_j}^{lu_r}}(t,j)\, x_{mou_{lu_j}^{lu_r}}$$

$$+ \left(A_{mou_{lu_r}^b}(t,i) + A_{mou_{lu_r}^b}(t,j)\right) x_{mou_{lu_r}^b} + A_{int_i}(t,i)\, x_{int_i} + A_{int_j}(t,j)\, x_{int_j} + \vec{d} + \vec{e} \quad (5.27)$$

In this case, equations (5.11- 5.17), would still be valid to update the normal equation matrices.

2. For a given point, the scanner that captured this point is the reference one ($i = r$ or $j = r$). In this case: $r_{lu_i}^{lu_r} = 0,\ R_{lu_i}^{lu_r} = I_3 - fixed$ or $r_{lu_j}^{lu_r} = 0,\ R_{lu_j}^{lu_r} = I_3 - fixed$

$A_{mou_{lu_i}^{lu_r}}(t_k, i) = 0$ *or* $A_{mou_{lu_j}^{lu_r}}(t_l, j) = 0$.

The term **"*fixed*"** means that these unknown parameters are not estimated through the calibration procedure.

If the i^{th} scanner is the reference one, Equation 5.2 will take the following form:

$$r_A^m(i, t_k) - r_B^m(j, t_l)$$

$$= \left[r_b^m(t_k) + R_b^m(t_k) r_{lu_r}^b + R_b^m(t_k) R_{lu_r}^b R_{lb_i}^{lu_i}(t_k) r_A^{lb_i}(t_k)\right]$$

$$- \left[r_b^m(t_l) + R_b^m(t_l) r_{lu_r}^b + R_b^m(t_l) R_{lu_r}^b r_{lu_j}^{lu_r} + R_b^m(t_l) R_{lu_r}^b R_{lu_j}^{lu_r} R_{lb_j}^{lu_j}(t_l) r_B^{lb_j}(t_l)\right] = \vec{d} \qquad (5.28)$$

After the linearization of this equation, the observation equations will take the following form:

$$y = A_{pos/ort}(t_k, i)\, x_{pos/ort_{t_k}} + A_{pos/ort}(t_l, j)\, x_{pos/ort_{t_l}} + A_{mou_{lu_j}^{lu_r}}(t_l, j) x_{mou_{lu_j}^{lu_r}} +$$

$$\left(A_{mou_{lu_r}^b}(t_k, i) + A_{mou_{lu_r}^b}(t_l, j)\right) x_{mou_{lu_r}^b} + A_{int_i}(t_k, i)\, x_{int_i} + A_{int_j}(t_l, j)\, x_{int_j} + \vec{d} +$$

$$\vec{e} \qquad (5.29)$$

In this case, equations (5.11- 5.17), would still be valid to update the normal equation matrices. While the components ($N_{12}, N_{21}, N_{22}, N_{23}, N_{32}, N_{24}, N_{42}$) that include the term $A_{mou_{lu_i}^{lu_r}}(t_k, i)$ will be zero.

If the j^{th} scanner is the reference one, Equation 5.2 will take the following form:

$$r_A^m(i,t_k) - r_B^m(j,t_l)$$

$$= \left[r_b^m(t_k) + R_b^m(t_k) r_{lu_r}^b + R_b^m(t_k) R_{lu_r}^b r_{lu_i}^{lu_r} + R_b^m(t_k) R_{lu_r}^b R_{lu_i}^{lu_r} R_{lb_i}^{lu_i}(t_k) r_A^{lb_i}(t_k)\right]$$

$$- \left[r_b^m(t_l) + R_b^m(t_l) r_{lu_r}^b + R_b^m(t_l) R_{lu_r}^b R_{lb_j}^{lu_j}(t_l) r_B^{lb_j}(t_l)\right] = \vec{d} \quad (5.30)$$

After the linearization of this equation, the observation equations will take the following form:

$$y =$$

$$A_{pos/ort}(t_k,i) x_{pos/ort_{t_k}} + A_{pos/ort}(t_l,j) x_{pos/ort_{t_l}} + A_{mou_{lu_i}^{lu_r}}(t_k,i) x_{mou_{lu_i}^{lu_r}} + \left(A_{mou_{lu_r}^b}(t_k,i) + A_{mou_{lu_r}^b}(t_l,j)\right) x_{mou_{lu_r}^b} + A_{int_i}(t_k,i) x_{int_i} + A_{int_j}(t_l,j) x_{int_j} + \vec{d} + \vec{e} \quad (5.31)$$

In this case, equations (5.11- 5.17), would still be valid to update the normal equation matrices. While the components $(N_{12}, N_{21}, N_{22}, N_{23}, N_{32}, N_{24}, N_{42})$ that include the term $A_{mou_{lu_j}^{lu_r}}(t_l,j)$ will be zero.

3. For in-door calibration, one can introduce a virtual reference frame for the navigation unit at the reference scanner.

In this case: $r_{lu_r}^b = 0, \quad R_{lu_r}^b = I_3 - \boldsymbol{fixed} \;\; \& \;\; A_{mou_{lu_r}^b}(t_k,i) = 0 \;\; \& \;\; A_{mou_{lu_r}^b}(t_l,j) = 0.$

For in-door calibration, Equation 5.2 will take the following form:

$$r_A^m(i,t_k) - r_B^m(j,t_l) = \left[r_b^m(t_k) + R_b^m(t_k) r_{lu_i}^{lu_r} + R_b^m(t_k) R_{lu_i}^{lu_r} R_{lb_i}^{lu_i}(t_k) r_A^{lb_i}(t_k)\right]$$

$$- \left[r_b^m(t_l) + R_b^m(t_l) r_{lu_j}^{lu_r} + R_b^m(t_l) R_{lu_j}^{lu_r} R_{lb_j}^{lu_j}(t_l) r_B^{lb_j}(t_l)\right] = \vec{d} \quad (5.32)$$

After the linearization of this equation, the observation equations will take the following form:

$$y = A_{pos/ort}(t_k, i)x_{\ pos/ort_{t_k}} + A_{pos/ort}(t_l, j)x_{pos/ort_{t_l}} + A_{mou_{lu_i}^{lu_r}}(t_k, i)x_{mou_{lu_i}^{lu_r}} +$$

$$A_{mou_{lu_j}^{lu_r}}(t_l, j)x_{mou_{lu_j}^{lu_r}} + A_{int_i}(t_k, i)x_{int_i} + A_{int_j}(t_l, j)x_{int_j} + \vec{d} + e \quad (5.33)$$

In this case, equations (5.11- 5.17), would still be valid to update the normal equation matrices. While the components (***N13, N31, N23, N32, N33, N34, N43***) will be zero.

After computing the appropriate contributions to the *N* and *C* components in each of the previous cases, the modified LSA procedure can be performed using Equations 5.22, 5.23, and 5.24 to come up with an estimate for the unknown involved parameters in the indoor calibration procedure.

5.3 The Proposed Mathematical Model for the Outdoor Calibration

In this step, the mounting parameters relating the reference scanner to IMU body frame will be estimated (refer to group 2 as shown in Figure 5.1). These parameters will be as follows:

- Three parameters for the lever arm (*ΔX_ref2b, ΔY_ref2b,* and *ΔZ_ref2b*) and,
- Three parameters for the boresight angles (*Δω_ref2b, Δφref2b,* and *Δκ_ref2b*).

As already mentioned, the advantage of this approach is that the position and orientation of the navigation frame are known from the GPS and IMU information. Thus, the mounting parameters relating the reference scanner to the IMU body frame can be determined in an open-sky environment (outdoor calibration) while having an unfavorable distribution of the calibration targets. In the proposed methodology, the following unknown parameters are considered in the outdoor calibration procedure:

- The mounting parameters relating the individual scanners to a reference scanner,
- The mounting parameters relating the reference scanner to the IMU body frame, and
- The intrinsic parameters of the individual scanners.

The general mathematical model, which can be used for the outdoor calibration procedure, is represented in Equation 5.1. Also, for the outdoor system calibration, one need to derive the discrepancy vector $(\vec{d})$ between the coordinates of two non-conjugate points in overlapping strips that have been captured by the same or different scanners (these non-conjugate points will be denoted by subscripts A and B). The difference between the true coordinates of these points can be expressed by Equation 5.34. In a similar way, if one is dealing with non-conjugate points in a LiDAR strip and control surface, the difference between the coordinates of the control point $r_{control}^{m}$ and the true coordinates of the LiDAR point in the strip denoted by the subscript B can be expressed as in Equation 5.35. Equations 5.34 and 5.35 represent the general observation equations corresponding to the discrepancy vector when dealing with overlapping strips and control data, respectively.

$$r_A^m(i,t_k) - r_B^m(j,t_l) =$$
$$\left[r_b^m(t_k) + R_b^m(t_k)r_{lu_r}^b + R_b^m(t_k)R_{lu_r}^b r_{lu_i}^{lu_r} + R_b^m(t_k)R_{lu_r}^b R_{lu_i}^{lu_r} R_{lb_i}^{lu_i}(t_k) r_A^{lb_i}(t_k)\right] -$$
$$\left[r_b^m(t_l) + R_b^m(t_l)r_{lu_r}^b + R_b^m(t_l)R_{lu_r}^b r_{lu_j}^{lu_r} + R_b^m(t_l)R_{lu_r}^b R_{lu_j}^{lu_r} R_{lb_j}^{lu_j}(t_l) r_B^{lb_j}(t_l)\right] = \vec{d} \quad (5.34)$$

$$r_{control}^m - r_B^m(j,t_l) =$$
$$r_{control}^m - \left[r_b^m(t_l) + R_b^m(t_l)r_{lu_r}^b + R_b^m(t_l)R_{lu_r}^b r_{lu_j}^{lu_r} + R_b^m(t_l)R_{lu_r}^b R_{lu_j}^{lu_r} R_{lb_j}^{lu_j}(t_l) r_B^{lb_j}(t_l)\right] = \vec{d} \quad (5.35)$$

Since these equations are not linear with respect to the unknown system parameters and measurement noise, a linearization process by Taylor series expansion is required for the LSA. The linearized equations when using overlapping strips and control information are presented in Equations 5.36 and 5.37, respectively. These equations are obtained using the initial approximations for the unknown system parameters associated with i^{th} and j^{th} scanner as the point of expansion while ignoring second and higher order terms.

$$y_t = A_{mou_{lu_r}^b}(t_k,i)x_{mou_{lu_r}^b} + A_{mou_{lu_i}^{lu_r}}(t_k,i)x_{mou_{lu_i}^{lu_r}} + A_{int_i}(t_k,i)x_{int_i} + A_{mou_{lu_r}^b}(t_l,j)x_{mou_{lu_r}^b} + A_{mou_{lu_j}^{lu_r}}(t_l,j)x_{mou_{lu_j}^{lu_r}} + A_{int_j}(t_l,j)x_{int_j} + \vec{d} + \vec{e} \quad (5.36)$$

$$y_c = A_{mou_{lu_r}^b}(t_l,j)x_{mou_{lu_r}^b} + A_{mou_{lu_j}^{lu_r}}(t_l,j)x_{mou_{lu_j}^{lu_r}} + A_{int_j}(t_l,j)x_{int_j} + \vec{d} + \vec{e} \quad (5.37)$$

Rearranging the terms in Equation 5.36, this equation will take the following form:

$$y_t = A_{mou_{lu_i}^{lu_r}}(t_k,i)x_{mou_{lu_i}^{lu_r}} + A_{mou_{lu_j}^{lu_r}}(t_l,j)x_{mou_{lu_j}^{lu_r}} + \left(A_{mou_{lu_r}^b}(t_k,i) + A_{mou_{lu_r}^b}(t_l,j)\right)x_{mou_{lu_r}^b} + A_{int_i}(t_k,i)x_{int_i} + A_{int_j}(t_l,j)x_{int_j} + \vec{d} + \vec{e} \quad (5.38)$$

One can get the final form of the linearized observations equations (Equations 5.37 and 5.38) according to the modified Gauss Markov stochastic model (Equation 5.39).

$$\vec{y}_{3m\times1} = A_{3m\times u}\,\delta\vec{x}_{u\times1} + \vec{e}_{\,3m\times1} + \vec{d}_{\,3m\times1} \quad \vec{e}\sim(0,\Sigma`) \;\; where \;\; \Sigma` = \sigma_o^2 P`^{+} \; and \; P`\vec{d} = 0 \quad (5.39)$$

Where:

- ***m*** is the number of conjugate points in overlapping strips as well as conjugates points among the overlapping strips and the control surface,
- ***u*** is the total number of the unknown parameters,

$u = \ 6(n-1) + 6 + 3n$

- ***n*** is the total number of involved scanners,
- $\boldsymbol{\delta\vec{x}}$ is the $u \times 1$ combined vector of unknown corrections to the approximate values of the system parameters, and
- ***A*** is the $(3m \times u)$ combined design matrix.

Using the LSA target function, the solution vector can be derived from the normal equation matrix (N) and the normal equation vector (C) as in Equation 5.40.

$$(N)_{(u\times u)}\ \delta\hat{\vec{x}}_{(u\times 1)} = (C\ )_{(u\times 1)} \qquad \text{(General Solution Vector)} \qquad (5.40)$$

Where:

$N = A^T P` A \quad \& \ C = A^T P` \vec{y}$

The structure of N, $\delta\vec{x}$ and C will be as follows:

$$\begin{bmatrix} N_{11_{(6(n-1)\times 6(n-1))}} & N_{12_{(6(n-1)\times 6)}} & N_{13_{(6(n-1)\times 3n)}} \\ N_{21_{(6\times 6(n-1))}} & N_{22_{(6\times 6)}} & N_{23_{(6\times 3n)}} \\ N_{31_{(3n\times 6(n-1))}} & N_{32_{(3n\times 6)}} & N_{33_{(3n\times 3n)}} \end{bmatrix} \begin{bmatrix} \delta x_{1_{(6(n-1)\times 1)}} \\ \delta x_{2_{(6\times 1)}} \\ \delta x_{3_{(3n\times 1)}} \end{bmatrix} = \begin{bmatrix} C_{1_{(6(n-1)\times 1)}} \\ C_{2_{(6\times 1)}} \\ C_{3_{(3n\times 1)}} \end{bmatrix} \qquad (5.41)$$

Where:

- $\boldsymbol{\delta\vec{x}_1}$ is the $6(n-1) \times 1$ vector of unknown corrections to the approximate values of the mounting parameters relating the different scanners to the reference one,
- $\boldsymbol{\delta\vec{x}_2}$ is the 6×1 vector of unknown corrections to the approximate values of the mounting parameters relating the reference scanner to the navigation frame, and
- $\boldsymbol{\delta\vec{x}_3}$ is the $3n \times 1$ vector of unknown corrections to the approximate values of the intrinsic parameters of the individual scanners.

One can note that rather than completely building the design matrix A, together with the discrepancy vector $\vec{y}$, and then deriving the normal equation matrix (*N*) and normal equation vector (*C*), one can use the resulting observation equations for a specific set of conjugate points in the overlapping strips (Equations 5.38) as well as conjugate points among the overlapping strips and control surface (Equations 5.37).

First, when the observations for a specific set of non-conjugate points result from the overlapping strips only, the following contributions are computed to build the sub-normal equation matrices and sub-normal equation vectors (as in Equations 5.42- 5.46).

$$N_{11}(lu_i, lu_i) = N_{11}\left(mou_{lu_i}^{lu_r}, mou_{lu_i}^{lu_r}\right) = A^T_{mou_{lu_i}^{lu_r}}(t_k, i)\ P`A_{mou_{lu_i}^{lu_r}}(t_k, i)$$

$$N_{11}(lu_i, lu_j) = N_{11}\left(mou_{lu_i}^{lu_r}, mou_{lu_j}^{lu_r}\right) = A^T_{mou_{lu_i}^{lu_r}}(t_k, i)\ P`A_{mou_{lu_j}^{lu_r}}(t_l, j)$$

$$N_{12}(lu_i, lu_r) = N_{12}\left(mou_{lu_i}^{lu_r}, mou_{lu_r}^{b}\right) = A^T_{mou_{lu_i}^{lu_r}}(t_k, i)\ P`[A_{mou_{lu_r}^{b}}(t_k, i) + A_{mou_{lu_r}^{b}}(t_l, j)]$$

$$N_{13}(lu_i, lu_i) = N_{13}\left(mou_{lu_i}^{lu_r}, int_i\right) = A^T_{mou_{lu_i}^{lu_r}}(t_k, i)\ P`A_{int_i}(t_k, i) \qquad (5.42)$$

$$N_{13}(lu_i, lu_j) = N_{13}\left(mou_{lu_i}^{lu_r}, int_j\right) = A^T_{mou_{lu_i}^{lu_r}}(t_k, i)\ P`A_{int_j}(t_l, j)$$

$$C_1(lu_i) = C_{x_{mou_{lu_i}^{lu_r}}} = A^T_{mou_{lu_i}^{lu_r}}(t_k, i)\ P`y_t$$

$$N_{11}(lu_j, lu_i) = N_{11}\left(mou_{lu_j}^{lu_r}, mou_{lu_i}^{lu_r}\right) = A_{mou_{lu_j}^{lu_r}}^{T}(t_l, j)\ P`A_{mou_{lu_i}^{lu_r}}(t_k, i)$$

$$N_{11}(lu_j, lu_j) = N_{11}\left(mou_{lu_j}^{lu_r}, mou_{lu_j}^{lu_r}\right) = A_{mou_{lu_j}^{lu_r}}^{T}(t_l, j)\ P`A_{mou_{lu_j}^{lu_r}}(t_l, j)$$

$$N_{12}(lu_j, lu_r) = N_{12}\left(mou_{lu_j}^{lu_r}, mou_{lu_r}^{b}\right) = A_{mou_{lu_j}^{lu_r}}^{T}(t_l, j)\ P`[A_{mou_{lu_r}^{b}}(t_k, i) + A_{mou_{lu_r}^{b}}(t_l, j)]$$

$$N_{13}(lu_j, lu_i) = N_{13}\left(mou_{lu_j}^{lu_r}, int_i\right) = A_{mou_{lu_j}^{lu_r}}^{T}(t_l, j)\ P`A_{int_i}(t_k, i) \tag{5.43}$$

$$N_{13}(lu_j, lu_j) = N_{13}\left(mou_{lu_j}^{lu_r}, int_j\right) = A_{mou_{lu_j}^{lu_r}}^{T}(t_l, j)\ P`A_{int_j}(t_l, j)$$

$$C_1(lu_j) = C_{x_{mou_{lu_j}^{lu_r}}} = A_{mou_{lu_j}^{lu_r}}^{T}(t_l, j)\ P`y_t$$

$$N_{21}(lu_r, lu_i) = N_{21}\left(mou_{lu_r}^{b}, mou_{lu_i}^{lu_r}\right) = [A_{mou_{lu_r}^{b}}(t_k, i) + A_{mou_{lu_r}^{b}}(t_l, j)]^T P`A_{mou_{lu_i}^{lu_r}}(t_k, i)$$

$$N_{21}(lu_r, lu_j) = N_{21}\left(mou_{lu_r}^{b}, mou_{lu_j}^{lu_r}\right) = [A_{mou_{lu_r}^{b}}(t_k, i) + A_{mou_{lu_r}^{b}}(t_l, j)]^T P`A_{mou_{lu_j}^{lu_r}}(t_l, j)$$

$$N_{22}(lu_r, lu_r) = N_{22}(mou_{lu_r}^{b}, mou_{lu_r}^{b}) = [A_{mou_{lu_r}^{b}}(t_k, i) + A_{mou_{lu_r}^{b}}(t_l, j)]^T P`\ [A_{mou_{lu_r}^{b}}(t_k, i) + A_{mou_{lu_r}^{b}}(t_l, j)] \tag{5.44}$$

$$N_{23}(lu_r, lu_i) = N_{23}(mou_{lu_r}^{b}, int_i) = [A_{mou_{lu_r}^{b}}(t_k, i) + A_{mou_{lu_r}^{b}}(t_l, j)]^T P`A_{int_i}(t_k, i)$$

$$N_{23}(lu_r, lu_j) = N_{23}(mou_{lu_r}^{b}, int_j) = [A_{mou_{lu_r}^{b}}(t_k, i) + A_{mou_{lu_r}^{b}}(t_l, j)]^T P`A_{int_j}(t_l, j)$$

$$C_2(lu_r) = C_{x_{mou_{lu_r}^{b}}} = [A_{mou_{lu_r}^{b}}(t_k, i) + A_{mou_{lu_r}^{b}}(t_l, j)]^T\ P`y_t$$

$$N_{31}(lu_i, lu_i) = N_{31}\left(int_i, mou_{lu_i}^{lu_r}\right) = A_{int_i}^{T}(t_k, i)\, P\, A_{mou_{lu_i}^{lu_r}}(t_k, i)$$

$$N_{31}(lu_i, lu_j) = N_{31}\left(int_i, mou_{lu_j}^{lu_r}\right) = A_{int_i}^{T}(t_k, i)\, P\, A_{mou_{lu_j}^{lu_r}}(t_l, j)$$

$$N_{32}(lu_i, lu_r) = N_{32}(int_i, mou_{lu_r}^{b}) = A_{int_i}^{T}(t_k, i)\, P\, [A_{mou_{lu_r}^{b}}(t_k, i) + A_{mou_{lu_r}^{b}}(t_l, j)] \quad (5.45)$$

$$N_{33}(lu_i, lu_i) = N_{33}(int_i, int_i) = A_{int_i}^{T}(t_k, i)\, P\, A_{int_i}(t_k, i)$$

$$N_{33}(lu_i, lu_j) = N_{33}(int_i, int_j) = A_{int_i}^{T}(t_k, i)\, P\, A_{int_j}(t_l, j)$$

$$C_3(lu_i) = C_{x_{int_i}} = A_{int_j}^{T}(t_k, i)\, P\, y_t$$

$$N_{31}(lu_j, lu_i) = N_{31}\left(int_j, mou_{lu_i}^{lu_r}\right) = A_{int_j}^{T}(t_l, j)\, P\, A_{mou_{lu_i}^{lu_r}}(t_k, i)$$

$$N_{31}(lu_j, lu_j) = N_{31}\left(int_j, mou_{lu_j}^{lu_r}\right) = A_{int_j}^{T}(t_l, j)\, P\, A_{mou_{lu_j}^{lu_r}}(t_l, j)$$

$$N_{32}(lu_j, lu_r) = N_{32}(int_j, mou_{lu_r}^{b}) = A_{int_j}^{T}(t_l, j)\, P\, [A_{mou_{lu_r}^{b}}(t_k, i) + A_{mou_{lu_r}^{b}}(t_l, j)] \quad (5.46)$$

$$N_{33}(lu_j, lu_i) = N_{33}(int_j, int_i) = A_{int_j}^{T}(t_l, j)\, P\, A_{int_i}(t_k, i)$$

$$N_{33}(lu_j, lu_j) = N_{33}(int_j, int_j) = A_{int_j}^{T}(t_l, j)\, P\, A_{int_j}(t_l, j)$$

$$C_3(lu_j) = C_{x_{int_j}} = A_{int_j}^{T}(t_l, j)\, P\, y_t$$

Second, when the observations for a specific set of conjugate points result from the overlapping strips and control surface, the following contributions are computed to build the sub-normal equation matrices and sub-normal equation vectors (as in Equations 5.47- 5.49).

$$N_{11}(lu_j, lu_j) = N_{11}\left(mou_{lu_j}^{lu_r}, mou_{lu_j}^{lu_r}\right) = A^T_{mou_{lu_j}^{lu_r}}(t_l, j)\ P`A_{mou_{lu_j}^{lu_r}}(t_l, j)$$

$$N_{12}(lu_j, lu_r) = N_{12}\left(mou_{lu_j}^{lu_r}, mou_{lu_r}^{b}\right) = A^T_{mou_{lu_j}^{lu_r}}(t_l, j)\ P`A_{mou_{lu_r}^{b}}(t_l, j) \qquad (5.47)$$

$$N_{13}(lu_j, lu_j) = N_{13}\left(mou_{lu_j}^{lu_r}, int_j\right) = A^T_{mou_{lu_j}^{lu_r}}(t_l, j)\ P`A_{int_j}(t_l, j)$$

$$C_1(lu_j) = C_{x_{mou_{lu_j}^{lu_r}}} = A^T_{mou_{lu_j}^{lu_r}}(t_l, j)\ P`y_c$$

$$N_{21}(lu_r, lu_j) = N_{21}\left(mou_{lu_r}^{b}, mou_{lu_j}^{lu_r}\right) = \left[A_{mou_{lu_r}^{b}}(t_l, j)\right]^T\ P`A_{mou_{lu_j}^{lu_r}}(t_l, j)$$

$$N_{22}(lu_r, lu_r) = N_{22}(mou_{lu_r}^{b}, mou_{lu_r}^{b}) = [A_{mou_{lu_r}^{b}}(t_l, j)]^T P`A_{mou_{lu_r}^{b}}(t_l, j) \qquad (5.48)$$

$$N_{23}(lu_r, lu_j) = N_{23}(mou_{lu_r}^{b}, int_j) = [A_{mou_{lu_r}^{b}}(t_l, j)]^T P`\ A_{int_j}(t_l, j)$$

$$C_2(lu_r) = C_{x_{mou_{lu_r}^{b}}} = [A_{mou_{lu_r}^{b}}(t_l, j)]^T\ P`\ y_c$$

$$N_{31}(lu_j, lu_j) = N_{31}\left(int_j, mou_{lu_j}^{lu_r}\right) = A^T_{int_j}(t_l, j)\ P`\ A_{mou_{lu_j}^{lu_r}}(t_l, j)$$

$$N_{32}(lu_j, lu_r) = N_{32}(int_j, mou_{lu_r}^{b}) = A^T_{int_j}(t_l, j)\ P`A_{mou_{lu_r}^{b}}(t_l, j) \qquad (5.49)$$

$$N_{33}(lu_j, lu_j) = N_{33}(int_j, int_j) = A^T_{int_j}(t_l, j)\ P`A_{int_j}(t_l, j)$$

$$C_3(lu_j) = C_{x_{int_j}} = A^T_{int_j}(t_l, j)\ P`y_c$$

Then, the resulting sub-matrices/vectors can be used to update the full normal equation matrix/vector as follows:

<u>N_{11} (6(n-1) x 6(n-1)):</u>

$\Sigma N_{11}(lu_1, lu_1)$ $\Sigma N_{11}(lu_1, lu_2)$..... $\Sigma N_{11}(lu_1, lu_i)$..... $\Sigma N_{11}(lu_1, lu_j)$..... $\Sigma N_{11}(lu_1, lu_{n-1})$

$\Sigma N_{11}(lu_2, lu_1)$ $\Sigma N_{11}(lu_2, lu_2)$..... $\Sigma N_{11}(lu_2, lu_i)$..... $\Sigma N_{11}(lu_2, lu_j)$..... $\Sigma N_{11}(lu_2, lu_{n-1})$

……

$\Sigma N_{11}(lu_i, lu_1)$ $\Sigma N_{11}(lu_i, lu_2)$..... $\Sigma N_{11}(lu_i, lu_i)$..... $\Sigma N_{11}(lu_i, lu_j)$..... $\Sigma N_{11}(lu_i, lu_{n-1})$

……

$\Sigma N_{11}(lu_j, lu_1)$ $\Sigma N_{11}(lu_j, lu_2)$..... $\Sigma N_{11}(lu_j, lu_i)$..... $\Sigma N_{11}(lu_j, lu_j)$..... $\Sigma N_{11}(lu_j, lu_{n-1})$

……

$\Sigma N_{11}(lu_{n-1}, lu_1)$ $\Sigma N_{11}(lu_{n-1}, lu_2)$.... $\Sigma N_{11}(lu_{n-1}, lu_i)$..... $\Sigma N_{11}(lu_{n-1}, lu_j)$.... $\Sigma N_{11}(lu_{n-1}, lu_{n-1})$

Where:

- For $\Sigma N_{11}(lu_i, lu_i)$, the summation of $N_{11}(lu_i, lu_i)$ is carried out for all the conjugate points, at least one of which has been captured by the i^{th} scanner,

- For $\Sigma N_{11}(lu_i, lu_j)$, the summation of $N_{11}(lu_i, lu_j)$ is carried out for all the conjugate points that have been captured by the i^{th} and j^{th} scanners, and

- For $\Sigma N_{11}(lu_j, lu_j)$, the summation of $N_{11}(lu_j, lu_j)$ is carried out for all the conjugate points, at least one of which has been captured by the j^{th} scanner.

NOTE: It should be noted that if the i^{th} or j^{th} scanner is the reference one, the corresponding N_{11} sub-block will be zero, since the terms $A_{mou_{lu_i}^{lu_r}}(t_k, i) = 0$ or $A_{mou_{lu_j}^{lu_r}}(t_l, j) = 0$.

N_{12} (6(n-1) x 6):

$\Sigma N_{12}(lu_1, lu_r)$

$\Sigma N_{12}(lu_2, lu_r)$

……

$\Sigma N_{12}\ (lu_i,\ lu_r)$

……

$\Sigma N_{12}\ (lu_j,\ lu_r)$

……

$\Sigma N_{12}\ (lu_{n-1},\ lu_r)$

Where:

- For $\Sigma N_{12}\ (lu_i,\ lu_r)$, the summation of $N_{12}\ (lu_i,\ lu_r)$ is carried out for all the conjugate points, at least one of which has been captured by the i^{th} scanner.

NOTE: It should be noted that if the i^{th} or j^{th} scanner is the reference one, the corresponding N_{12} sub-block will be zero, since the terms $A_{mou_{lu_i}^{lu_r}}(t_k, i) = 0$ or $A_{mou_{lu_j}^{lu_r}}(t_l, j) = 0$. It should also be noted that $N_{12} = {N_{21}}^T$.

N_{13} (6(n-1) x 3n):

$\Sigma N_{13}\ (lu_1,\ lu_1)$ $\Sigma N_{13}\ (lu_1,\ lu_2)$..... $\Sigma N_{13}\ (lu_1,\ lu_i)$..... $\Sigma N_{13}\ (lu_1,\ lu_j)$ ..... $\Sigma N_{13}\ (lu_1,\ lu_n)$

$\Sigma N_{13}\ (lu_2,\ lu_1)$ $\Sigma N_{13}\ (lu_2,\ lu_2)$ ..... $\Sigma N_{13}\ (lu_2,\ lu_i)$ ..... $\Sigma N_{13}\ (lu_2,\ lu_j)$..... $\Sigma N_{13}\ (lu_2,\ lu_n)$

……

$\Sigma N_{13}\ (lu_i,\ lu_1)$ $\Sigma N_{13}\ (lu_i,\ lu_2)$ ..... $\Sigma N_{13}\ (lu_i,\ lu_i)$ ..... $\Sigma N_{13}\ (lu_i,\ lu_j)$..... $\Sigma N_{13}\ (lu_i,\ lu_n)$

....

$\Sigma N_{13}\ (lu_j,\ lu_1)$ $\Sigma N_{13}\ (lu_j,\ lu_2)$ ..... $\Sigma N_{13}\ (lu_j,\ lu_i)$ ..... $\Sigma N_{13}\ (lu_j,\ lu_j)$..... $\Sigma N_{13}\ (lu_j,\ lu_n)$

……

$\Sigma N_{13}\ (lu_{n-1},\ lu_1)$ $\Sigma N_{13}\ (lu_{n-1},\ lu_2)$ .....$\Sigma N_{13}\ (lu_{n-1},\ lu_i)$ .....$\Sigma N_{13}\ (lu_{n-1},\ lu_j)$ ..... $\Sigma N_{13}\ (lu_{n-1},\ lu_n)$

Where:

- For $\Sigma N_{13}\ (lu_i,\ lu_i)$, the summation of $N_{13}\ (lu_i,\ lu_i)$ is carried out for all the conjugate points, at least one of which has been captured by the i^{th} scanner,

- For $\Sigma N_{13}\ (lu_i,\ lu_j)$, the summation of $N_{13}\ (lu_i,\ lu_j)$ is carried out for all the conjugate points that have been captured by the i^{th} and j^{th} scanners, and

- For $\Sigma N_{13}\ (lu_j,\ lu_j)$, the summation of $N_{13}\ (lu_j,\ lu_j)$ is carried out for all the conjugate points, at least one of which has been captured by the j^{th} scanner.

NOTE: It should be noted that if the i^{th} or j^{th} scanner is the reference one, the corresponding N_{13} sub-block will be zero, since the terms $A_{mou_{lu_i}^{lu_r}}(t_k, i) = 0$ or $A_{mou_{lu_j}^{lu_r}}(t_l, j) = 0$. It should also be noted that $N_{13} = {N_{31}}^T$

<u>C_1 (6(n-1) x 1):</u>

$\Sigma C_1\ (lu_1)$

$\Sigma C_1\ (lu_2)$

....

$\Sigma C_1\ (lu_i)$

.....

$\Sigma C_1\ (lu_j)$

.....

$\Sigma C_1\ (lu_{n-1})$

Where:

- For $\Sigma C_1\ (lu_i)$, the summation of $C_1\ (lu_i)$ is carried out for all the conjugate points, at least one of which has been captured by the i^{th} scanner.

NOTE: It should be noted that if the i^{th} or the j^{th} scanner is the reference one, the corresponding C_1 sub-vector will be zero, since the terms $A_{mou_{lu_i}^{lu_r}}(t_k, i) = 0$ or $A_{mou_{lu_j}^{lu_r}}(t_l, j) = 0$.

N_{22} (6 x 6):

$\Sigma N_{22}\ (lu_r)$

Where for $\Sigma N_{22}\ (lu_r)$, the summation of $N_{22}\ (lu_r)$ is carried out for all the conjugate points.

N_{23} (6 x 6n):

$\Sigma N_{23}\ (lu_r, lu_1)\ \Sigma N23\ (lu_r, lu_2)\ ....\ \ \Sigma N_{23}\ (lu_r, lu_i)\ ...\ \Sigma N_{23}\ (lu_r, lu_j)\ ...\ \Sigma N23\ (lu_r, lu_n)$

Where for $\Sigma N_{23}\ (lu_r, lu_i)$, the summation of $N_{23}\ (lu_r, lu_i)$ is carried out for all the conjugate points, at least one of which has been captured by the i^{th} scanner.

NOTE: It should be noted that $N_{23} = {N_{32}}^T$.

C_2 (6 x1):

$\Sigma C_2\ (lu_r)$

Where for $\Sigma C_2\ (lu_r)$ the summation of $C_2\ (lu_r)$ is carried out for all the conjugate points.

N_{33} (6nx6n):

$\Sigma N_{33}\ (lu_1, lu_1)\ \ \Sigma N_{33}\ (lu_1, lu_2).....\ \Sigma N_{33}\ (lu_1, lu_i)\ ...\ \Sigma N33\ (lu_1, lu_j)\ ...\ \ \Sigma N_{33}\ (lu_1, lu_n)$

$\Sigma N_{33}\ (lu_2, lu_1)\ \ \Sigma N_{33}\ (lu_2, lu_2).....\ \Sigma N_{33}\ (lu_2, lu_i)\ ...\ \Sigma N33\ (lu_2, lu_j)\ ...\ \ \Sigma N_{33}\ (lu_2, lu_n)$

...

$\Sigma N_{33}(lu_i, lu_1)$ $\Sigma N_{33}(lu_i, lu_2)$..... $\Sigma N_{33}(lu_i, lu_i)$ ... $\Sigma N33(lu_i, lu_j)$ ... $\Sigma N_{33}(lu_i, lu_n)$

...

$\Sigma N_{33}(lu_j, lu_1)$ $\Sigma N_{33}(lu_j, lu_2)$..... $\Sigma N_{33}(lu_j, lu_i)$ ... $\Sigma N33(lu_j, lu_j)$ ... $\Sigma N_{33}(lu_j, lu_n)$

...

$\Sigma N_{33}(lu_n, lu_1)$ $\Sigma N_{33}(lu_n, lu_2)$ ... $\Sigma N_{33}(lu_n, lu_i)$ ... $\Sigma N_{33}(lu_n, lu_j)$ ... $\Sigma N_{33}(lu_n, lu_n)$

Where:

- For $\Sigma N_{33}(lu_i, lu_i)$, the summation of $N_{33}(lu_i, lu_i)$ is carried for all the conjugate points, at least one of which has been captured by the i^{th} scanner,
- For $\Sigma N_{33}(lu_i, lu_j)$, the summation of $N_{33}(lu_i, lu_j)$ is carried for all the conjugate points that have been captured by the i^{th} and j^{th} scanners, and
- For $\Sigma N_{33}(lu_j, lu_j)$, the summation of $N_{33}(lu_j, lu_j)$ is carried for all the conjugate points, at least one of which has been captured by the j^{th} scanner.

C_3 (6n x 1):

$\Sigma C_3(lu_1)$

$\Sigma C_3(lu_2)$

...

$\Sigma C_3(lu_i)$

...

$\Sigma C_3(lu_j)$

...

$\Sigma C_3(lu_n)$

Where for $\Sigma C_3\ (lu_i)$, the summation of $C_3\ (lu_i)$ is carried out for all the conjugate points, at least one of which has been captured by the i^{th} scanner.

In summary, the mathematical model of the outdoor calibration procedure that has been developed so far is based on the availability of a specific set of non-conjugate points in the overlapping LiDAR strips (Equation 5.38) and control surface (Equation 5.37) that have been captured by different scanners. Assuming that non-conjugate points in the overlapping strips exist, observations representing the discrepancy between these points follow the modified Gauss Markov stochastic model in Equation 5.39. The modified LSA procedure aims at estimating the correction to the approximate values of the unknown parameters which would lead to the solution in Equations 5.22, 5.23, and 5.24.

One should note that the observation equations and the normal equations matrices are manipulated to achieve the following cases:

1. If the same point is captured by two scanners at the same time (i.e., $t_k = t_l = t$)

   In this case, Equation 5.34 will take the following form:

$$r_A^m(i,t) - r_B^m(j,t) = \left[r_b^m(t) + R_b^m(t)r_{lu_r}^b + R_b^m(t)R_{lu_r}^b r_{lu_i}^{lu_r} + R_b^m(t)R_{lu_r}^b R_{lu_i}^{lu_r} R_{lb_i}^{lu_i}(t)r_A^{lb_i}(t)\right] -$$

$$\left[r_b^m(t) + R_b^m(t)r_{lu_r}^b + R_b^m(t)R_{lu_r}^b r_{lu_j}^{lu_r} + R_b^m(t)R_{lu_r}^b R_{lu_j}^{lu_r} R_{lb_j}^{lu_j}(t)r_B^{lb_j}(t)\right] = \vec{d} \qquad (5.50)$$

After the linearization and rearranging the terms of this equation, the observation equations will take the following form:

$$\mathrm{y} = A_{mou_{lu_i}^{lu_r}}(t,i)x_{mou_{lu_i}^{lu_r}} + A_{mou_{lu_j}^{lu_r}}(t,j)x_{mou_{lu_j}^{lu_r}} + \left(A_{mou_{lu_r}^{b}}(t,i) + A_{mou_{lu_r}^{b}}(t,j)\right)x_{mou_{lu_r}^{b}} +$$

$$A_{int_i}(t,i)x_{int_i} + A_{int_j}(t,j)x_{int_j} + \vec{d} + \vec{e} \qquad (5.51)$$

In this case, equations (5.42- 5.46), would still be valid to update the normal equation matrices.

2. For a given point, the scanner that captured this point is the reference one ($i = r$ or $j = r$).

   In this case: $r_{lu_i}^{lu_r} = 0, \quad R_{lu_i}^{lu_r} = I_3 - \boldsymbol{fixed}$ or $r_{lu_j}^{lu_r} = 0, \quad R_{lu_j}^{lu_r} = I_3 - \boldsymbol{fixed}$

   $A_{mou_{lu_i}^{lu_r}}(t_k, i) = 0$ or $A_{mou_{lu_j}^{lu_r}}(t_l, j) = 0$.

If the i^{th} scanner is the reference one, Equation 5.34 will take the following form:

$$r_A^m(i, t_k) - r_B^m(j, t_l)$$

$$= \left[r_b^m(t_k) + R_b^m(t_k) r_{lu_r}^b + R_b^m(t_k) R_{lu_r}^b R_{lb_i}^{lu_i}(t_k) r_A^{lb_i}(t_k)\right]$$

$$- \left[r_b^m(t_l) + R_b^m(t_l) r_{lu_r}^b + R_b^m(t_l) R_{lu_r}^b r_{lu_j}^{lu_r} + R_b^m(t_l) R_{lu_r}^b R_{lu_j}^{lu_r} R_{lb_j}^{lu_j}(t_l) r_B^{lb_j}(t_l)\right] = \vec{d} \quad (5.52)$$

After the linearization of this equation, the observation equations will take the following form:

$$y = A_{mou_{lu_j}^{lu_r}}(t_l, j) x_{mou_{lu_j}^{lu_r}} + \left(A_{mou_{lu_r}^b}(t_k, i) + A_{mou_{lu_r}^b}(t_l, j)\right) x_{mou_{lu_r}^b} + A_{int_i}(t_k, i) x_{int_i} +$$

$$A_{int_j}(t_l, j) x_{int_j} + \vec{d} + \vec{e} \quad (5.53)$$

In this case the equations (5.42- 5.46), would still be valid to update the normal equation matrices. While the components ($N_{11}, N_{12}, N_{21}, N_{13}, N_{31}$) that include the term $A_{mou_{lu_i}^{lu_r}}(t_k, i)$ will be zero.

If the j^{th} scanner is the reference one, Equation 5.34 will take the following form:

$$r_A^m(i, t_k) - r_B^m(j, t_l)$$

$$= \left[r_b^m(t_k) + R_b^m(t_k) r_{lu_r}^b + R_b^m(t_k) R_{lu_r}^b r_{lu_i}^{lu_r} + R_b^m(t_k) R_{lu_r}^b R_{lu_i}^{lu_r} R_{lb_i}^{lu_i}(t_k) r_A^{lb_i}(t_k)\right]$$

$$- \left[r_b^m(t_l) + R_b^m(t_l) r_{lu_r}^b + R_b^m(t_l) R_{lu_r}^b R_{lb_j}^{lu_j}(t_l) r_B^{lb_j}(t_l)\right] = \vec{d} \quad (5.54)$$

After the linearization of this equation, the observation equations will take the following form:

$$y = A_{mou_{lu_i}^{lu_r}}(t_k, i)x_{mou_{lu_i}^{lu_r}} + \left(A_{mou_{lu_r}^{b}}(t_k, i) + A_{mou_{lu_r}^{b}}(t_l, j)\right)x_{mou_{lu_r}^{b}} + A_{int_i}(t_k, i)x_{int_i} +$$

$$A_{int_j}(t_l, j)x_{int_j} + \vec{d} + \vec{e} \qquad (5.55)$$

In this case the equations (5.42-5.46) would still be valid to update the normal equation matrices. While the components $(N_{11}, N_{12}, N_{21}, N_{13}, N_{31})$ that include the term $A_{mou_{lu_j}^{lu_r}}(t_l, j)$ will be zero.

After computing the appropriate contributions to *N* and *C* components in each of the previous cases, the modified LSA procedure can be carried out using Equations 5.22, 5.23, and 5.24 to come up with an estimate for the unknown involved parameters in the outdoor calibration procedure.

So far, the mathematical model of indoor and outdoor calibration procedures has been introduced. The idea of the proposed two-step calibration procedure is that the values of the estimated system parameters in the indoor calibration step (the mounting parameters relating the different scanners to a reference one and the intrinsic parameters of each scanner) as well as the estimated values of their standard deviations are used as a priori information in outdoor calibration procedure. One should note that the mathematical model in Equation 5.1 can incorporate prior information on the mounting parameters relating the different scanners to a reference scanner and the intrinsic parameters of each scanner through the use of the pseudo-observations in the Equations 5.56 and 5.57.

$$X_{mou_{lu_i}^{lu_r}}(indoor) = X_{mou_{lu_i}^{lu_r}} + e_{x_{mou_{lu_i}^{lu_r}}}(indoor) \text{ where } e_{x_{mou_{lu_i}^{lu_r}}} \sim \left(0, \Sigma_{mou_{lu_i}^{lu_r}}(indoor)\right) \quad (5.56)$$

$$X_{int_i}(indoor) = X_{int_i} + e_{x_{int_i}}(indoor \quad \text{where} \quad e_{x_{int_i}} \sim \left(0, \Sigma_{int_i}(indoor)\right) \quad (5.57)$$

where:

- $X_{mou_{lu_i}^{lu_r}}(indoor)$ is a prior information coming from the indoor calibration of the mounting parameters relating the different scanners to a reference scanner, and
- $X_{int_i}(indoor)$ is a prior information coming from the indoor calibration of the intrinsic parameters of each scanner.

After linearization of equations 5.56 and 5.57, the observations equations will take the following forms:

$$X_{mou_{lu_i}^{lu_r}}(indoor) = X^o_{mou_{lu_i}^{lu_r}} + x_{mou_{lu_i}^{lu_r}} + e_{x_{mou_{lu_i}^{lu_r}}}(indoor) \quad (5.58)$$

$$X_{int_i}(indoor) = X^o_{int_i} + x_{int_i} + e_{x_{int_i}}(indoor) \quad (5.59)$$

where:

- $X^o_{mou_{lu_i}^{lu_r}}$ is the initial approximation for unknown mounting parameters relating the different scanners to a reference scanner,
- $x_{mou_{lu_i}^{lu_r}}$ is the unknown corrections to the approximate values of the mounting parameters relating the different scanners to the reference scanner,

- $X^{o}_{int_i}$ is the initial approximations for the unknown intrinsic parameters of each scanner, and
- x_{int_i} is the unknown corrections to the approximate values of the intrinsic parameters of each scanner.

Rearranging the terms in Equations 5.58 and 5.59, these equations will take the following forms:

$$X_{mou^{lu_r}_{lu_i}}(indoor) - X^{o}_{mou^{lu_r}_{lu_i}} = x_{mou^{lu_r}_{lu_i}} + e_{x_{mou^{lu_r}_{lu_i}}}(indoor) \quad (5.60)$$

$$X_{int_i}(indoor) - X^{o}_{int_i} = x_{int_i} + e_{x_{int_i}}(indoor) \quad (5.61)$$

One can get the final form of Equations 5.60 and 5.61 according to the Gauss Markov atochastis model (Equations 5.62 and 5.63).

$$y_{mou^{lu_r}_{lu_i}} = x_{mou^{lu_r}_{lu_i}} + e_{x_{mou^{lu_r}_{lu_i}}}(indoor) \quad (5.62)$$

$$y_{int_i} = x_{int_i} + e_{x_{int_i}}(indoor) \quad (5.63)$$

In this case, the following contributions are computed as follows:

$N_{mou^{lu_r}_{lu_i}} = I^T \Sigma^{-1}{}_{mou^{lu_r}_{lu_i}}(indoor)\ I$

$C_{mou^{lu_r}_{lu_i}} = I^T\ \Sigma^{-1}{}_{mou^{lu_r}_{lu_i}}(indoor)\ \vec{y}_{mou^{lu_r}_{lu_i}}$

$N_{int_i} = I^T \Sigma^{-1}{}_{int_i}(indoor)\ I$, and

$C_{int_i} = I^T\ \Sigma^{-1}{}_{int_i}(indoor)\ \vec{y}_{int_i}$

Finally, the following sub-normal matrices and sub-normal vectors (as in Equations 5.64 and 5.65) will be used to update the normal equation matrix *N* and normal vector *C* according to Equation 5.41.

$$N_{11}(lu_i, lu_i) = N_{11}\left(mou_{lu_i}^{lu_r}, mou_{lu_i}^{lu_r}\right) = I^T \Sigma^{-1}{}_{mou_{lu_i}^{lur}}(indoor)\ I$$

$$N_{11}(lu_j, lu_j) = N_{11}\left(mou_{lu_j}^{lu_r}, mou_{lu_j}^{lu_r}\right) = I^T \Sigma^{-1}{}_{mou_{lu_j}^{lu_r}}(indoor)\ I$$

$$C_1(lu_i) = C_{x_{mou_{lu_i}^{lur}}} = I^T\ \Sigma^{-1}{}_{mou_{lu_i}^{lu_r}}(indoor)\ \vec{y}_{mou_{lu_i}^{lur}} \tag{5.64}$$

$$C_1(lu_j) = C_{x_{mou_{lu_j}^{lur}}} = I^T\ \Sigma^{-1}{}_{mou_{lu_j}^{lu_r}}(indoor)\ \vec{y}_{mou_{lu_j}^{lur}}$$

$$N_{33}(lu_i, lu_i) = N_{33}(int_i, int_i) = I^T \Sigma^{-1}{}_{int_i}(indoor)\ I$$

$$C_3(lu_i) = C_{x_{int_i}} = I^T\ \Sigma^{-1}{}_{int_i}(indoor)\ \vec{y}_{int_i} \tag{5.65}$$

$$N_{33}(lu_j, lu_j) = N_{33}(int_j, int_j) = I^T \Sigma^{-1}{}_{int_j}(indoor)\ I$$

$$C_3(lu_j) = C_{x_{int_j}} = I^T\ \Sigma^{-1}{}_{int_j}(indoor)\ \vec{y}_{int_j}$$

5.4 Summary

In this chapter, an innovative method for accurately determining the intrinsic and mounting parameters of multi-TMLS systems has been introduced. The proposed calibration method investigates a two-step calibration procedure for calibrating terrestrial mobile multi-laser scanning systems (indoor followed by outdoor). The idea of the proposed calibration method is that the mounting parameters relating the individual scanners to the reference frame of the navigation unit will be divided into two groups as follows:

1. The mounting parameters relating the individual scanners to a reference scanner, and
2. The mounting parameters relating the reference scanner to the reference frame of the navigation unit.

The advantage of the proposed two-step calibration procedure can be summarized as follows:

- The first group of parameters (the mounting parameters relating the different laser scanners to the reference one as well as the intrinsic parameters of the involved scanners in the TMLS system) can be determined through an indoor calibration test field, where one can have access to a favorable distribution of the calibration targets (e.g., good distribution of planar features with different slope and aspect values). During the indoor calibration stage, data will be collected from a few locations in a static mode,
- The second group (the mounting parameters relating the reference scanner to the reference frame of the navigation unit) can be determined in an open-sky environment (outdoor calibration) to ensure reliable derivation of the position and orientation of the navigation frame while having an unfavorable distribution of the calibration targets.

As well, in this chapter, the proposed mathematical model of the indoor and outdoor calibration procedures is introduced. The contributions of the proposed two-step calibration procedure can be summarized as follows:

- The indoor calibration is fully automated and requires features in the covered area with good distribution (e.g., planar features with different slope and aspect values). During the indoor calibration step, data will be collected from a few locations in a static mode.

– The outdoor calibration is fully automated and requires good quality information regarding the position and orientation of the navigation frame (i.e., GPS/IMU information).

– In the proposed indoor and outdoor calibration procedures one can note that the appropriate contributions are computed to build the sub-normal equation matrices and sub-normal equation vectors rather than completely building the design matrix A together with the misclosure vector $\vec{y}$ and then deriving the normal equation matrix (N) and normal equation vector (C).

– The modified LSA procedure is performed to come up with an estimate for the unknown involved system parameters in the indoor and outdoor calibration procedures while dealing with non-conjugate points along correspondence point-patch pairs.

The general hypothesis, which will be verified in the experimental results section, is that the proposed two-step calibration procedure is more robust than the one-step calibration procedure for the estimation of the unknown system parameters. The following specific hypotheses will be tested in the experimental results section:

- The proposed two-step calibration procedure provides parameters that are closer to the true values of the unknown system parameters.

- The performance of the two-step calibration procedure is not as sensitive to the strength of the scanning configuration as the one-step calibration procedure.

- The deterioration in the quality of the navigation data (i.e., GPS/IMU information) affects the quality of the estimated system parameters.

- The two-step calibration procedure is more robust than the one-step calibration procedure to deterioration in the quality of the navigation data.

Chapter Six: **Experimental Results**

6.1 Introduction

In this chapter, experimental results of automatic selection of overlapping strip pairs/regions using real dataset are performed. As well, experimental results of the calibration technique of airborne multi-laser scanning systems using real dataset were carried out. Moreover, the description of the simulation program to generate simulated data such as a Velodyne laser scanner was introduced. Also, the experimental results of the two-step (indoor and outdoor) and one-step calibration procedures of terrestrial mobile multi laser scanning system were demonstrated.

6.2 Experimental Results of Automatic Selection of Overlapping Strip Pairs/Regions

In this research work, automatic selection of suitable overlapping strip pairs/regions among the overlapping area was proposed (as previously discussed in chapter 3). The objective of the experimental results in this section is to show the comparative analysis (i.e., the quality of the estimated parameters, quality of fit between conjugate surfaces in overlapping strips, and the data processing speed) between a manual and automatic selection of regions among overlapping LiDAR strips. This comparative analysis was performed using the "Rigorous Calibration" Procedure proposed by (Kersting, 2011). The experiments were carried out using a real dataset which was selected to evaluate the performance of the proposed method. The explanation of the data acquisition system and the technical specification of the real dataset are presented in section 3.1. To estimate the boresight angles and the lever arm offset components together, overlapping strip pairs flown in opposite directions at different flying heights must be available. For this dataset, the flying height difference between the overlapping strip pairs 2&4 and 5&7 is very

small (~100m) and therefore they do not allow for the decoupling of the planimetric lever arm offset components and the boresight angles, which would reduce the reliability of the estimated parameters. For the utilized LiDAR system, the lever arm offset has been determined by a laboratory calibration with accuracy better than ±1 cm and was independent of the system installation. Therefore, there was no need for estimating the lever arm offset during the in-flight calibration procedure. As a result, only the boresight angles, the range bias, and the mirror angle scale were considered in the calibration procedure. One should note that for reliable estimation of the range bias, ground control points should be used since the magnitude of the discrepancies among overlapping strips caused by the range bias is very small. As well, for reliable estimation of the scale factor of mirror scanning angles, well distributed data in the across flight direction should be used. The manual and automatic approaches for selecting the regions among the overlapping strip pairs were studied to estimate the system parameters for 3 test scenarios: Test scenario "I" corresponds to the minimum optimal configuration, consisting of three overlapping pairs (two flown in different flying heights in opposite directions and one flown in parallel direction). The results for the optimum minimum selection of appropriate overlapping strip pairs have been already presented in chapter 3. Test scenario "II" adds one more overlapping pair to the minimum configuration, for a total of four overlapping pairs. Finally, test scenario "III" adds control data to the scenario "II". The objective of Test scenarios "II" and "III" is evaluating the performance of the proposed calibration procedure by adding one more overlapping pair and control data to the minimum configuration. Table 6.1 presents the characteristics of involved overlapping strip pairs utilized in the calibration procedure using manual and automatic selection of regions among these overlapping strip pairs. The number of matched point-patch pairs in the

calibration process, using manual and automatic selection of regions among overlapping strip pairs was, also reported in Table 6.1. From Table 6.1, one can note that the number of matched point-patch pairs for each given overlapping pair in manual and automatic selection is different.

As mentioned in chapter 4, the point-patch correspondence, due to the high density of the LiDAR data, was used as suitable primitives to be used in the calibration procedure. Therefore, one of the overlapping strip pairs, denoted by "S_1", was represented by LiDAR points while the second strip, denoted by "S_2", was represented by triangular patches. In case of manual selection, S_1 and S_2 were manually selected regions while in the automatic selection S_1 was presented by the entire original overlapping area and S_2 was represented by the automatically selected clustered regions with varying slope, aspect, and distribution among the overlapping strip pairs). Table 6.2 shows the tested scenarios. Tables 6.3 and 6.4 report the estimated system parameters using the "Rigorous Calibration" method for the 3 test scenarios in case of manual and automatic selection of regions among overlapping strip pairs, respectively. Figures 6.1 and 6.2 show sample of manually and automatically selected regions among overlapping strip pairs, respectively.

Table 6.1. Characteristics of the LiDAR overlapping strip pairs used in the calibration procedure

Overlap Pair	**Flight Configuration**	**Average Flying Height (m)**	**Number of matched point-patch pairs out of the total number of points in S_1 using manual selection**	**Number of matched point-patch pairs out of the total number of points in S_1 using automatic selection**
(a) Strips 1&9	Parallel direction	699	16545 out of 20608	23820 out of 144656
(b) Strips 2&4	Opposite direction	703	8039 out of 11677	12241 out of 85989
(c) Strips 5&7	Opposite direction	795	10783 out of 13690	12240 out of 115688
(d) Strips 5&6	Cross direction	804	12842 out of 17123	14726 out of 137985

Table 6.2. List of overlapping strip pairs used in the tested scenarios

Test Scenario	Overlapping Pairs
I	(a), (b), and (c)
II	(a),(b), (c), and (d)
III	(a), (b), (c), (d) and Control Data

Table 6.3. Estimated system parameters using manual selection of regions among overlapping strip pairs

	$\Delta\omega$ (Sec±Sec)	**$\Delta\varphi$ (Sec±Sec)**	**$\Delta\kappa$ (Sec±Sec)**	**S**	**$\Delta\rho$ (m±m)**	**Processing time (Sec)**
Proposed Calibration (Overlapping Strips Only: Scenario I)	-342.2 ±0.5	104.3 ±0.7	226.8 ±2.7	1.00009 ±0.00001	-	170
Proposed Calibration (Overlapping Strips Only: Scenario II)	-336.9 ±0.5	114.7 ±0.6	230.0 ±2.2	1.00017 ±0.00001	-	125
Proposed Calibration (Overlapping Strips + Control Data : Scenario III)	-340.8 ±0.5	115.6 ±0.6	227.9 ±2.2	1.00005 ±0.00001	0.023 ±0.001	172

Table 6.4. Estimated system parameters using automatic selection of appropriate regions among overlapping strip pairs

	$\Delta\omega$ (Sec±Sec)	**$\Delta\varphi$ (Sec±Sec)**	**$\Delta\kappa$ (Sec±Sec)**	**S**	**$\Delta\rho$ (m±m)**	**Processing time (Sec)**
Proposed Calibration (Overlapping Strips Only: Scenario I)	-332.9 ±0.4	103.5 ±0.6	237.6 ±2.7	1.00007 ±0.00001	-	85
Proposed Calibration (Overlapping Strips Only: Scenario II)	-328.9 ±0.4	109.4 ±0.6	230.4 ±2.4	1.00024 ±0.00001	-	90
Proposed Calibration (Overlapping Strips + Control Data : Scenario III)	-331.2 ±0.4	110.3 ±0.6	224.6 ±2.4	1.00019 ±0.00001	0.020 ±0.001	92

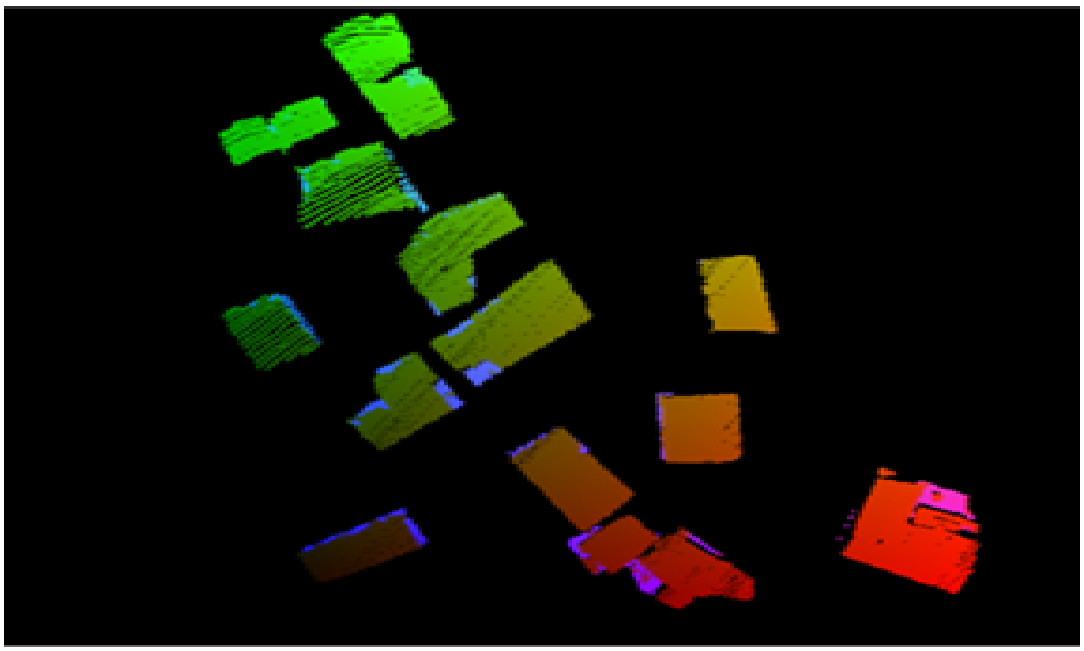

Figure 6.1. Visualization of manually selected regions among the overlapping strip pair 1&9

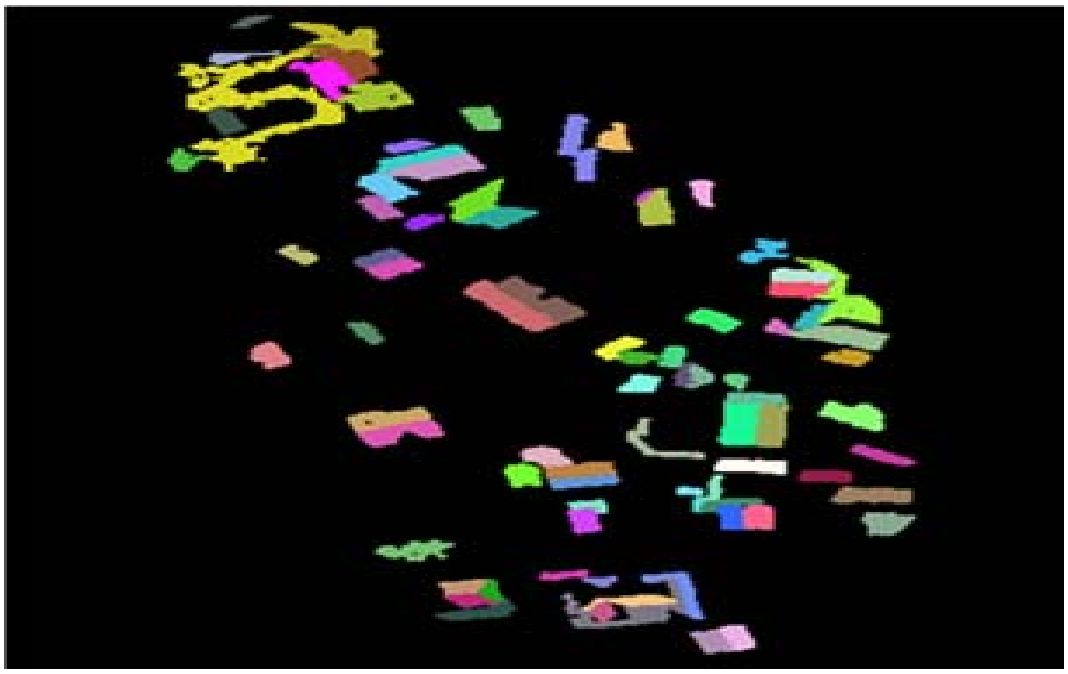

Figure 6.2. Visualization of automatically selected regions among the overlapping strip pair 1&9

One can note in Tables 6.3 and 6.4 that the largest estimated parameter is the boresight roll angle followed by the boresight yaw and pitch angles. Furthermore, the estimation of the scale factor of mirror scanning angles and range bias using the proposed method are not significantly large. It can be noticed in the experiments including overlapping strips only that adding one more overlapping strip pairs to the minimum optimum configuration do not lead to significant improvement in the quality of the estimated calibration parameters. To verify the quality of the estimated parameters, the discrepancies among conjugate surface elements in overlapping strips have been computed before and after the calibration process using the nominal and estimated system parameters, respectively. The utilized nominal values for the system parameters are $\Delta\omega = \Delta\varphi = \Delta k = 0$ [deg], $\Delta\rho = 0$[m], and $S=1$. Tables 6.5 and 6.6 report the determined discrepancies between overlapping strip pairs before and after applying the calibration process for the 3 test scenarios in case of manual and automatic selection of regions among overlapping strip pairs respectively.

Table 6.5. Discrepancies (i.e., three shifts and three rotations) between overlapping strips before and after the calibration process reconstructed using nominal and estimated system parameters) in manual selection

Before Calibration			Proposed Calibration Overlapping Strips Only (Scenario I / Scenario II)			Proposed Calibration (Overlapping Strips + Control Data : Scenario III)		
1&9								
X_T(m)	Y_T(m)	Z_T(m)	X_T(m)	Y_T(m)	Z_T(m)	X_T(m)	Y_T(m)	Z_T(m)
0.0685	-0.1989	-0.0719	0.0084/ 0.0163	-0.0059/ 0.0012	0.0152/ 0.0136	0.0173	-0.004	0.0145
ω(°)	φ(°)	κ(°)	ω(°)	φ(°)	κ(°)	ω(°)	φ(°)	κ(°)
-0.0224	0.0098	0.0432	0.0139/ 0.0137	0.014/ 0.0116	0.0173/ 0.0155	0.0137	0.0128	0.0176
2&4								
X_T(m)	Y_T(m)	Z_T(m)	X_T(m)	Y_T(m)	Z_T(m)	X_T(m)	Y_T(m)	Z_T(m)
0.0517	0.5642	0.0639	-0.0167/ -0.0367	0.0614/ 0.0694	-0.003/ -0.0006	-0.0402	0.0767	-0.0013
ω(°)	φ(°)	κ(°)	ω(°)	φ(°)	κ(°)	ω(°)	φ(°)	κ(°)
0.1408	0.0572	0.0008	-0.0137/ -0.0058	0.021/ 0.0226	-0.0081/ -0.006	-0.009	0.0223	-0.0084
5&6								
X_T(m)	Y_T(m)	Z_T(m)	X_T(m)	Y_T(m)	Z_T(m)	X_T(m)	Y_T(m)	Z_T(m)
0.3349	-0.4631	0.0095	-0.0102/ NA	-0.0184/ NA	0.0222/ NA	-0.0114	-0.0191	0.0227
ω(°)	φ(°)	κ(°)	ω(°)	φ(°)	κ(°)	ω(°)	φ(°)	κ(°)
-0.0626	-0.1021	-0.0083	0.0011/ NA	0.0069/ NA	0.0018/ NA	0.0018	0.0078	0.0019
5&7								
X_T(m)	Y_T(m)	Z_T(m)	X_T(m)	Y_T(m)	Z_T(m)	X_T(m)	Y_T(m)	Z_T(m)
0.7591	-0.1461	0.0961	0.0068/ 0.0127	-0.0152/ 0.0058	0.025/ 0.027	0.0115	0.0071	0.027
ω(°)	φ(°)	κ(°)	ω(°)	φ(°)	κ(°)	ω(°)	φ(°)	κ(°)
0.0832	-0.1677	0.0032	0.0033/ 0.0028	0.0158/ 0.0135	0.0223/ 0.0229	0.0024	0.0141	0.0229

Table 6.6. Discrepancies (i.e., three shifts and three rotations) between overlapping strips before and after the calibration process (reconstructed using nominal and estimated system parameters) in automatic selection

Before Calibration			Proposed Calibration Overlapping Strips Only (Scenario I / Scenario II)			Proposed Calibration (Overlapping Strips + Control Data : Scenario III)		
1&9								
X_T(m)	Y_T(m)	Z_T(m)	X_T(m)	Y_T(m)	Z_T(m)	X_T(m)	Y_T(m)	Z_T(m)
0.0619	-0.1751	-0.0664	0.0045/ 0.0140	-0.0204/ -0.0163	0.0081/ 0.0060	0.0131	-0.0179	0.0066
ω(o)	φ(o)	κ(o)	ω(o)	φ(o)	κ(o)	ω(o)	φ(o)	κ(o)
-0.0112	0.0115	0.0257	0.0049/ 0.0060	0.0203/ 0.0146	0.0240/ 0.0221	0.0059	0.0161	0.0230
2&4								
X_T(m)	Y_T(m)	Z_T(m)	X_T(m)	Y_T(m)	Z_T(m)	X_T(m)	Y_T(m)	Z_T(m)
-0.0690	-0.6106	-0.0689	0.0309/ 0.0381	-0.0973/ -0.0950	0.0008/ -0.0025	0.0341	-0.0983	-0.0013
ω(o)	φ(o)	κ(o)	ω(o)	φ(o)	κ(o)	ω(o)	φ(o)	κ(o)
-0.1765	-0.0553	0.0114	-0.0113/ -0.0244	-0.0137/ -0.0169	0.0201/ 0.0186	-0.0201	-0.0158	0.0164
5&6								
X_T(m)	Y_T(m)	Z_T(m)	X_T(m)	Y_T(m)	Z_T(m)	X_T(m)	Y_T(m)	Z_T(m)
-0.3219	0.4668	-0.0233	0.0030/ NA	0.0110/ NA	-0.0289/ NA	0.0046	0.0085	-0.0297
ω(o)	φ(o)	κ(o)	ω(o)	φ(o)	κ(o)	ω(o)	φ(o)	κ(o)
0.0627	0.1029	0.0296	0.0027/ NA	-0.0044/ NA	0.0070/ NA	0.0021	-0.0056	0.0054
5&7								
X_T(m)	Y_T(m)	Z_T(m)	X_T(m)	Y_T(m)	Z_T(m)	X_T(m)	Y_T(m)	Z_T(m)
0.7379	-0.1190	0.0500	0.0006/ -0.0021	-0.0096/ 0.0041	0.0220/ 0.0230	-0.0042	0.0068	0.0228
ω(o)	φ(o)	κ(o)	ω(o)	φ(o)	κ(o)	ω(o)	φ(o)	κ(o)
0.0737	-0.1728	-0.0006	0.0078/ 0.0075	0.0078/ 0.0074	0.0164/ 0.0148	0.0072	0.0079	0.0157

From Tables 6.5 and 6.6, one can observe large discrepancies among the overlapping strip pairs before the calibration procedure in case of manual and automatic selection of regions among overlapping strip pairs. For instance, the overlapping strip pair 2 and 4 (flown in opposite directions—East-West) had a large shift in the y-axis, which is approximately the across flight direction. This discrepancy can be attributed to large deviation between the nominal and estimated boresight roll angle, which mainly affects the across-flight direction, i.e., a constant shift across the flight direction and a rotation around the flight direction. Similarly, the overlapping strip pair 5 and 7 (also flown in opposite directions—North-South) had a large shift in the x-axis, which is approximately the across flight direction. The impact of the boresight roll angle is larger for the overlapping strip pair 5 and 7 due to the fact that it was flown at higher flying height. One should note that for the overlapping strip pair 1 and 9, no significant discrepancy in the across flight direction had been observed before the calibration process. This is due to the fact that for strips flown in the same direction, inaccurate boresight roll angle only causes a constant vertical shift between conjugate surface elements with a much smaller magnitude (the magnitude increases with an increased lateral distance between the strips—which is not the case for this strip pair). The slightly larger shift in the y-axis for the strip pair 1 and 9, which is approximately along the flight direction of these strips, can be attributed to an inaccurate nominal value for the boresight yaw angle. Similar to the other strip pairs, a significant improvement after the calibration process was noticeable.

In summary, in this research work a new approach was presented for automatic selection of appropriate overlapping strip pairs/regions, which should achieve the minimum optimal flight configuration to be used in the LiDAR system calibration. The experimental results have shown

that the quality of the estimated parameters using the automatic selection are quite similar to the estimated parameters using the manual selection, while the processing time of automatic selection is 2 times faster than the manual selection. These results prove that accurate estimation of the calibration parameters and faster data processing speed can be obtained using the proposed method.

The contributions of the proposed method can be summarized as follows:

- The proposed method is fully automated and it doesn't depend on the operator, while the manual selection of overlapping pairs/regions proposed by (Kersting, 2011) relies on the experience of the operator,
- Appropriate overlapping strip pairs which should achieve the minimum optimum flight configuration are automatically selected. Also, regions which represent suitable LiDAR surfaces (regions with varying slope, aspect, and distribution within the overlapping strips) to be used in the calibration procedure are automatically selected compared to the manual selection of overlapping pairs/regions proposed by (Kersting, 2011),
- The proposed method leads to accurate estimation of the calibration parameters, and
- The proposed method leads to faster and reliable LiDAR system calibration.

6.3 Experimental Results of the Calibration Technique for Airborne Multi-Laser Scanning Systems

The calibration technique proposed in (Kersting, 2011) denoted as "Rigorous Calibration", deals with overlapping strips, which are imaged by one laser scanner in the airborne LiDAR system. In this research work, new calibration technique for dealing with airborne multi-laser scanning systems is introduced. The experiments presented in this section using a real dataset had the following objectives:

- Test the feasibility of the proposed calibration technique for the estimation of the mounting parameters relating the individual scanners to the IMU body frame and the intrinsic parameters of each scanner.
- Verify whether adding more overlapping strip pairs than the optimum recommended configuration significantly improves the results.
- Evaluate the improvement in the relative accuracy of the LiDAR point cloud after the proposed calibration technique quantitatively.

In this section, the real dataset used to perform the experiments is the same dataset that was used in section 6.2. The hypothesis to test the performance of the proposed calibration technique is that the 9 flight lines (as illustrated in Figure 3.3) are captured by 2 scanners (e.g., scanner 1 and 2). For instance, the strips 1, 2, 3, 4 and 5 are captured by scanner 1 and strips 6, 7, 8 and 9 are captured by scanner 2. Table 6.7 shows the characteristics of the utilized overlapping strip pairs in the proposed calibration technique, which are captured by involved scanners (scanner 1 and/or scanner 2). The utilized test scenarios in the proposed calibration technique are listed in Table 6.2. One can note that the automatically selected regions among the overlapping strip pairs

are utilized in the proposed calibration procedure. Table 6.8 reports the estimated calibration parameters using the proposed calibration procedure for the 3 test scenarios for scanners 1 and 2.

Table 6.7. Characteristics of the LiDAR overlapping strip pairs used in the proposed calibration procedure

Overlap Pair	**Flight Configuration**	**Captured by involved scanner (Scanner 1/scanner 2)**
(a) Strips 1&9	Parallel direction	Scanner 1& Scanner 2
(b) Strips 2&4	Opposite direction	Scanner 1
(c) Strips 5&7	Opposite direction	Scanner 1& Scanner 2
(d) Strips 5&6	Cross direction	Scanner 1& Scanner 2

Table 6.8. Estimated system parameters of scanners 1and 2

	Proposed Calibration (Overlapping Strips Only: Scenario I)	**Proposed Calibration (Overlapping Strips Only: Scenario II)**	**Proposed Calibration (Overlapping Strips + Control Data : Scenario III**
Estimated system parameters of scanner 1			
Δω (Sec±Sec)	-337.8 ±0.5	-333.9 ±0.6	-335.4 ±0.5
Δφ (Sec±Sec)	102.8 ±0.6	108.5 ±0.8	106.8 ±0.5
Δκ (Sec±Sec)	245.1 ±2.9	234.0 ±2.6	220.8 ±2.2
S	1.00007 ±0.00001	1.00006 ±0.00001	0.999921 ±0.00001
Δρ (m±m)	-	-	0.029 ±0.001
Processing time (Sec)	95	100	105
Estimated system parameters of scanner 2			
Δω (Sec±Sec)	-330.9 ±0.4	-334.5 ±0.6	-338.2 ±0.5
Δφ (Sec±Sec)	105.5 ±0.8	104.4 ±0.5	108.8 ±0.6
Δκ (Sec±Sec)	235.4 ±2.6	233.0 ±2.5	223.6 ±2.4
S	1.00007 ±0.00001	1.00006 ±0.00001	1.00008 ±0.00001
Δρ (m±m)	-	-	0.031 ±0.001
Processing time (Sec)	95	100	105

From the results in Table 6.8 in comparison with the results in Table 6.4, one should note that the estimated parameters using the proposed calibration procedure (the hypothesis that the LiDAR system consists of 2 scanners) are quite similar to the estimated parameters using "Rigorous Calibration" process (LiDAR system has one scanner). To quantitatively evaluate the performance of the proposed calibration procedure, the discrepancies, i.e., three shifts (X_T,Y_T,Z_T) and three rotations (ω, φ, κ) between conjugate surface elements in overlapping strips, are computed before the calibration and after reconstructing the LiDAR point cloud using the estimated system parameters. Table 6.9 reports the estimated discrepancies before and after applying the proposed calibration technique using the different test scenarios. From the results in Table 6.9 in comparison with the results in Table 6.6, one can note that the determined discrepancies between overlapping strip pairs before and after applying the proposed calibration procedure are quite closer to the estimated discrepancies before and after using "Rigorous Calibration" process.

Table 6.9. Discrepancies (i.e., three shifts and three rotations) between overlapping strips before and after the proposed calibration process

Before Calibration			Proposed Calibration Overlapping Strips Only (Scenario I / Scenario II)			Proposed Calibration (Overlapping Strips + Control Data : Scenario III)		
1&9								
X_T(m)	Y_T(m)	Z_T(m)	X_T(m)	Y_T(m)	Z_T(m)	X_T(m)	Y_T(m)	Z_T(m)
0.0619	-0.1751	-0.0664	0.0125/ 0.0171	-0.0117/ -0.0078	0.0047/ 0.0037	0.0165	-0.0129	0.0047
ω(o)	φ(o)	κ(o)	ω(o)	φ(o)	κ(o)	ω(o)	φ(o)	κ(o)
-0.0112	0.0115	0.0257	0.0087/ 0.0091	0.0193/ 0.0163	0.0312/ 0.0293	0.0089	0.0188	0.0306
2&4								
X_T(m)	Y_T(m)	Z_T(m)	X_T(m)	Y_T(m)	Z_T(m)	X_T(m)	Y_T(m)	Z_T(m)
-0.0690	-0.6106	-0.0689	0.0166/ 0.0278	-0.0939/ -0.0980	0.0068/ -0.0037	0.0133	-0.0935	0.0067
ω(o)	φ(o)	κ(o)	ω(o)	φ(o)	κ(o)	ω(o)	φ(o)	κ(o)
-0.1765	-0.0553	0.0114	-0.0047/ -0.0121	-0.0172/ -0.0191	0.0064/ 0.0047	-0.0049	-0.0173	0.0061
5&6								
X_T(m)	Y_T(m)	Z_T(m)	X_T(m)	Y_T(m)	Z_T(m)	X_T(m)	Y_T(m)	Z_T(m)
-0.3219	0.4668	-0.0233	0.0133/ NA	0.0241/ NA	-0.0287/ NA	0.0146	0.0185	-0.0293
ω(o)	φ(o)	κ(o)	ω(o)	φ(o)	κ(o)	ω(o)	φ(o)	κ(o)
0.0627	0.1029	0.0296	0.0048/ NA	-0.0101/ NA	0.0120/ NA	0.0036	-0.0111	0.0293
5&7								
X_T(m)	Y_T(m)	Z_T(m)	X_T(m)	Y_T(m)	Z_T(m)	X_T(m)	Y_T(m)	Z_T(m)
0.7379	-0.1190	0.0500	0.0015/ -0.0020	-0.0016/ 0.0042	0.0213/ 0.0231	-0.0042	0.0066	0.0225
ω(o)	φ(o)	κ(o)	ω(o)	φ(o)	κ(o)	ω(o)	φ(o)	κ(o)
0.0737	-0.1728	-0.0006	0.0075/ 0.0076	0.0083/ 0.0075	0.0281/ 0.0151	0.0068	0.0085	0.0287

In summary, in this research work a new calibration technique for dealing with airborne multi-laser scanning systems is introduced. The experiments were performed using the hypothesis that real dataset (9 flight lines) were captured by 2 scanners involving the LiDAR system. The experimental results showed that accurate estimation of the calibration parameters of each laser scanner can be obtained using the proposed method. The contributions of the proposed method can be summarized as follows:

- The proposed method is fully automated,
- The proposed method is reliable for calibrating airborne LiDAR system characterized by the use of multiple laser scanners, and
- The proposed approach can be used to test the stability analysis of a single scanner data acquisition system and verify the quality of the navigation data within the data collection mission.

6.4 Data Simulation Program for Generating 3D LiDAR Data Using a Velodyne Mobile Laser Scanning System (HDL-32E)

6.4.1 Introduction

Laser scanning, often also referred to as LiDAR at different platforms (TLS, TMLS and ALS) systems are considered as a well-accepted tool that can quickly acquire precise 3D point clouds of the terrain surfaces. The LiDAR points can be efficiently utilized for automatic reconstruction of 3D models of the objects on the terrain and the terrain itself. Even though LiDAR data have some drawbacks; such as hazy breaklines, relatively low horizontal accuracy (this is mainly the case of ALS systems) and no inherent redundancy, it has been widely used because of its time and cost-effectiveness, in addition to its reliability. Over the past few years, TMLS systems have become of the most dominant tools for performing many geomatics applications such as urban road survey, 3D city model, national mapping and infrastructure deformation monitoring. The captured point cloud form TMLS system has to meet certain accuracies, which strictly relies on a rigorous system calibration.

Several studies have been performed to develop more efficient algorithms to generate 3D spatial information using LiDAR data. Many algorithms have been developed for, segmentation (Lee, 2002), building/road reconstruction (Haala and Brenner, 1999; Rottensteiner, 2003; Vosselman, 2002), forest management (Perrson et al, 2002) and others. These algorithms can be easily and reliably verified by using simulated LiDAR data with various properties in diverse environments. In other words, the data simulation of such a LiDAR system is significantly useful not only to design an optimal sensor for a specific application but also to assess data processing algorithms with various kinds of test data. For instance, NASA has used simulation software to design and

verify the hardware of GLAS (Geoscience Laser Altimeter System) on ICESat spacecraft (Filin et al, 2000). In a similar way, CAIL (Center for Advanced Imaging LADAR) at the University of Utah developed simulation software, "LadarSIM", and performed various experiments related with LADAR (Pack et al, 2006). The earlier studies on the simulation of LiDAR data were performed by only a few researchers. In this research work, due to the unavailability of real a dataset, simulation program was developed for generating 3D LiDAR data such as a Velodyne Mobile laser scanning system (HDL-32E) to investigate the indoor and outdoor LiDAR system calibration algorithms. In this study, the geometric modeling of the simulated indoor and outdoor LiDAR system consisted of three main subsystems (sensors) such as GPS, IMU, and any number of Velodyne laser scanners. The LiDAR point positioning equation was derived based on the geometric relationship between these sensors. In the next sections, the specification and description of the Velodyne Mobile laser scanning system (HDL-32E) will be introduced. As well, the concept and the geometric modeling for the data simulation will be presented.

6.4.2 The Specifications and Description of the Velodyne Mobile Laser Scanning System (HDL-32E)

In the past few years, different types of LiDAR devices existed with varying scanning mechanisms, number of lasers, and geometric configurations. For this investigation, a Velodyne HDL-32E was used. The HDL-32E measures just 5.7 inches high by 3.4 inches wide, weighs less than three pounds and is designed to meet rigorous military and automotive environmental specifications (Source: http://www.velodynelidar.com/lidar/hdlpressroom/08_24_10_press.aspx) as shown in Figure 6.3.

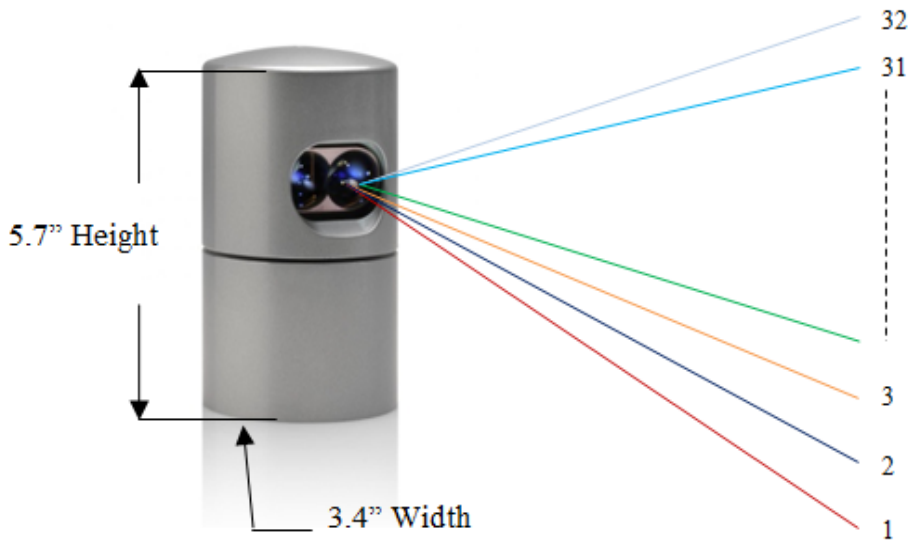

Figure 6.3. Velodyne HDL-32E scanner

The HDL-32E features up to 32 lasers aligned over a 41.34 degree vertical field of view (α) (from +10.67 to -30.67 degrees), and its patent pending rotating head design delivers a 360 degree horizontal field of view (β), as shown in Figure 6.4. The HDL-32E generates 700,000 distance points per second, and provides measurement and intensity information over a range of five centimeters to 100 meters, with a typical accuracy better than ±2 cm at 10 Hz revolutions per second. The output from HDL-32E is a rich and high definition 3D point cloud that provides mobile mapping applications with more useful environmental data than conventional LiDAR sensors. According to the aforementioned descriptions, the scanner can be identified as a hybrid scanner on the market. An overview of the specifications for the Velodyne scanner is given in Table 6.10 (Source: http://www.velodynelidar.com).

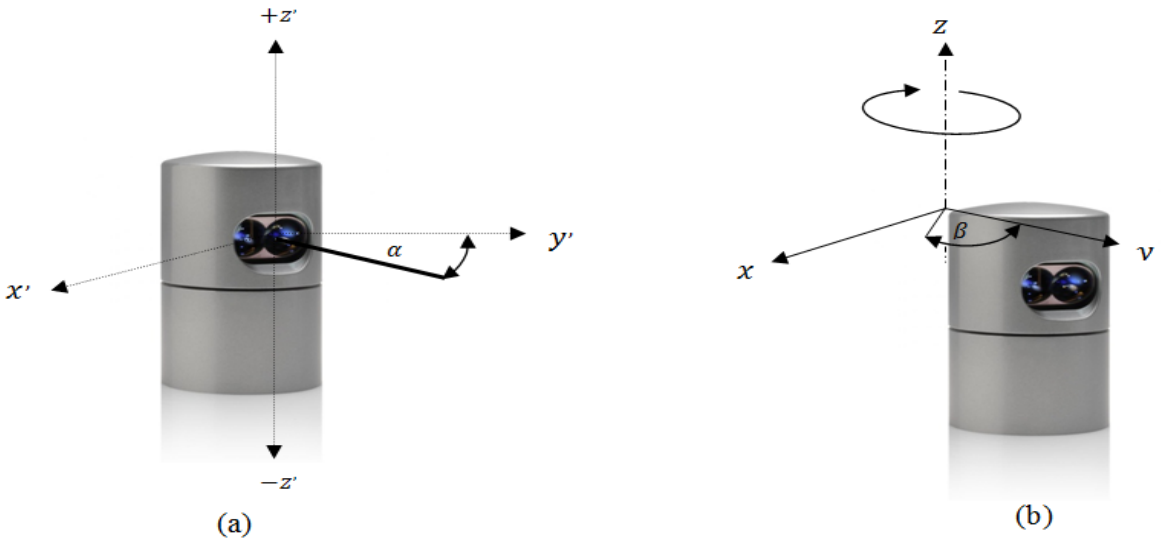

Figure 6.4. The Velodyne LiDAR HDL-32E is composed of 32 beams. Each laser orientation is function of α and β. The α angle is fixed by the beams (a). The β angle is achieved by utilizing the Velodyne rotation (b)

Table 6.10. Manufacturer Specifications for the HDL-32E Scanner

Sensor	32 lasers
	+10.67 to -30.67 degree field of view (vertical)
	360 degree field of view (horizontal)
	10 Hz frame rate (revolutions / Sec)
	Approximately 700,000 points/second
	Accuracy :< 2 cm (one sigma at 25 m)
	Angular resolution (vertical) ~ 1.33 degree
	Angular resolution (horizontal) ~ 0.16 degrees at 600 rpm
Laser	Class 1
	905 nm wavelength
	Time of flight distance measurement with intensity
	Measurement range 100 m (5 cm to 100 m)

6.4.3 Concept and the Geometric Modeling for the Data Simulation

6.4.3.1 Overview

Basically, data generated by the simulation program should exhibit all characteristics of the data acquired by an actual scanner. In general, the geometric modeling to develop the LiDAR simulation program comprises three main components, as shown in Figure 6.5.

Sensors, which consist of GPS (Global Positioning System), IMU (Inertial Measuring Unit) and one or multiple laser scanners, can compute the origin and the direction of laser beams by geometrically integrating the data from the individual sensors.

Target/Terrain is used as the input data for the simulation program. This module contains the shapes of the indoor and outdoor objects (3D CAD models), which are used to investigate the indoor and outdoor LiDAR system calibration algorithms.

Beam Interaction operates by finding the surface of the target which intersects with the beam ray. This is realized by determining the point of intersection of the beam with the surface of the target at the firing time of the beam ray. Finally, the returned intersection points are collected to represent the simulated surface.

The main components of the geometric modeling and the detailed process of each component will be explained in the following sub-sections.

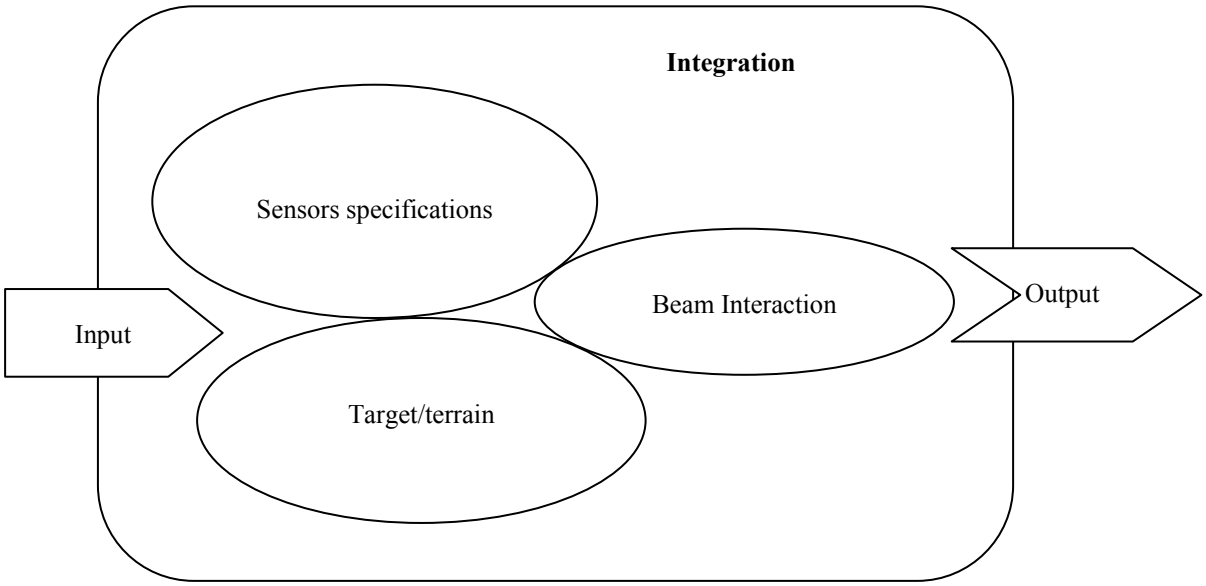

Figure 6.5. Essential components in LiDAR simulation

6.4.3.2 Sensor Modeling

To generate the simulated LiDAR data, it is necessary to explain the principle of LiDAR system. In general the LiDAR system consists of GPS, IMU and one or multiple laser scanners, as shown in Figure 6.6.

The coordinates of the LiDAR points on a surface of a target are computed using the derived measurements from each sensor as well as the mounting parameters relating such sensors. The mathematical relationship between the LiDAR point coordinates, the system measurements, and parameters associated with the j^{th} scanner of n available scanners are expressed through the LiDAR point positioning equation as represented in Equation 6.1.

$$r_I^m = r_b^m(t) + R_b^m(t) r_{lu_j}^b + R_b^m(t) R_{lu_j}^b R_{lb_j}^{lu_j}(t) r_l^{lb_j}(t) \tag{6.1}$$

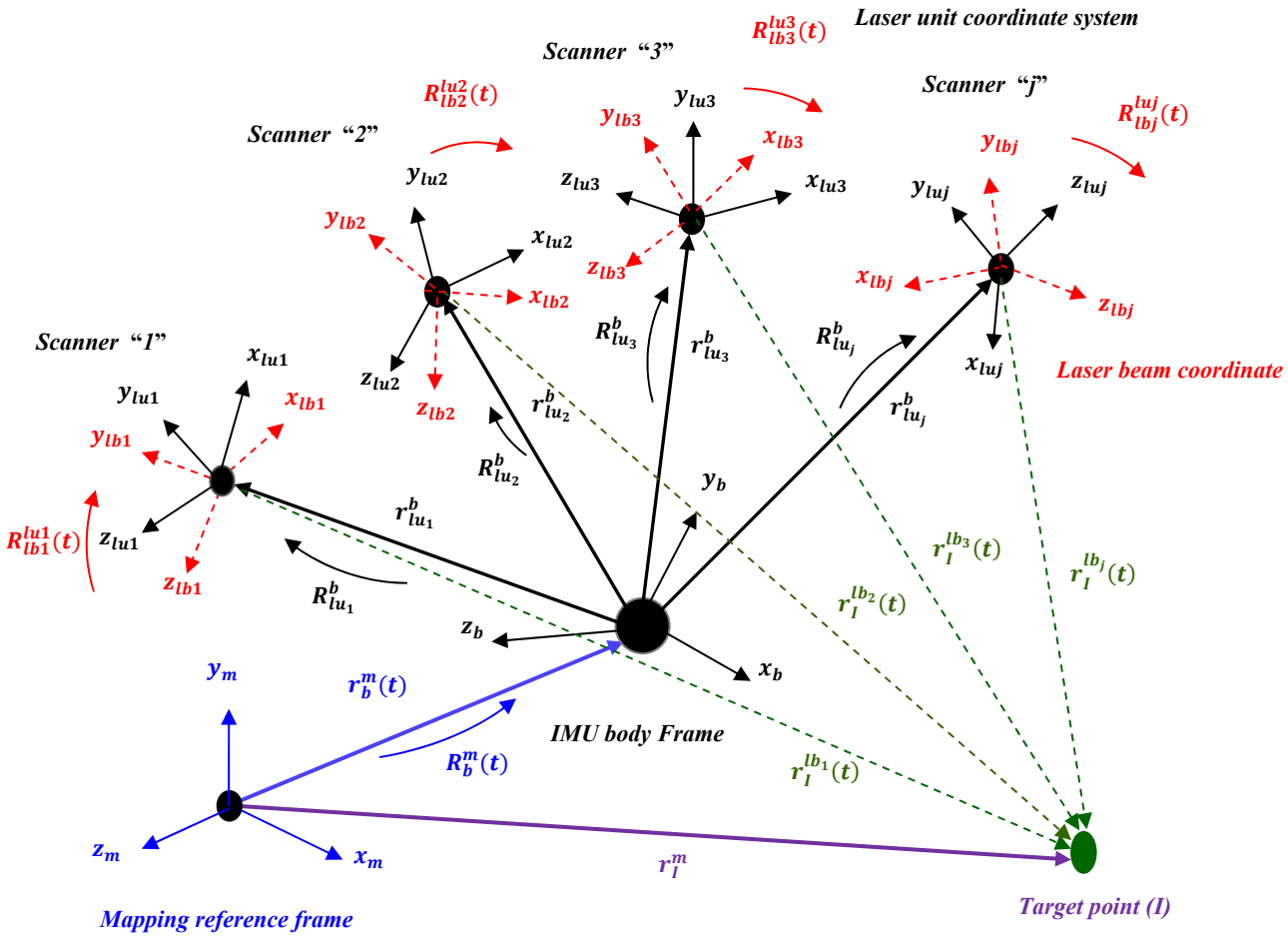

Figure 6.6. Geometric relationship between the coordinate systems of the individual sensors

As shown in Figure 6.6, the position of the laser point r_I^m is derived through the summation of three vectors, $r_b^m(t), r_{lu_j}^b$, and $r_I^{lb_j}(t)$ associated with the j^{th} scanner after applying the appropriate rotation matrices: $R_b^m(t)$, $R_{lu_j}^b$, and $R_{lb_j}^{lu_j}(t)$ associated with the j^{th} scanner. The definition and description of the parameters introduced in the LiDAR point positioning equation are explained in Table 6.11. One can note that these parameters are the input for the simulation process.

Table 6.11. Definition and description of the variables embedded in the LiDAR point positioning equation

Parameters	Definition and description
r_l^m	The position of the laser point
$r_b^m(t)(X_b, Y_b, Z_b)$	The vector from the origin of the mapping (ground) reference frame coordinate system to the origin of the IMU coordinate system
$R_b^m(t)(\omega_b, \varphi_b, \kappa_b)$	The rotation matrix relating the ground and IMU coordinate systems
$r_{lu_j}^b(\Delta X_j, \Delta Y_j, \Delta Z_j)$	Lever arm offset – is the vector from the origin of the IMU coordinate system to the origin of the j^{th} scanner coordinate system
$R_{lu_j}^b(\Delta\omega_j, \Delta\varphi_j, \Delta\kappa_j)$	The rotation matrix relating the IMU and the j^{th} scanner coordinate systems
$R_{lb_j}^{lu_j}(t)$	The rotation matrix relating the laser unit and laser beam coordinate systems associated with the j^{th} scanner, which is defined by the mirror scan angles α and β
$r_l^{lb_j}(t)$	The laser range vector associated with the j^{th} scanner

The proposed simulated LiDAR system consists of GPS/INS (POS LV 420) and two Velodyne laser scanners. POS LV is a compact, fully integrated position and orientation system, utilizing integrated inertial technology to generate stable, reliable and repeatable positioning solutions for land-based vehicle applications. The POS LV Designed to operate under the most difficult GPS conditions found in urban and suburban environments. It also, generates precise, robust positioning and orientation information for mobile data acquisition systems. By utilizing the POS LV system, data capture can be undertaken quickly and efficiently (Source: http://www.applanix.com/products/land/pos-lv.html). The accuracy of the introduced sensors in the simulated LiDAR system is reported in Table 6.12.

Table 6.12. The introduced random errors in the simulation procedure

Error type	Value
Accuracy (Noise level) of range in Velodyne HDL-32E laser scanner	± 0.02 m
Accuracy (Noise level) of mirror scanning angle β in Velodyne HDL-32E laser scanner	± 0.001 deg
Accuracy (Noise level) of GPS/INS (POS LV 420) post-processed position	± 0.05 m
Accuracy (Noise level) of GPS/INS (POS LV 420) post-processed attitude Roll, Pitch Heading	 ± 0.005 deg ± 0.015 deg

6.4.3.3 Target Modeling

In order to perform the simulation procedure, it is necessary to design the target CAD model. There are many existing data models software to represent, record, and visualize terrain and building objects. In this study, the SketchUp software from Trimble is used to design a suitable indoor target and to select an appropriate outdoor target. The obtained targets are stored as a set of polygons to represent the structure of these targets. One can note that the polygon structure is selected because it offers fast and effective performance of the simulation algorithm. Figure 6.7 shows the designed indoor and selected outdoor targets.

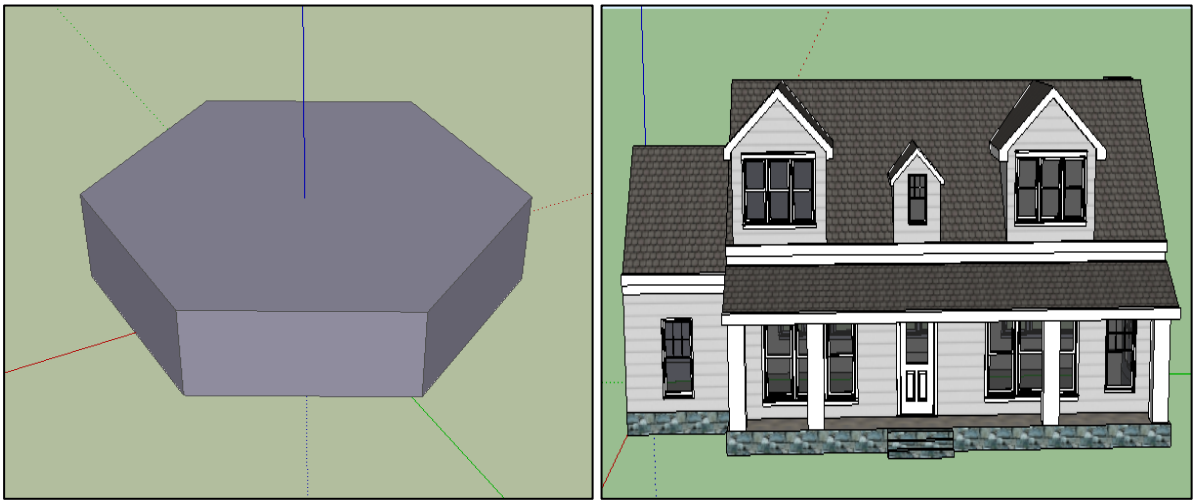

(a) (b)

Figure 6.7. The designed indoor CAD model (a) and selected outdoor CAD model (b)

6.4.3.4 Workflow of the Data Simulation Procedure

The following parameters of a LiDAR system are used as an input to the simulation program:

- The trajectory $r_b^m(t)$ and attitude $R_b^m(t)$ parameters of the platform. These parameters are used to achieve the outdoor calibration procedure, where one can have access to the GPS/IMU information. The proposed simulated platform (outdoor LiDAR system) is moved from known starting position with constant velocity and attitude. Therefore, the trajectory and attitude parameters of the platform are mathematically defined by a time-dependent polynomial.
- The mounting parameters $r_{lu_j}^b$, $R_{lu_j}^b$ relating j^{th} scanner and the IMU body frame,
- Laser emitter parameters $R_{lb_j}^{lu_j}(t)$. These parameters are defined from the specifications of the Velodyne laser scanner as reported in Table 6.10.
- Target models.

With these input data, the computation of each position of the 3D points where laser pulses are emitted can be performed by following procedures:

1. Determine the origin of a transmitted laser pulse, denoted by $L\_unit(x_o, y_o, z_o)$ using the position $r_b^m(t)$ and the attitude $R_b^m(t)$ of the platform at the firing time (t) of the laser pulse and the lever-arm between the IMU body frame and the j^{th} scanner as follows:

$$L\_unit = r_b^m(t) + R_b^m(t) r_{lu_j}^b \tag{6.2}$$

2. At the same firing time (t) of the laser pulse, calculate the direction of the laser pulse using the scanning angles α and β as follows:

$$R_{lb_j}^{lu_j}(t) = R_\beta(t).R_\alpha \tag{6.3}$$

Where $R_\beta(t).R_\alpha$ are the rotation matrices relating the laser unit and laser beam coordinate systems, which is defined by the mirror scanning angles α and β.

3. In this step, the vector-polygon intersection will be discussed. Also, investigating whether the point of intersection is inside or outside the polygon and the visibility analysis for selecting the closest polygon are presented.

A. Vector-polygon intersection

I. Assume arbitrary range to define the range $r_I^{lb_j}(t)$ (arbitrary vector) and then from steps 1 and 2, one can note that all parameters in Equation 1 are known except that the position of the laser point r_I^m is the only unknown.

II. Then, apply Equation 6.1 to calculate the 3D position of the point r_I^m, denoted by $P_V(x_v, y_v, z_v)$. Thus, arbitrary vector, denoted by R_V, that the laser pulse travels along can be represented by two points $L\_unit(x_o, y_o, z_o)$ and $P_V(x_v, y_v, z_v)$.

III. For each polygon in the object calculate the point of intersection, denoted by $P_i(x_i, y_i, z_i)$, between the vector R_V and the given polygon. Then check whether $P_i(x_i, y_i, z_i)$ lies inside or outside this polygon.

B. Analysis of the intersection point and closest polygon

I. The simple way of finding whether the point of intersection $P_i(x_i, y_i, z_i)$ is inside or outside a polygon is to count the number of times a vector, going in any fixed direction, crosses the polygon boundary edges. The point is outside when this "crossing number" is even; otherwise, when it is odd, the point is inside (as shown in Figure 6.8). This algorithm is sometimes known as the crossing number algorithm or the even-odd rule algorithm (Haines, Eric.1994).

II. If $P_i(x_i, y_i, z_i)$ is inside the polygon, calculate the distance, denoted by *D*, between this point and the origin of the laser unit $L\_unit(x_o, y_o, z_o)$ as follows:

$$D = \sqrt{(x_i - x_o)^2 + (y_i - y_o)^2 + (z_i - z_o)^2} \tag{6.4}$$

III. Search for the closest object polygon (i.e., search for the minimum *D*). If the minimum *D* is determined, the 3D coordinates of the true intersection point, denoted by $P_T(x_T, y_T, z_T)$, at which the ray R_V intersects with the candidate polygon (i.e., closest polygon) is defined.

4. Compute the true value of the range, denoted by R_T, (distance from the origin of the laser unit $L\_unit(x_o, y_o, z_o)$ to the true intersection point $P_T(x_T, y_T, z_T)$ on the surface of the candidate polygon, as shown in Figure 6.9) as follows:

$$R_T = \sqrt{(x_T - x_o)^2 + (y_T - y_o)^2 + (z_T - z_o)^2} \tag{6.5}$$

5. Use the introduced random errors in the LiDAR system to compute the 3D position of the erroneous intersection point.

The proposed simulation method has been tested by using the models that have been introduced in Table 6.7. Figure 6.10 shows the indoor and outdoor simulated targets.

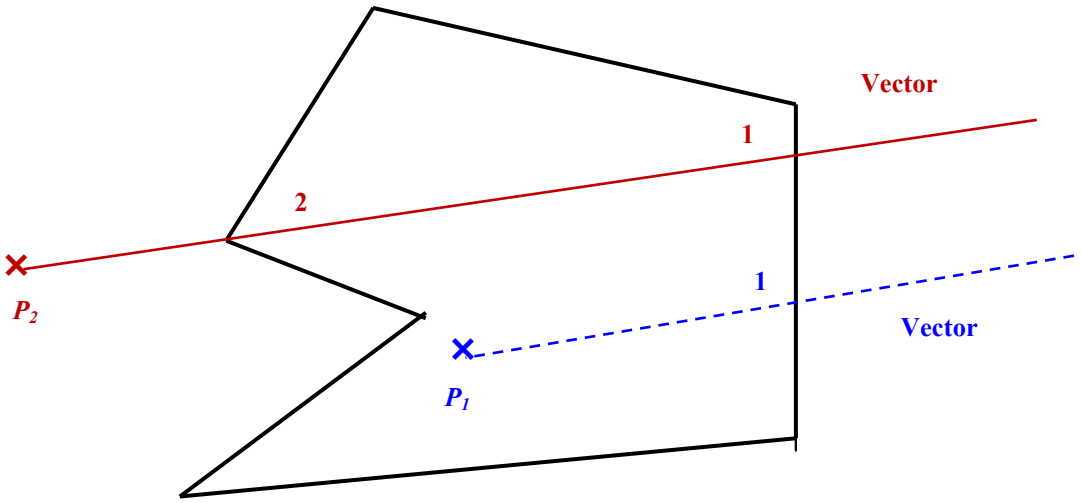

Figure 6.8. The number of intersections for a vector to polygon boundary edges; if odd, it shows that the point lies inside the polygon (as Point P1). If it is even, the point lies outside the polygon (as Point P2)

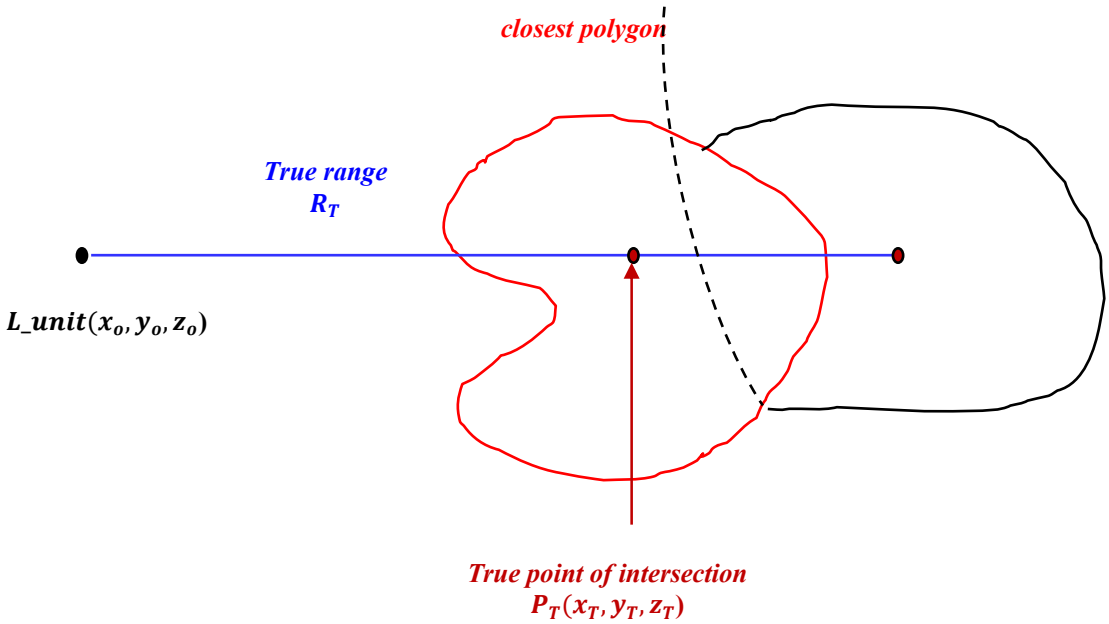

Figure 6.9. The Visibility analysis of laser beam intersects with a closest polygon surface

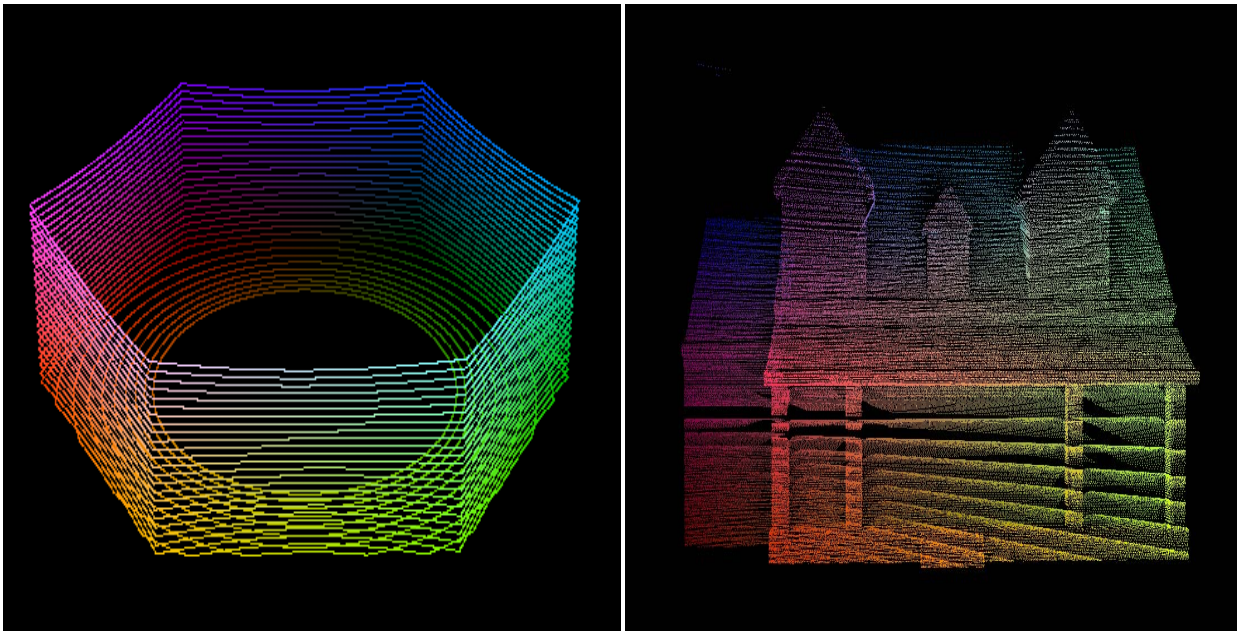

(a) (b)

Figure 6.10. The simulated indoor CAD model (a) and outdoor CAD model (b)

6.5 The Experimental Results of the Two-Step and One-Step Calibration Procedures of Terrestrial Mobile Multi-Laser Scanning System

In the following sub-sections, the description of the simulated indoor dataset is demonstrated. Then, the experimental results using the simulated indoor dataset for investigating the indoor LiDAR system calibration algorithm are presented. As well, the description of the simulated outdoor dataset is introduced. Finally, the experimental results using the simulated outdoor dataset for investigating the two-step and one-step calibration processes are presented.

6.5.1 Description of the Simulated Indoor Dataset

The general geometric modeling of the LiDAR system consists of three main subsystems (sensors) such as GPS, IMU, and any number of laser scanners. For simplification to achieve the indoor and outdoor LiDAR system calibration, the proposed simulated LiDAR system consists of GPS, IMU and two Velodyne laser scanners as shown in Figure 6.11.

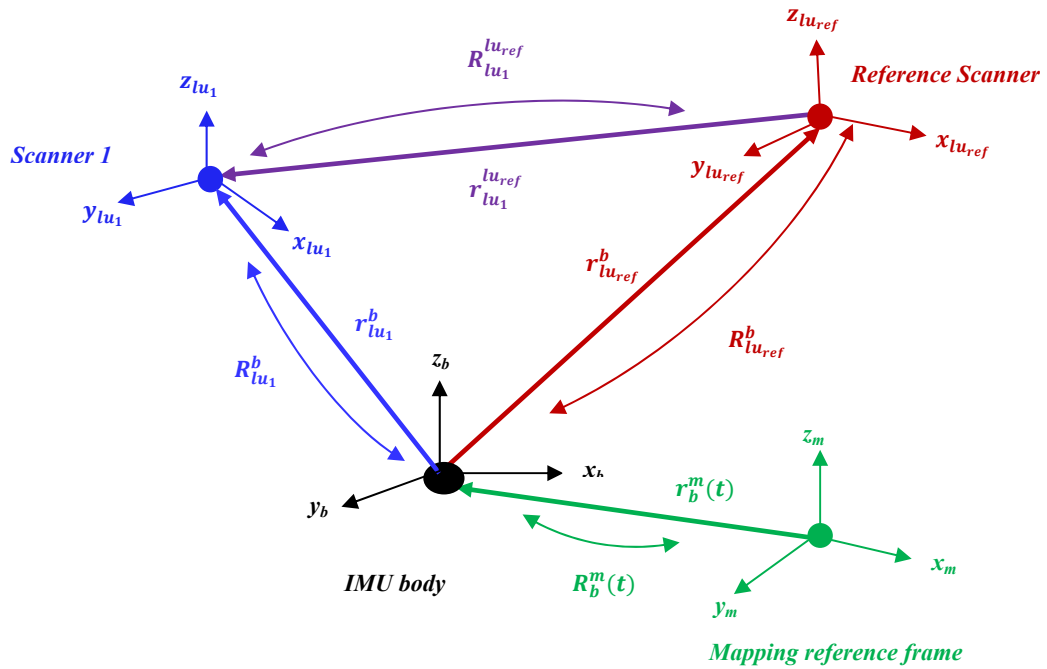

Figure 6.11. The components of the proposed simulated LiDAR System

From Figure 6.11, the parameters that are used in the general modeling of the simulated LiDAR system as follows:

1. Mounting parameters relating IMU body frame to the ground (mapping) reference frame
   - $r_b^m(t)$ (*X_b2m, Y_b2m, Z_b2m*) – is the vector from the origin of the mapping reference frame coordinate system, denoted by (*m*), to the origin of the IMU coordinate system, denoted by (*b*) , and
   - $R_b^m(t)$ $(\omega\_b2m,\ \varphi\_b2m,\ \kappa\_b2m)$ – is the rotation matrix relating the ground and IMU coordinate systems.
2. Mounting parameters relating scanner 1 to the IMU unit
   - $r_{lu_1}^b$ (*ΔX_*lu_1*2b, ΔY_*lu_1*2b, ΔZ_*lu_1*2b*) – lever arm offset – is the vector from the origin of the IMU coordinate system to the origin of scanner 1 coordinate system, denoted by (*lu1*), and
   - $R_{lu_1}^b$ $(\Delta\omega\_lu_12b,\ \Delta\varphi\_lu_12b,\ \Delta\kappa\_lu_12b)$ is the rotation matrix relating scanner 1 and the IMU coordinate systems.
3. Mounting parameters relating the reference scanner to the IMU unit
   - $r_{lu_{ref}}^b$ (*ΔX_ref2b, ΔY_ref2b, ΔZ_ref2b*) – lever arm offset – is the vector from the origin of the IMU coordinate system to the origin of the reference scanner coordinate system, denoted by (*ref*), and
   - $R_{lu_{ref}}^b$ $(\Delta\omega\_ref2b,\ \Delta\varphi\_ref2b,\ \Delta\kappa\_ref2b)$ is the rotation matrix relating the reference scanner and the IMU unit coordinate systems.

4. Mounting parameters relating scanner 1 to the reference scanner

   – $r_{lu_1}^{lu_{ref}}$ ($\Delta X\_lu_1 2ref$, $\Delta Y\_lu_1 2ref$, $\Delta Z\_lu_1 2ref$) – lever arm offset – is the vector from the origin of the reference scanner coordinate system to the origin of scanner 1 coordinate system, and

   – $R_{lu_1}^{lu_{ref}}$ $(\Delta\omega\_lu_1 2ref,\ \Delta\varphi\_lu_1 2ref,\ \Delta\kappa\_lu_1 2ref)$ is the rotation matrix relating scanner 1 and the reference scanner coordinate systems.

As already mentioned, in the indoor calibration stage one can have access to neither the GPS nor IMU information. As a result, one introduces a virtual reference frame for the IMU unit at the reference scanner. In this case: $r_{lu_{ref}}^{b} = 0$, $R_{lu_{ref}}^{b} = I_3$. Thus, the geometric modeling of the simulated indoor LiDAR system will consist of two Velodyne laser scanners as shown in Figure 6.12. The layout of the indoor LiDAR system is shown in Figure 6.13.

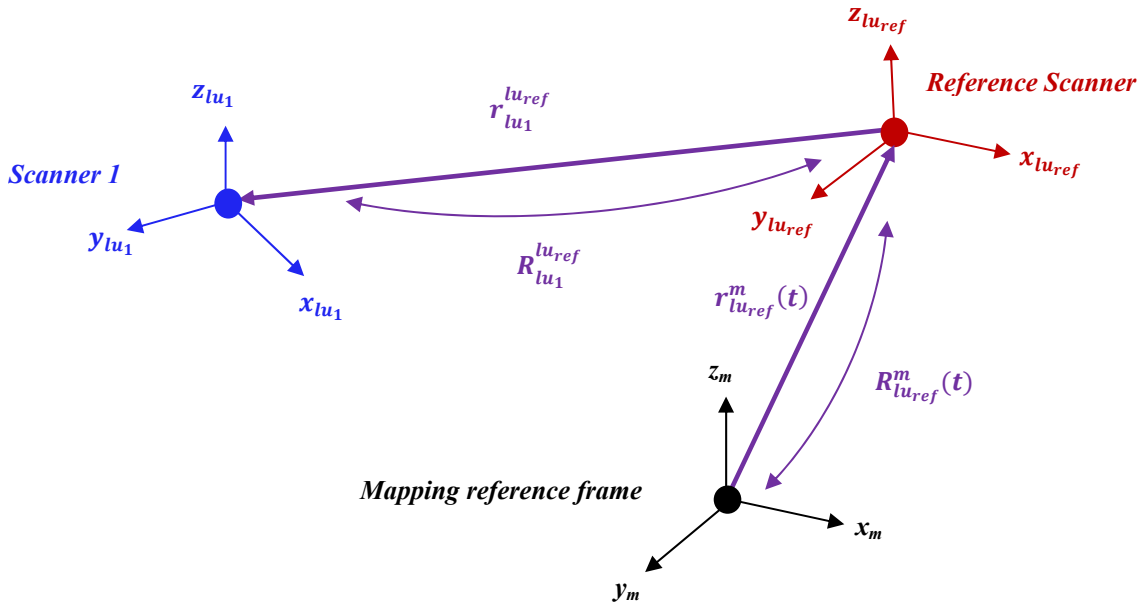

Figure 6.12. The components of the simulated indoor LiDAR System

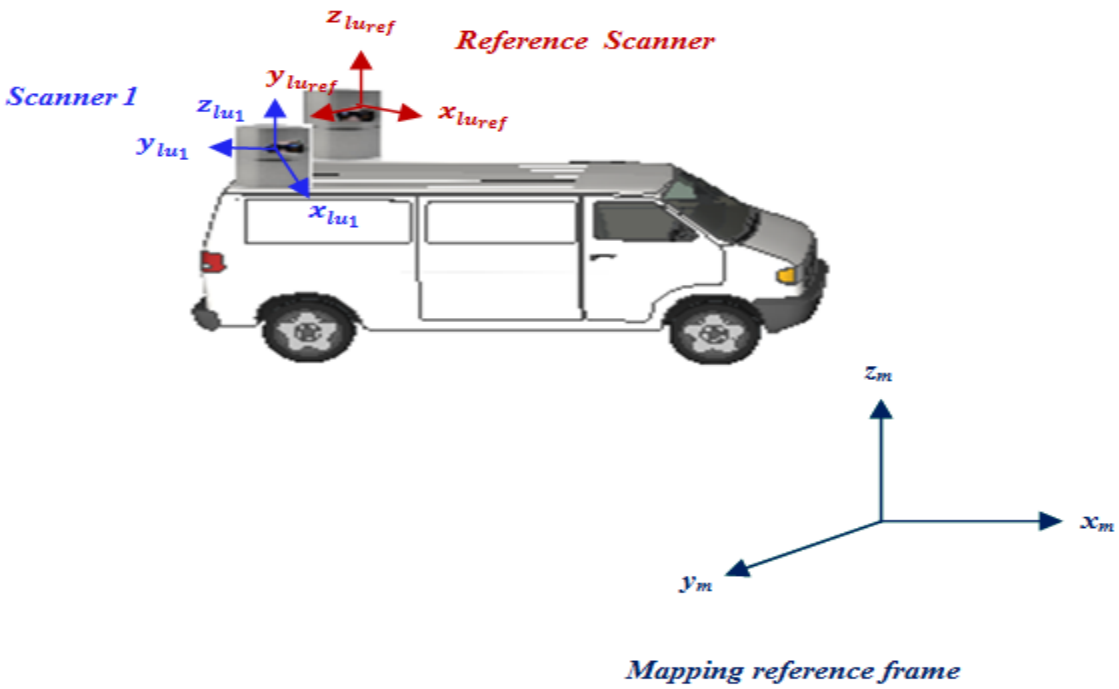

Figure 6.13 The layout of the indoor LiDAR system

From Figure 6.13, the parameters that are used in the modeling of the simulated indoor LiDAR system as follows:

- Mounting parameters relating the reference scanner to the mapping reference frame
  - $r^m_{lu_{ref}}(t)$ (ΔX_ref2m, ΔY_ref2m, ΔZ_ref2m) is the vector from the origin of the mapping reference frame coordinate system to the origin of the reference scanner coordinate system, and
  - $R^m_{lu_{ref}}(t)$ ($\Delta\omega\_ref2m$, $\Delta\varphi\_ref2m$, $\Delta\kappa\_ref2m$) is the rotation matrix relating the mapping and reference scanner coordinate systems.

- Mounting parameters relating scanner 1 to the reference scanner
  - $r_{lu_1}^{lu_{ref}}$ ($\Delta X\_lu_1 2ref$, $\Delta Y\_lu_1 2ref$, $\Delta Z\_lu_1 2ref$) is the vector from the origin of the reference scanner coordinate system to the origin of scanner 1 coordinate system, and
  - $R_{lu_1}^{lu_{ref}}$ ($\Delta\omega\_lu_1 2ref$, $\Delta\varphi\_lu_1 2ref$, $\Delta\kappa\_lu_1 2ref$) is the rotation matrix relating scanner 1 and the reference scanner coordinate systems.

One can note that there are no random errors caused by the GPS and IMU in the simulated indoor dataset because the system is stationary. The random error caused by the range (± 0.02 m) and the mirror scanning angle β (± 0.0001 deg) are considered in the simulated indoor dataset. The simulated true values for the indoor system parameters introduced in the LiDAR point positioning equation are listed in Table 6.13.

Table 6.13. The simulated true values for the indoor system parameters

$r_{lu_1}^{lu_{ref}}$ ($\Delta X\_lu_1 2ref$, $\Delta Y\_lu_1 2ref$, $\Delta Z\_lu_1 2ref$)	-1.0 m, 1.0 m, and 0.0 m
$R_{lu_1}^{lu_{ref}}$ ($\Delta\omega\_lu_1 2ref$, $\Delta\varphi\_lu_1 2ref$, $\Delta\kappa\_lu_1 2ref$)	-5.0 deg, 5.0 deg, and -5.0 deg
$\Delta\rho\_lu_{ref}$, $S_\alpha\_lu_{ref}$, and $S_\beta\_lu_{ref}$	0.0 m, 1.0, and 1.0
$\Delta\rho\_lu_1$, $S_\alpha\_lu_1$, and $S_\beta\_lu_1$	0.0 m, 1.0, and 1.0

The initial approximations for the unknown parameters (deviated values from the true values for the unknown parameters) are listed in Table 6.14. The objective of using the initial values is to test the ability of the proposed algorithm to estimate the indoor calibration parameters.

Table 6.14. The initial values for the indoor system parameters

$r_{lu_1}^{lu_{ref}}$ ($\Delta X\_lu_1 2ref$, $\Delta Y\_lu_1 2ref$, $\Delta Z\_lu_1 2ref$)	-1.1 m, 1.1 m, and -0.1 m
$R_{lu_1}^{lu_{ref}}$ $(\Delta\omega\_lu_1 2ref, \Delta\varphi\_lu_1 2ref, \Delta\kappa\_lu_1 2ref)$	-5.1 deg, 4.9 deg, and -4.9 deg
$\Delta\rho\_lu_{ref}$, and $S_\beta\_lu_{ref}$	0.02 m, and 1.0001
$\Delta\rho\_lu_1$, and $S_\beta\_lu_1$	-0.02 m, and 0.9999

The simulated true and initial values for the position and orientation relating the reference scanner to the mapping reference frame at 2 different data collection epochs (t_1 and t_2) are listed in Tables 6.15 and 6.16, respectively.

Table 6.15. The simulated true values of the simulated position and orientation relating the reference scanner to the mapping reference frame at 2 different data collection epochs

Epoch number	$r_{lu_{ref}}^{m}(t_k)$ $(\Delta X\_ref2m, \Delta Y\_ref2m, \Delta Z\_ref2m)$	$R_{lu_{ref}}^{m}(t_k)$ $(\Delta\omega\_ref2m, \Delta\varphi\_ref2m, \Delta\kappa\_ref2m)$
t_1	0.0 m, 0.0 m, and 3.0 m	0.0 deg, 0.0 deg, and 0.0 deg
t_2	-2.0 m, -2.0 m, and 3.0 m	0.0 deg, 0.0 deg, and 0.0 deg

Table 6.16. The initial values for the position and orientation relating the reference scanner to the mapping reference frame at 2 different data collection epochs

Epoch number	$r_{lu_{ref}}^{m}(t_k)$ $(\Delta X\_ref2m, \Delta Y\_ref2m, \Delta Z\_ref2m)$	$R_{lu_{ref}}^{m}(t_k)$ $(\Delta\omega\_ref2m, \Delta\varphi\_ref2m, \Delta\kappa\_ref2m)$
t_1	0.1 m, -0.1 m, and 3.1 m	0.1 deg, -0.1 deg, and 0.1 deg
t_2	-2.1 m, -1.9 m, and 3.1 m	0.1 deg, -0.1 deg, and 0.1 deg

6.5.2 Experimental Results of the Indoor LiDAR System Calibration

As mentioned earlier, the objective of the indoor calibration process (i.e., first step) is to estimate the following parameters:

- The relative mounting parameters relating any number of scanners and the reference scanner and,
- The intrinsic parameters of the involved scanners in the LiDAR system.

The experiments presented in this section using a simulated indoor dataset have the following objectives:

- Investigate the feasibility of the proposed indoor LiDAR system calibration procedure in a controlled environment,
- Verify the optimum configuration for the indoor LiDAR system calibration procedure,
- Check the need for ground control points for the estimation of the system parameters,
- Test the effectiveness of the proposed indoor LiDAR system calibration procedure and control configuration by analyzing the closeness of the estimated system parameters to the true simulated ones, and
- Evaluate the improvement in the relative accuracy of the LiDAR point cloud after the indoor calibration process qualitatively and quantitatively.

The indoor calibration procedure has been performed using overlapping strips only and using overlapping strips along with control points. Table 6.17 summarizes the investigated experiments. The results of the estimated system parameters for the different experiments are reported in Tables 6.18-6.21. These tables present the following:

- The true values of the unknown parameters,
- The initial values for the unknown parameters used as an input to the proposed indoor calibration algorithm,
- The initial standard deviation of the initial values for the unknown parameters. One should note that when using the value $1e^{-9}$ as the initial standard deviation of the unknown parameter, it means that this parameter will not be determined during the calibration process (i.e., fixed parameter). As well, when using the value $1e^{9}$ as the initial standard deviation of the unknown parameter, it implies that this parameter will be estimated during the calibration process (i.e., completely unknown parameter).
- The estimated parameters from the proposed method,
- The estimated standard deviation of the estimated parameters, and
- The absolute value of the difference between the true and estimated values, denoted by Abs (diff).

Table 6.17. The performed experiments

Experiments	**Characteristics**
I	One overlapping strip pair (overlap among one strip from the reference scanner and the second strip from scanner 1) at epoch 1 is used.
II	I + 30 control points
III	Two overlapping strip pairs (one overlapping strip pair at epoch 1 and the second overlapping strip pair at epoch 2) are used.
IV	III + 30 control points

One should note that in experiment I and III the relative mounting parameters relating scanner 1 and the reference scanner as well as the intrinsic parameters of each scanner are estimated while the position and orientation parameters relating the reference scanner and the mapping reference frame are fixed. These parameters cannot be estimated because there is no information available for defining the datum. Therefore, ground control points or GPS/INS information should be available in order to define the datum. One should note that the selected ground control points are simulated using the true values of the unknown system parameters after adding some noise. The accuracy of the utilized control points is (±0.05 m). Figure 6.14 shows the distribution of the control points. One can note that experiment II and IV are performed to estimate the relative mounting parameters relating scanner 1 and the reference scanner, the intrinsic parameters of each scanner as well as the position and orientation parameters relating the reference scanner and the mapping reference frame.

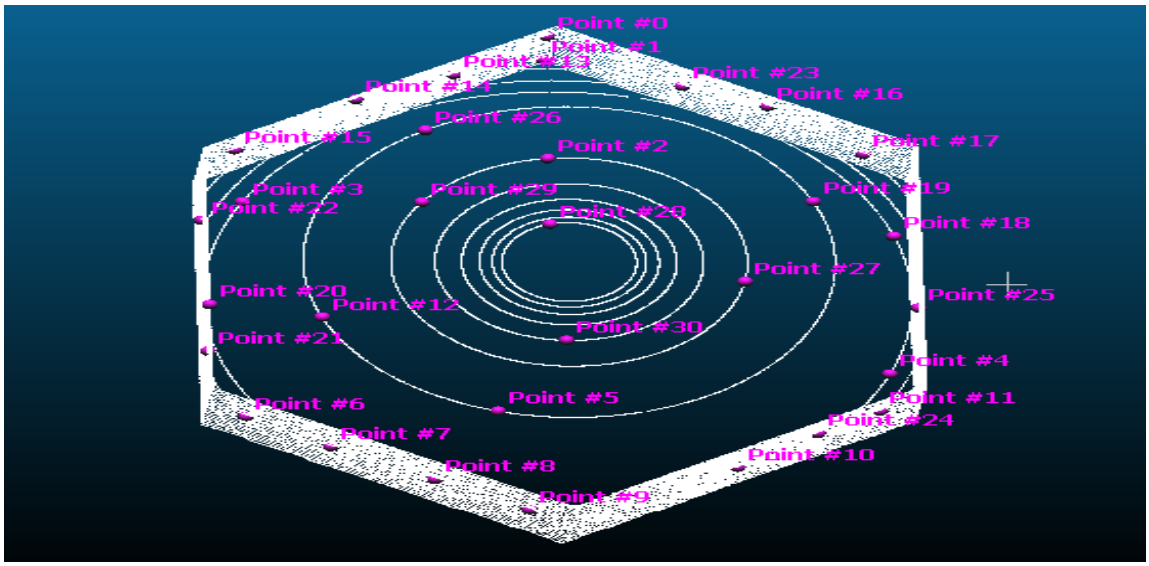

Figure 6.14. The distribution of the utilized ground control points (30 GCP) on the indoor calibration site

Table 6.18. The results of estimated system parameters using the indoor calibration procedure for experiment I

Parameters	True value	Initial value	Initial standard deviation	Estimated value	Estimated standard deviation	Abs (diff)
The mounting parameters relating the reference scanner and the mapping reference frame at epoch 1						
ΔX_ref2m [m]	0.0	0.0	1.0e-9	Fixed parameters		
ΔY_ref2m [m]	0.0	0.0	1.0e-9			
ΔZ_ref2m [m]	3.0	3.0	1.0e-9			
$\Delta\omega\_ref2m$ *[deg]*	0.0	0.0	1.0e-9			
$\Delta\varphi\_ref2m$ *[deg]*	0.0	0.0	1.0e-9			
$\Delta\kappa\_ref2m$ *[deg]*	0.0	0.0	1.0e-9			
The mounting parameters relating scanner 1 and the reference scanner						
$\Delta X\_lu_1 2ref$ *[m]*	-1.0	-1.1	1.0e9	-1.0007	0.00001	0.0007
$\Delta Y\_lu_1 2ref$ *[m]*	1.0	1.1	1.0e9	0.9993	0.00001	0.0007
$\Delta Z\_lu_1 2ref$ *[m]*	0.0	-0.1	1.0e9	-0.0099	0.0001	0.0099
$\Delta\omega\_lu_1 2ref$ *[deg]*	-5.0	-5.1	1.0e9	-4.9937	0.0008	0.0063
$\Delta\varphi\_lu_1 2ref$ *[deg]*	5.0	4.9	1.0e9	4.9867	0.0013	0.0133
$\Delta\kappa\_lu_1 2ref$ *[deg]*	-5.0	-4.9	1.0e9	-5.0049	0.0004	0.0049
Intrinsic parameters of the reference scanner						
$\Delta\rho\_ref$ *[m]*	0.0	0.02	1.0e9	0.0202	0.0003	0.0202
S_β_ref	1.0	1.0001	1.0e9	1.0000	0.00001	0.0
Intrinsic parameters of scanner 1						
$\Delta\rho\_lu_1$ *[m]*	0.0	-0.02	1.0e9	0.0204	0.0003	0.0204
$S_\beta\_lu_1$	1.0	0.9999	1.0e9	1.0000	0.00001	0.0

Table 6.19. The results of estimated system parameters using the indoor calibration procedure for experiment II

Parameters	True value	Initial value	Initial standard deviation	Estimated value	Estimated standard deviation	Abs (diff)
The mounting parameters relating the reference scanner and the mapping reference frame at epoch 1						
ΔX_ref2m [m]	0.0	0.1	1.0e9	0.0508	0.0003	0.0508
ΔY_ref2m [m]	0.0	-0.1	1.0e9	0.0503	0.0003	0.0503
ΔZ_ref2m [m]	3.0	3.1	1.0e9	2.9296	0.0052	0.0704
$\Delta\omega\_ref2m$ *[deg]*	0.0	0.1	1.0e9	-0.0411	0.0103	0.0411
$\Delta\varphi\_ref2m$ *[deg]*	0.0	-0.1	1.0e9	0.0550	0.0102	0.0550
$\Delta\kappa\_ref2m$ *[deg]*	0.0	0.1	1.0e9	-0.0172	0.0055	0.0172
The mounting parameters relating scanner 1 and the reference scanner						
*ΔX_*$lu_1 2ref$ *[m]*	-1.0	-1.1	1.0e9	-1.0006	0.00001	0.0006
*ΔY_*$lu_1 2ref$ *[m]*	1.0	1.1	1.0e9	0.9995	0.00001	0.0005
*ΔZ_*$lu_1 2ref$ *[m]*	0.0	-0.1	1.0e9	-0.0092	0.0001	0.0092
$\Delta\omega\_lu_1 2ref$ *[deg]*	-5.0	-5.1	1.0e9	-4.9939	0.0007	0.0061
$\Delta\varphi\_lu_1 2ref$ *[deg]*	5.0	4.9	1.0e9	4.9869	0.0012	0.0131
$\Delta\kappa\_lu_1 2ref$ *[deg]*	-5.0	-4.9	1.0e9	-5.0048	0.0004	0.0048
Intrinsic parameters of the reference scanner						
$\Delta\rho\_ref$ *[m]*	0.0	0.02	1.0e9	0.0201	0.0002	0.0201
S_β_ref	1.0	1.0001	1.0e9	1.0000	0.00001	0.0
Intrinsic parameters of scanner 1						
$\Delta\rho\_lu_1$ *[m]*	0.0	-0.02	1.0e9	0.0199	0.0002	0.0199
$S_\beta\_lu_1$	1.0	0.9999	1.0e9	1.0000	0.00001	0.0

Table 6.20. The results of estimated system parameters using the indoor calibration procedure for experiment III

Parameters	True value	Initial value	Initial standard deviation	Estimated value	Estimated standard deviation	Abs (diff)
The mounting parameters relating the reference scanner and the mapping reference frame at epoch 1						
$\Delta X\_ref2m\ [m]$	0.0	0.0	1.0e-9	Fixed parameters		
$\Delta Y\_ref2m\ [m]$	0.0	0.0	1.0e-9			
$\Delta Z\_ref2m\ [m]$	3.0	3.0	1.0e-9			
$\Delta\omega\_ref2m\ [deg]$	0.0	0.0	1.0e-9			
$\Delta\varphi\_ref2m\ [deg]$	0.0	0.0	1.0e-9			
$\Delta\kappa\_ref2m\ [deg]$	0.0	0.0	1.0e-9			
The mounting parameters relating the reference scanner and the mapping reference frame at epoch 2						
$\Delta X\_ref2m\ [m]$	-2.0	-2.0	1.0e-9	Fixed parameters		
$\Delta Y\_ref2m\ [m]$	-2.0	-2.0	1.0e-9			
$\Delta Z\_ref2m\ [m]$	3.0	3.0	1.0e-9			
$\Delta\omega\_ref2m\ [deg]$	0.0	0.0	1.0e-9			
$\Delta\varphi\_ref2m\ [deg]$	0.0	0.0	1.0e-9			
$\Delta\kappa\_ref2m\ [deg]$	0.0	0.0	1.0e-9			
The mounting parameters relating scanner 1 and the reference scanner						
$\Delta X\_lu_1 2ref\ [m]$	-1.0	-1.1	1.0e9	-1.0005	0.00001	0.0005
$\Delta Y\_lu_1 2ref\ [m]$	1.0	1.1	1.0e9	0.9996	0.00001	0.0004
$\Delta Z\_lu_1 2ref\ [m]$	0.0	-0.1	1.0e9	-0.0090	0.0001	0.0090
$\Delta\omega\_lu_1 2ref\ [deg]$	-5.0	-5.1	1.0e9	-4.9942	0.0007	0.0058
$\Delta\varphi\_lu_1 2ref\ [deg]$	5.0	4.9	1.0e9	4.9935	0.0008	0.0065
$\Delta\kappa\_lu_1 2ref\ [deg]$	-5.0	-4.9	1.0e9	-5.0047	0.0003	0.0047
Intrinsic parameters of the reference scanner						
$\Delta\rho\_ref\ [m]$	0.0	0.02	1.0e9	0.0195	0.0001	0.0195
S_β_ref	1.0	1.0001	1.0e9	1.0000	0.00001	0.0
Intrinsic parameters of scanner 1						
$\Delta\rho\_lu_1\ [m]$	0.0	-0.02	1.0e9	0.0197	0.0001	0.0197
$S_\beta\_lu_1$	1.0	0.9999	1.0e9	1.0000	0.00001	0.0

Table 6.21. The results of estimated system parameters using the indoor calibration procedure for experiment IV

Parameters	True value	Initial value	Initial standard deviation	Estimated value	Estimated standard deviation	Abs (diff)
The mounting parameters relating the reference scanner and the mapping reference frame at epoch 1						
ΔX_ref2m [m]	0.0	0.1	1.0e9	0.0495	0.0003	0.0495
ΔY_ref2m [m]	0.0	-0.1	1.0e9	0.0485	0.0003	0.0485
ΔZ_ref2m [m]	3.0	3.1	1.0e9	2.9737	0.0049	0.0263
$\Delta\omega\_ref2m$ *[deg]*	0.0	0.1	1.0e9	0.0150	0.0089	0.0150
$\Delta\varphi\_ref2m$ *[deg]*	0.0	-0.1	1.0e9	-0.0159	0.0093	0.0159
$\Delta\kappa\_ref2m$ *[deg]*	0.0	0.1	1.0e9	-0.0138	0.0054	0.0138
The mounting parameters relating the reference scanner and the mapping reference frame at epoch 2						
ΔX_ref2m [m]	-2.0	-2.1	1.0e9	-1.9500	0.0003	0.0500
ΔY_ref2m [m]	-2.0	-1.9	1.0e9	-1.9499	0.0003	0.0501
ΔZ_ref2m [m]	3.0	3.1	1.0e9	3.0499	0.0003	0.0499
$\Delta\omega\_ref2m$ *[deg]*	0.0	0.1	1.0e9	0.0009	0.0046	0.0009
$\Delta\varphi\_ref2m$ *[deg]*	0.0	-0.1	1.0e9	-0.0009	0.0049	0.0009
$\Delta\kappa\_ref2m$ *[deg]*	0.0	0.1	1.0e9	-0.0154	0.0064	0.0154
The mounting parameters relating scanner 1 and the reference scanner						
$\Delta X\_lu_1 2ref$ *[m]*	-1.0	-1.1	1.0e9	-1.0005	0.00001	0.0005
$\Delta Y\_lu_1 2ref$ *[m]*	1.0	1.1	1.0e9	0.9996	0.00001	0.0004
$\Delta Z\_lu_1 2ref$ *[m]*	0.0	-0.1	1.0e9	-0.0090	0.0001	0.0090
$\Delta\omega\_lu_1 2ref$ *[deg]*	-5.0	-5.1	1.0e9	-4.9943	0.0007	0.0057
$\Delta\varphi\_lu_1 2ref$ *[deg]*	5.0	4.9	1.0e9	4.9934	0.0008	0.0066
$\Delta\kappa\_lu_1 2ref$ *[deg]*	-5.0	-4.9	1.0e9	-5.0047	0.0003	0.0047
Intrinsic parameters of the reference scanner						
$\Delta\rho\_ref$ *[m]*	0.0	0.02	1.0e9	0.0195	0.0001	0.0195
S_β_ref	1.0	1.0001	1.0e9	1.0000	0.00001	0.0
Intrinsic parameters of scanner 1						
$\Delta\rho\_lu_1$ *[m]*	0.0	-0.02	1.0e9	0.0197	0.0001	0.0197
$S_\beta\_lu_1$	1.0	0.9999	1.0e9	0.9998	0.00001	0.0002

The findings from the performed experiments can be summarized as follows:

- In experiments I, II, III, and IV one can observe that the estimated values of the mounting parameters relating scanner 1 and the reference scanner when using overlapping strips only captured at specific data collection epoch, and when using overlapping strips along with control points, are quite close.
- The estimated values of the position and orientation parameters relating the reference scanner and the mapping reference frame cannot be estimated when using overlapping strips only because there is no information available in order to define the datum. Therefore, control points should be used to estimate these parameters (as shown in experiments III, IV).
- The estimated values of the mounting parameters relating scanner 1 and the reference scanner are improved when using two overlapping strip pairs captured from two different data collection epochs. This can be noticed in the results of experiments III in comparison with the results in the experiments I.
- Also, the estimated values of the position and orientation parameters relating the reference scanner and the mapping reference frame were improved when using two overlapping strip pairs captured from two different data collection epochs along with control points. This can be noticed in the results of experiments IV in comparison with the results in experiments II.

The qualitative analysis of the indoor calibration results are performed by visual inspection of profiles generated before the indoor calibration procedure using the initial values for the

unknown system parameters and after the indoor calibration procedure using the estimated values from experiments III and IV. The objective of the visual inspection is to check any improvements in the quality of fit between overlapping strips (an illustration of one profile is shown in Figure 6.15. Through visual inspection of the profiles in Figure 6.15, significant improvement in the compatibility of the reconstructed point cloud using the estimated system parameters from experiments III and IV can be noticed.

To quantitatively evaluate the performance of the proposed indoor calibration procedure, the discrepancies (i.e., three shifts (X_T, Y_T, Z_T) and three rotations (ω, φ, κ)) between conjugate surface elements in overlapping strips are computed before the indoor calibration process using the initial values for the unknown system parameters and after reconstructing the LiDAR point cloud using the estimated system parameters from experiments III and IV. For example, Table 6.22 reports the estimated discrepancies before and after applying the indoor calibration procedure. From Table 6.22, one can observe large discrepancies among the overlapping strip pairs before the indoor calibration procedure (large shifts in the X-axis, Y-axis and Z-axis). A significant improvement after the indoor calibration procedure is noticeable. One can also note that there is almost no improvement in the compatibility of the overlapping strip pairs when adding the control information (i.e., the results from experiments III and IV are quite comparable).

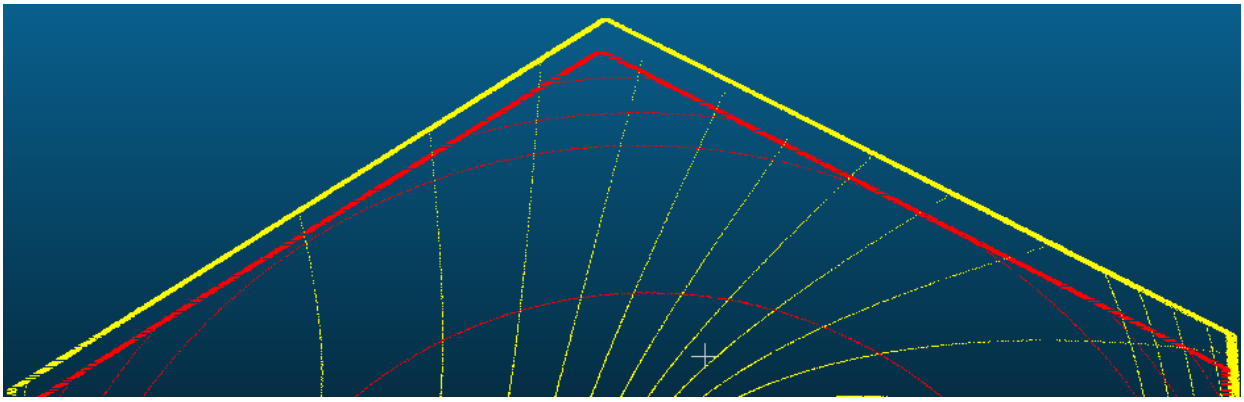

(a)

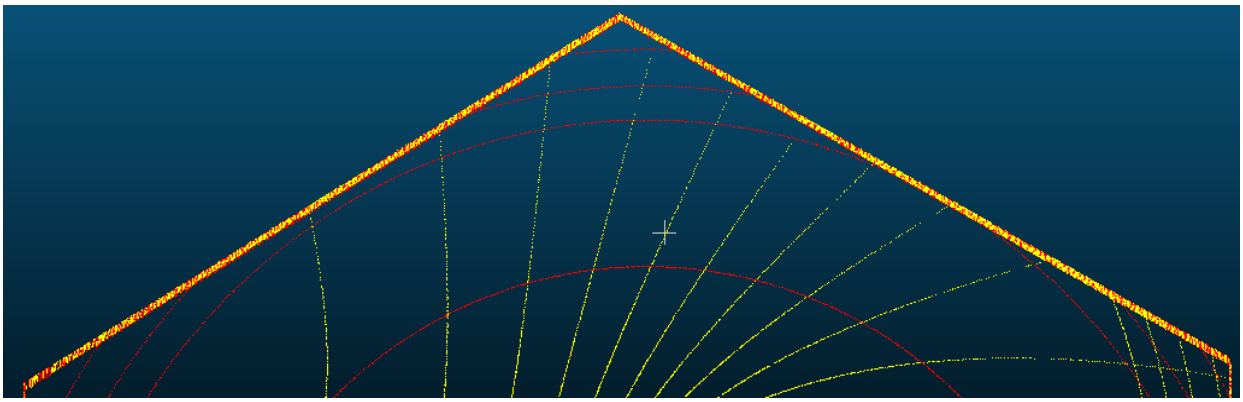

(b)

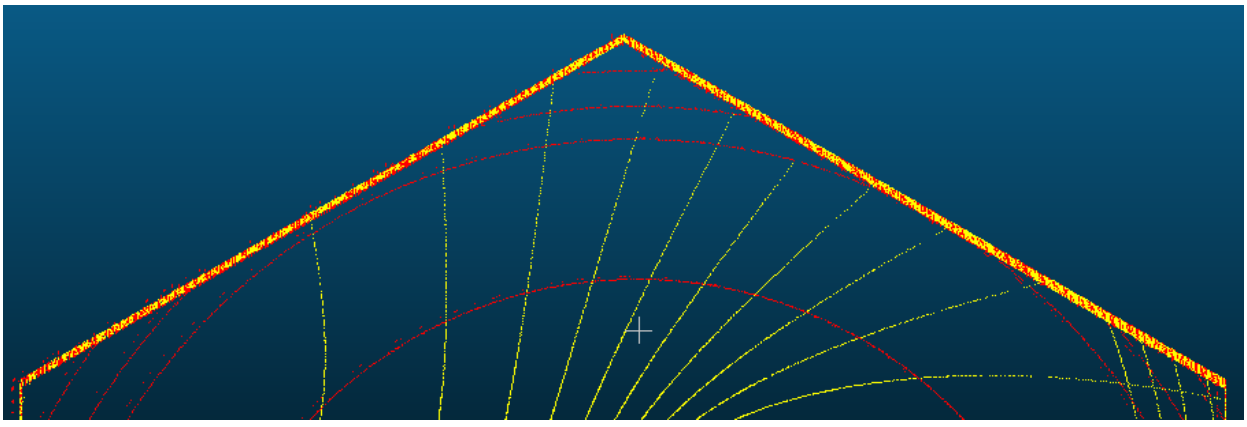

(c)

Figure 6.15. Profiles of the simulated surface before the indoor calibration (a), after the indoor calibration of experiment III (b), and after the indoor calibration of experiment IV (c)

Table 6.22. Discrepancies (i.e., three shifts and three rotations) between overlapping strips before and after the indoor calibration process

Before Calibration			**Proposed Calibration Overlapping Strips Only (Experiment III)**			**Proposed Calibration Overlapping Strips + Control points (Experiment IV)**		
X_T(m)	**Y_T(m)**	**Z_T(m)**	**X_T(m)**	**Y_T(m)**	**Z_T(m)**	**X_T(m)**	**Y_T(m)**	**Z_T(m)**
0.2039	-0.1965	0.2001	0.0001	-0.0001	0.0176	-0.0004	-0.0003	0.0202
$\omega(^o)$	**$\varphi(^o)$**	**$\kappa(^o)$**	**$\omega(^o)$**	**$\varphi(^o)$**	**$\kappa(^o)$**	**$\omega(^o)$**	**$\varphi(^o)$**	**$\kappa(^o)$**
0.1944	-0.2367	-0.1874	-0.0093	-0.0257	0.0029	-0.0103	-0.0296	0.0015

The conclusions from the performed experiments in this section can be summarized as follows:

- The proposed recommended configuration for the indoor calibration step consists of two overlapping strip pairs captured from two different data collection epochs while the calibration site should have good topography with varying slope and aspect values.
- For reliable estimation of the mounting parameters relating scanner 1 and the reference scanner, overlapping strips only are used while there is no need of using control points.

6.5.3 Description of the Simulated Outdoor Dataset

As early mentioned, in the outdoor calibration stage one can have access to the GPS and the IMU information. As a result, the geometric modeling of the simulated outdoor LiDAR system consists of three main sensors such as GPS, IMU, and two Velodyne laser scanners (as shown in Figure 6.11). The layout of the outdoor LiDAR system is shown in Figure 6.16.

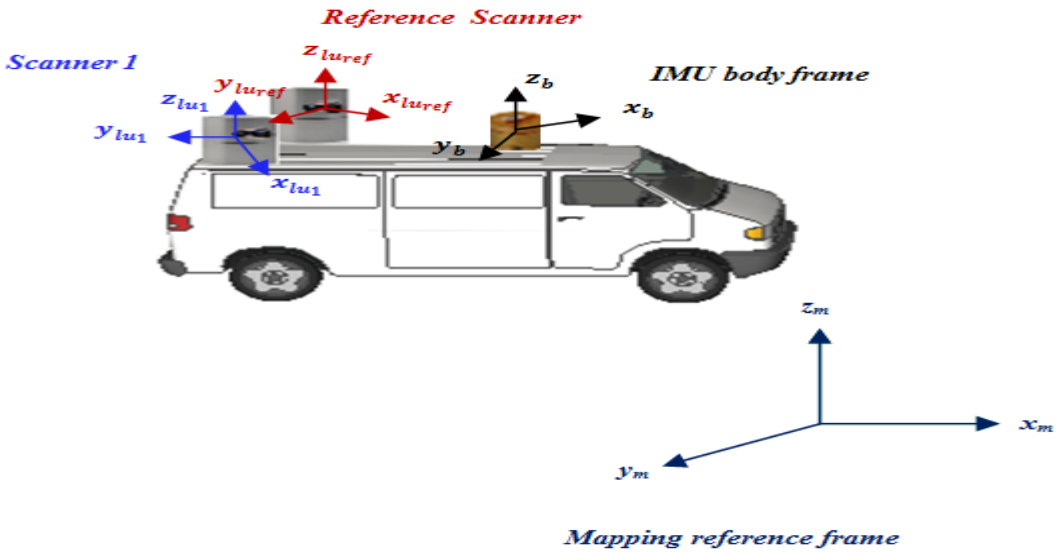

Figure 6.16. The layout of the outdoor LiDAR system

The simulated true values of the mounting parameters ($r_{lu_1}^{lu_{ref}}$ and $R_{lu_1}^{lu_{ref}}$) relating the reference scanner and scanner 1 as well as the simulated true values of the mounting parameters ($r_{lu_{ref}}^{b}$ and $R_{lu_{ref}}^{b}$) relating the IMU body frame and the reference scanner are used to calculate the simulated true values of the mounting parameters ($r_{lu_1}^{b}$ and $R_{lu_1}^{b}$) relating the IMU body frame and scanner 1 as follows:

$$r_{lu_1}^{b} = r_{lu_{ref}}^{b} + R_{lu_{ref}}^{b} \cdot r_{lu_1}^{lu_{ref}} \tag{6.6}$$

$$R_{lu_1}^{b} = R_{lu_{ref}}^{b} . R_{lu_1}^{lu_{ref}} \quad (6.7)$$

The simulated true and initial values for the outdoor system parameters introduced in the LiDAR point positioning equation are listed in Tables 6.23 and 6.24, respectively.

Table 6.23. The simulated true values for the outdoor system parameters

$r_{lu_{ref}}^{b}$ *(ΔX_ref2b, ΔY_ref2b, ΔZ_ref2b)*	1.0 m, 1.0 m, and 0.0 m
$R_{lu_{ref}}^{b}$ $(\Delta\omega\_ref2b, \Delta\varphi\_ref2b, \Delta\kappa\_ref2b)$	5.0 deg, -5.0 deg, and 5.0 deg
$r_{lu_1}^{b}$ *(ΔX_*lu_1*2b, ΔY_*lu_1*2b, ΔZ_*lu_1*2b)*	-0.0792 m, 1.9138 m, and -0.0148 m
$R_{lu_1}^{b}$ $(\Delta\omega\_lu_1 2b, \Delta\varphi\_lu_1 2b, \Delta\kappa\_lu_1 2b)$	-0.3991 deg, -0.4319 deg, and -0.4747 deg
$r_{lu_1}^{lu_{ref}}$ *(ΔX_*lu_1*2ref, ΔY_*lu_1*2ref, ΔZ_*lu_1*2ref)*	-1.0 m, 1.0 m, and 0.0 m
$R_{lu_1}^{lu_{ref}}$ $(\Delta\omega\_lu_1 2ref, \Delta\varphi\_lu_1 2ref, \Delta\kappa\_lu_1 2ref)$	-5.0 deg, 5.0 deg, and -5.0 deg
$\Delta\rho\_ref,\ and\ S_\beta\_ref$	0.0 m, and 1.0
$\Delta\rho_{lu_1},\ and\ S_\beta\_lu_1$	0.0 m, and 1.0

Table 6.24. The initial values for the outdoor system parameters

$r_{lu_{ref}}^{b}$ *(ΔX_ref2b, ΔY_ref2b, ΔZ_ref2b)*	1.1 m, 0.9 m, and 0.1 m
$R_{lu_{ref}}^{b}$ $(\Delta\omega\_ref2b, \Delta\varphi\_ref2b, \Delta\kappa\_ref2b)$	5.1 deg, -5.1 deg, and 4.9 deg
$r_{lu_1}^{b}$ *(ΔX_*lu_1*2b, ΔY_*lu_1*2b, ΔZ_*lu_1*2b)*	-0.1792 m, 2.0138 m, and -0.1148 m
$R_{lu_1}^{b}$ $(\Delta\omega\_lu_1 2b, \Delta\varphi\_lu_1 2b, \Delta\kappa\_lu_1 2b)$	-0.4991 deg, -0.3319 deg, and -0.3747 deg
$r_{lu_1}^{lu_{ref}}$ *(ΔX_*lu_1*2ref, ΔY_*lu_1*2ref, ΔZ_*lu_1*2ref)*	-1.1 m, 1.1 m, and -0.1 m
$R_{lu_1}^{lu_{ref}}$ $(\Delta\omega\_lu_1 2ref, \Delta\varphi\_lu_1 2ref, \Delta\kappa\_lu_1 2ref)$	-5.1 deg, 4.9 deg, and -4.9 deg
$\Delta\rho\_ref,\ and\ S_\beta\_ref$	0.02 m, and 1.0001
$\Delta\rho_{lu_1},\ and\ S_\beta\_lu_1$	-0.20 m, and 0.9999

6.5.4 Two-Step and One-Step LiDAR System Calibration Experimental Results

The experiments presented in this section using a simulated outdoor dataset have the following objectives:

- Test the ability of the proposed one-step LiDAR system calibration process for the estimation of the mounting parameters relating the reference scanner and scanner 1 and the intrinsic parameters of each scanner as well as the mounting parameters relating the reference scanner to the IMU body frame.

- Test the feasibility of the proposed two-step (indoor followed by outdoor) LiDAR system calibration procedures for the estimation of the mounting parameters relating the reference scanner to the IMU body frame. One can note that the estimated values in the indoor calibration step (the mounting parameters relating the reference scanner and scanner 1 and the intrinsic parameters of each scanner) are used as a priori information in proposed outdoor LiDAR system calibration process.

- Demonstrate the comparative performance of the two-step and one-step calibration procedures by using different proposed configurations for the estimation of the system parameters.

- Verify the hypothesis that the quality of the utilized GPS/IMU would affect the estimation of the system parameters from the one-step and two-step calibration procedures while the impact on the one-step approach is more significant.

- Check the need for ground control points for the estimation of the system parameters.

- Test the effectiveness of the proposed two-step and one-step calibration procedures and control configuration by analyzing the closeness of the estimated system parameters to the true simulated ones.

- Evaluate the improvement in the relative accuracy of the LiDAR point cloud after the two-step and one-step calibration procedures qualitatively and quantitatively.

The one-step and two-step calibration procedures have been performed using overlapping strips only and using overlapping strips along with control points. The mobile scanning of the calibration site (house) from 3 different driving directions (D_1, D_2, and D_3) is shown in Figure 6.17. From this figure one can note that in each deriving direction, forward (denoted by F) and backward (denoted by B) directions are performed. As well, for each forward and backward direction, 2 strips are generated as follows:

- One strip is captured by the reference scanner, denoted by S_{ref}, and
- The second strip is captured by scanner 1, denoted by S_1.

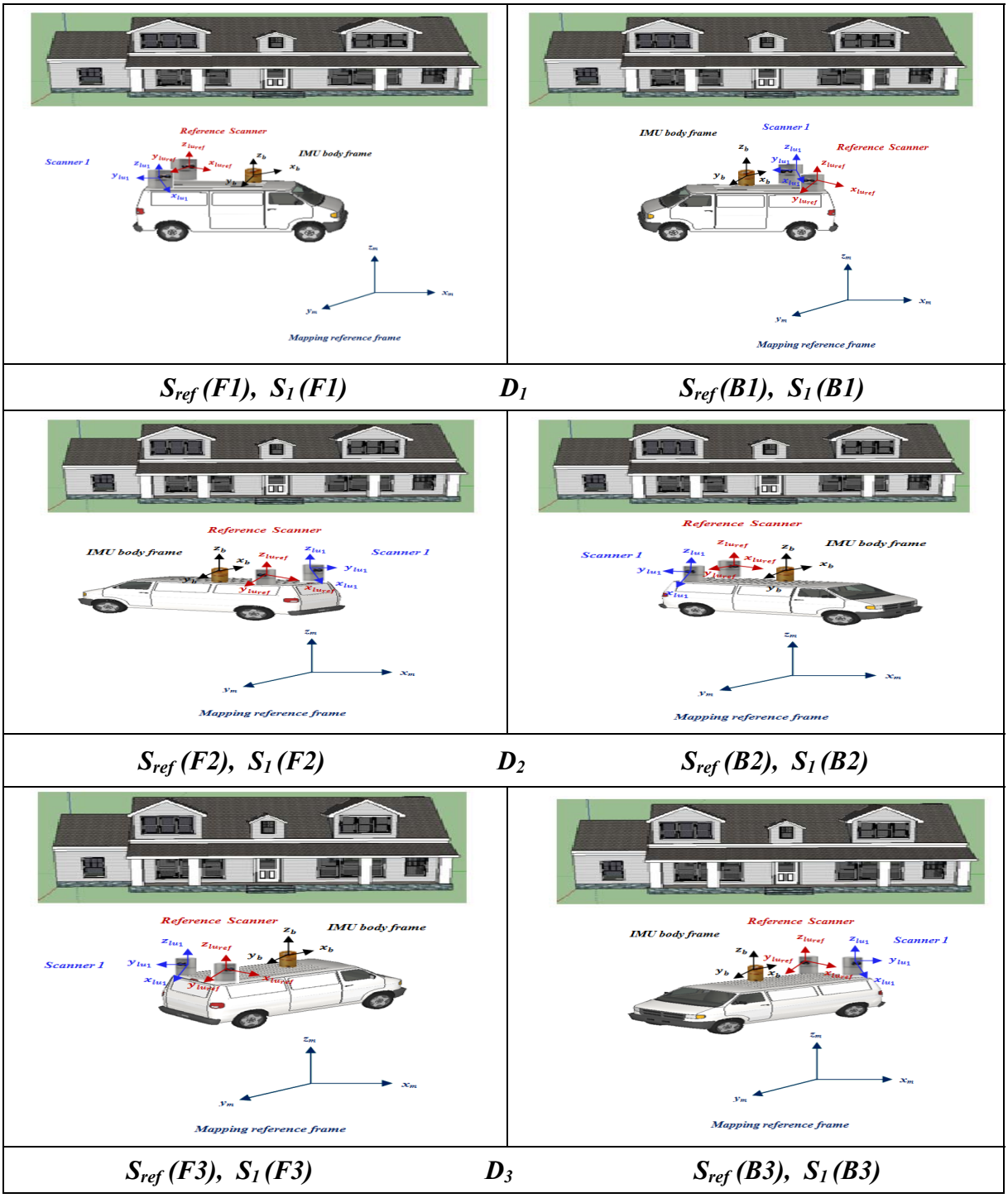

Figure 6.17. The mobile scanning of the house from 3 different driving directions for simulated 12 strips

The simulated true values for the position, velocity and orientation of the IMU body frame from 3 different driving directions are listed in Table 6.25. These values are used to simulate 12 strips. The experiments setup and performed experiments are presented in the following sub-sections.

Table 6.25. The simulated true values for the position, velocity and orientation of the IMU body frame from 3 different driving directions

Simulated Strips	Driving Directions	Starting Position			Velocity of the vehicle (Km/hr)	Constant Attitude		
		ΔX_b2m (m)	ΔY_b2m (m)	ΔZ_bm (m)		$\Delta\omega\_b2m$ (deg)	$\Delta\varphi\_b2m$ (deg)	$\Delta\kappa\_b2m$ (deg)
S_{ref} (F1), S_1 (F1)	D1	20.0	-5.0	2.0	15	0.0	0.0	0.0
S_{ref} (B1), S_1 (B1)	D1	20.0	15.0	2.0	15	0.0	0.0	180.0
S_{ref} (F2), S_1 (F2)	D2	30.0	15.0	2.0	15	0.0	0.0	135.0
S_{ref} (B2), S_1 (B2)	D2	15.0	0.0	2.0	15	0.0	0.0	315.0
S_{ref} (F3), S_1 (F3)	D3	30.0	0.0	2.0	15	0.0	0.0	45
S_{ref} (B3), S_1 (B3)	D3	15.0	15.0	2.0	15	0.0	0.0	225

6.5.4.1 Experiment setup

In this section, 3 different configurations used for different experiments will be explained as follows:

A. Weak configuration

Figure 6.18 shows the structure of the weak configuration. This configuration consists of 3 overlapping strip pairs as follows:

- ***1st overlap*** among S_{ref} ***(F1)*** and S_{ref} ***(B1)***,
- ***2nd overlap*** among S_1 ***(F1)*** and S_1 ***(B1)***, and
- ***3rd overlap*** among S_{ref} ***(F1)*** and S_1 ***(B1)***.

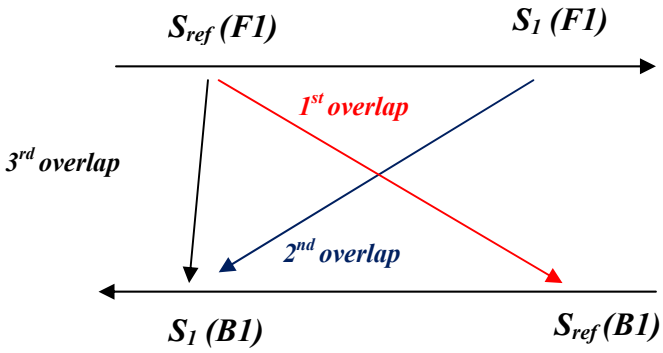

Figure 6.18. Structure of the weak configuration

B. Moderate configuration

Figure 6.19 shows the structure of the moderate configuration. This configuration consists of the weak configuration while adding 4 overlapping strip pairs as follows:

- ***4th overlap*** among S_{ref} ***(F2)*** and S_{ref} ***(B2)***,
- ***5th overlap*** among S_1 ***(F2)*** and S_1 ***(B2)***,
- ***6th overlap*** among S_1 ***(F2)*** and S_{ref} ***(B2)***, and
- ***7th overlap*** among S_{ref} ***(B1)*** and S_1 ***(F2)***.

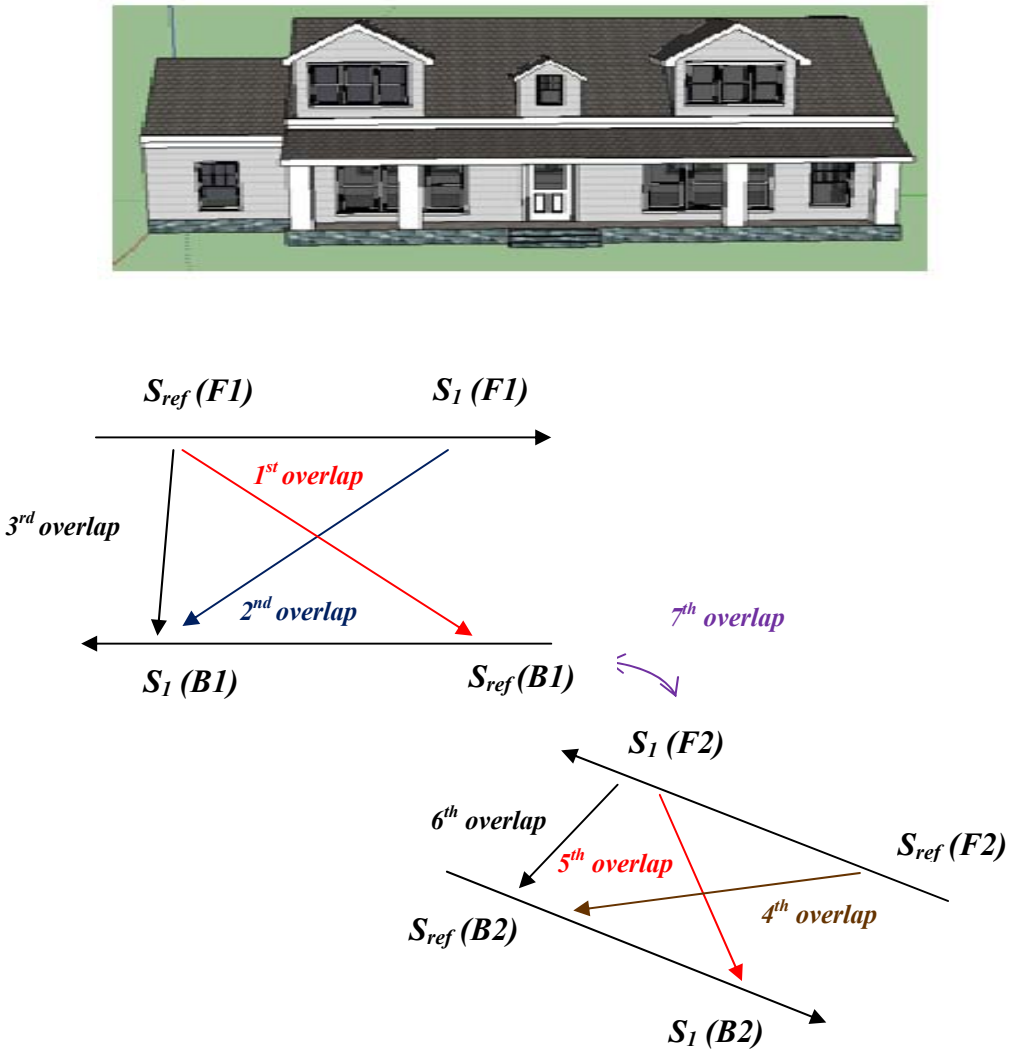

Figure 6.19. Structure of the moderate configuration

C. Strong configuration

Figure 6.20 shows the structure of the strong configuration. This configuration consists of the moderate configuration with 4 overlapping strip pairs added as follows:

- ***8th overlap*** among ***S_{ref} (F3)*** and ***S_{ref} (B3)***,
- ***9th overlap*** among ***S_1 (F3)*** and ***S_1 (B3)***,

- ***10th overlap*** among ***Sref (F3)*** and ***S1 (B3)***, and
- ***11th overlap*** among ***S1 (B1)*** and ***Sref (F3)***.

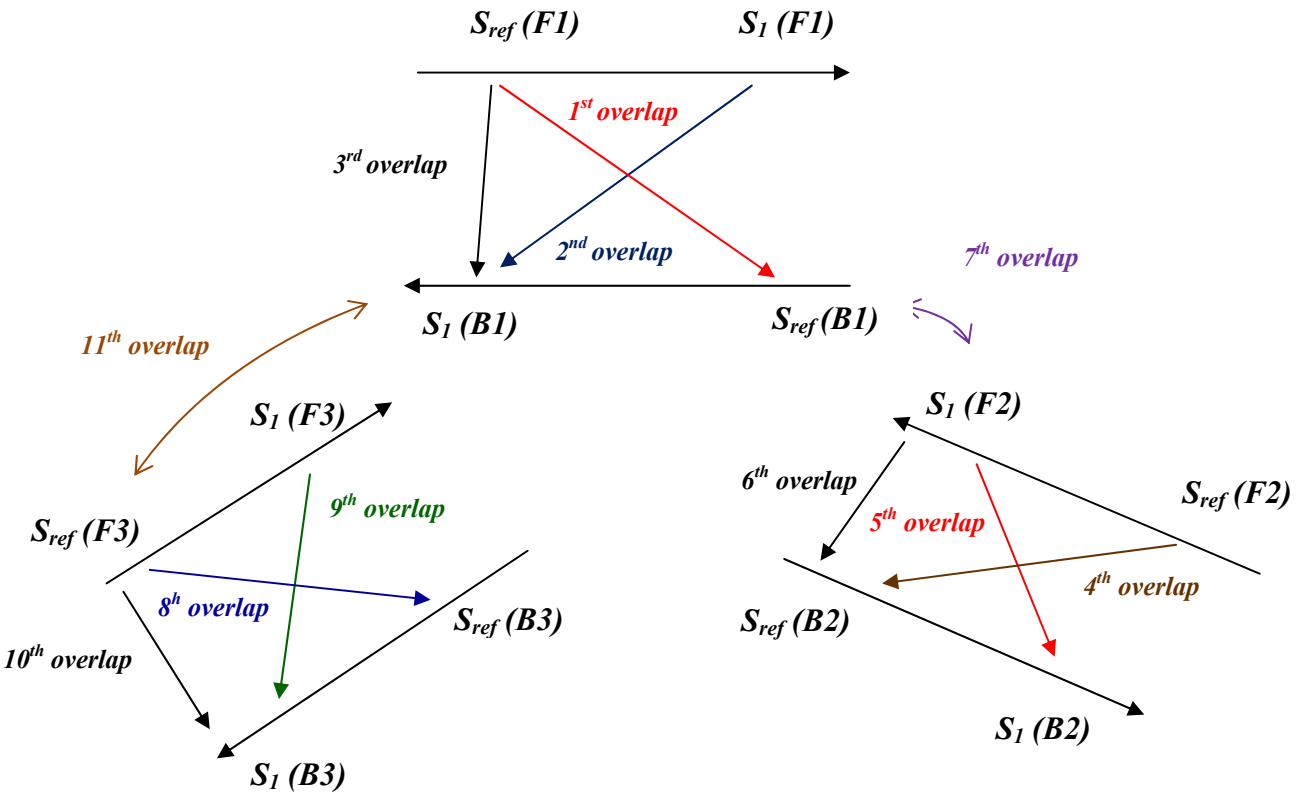

Figure 6.20. Structure of the strong configuration

The proposed scenarios by using different configurations to achieve the one-step and two-step calibration techniques for the different performed experiments are summarized in Table 6.26.

Table 6.26. The performed scenarios used in different experiments to achieve the one-step and two-step calibration techniques

Scenarios	Configuration
I	Weak configuration is used to estimate the unknown system parameters while applying the one-step calibration process.
II	Weak configuration is used to estimate the system unknown parameters while using the outcome from the indoor calibration (two-step procedure).
III	I + 30 control points.
IV	II+ 30 control points
V	Moderate configuration is used to estimate the unknown system parameters while applying the one-step calibration process.
VI	Moderate configuration is used to estimate the unknown system parameters while using the outcome from the indoor calibration (two-step procedure).
VII	V+ 30 control points
VIII	VI + 30 control points
IX	Strong configuration is used to estimate the unknown system parameters while applying the one-step calibration process.
X	Strong configuration is used to estimate the unknown system parameters while using the outcome from the indoor calibration (two-step procedure).
XI	IX+ 30 control points
XII	X+ 30 control points

6.5.4.2 Experiment "1"

In this experiment, the expected accuracy of the integrated GPS/INS position and orientation information (as per the system's specification) is used to derive the system parameters while applying the proposed one-step and two-step calibration procedures. The accuracy of the utilized GPS/INS and the introduced random errors used for this experiment are reported in Table 6.12. The results of the estimated system parameters from different scenarios using the one-step and two-step calibration procedures are reported in Tables 1.A-12.A (refer to Appendix A).

The absolute values of the differences between the estimated and true values of the unknown system parameters using the weak configuration (as reported in Tables 1.A- 4.A) are illustrated in figures 6.21-6.26.

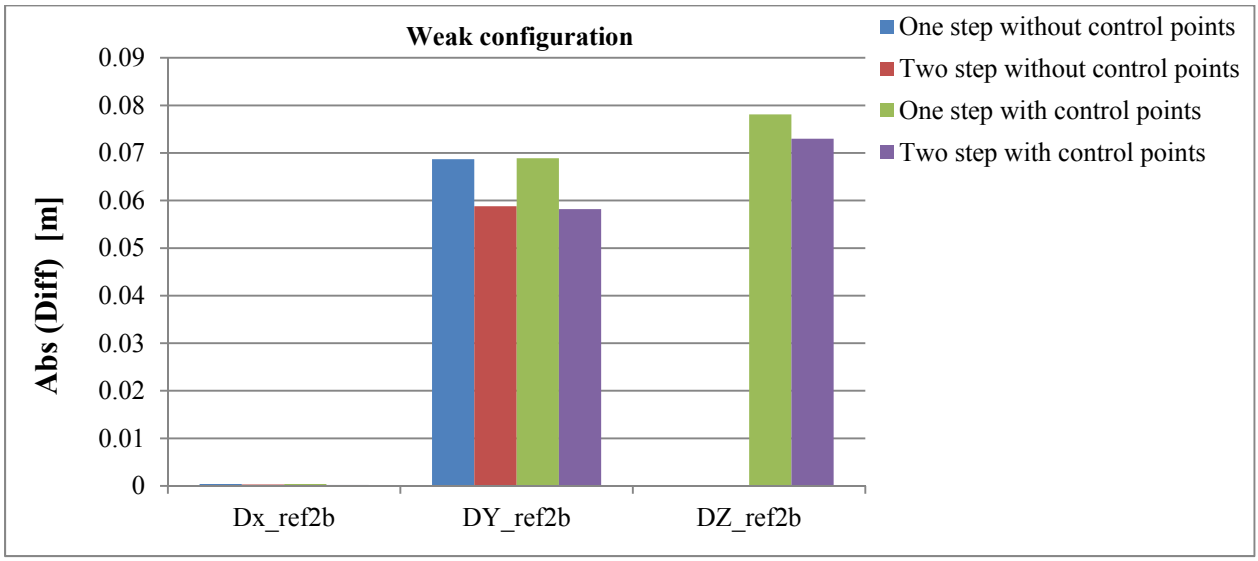

Figure 6.21. The difference between the estimated and true values of the lever arm offset relating the reference scanner and the IMU body frame in experiment 1

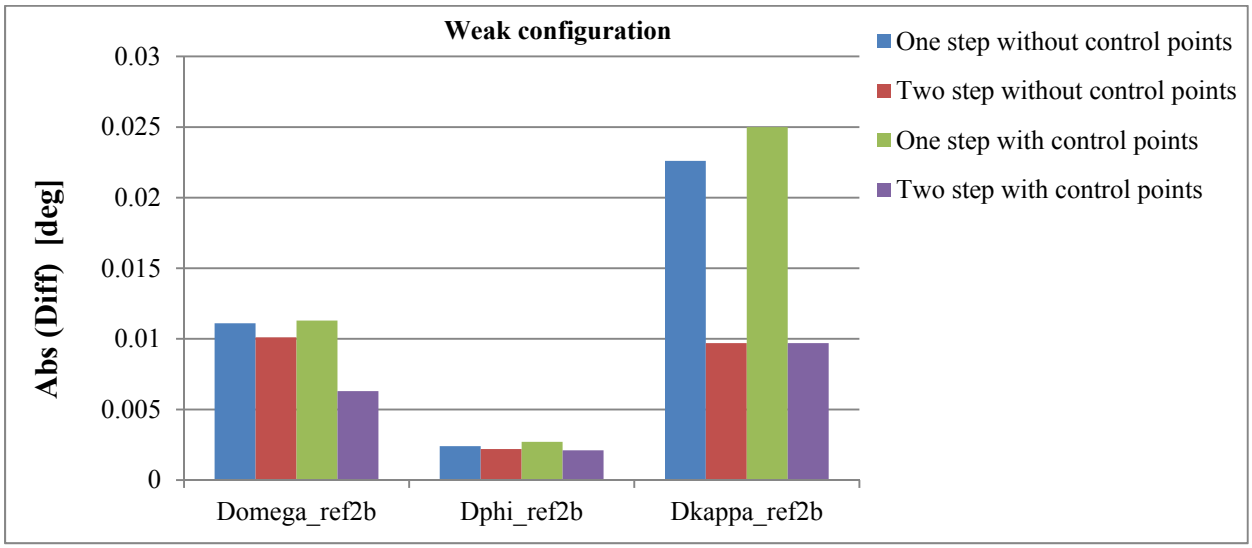

Figure 6.22. The difference between the estimated and true values of the rotation angles relating the reference scanner and the IMU body frame coordinate systems in experiment 1

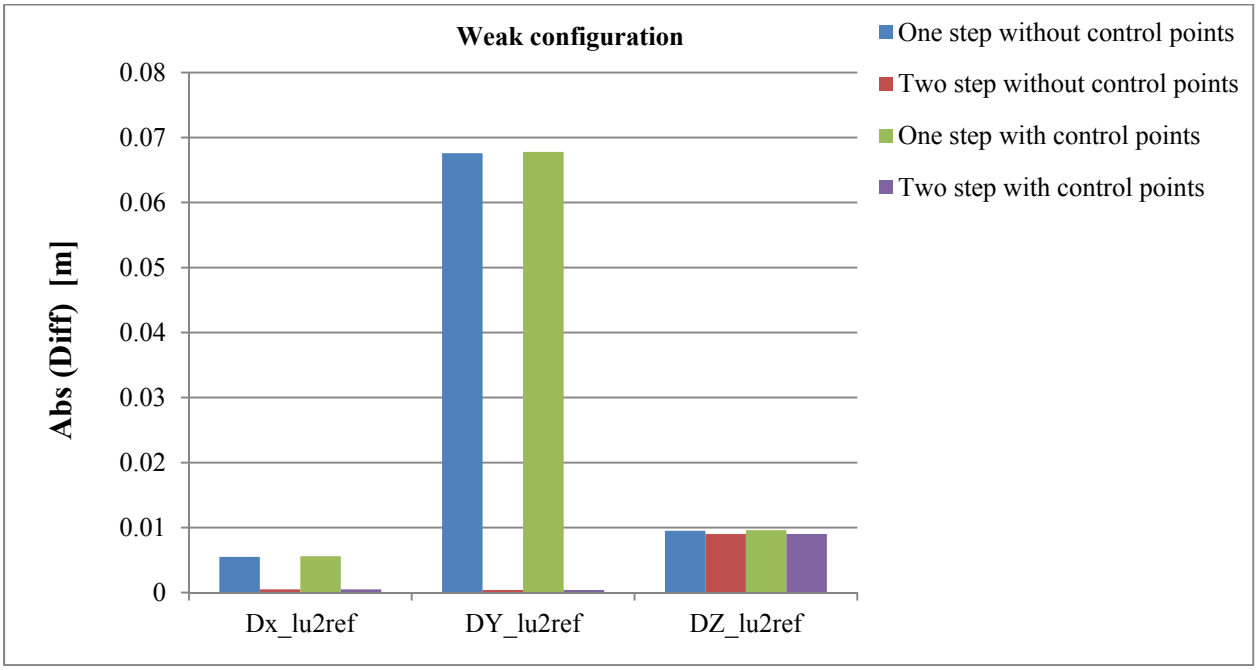

Figure 6.23. The difference between the estimated and true values of the lever arm offset relating scanner 1 and the reference scanner in experiment 1

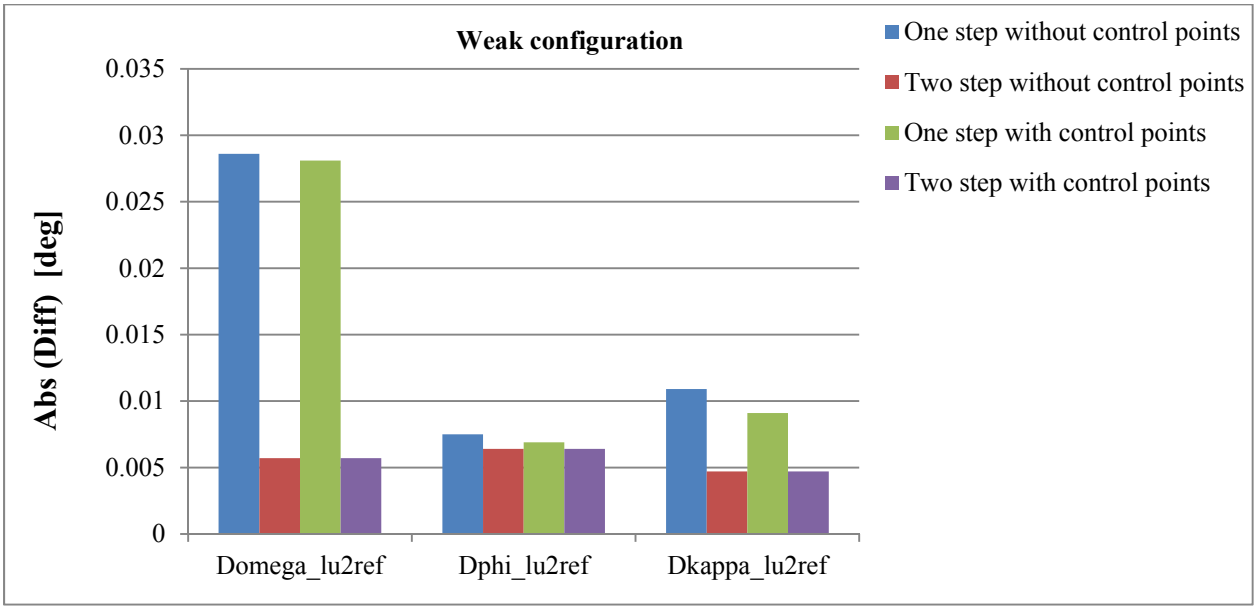

Figure 6.24. The difference between the estimated and true values of the rotation angles relating scanner 1 and the reference scanner coordinate systems in experiment 1

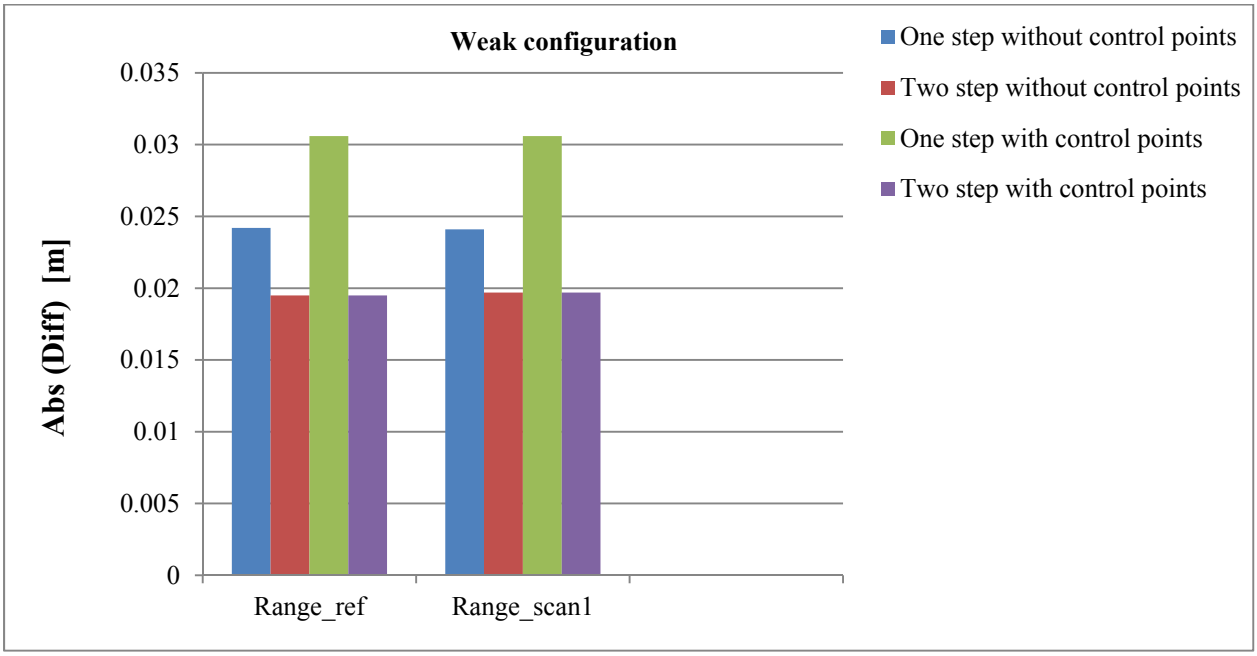

Figure 6.25. The difference between the estimated and true values of the range of the reference scanner and scanner 1 in experiment 1

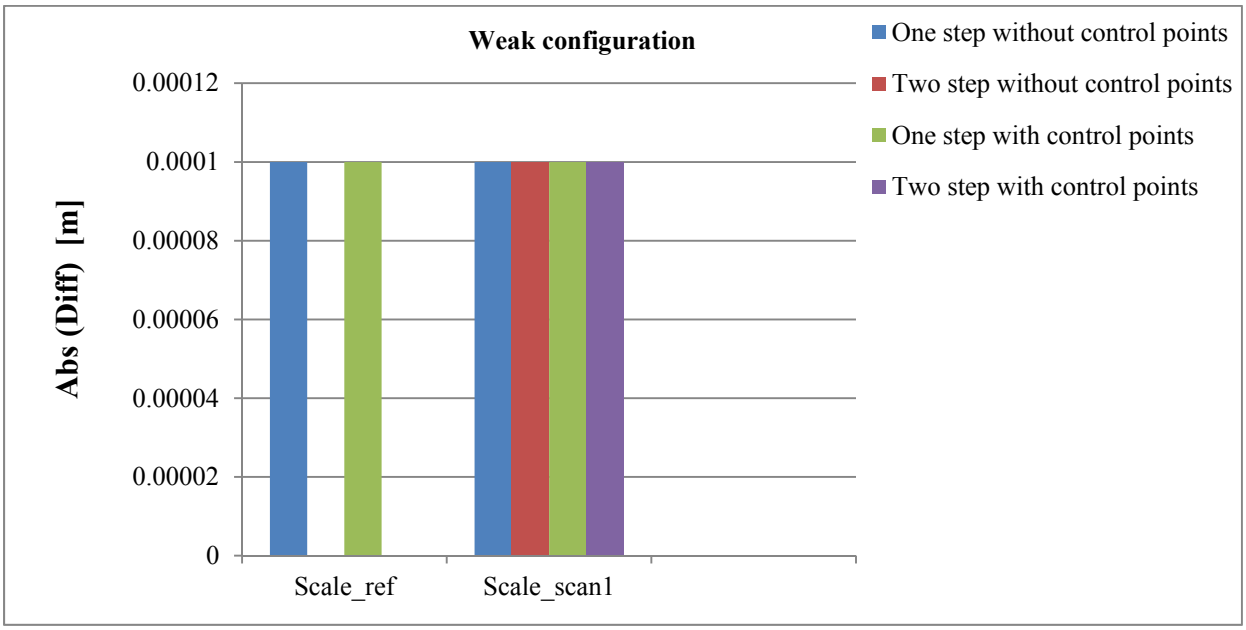

Figure 6.26. The difference between the estimated and true values of the scale of the mirror scanning angle β of the reference scanner and scanner 1 in experiment 1

The absolute values of the differences between the estimated and true values of the unknown system parameters using the moderate configuration (as reported in Tables 5.A-8.A) are illustrated in figures 6.27-6.32.

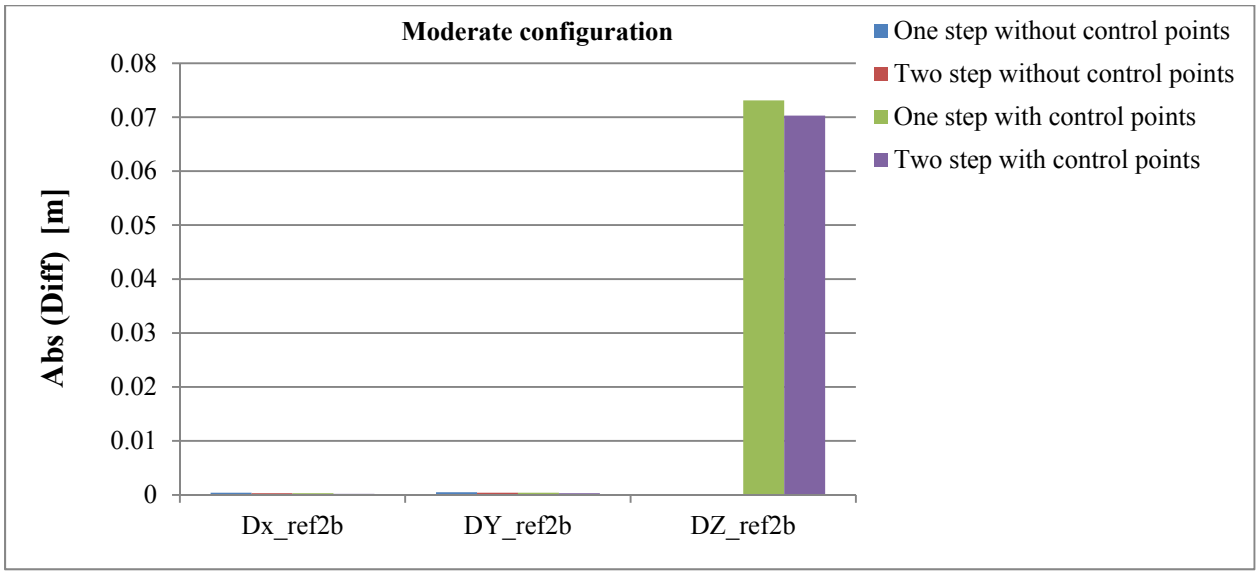

Figure 6.27. The difference between the estimated and true values of the lever arm offset relating the reference scanner and the IMU body frame in experiment 1

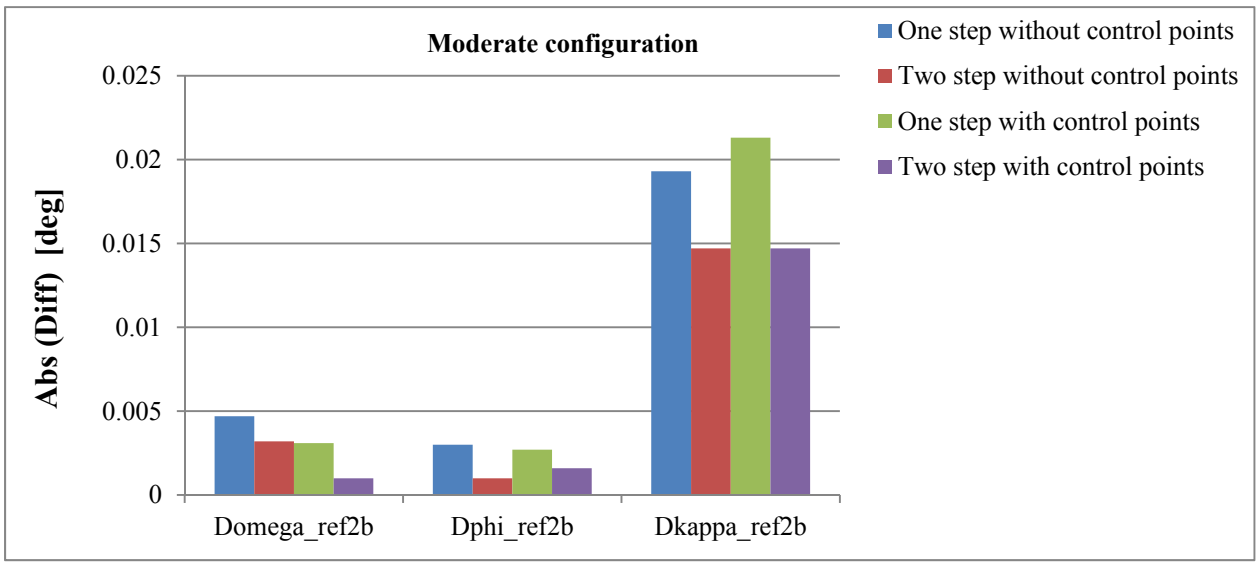

Figure 6.28. The difference between the estimated and true values of the rotation angles relating the reference scanner and the IMU body frame coordinate systems in experiment 1

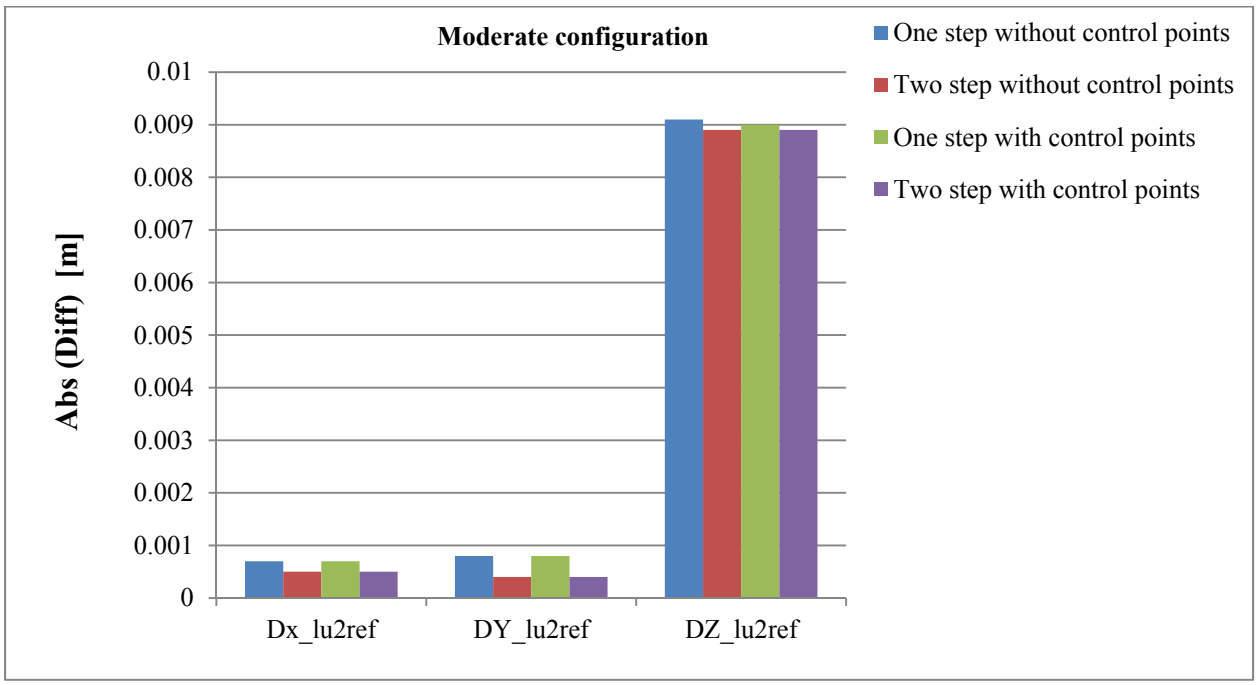

Figure 6.29. The difference between the estimated and true values of the lever arm offset relating scanner 1 and the reference scanner in experiment 1

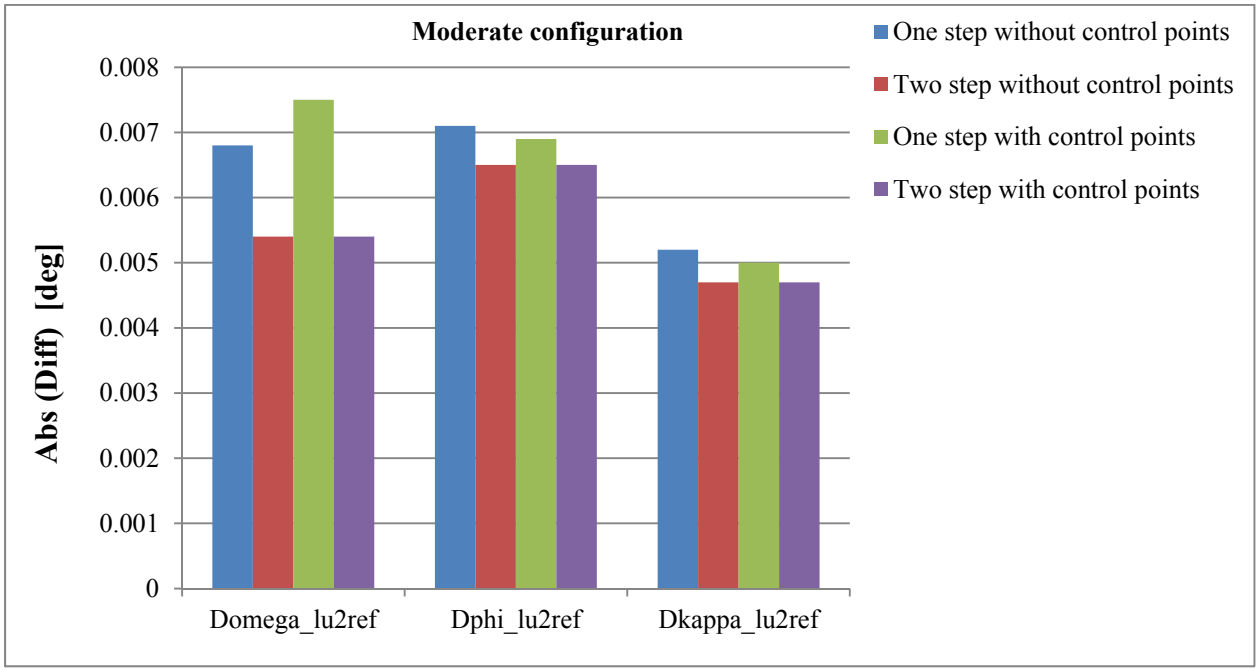

Figure 6.30. The difference between the estimated and true values of the rotation angles relating scanner 1 and the reference scanner coordinate systems in experiment 1

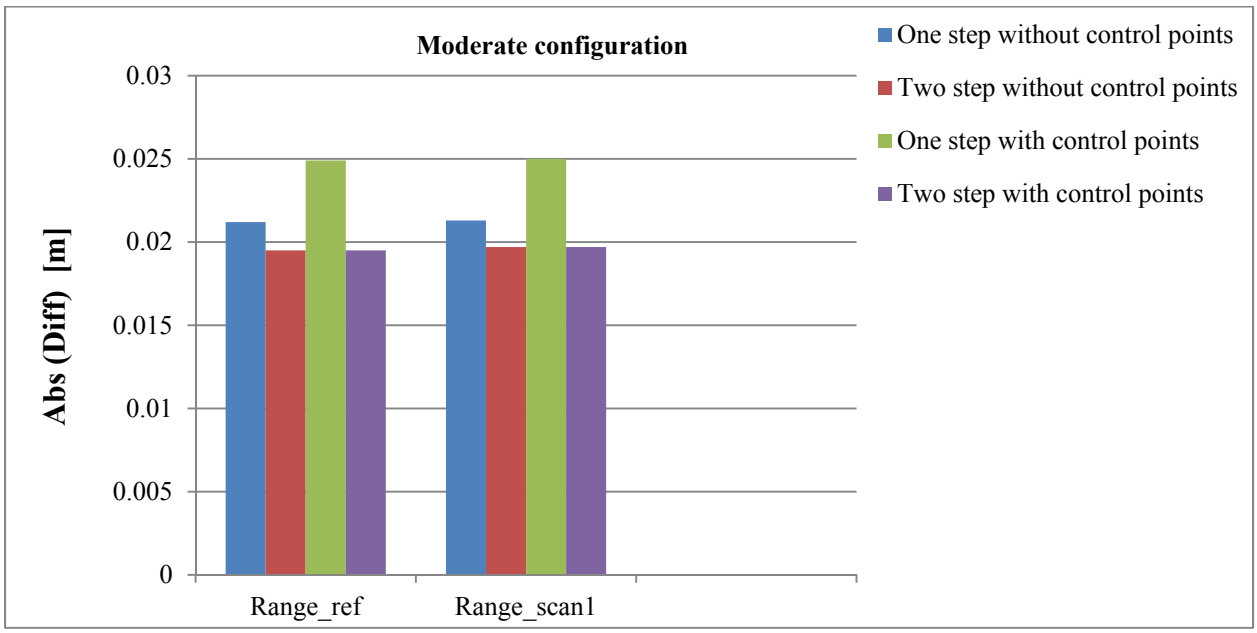

Figure 6.31. The difference between the estimated and true values of the range of the reference scanner and scanner 1 in experiment 1

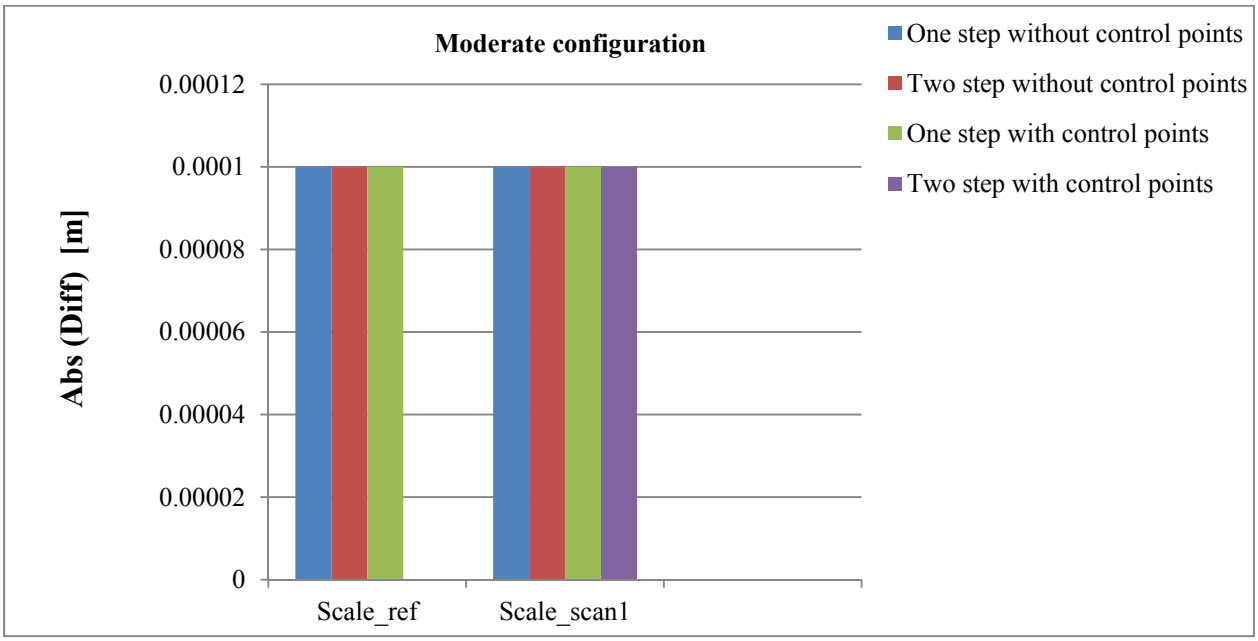

Figure 6.32. The difference between the estimated and true values of the scale of the mirror scanning angle β of the reference scanner and scanner 1 in experiment 1

The absolute values of the differences between the estimated and true values of the unknown system parameters using the strong configuration (as reported in Tables 9.A-12.A) are illustrated in figures 6.33-6.38.

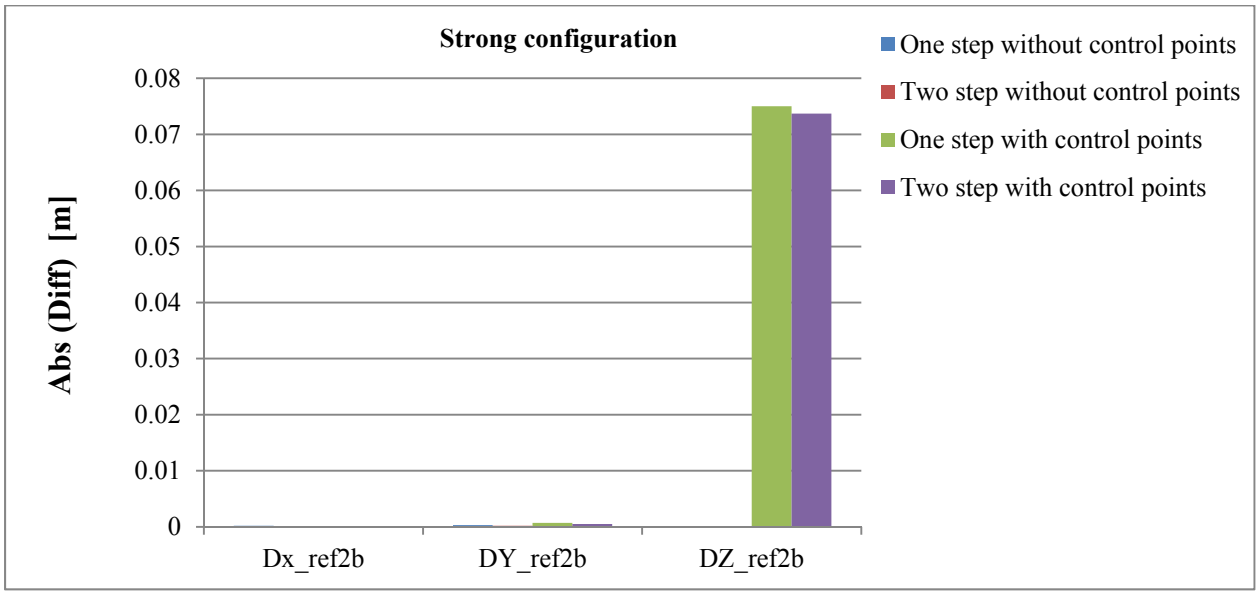

Figure 6.33. The difference between the estimated and true values of the lever arm offset relating the reference scanner and the IMU body frame in experiment 1

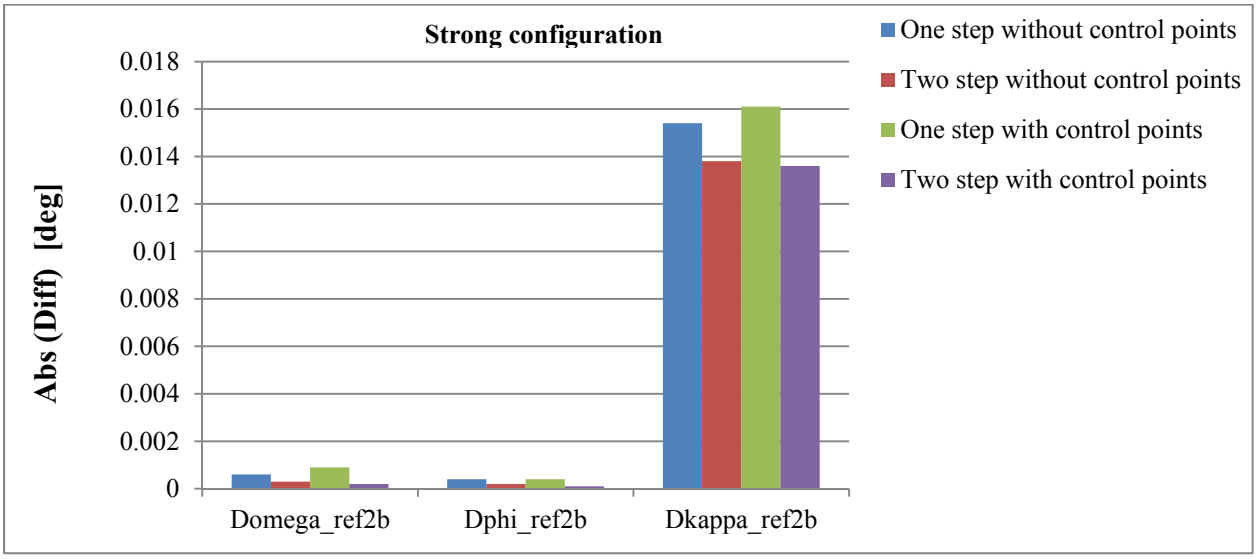

Figure 6.34. The difference between the estimated and true values of the rotation angles relating the reference scanner and the IMU body frame coordinate systems in experiment 1

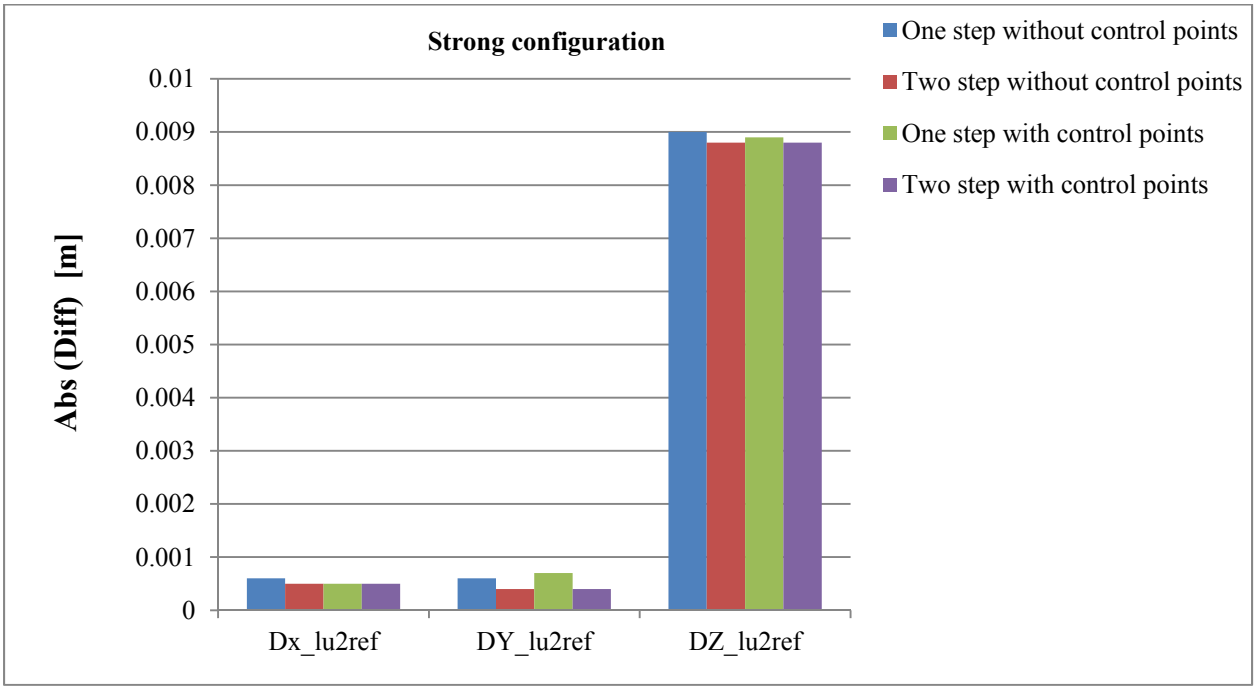

Figure 6.35. The difference between the estimated and true values of the lever arm offset relating scanner 1 and the reference scanner in experiment 1

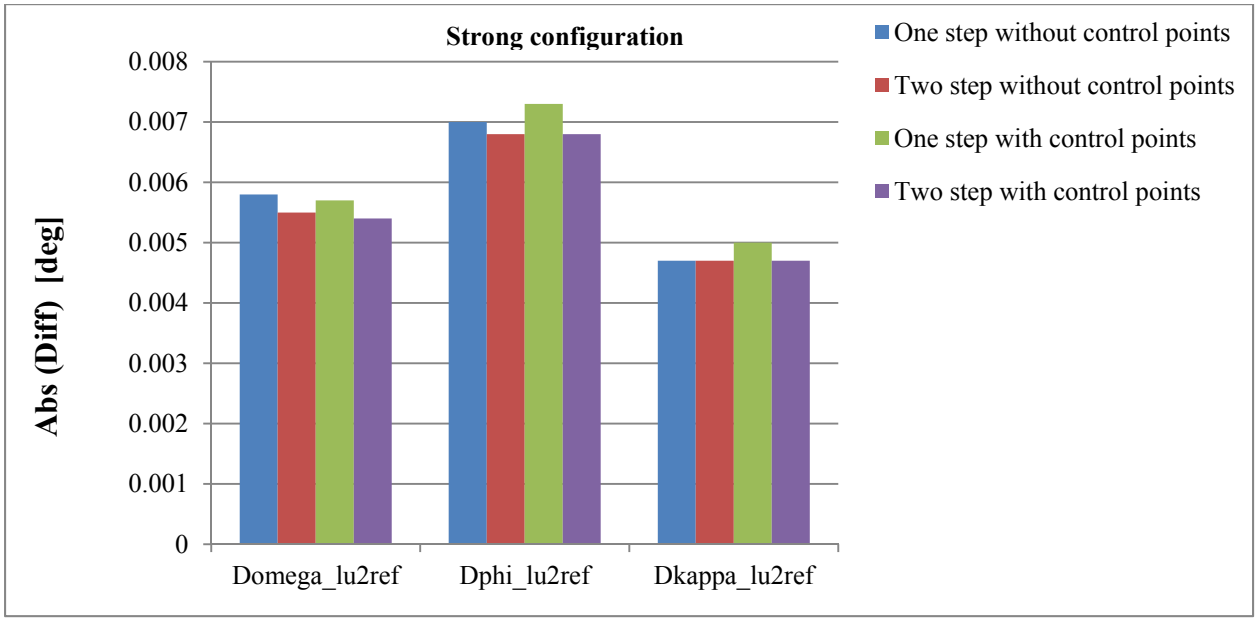

Figure 6.36. The difference between the estimated and true values of the rotation angles relating scanner 1 and the reference scanner coordinate systems in experiment 1

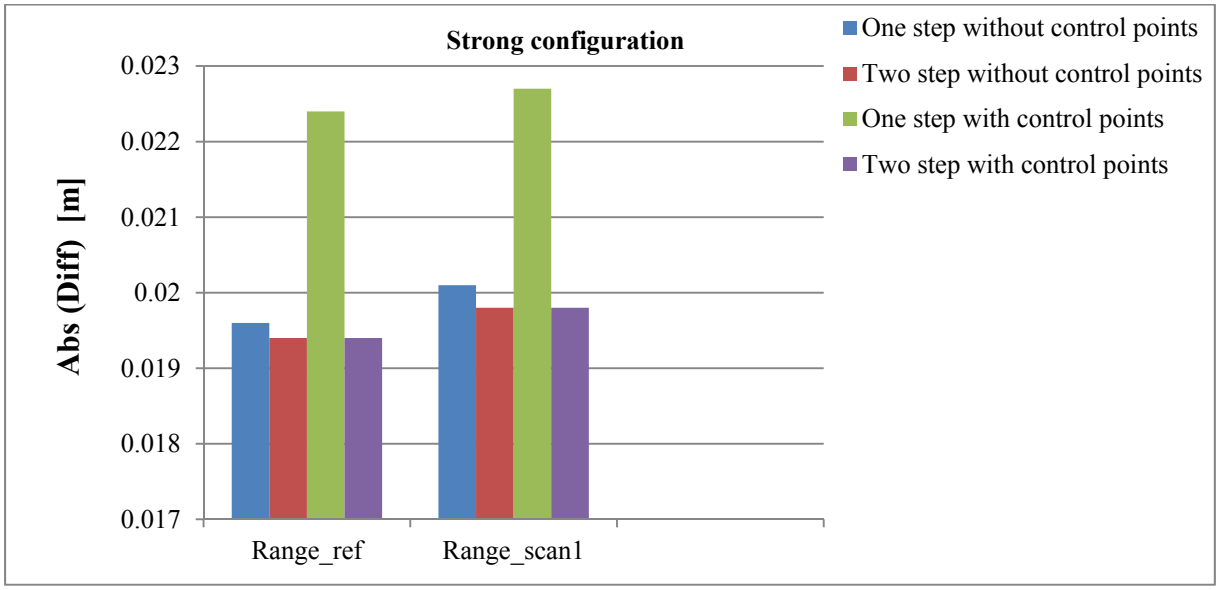

Figure 6.37. The difference between the estimated and true values of the range of the reference scanner and scanner 1in experiment 1

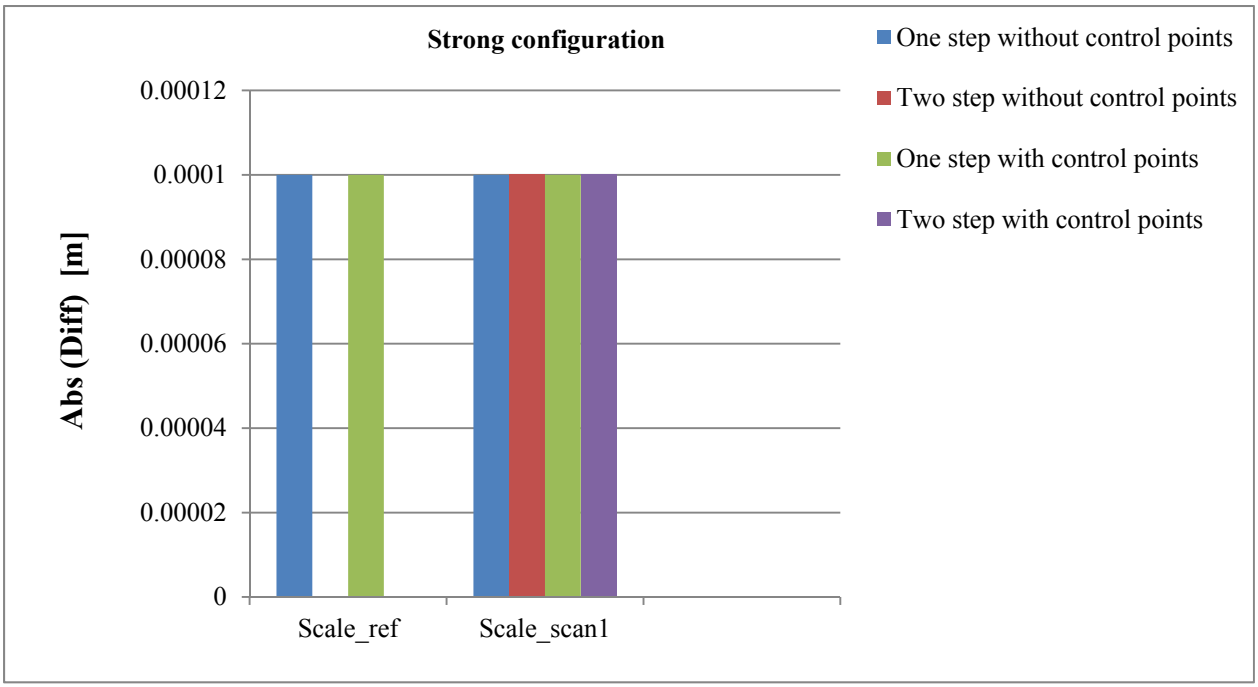

Figure 6.38. The difference between the estimated and true values of the scale of the mirror scanning angle β of the reference scanner and scanner 1in experiment 1

6.5.4.3 Experiment "2"

In this experiment, one is interested in evaluating the impact of some deterioration in the quality of the integrated GPS/INS position and orientation information on the estimated system parameters from the one-step and two-step calibration procedures. The accuracy of the utilized GPS/INS and the introduced random errors used for this experiment are reported in Table 6.27.

Table 6.27. The accuracy of the utilized GPS/INS and the introduced random errors used for experiment "2"

Error type	**Value**
Accuracy (Noise level) of range in Velodyne HDL β 32E laser scanner	± 0.02 m
Accuracy (Noise level) of mirror scanning angle β in Velodyne HDL-32E laser scanner	± 0.001 deg
Accuracy (Noise level) of GPS	± 0.1 m
Accuracy (Noise level) of IMU Roll, Pitch Heading	 ± 0.01 deg ± 0.03 deg
The accuracy of the ground control point	± 0.05 m

In a similar fashion, the performed scenarios used in experiment "1" are used in this experiment. The results of the estimated system parameters from different scenarios using the one-step and two-step calibration procedures are reported in Tables 1.B-12.B (refer to Appendix B).

The absolute values of the differences between the estimated and true values of the unknown system parameters using the weak configuration (as reported in Tables 1.B- 4.B) are illustrated in figures 6.39-6.44.

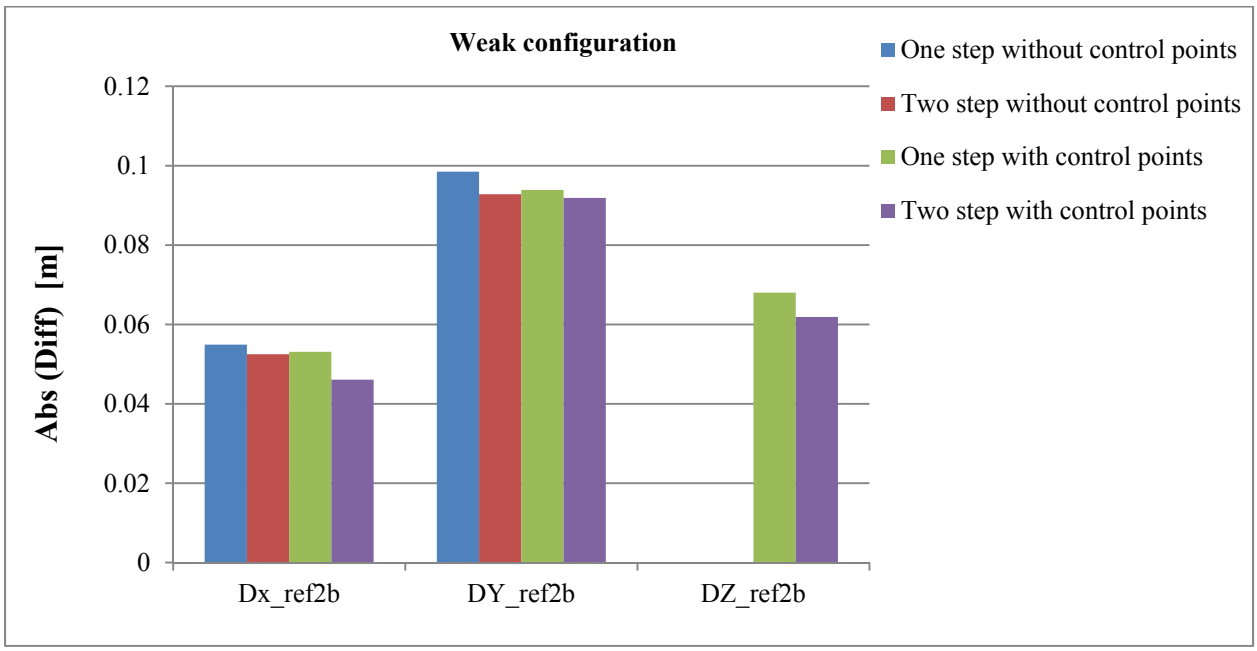

Figure 6.39. The difference between the estimated and true values of the lever arm offset relating the reference scanner and the IMU body frame in experiment 2

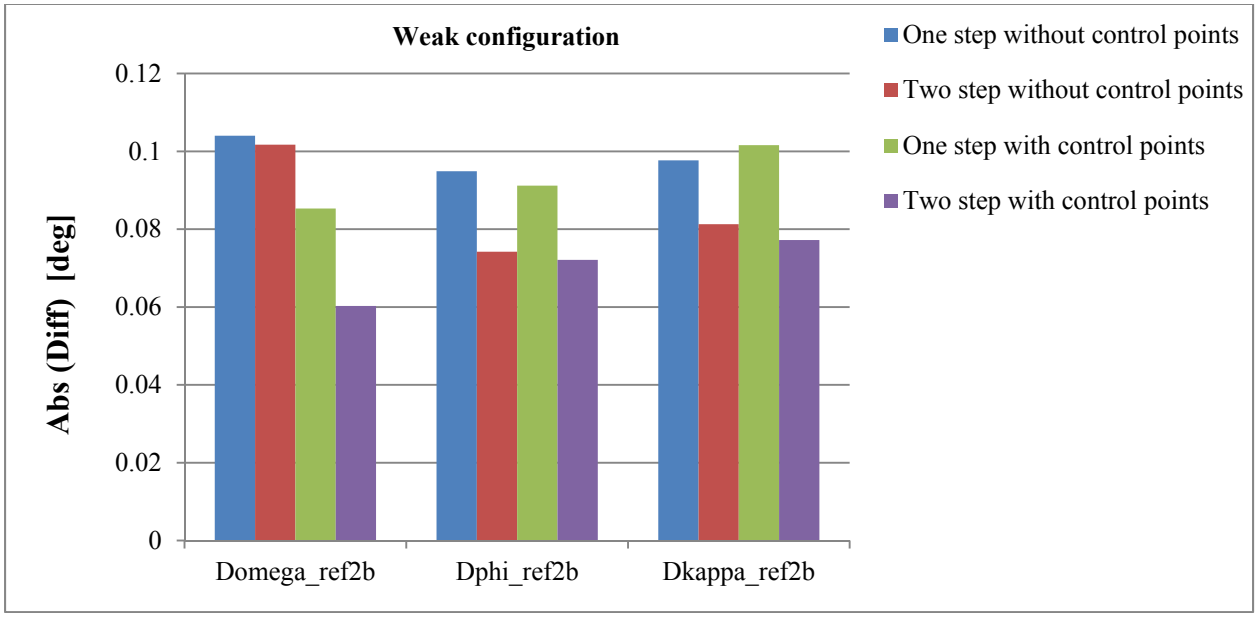

Figure 6.40. The difference between the estimated and true values of the rotation angles relating the reference scanner and the IMU body frame coordinate systems in experiment 2

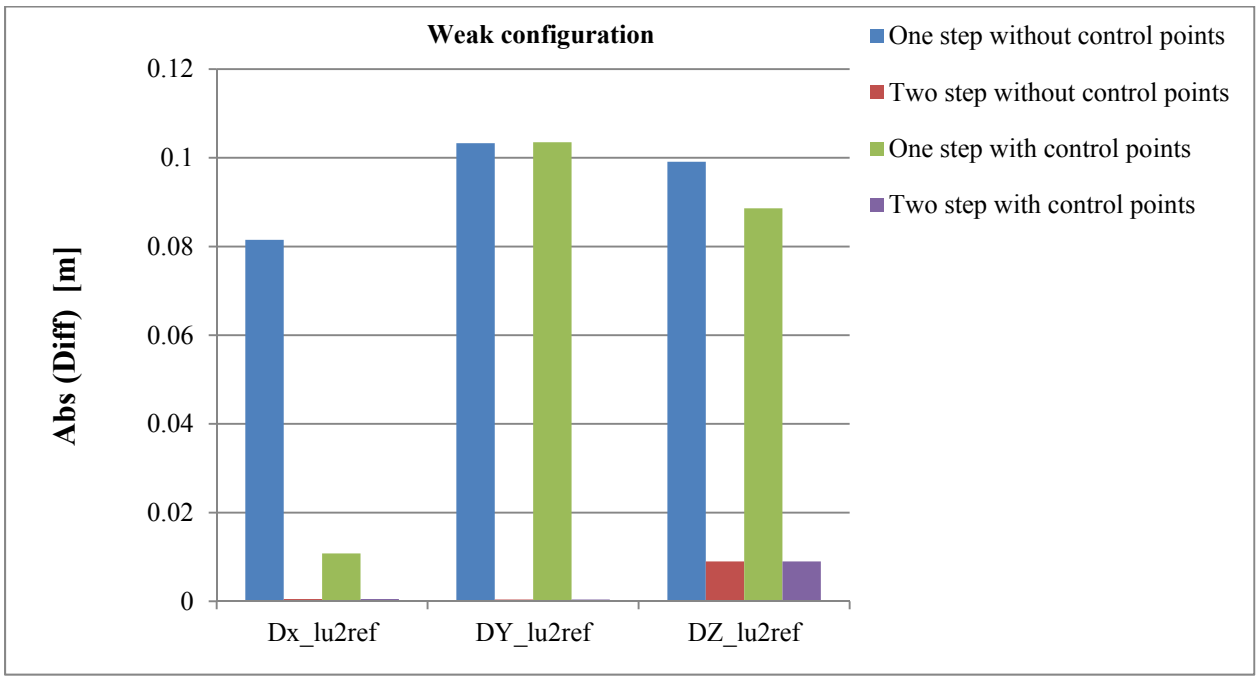

Figure 6.41. The difference between the estimated and true values of the lever arm offset relating scanner 1 and the reference scanner in experiment 2

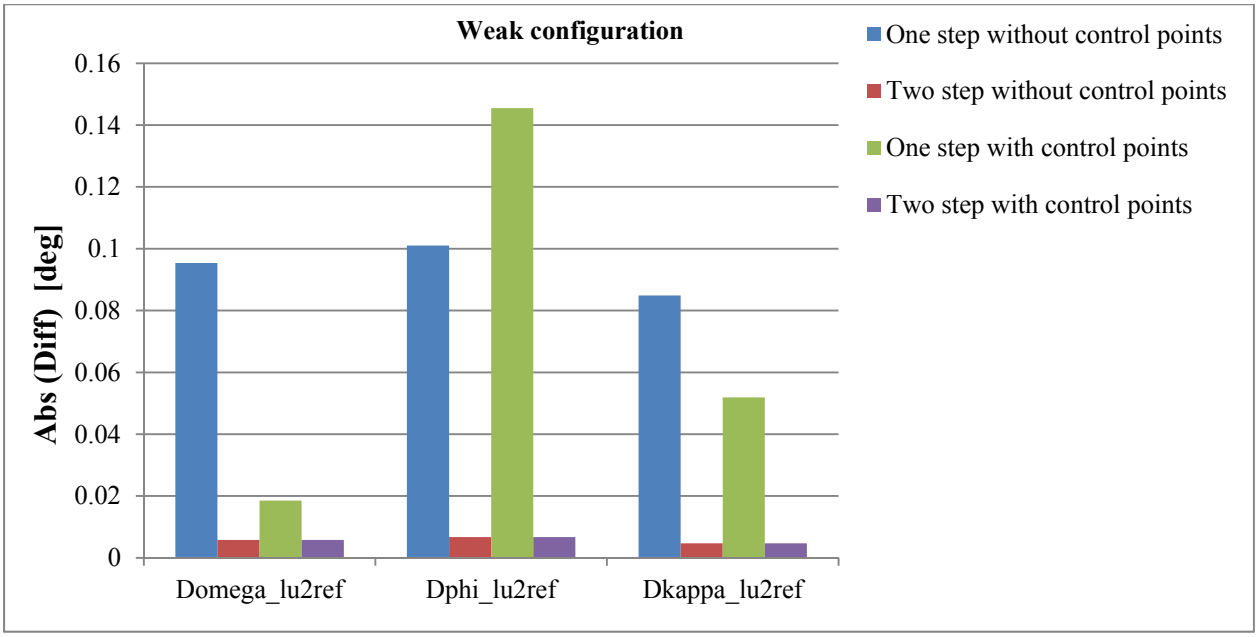

Figure 6.42. The difference between the estimated and true values of the rotation angles relating scanner 1 and the reference scanner coordinate systems in experiment 2

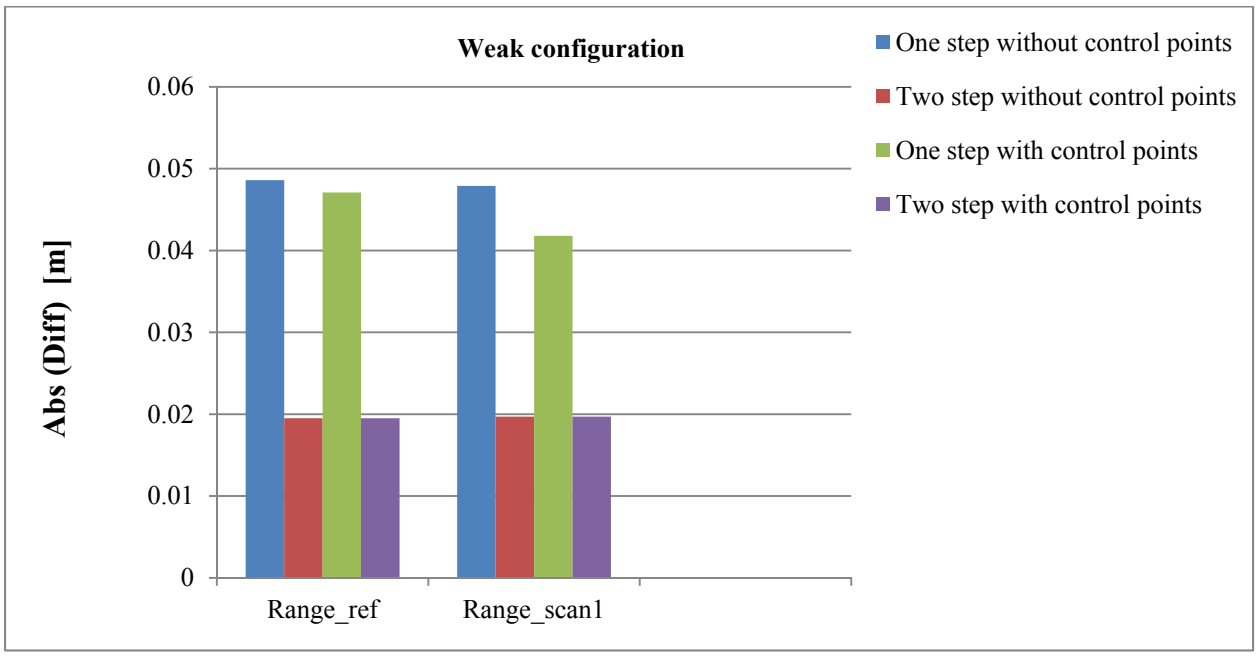

Figure 6.43. The difference between the estimated and true values of the range of the reference scanner and scanner 1 in experiment 2

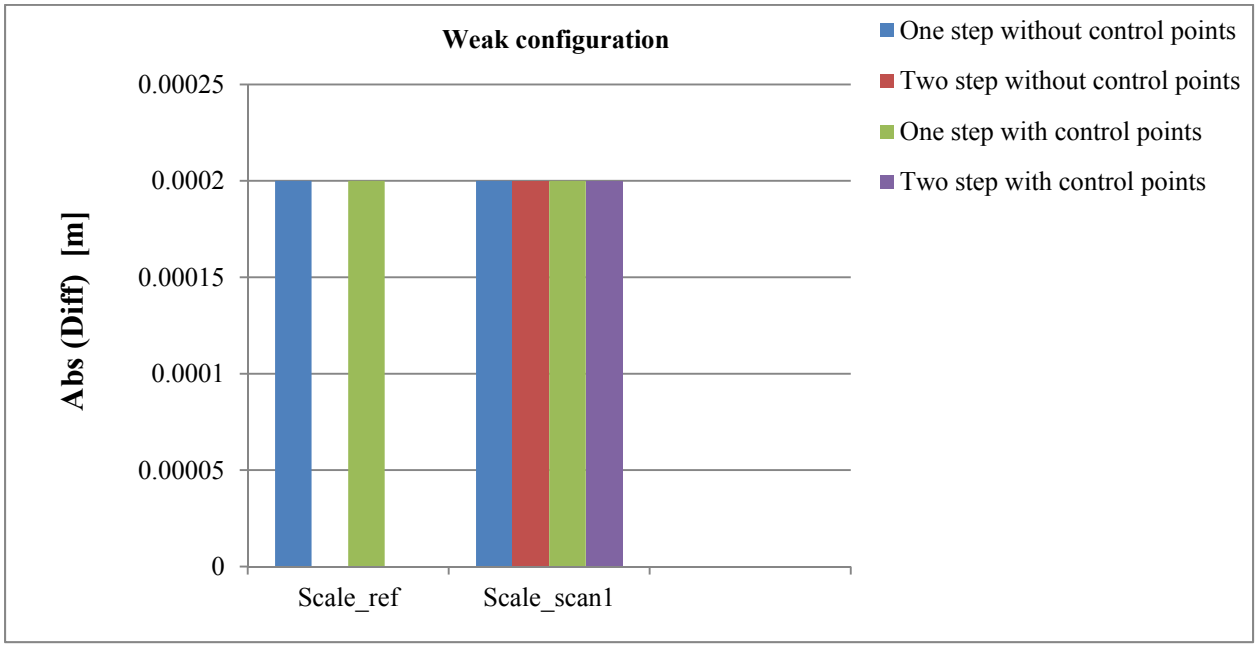

Figure 6.44. The difference between the estimated and true values of the scale of the mirror scanning angle β of the reference scanner and scanner 1 in experiment 2

The absolute values of the differences between the estimated and true values of the unknown system parameters using the moderate configuration (as reported in Tables 5.B-8.B) are illustrated in figures 6.45-6.50.

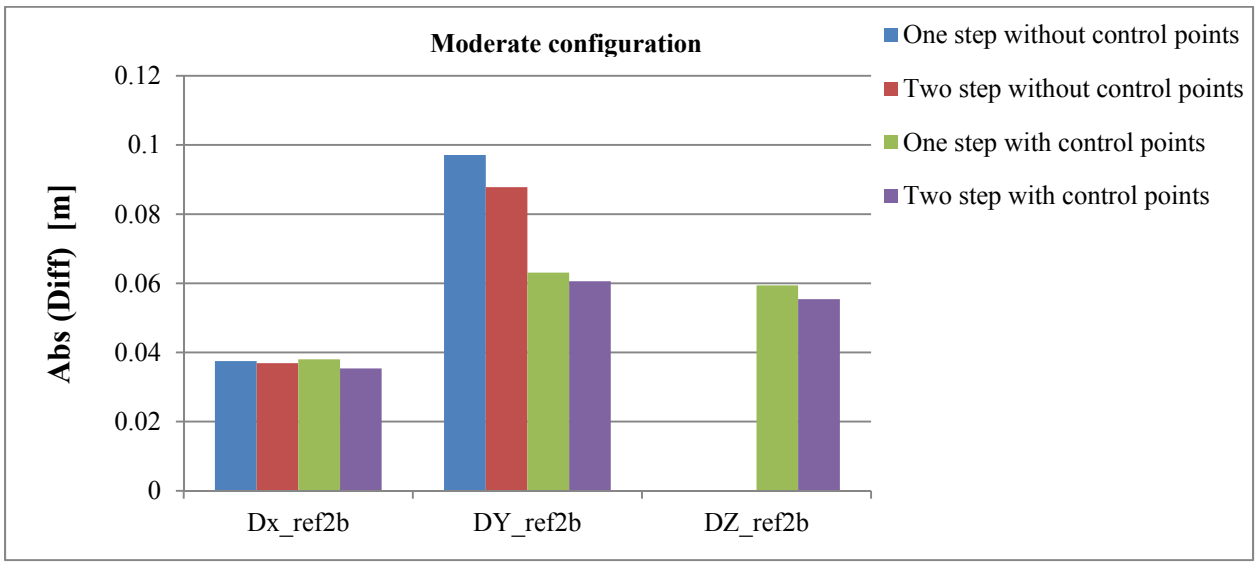

Figure 6.45. The difference between the estimated and true values of the lever arm offset relating the reference scanner and the IMU body frame in experiment 2

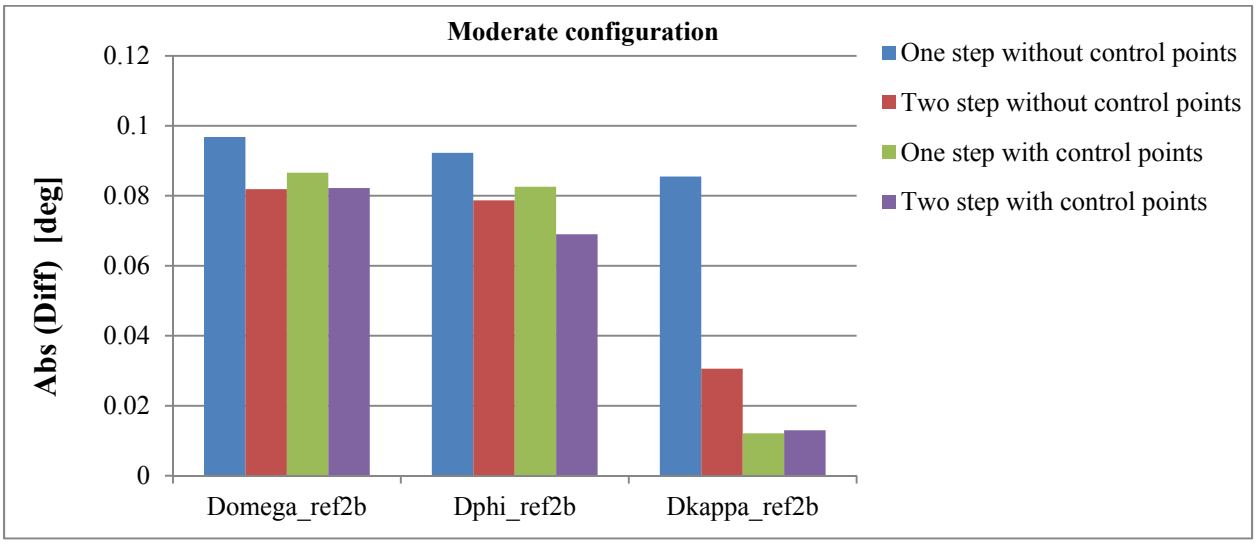

Figure 6.46. The difference between the estimated and true values of the rotation angles relating the reference scanner and the IMU body frame coordinate systems in experiment

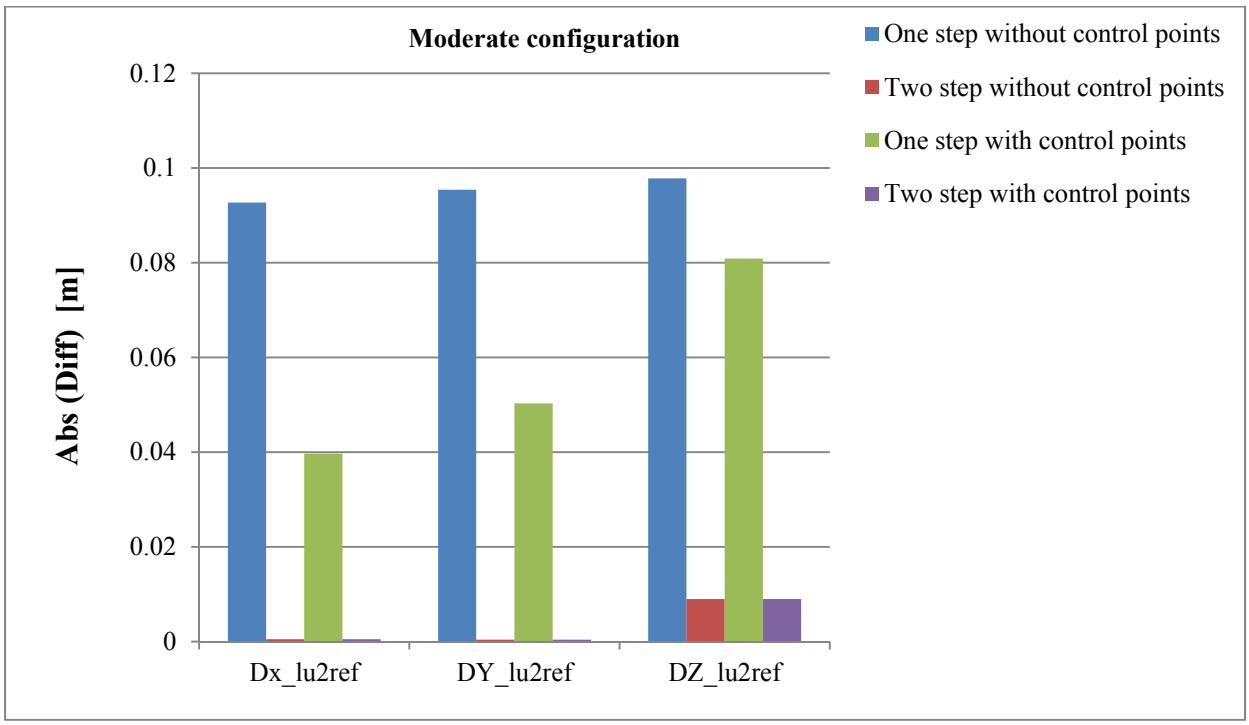

Figure 6.47. The difference between the estimated and true values of the lever arm offset relating scanner 1 and the reference scanner in experiment 2

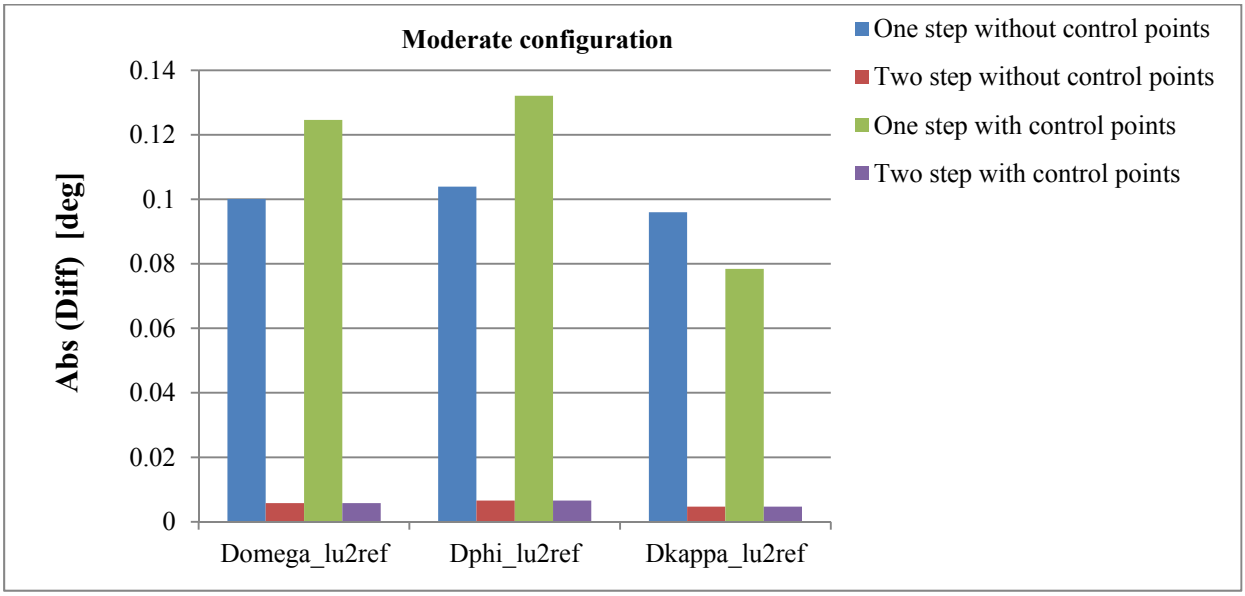

Figure 6.48 The difference between the estimated and true values of the rotation angles relating scanner 1 and the reference scanner coordinate systems in experiment 2

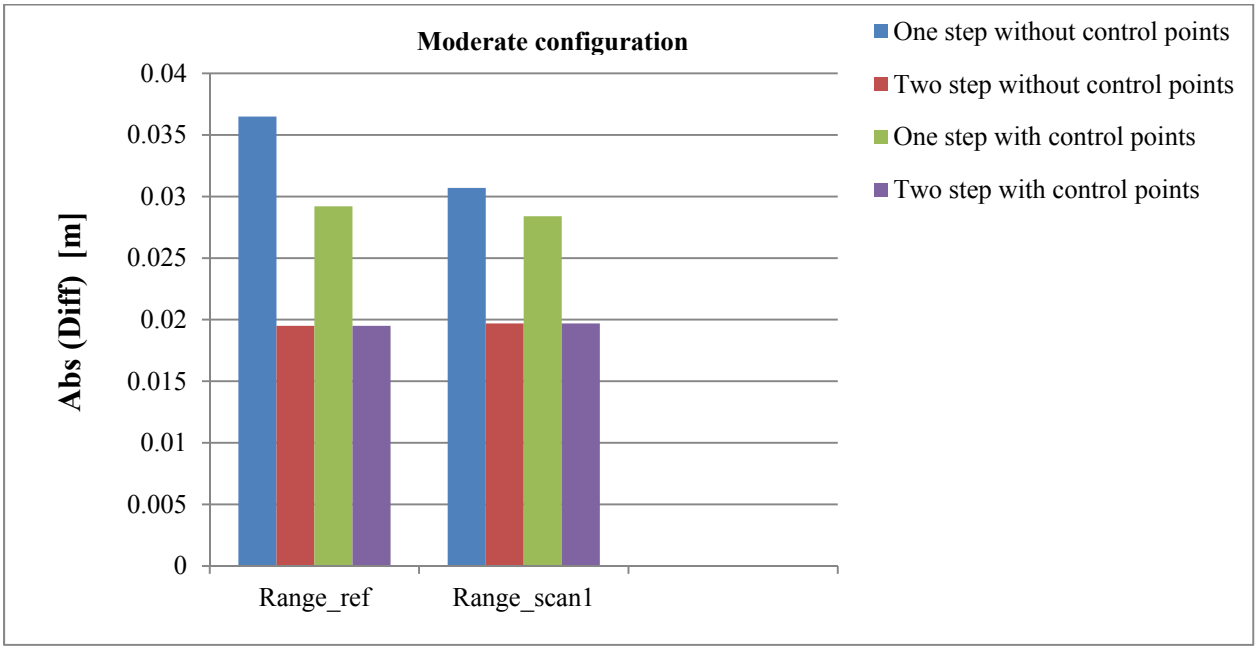

Figure 6.49. The difference between the estimated and true values of the range of the reference scanner and scanner 1 in experiment 2

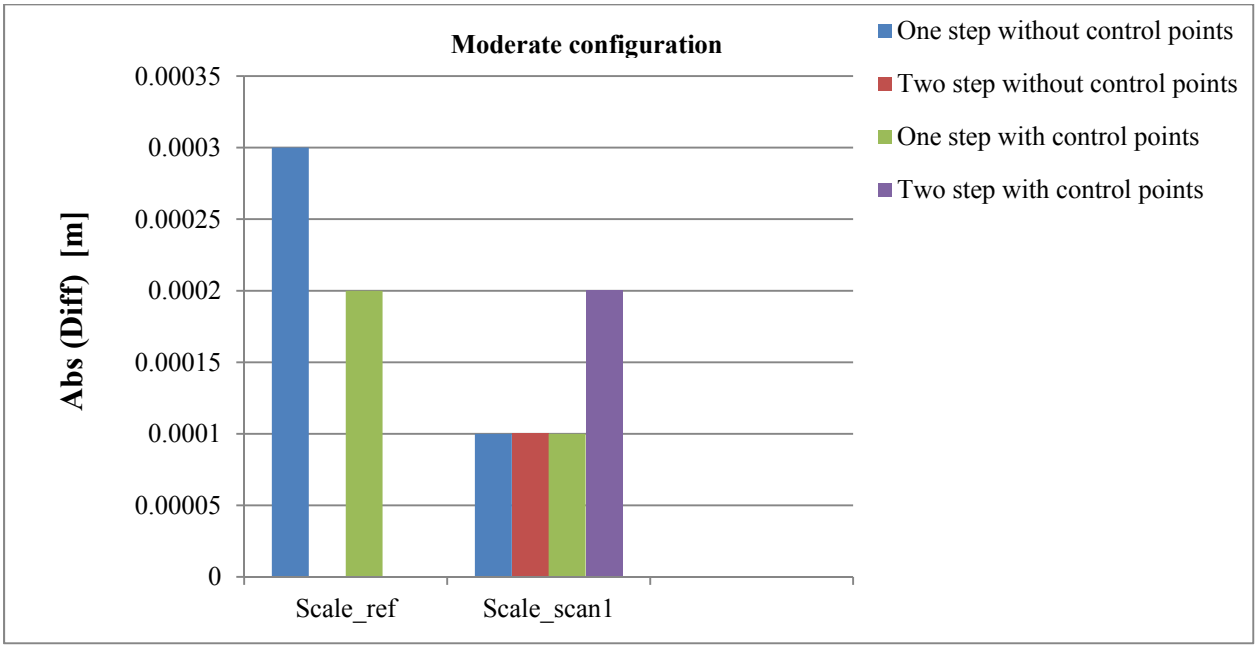

Figure 6.50. The difference between the estimated and true values of the scale of the mirror scanning angle β of the reference scanner and scanner 1 in experiment 2

The absolute values of differences between the estimated and true values of the unknown system parameters using the strong configuration (as reported in Tables 9.B-12.B) are illustrated in figures 6.51-6.56.

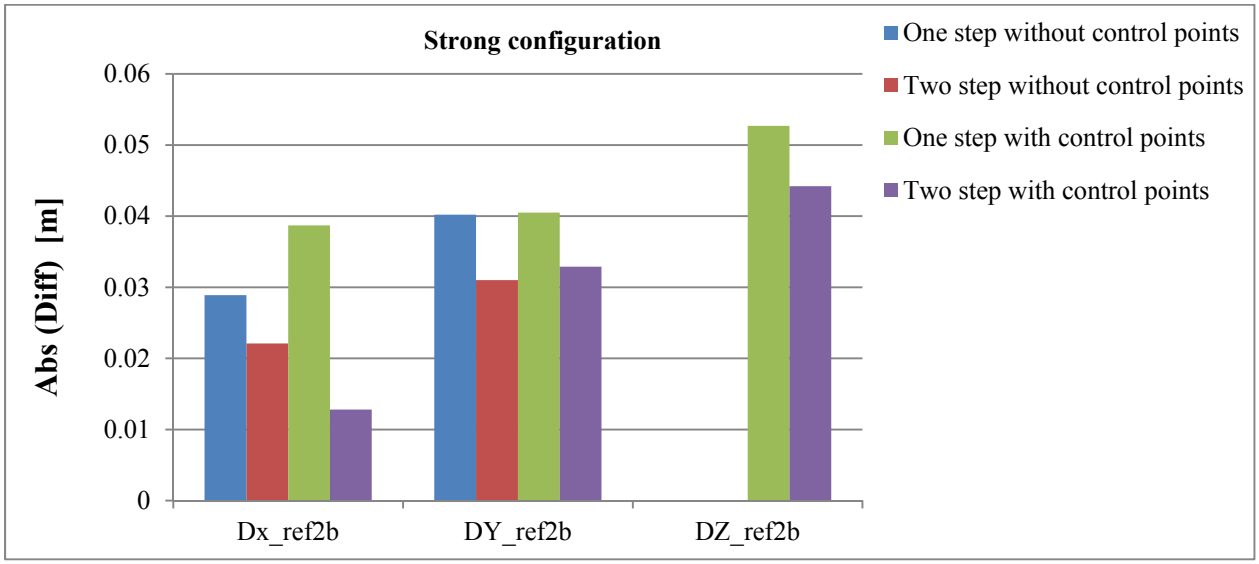

Figure 6.51. The difference between the estimated and true values of the lever arm offset relating the reference scanner and the IMU body frame in experiment 2

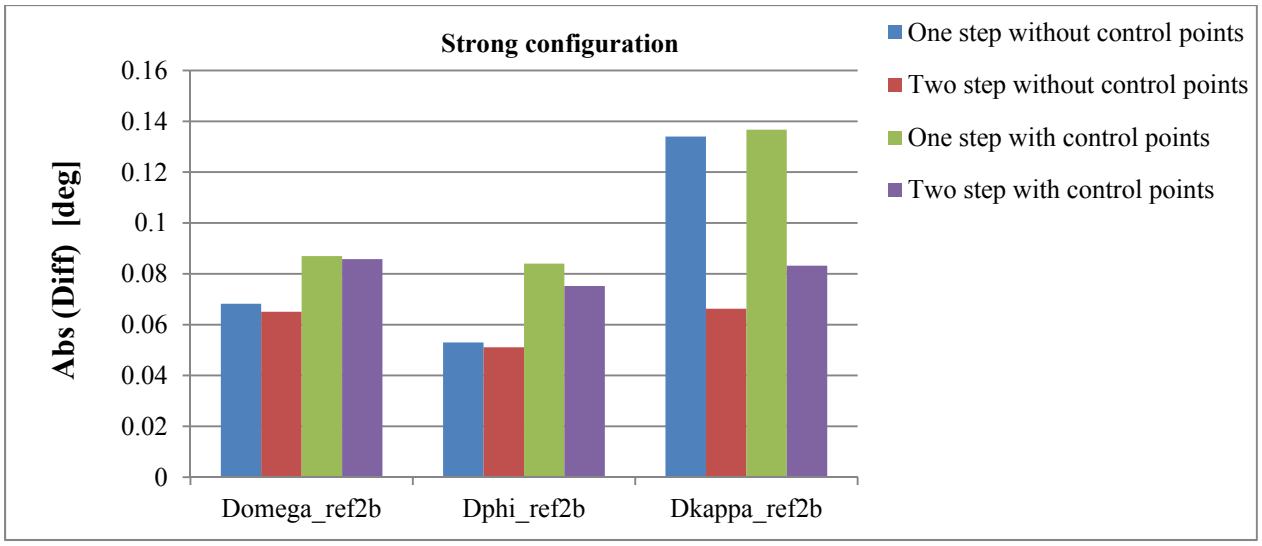

Figure 6.52 The difference between the estimated and true values of the rotation angles relating the reference scanner and the IMU body frame coordinate systems in experiment 2

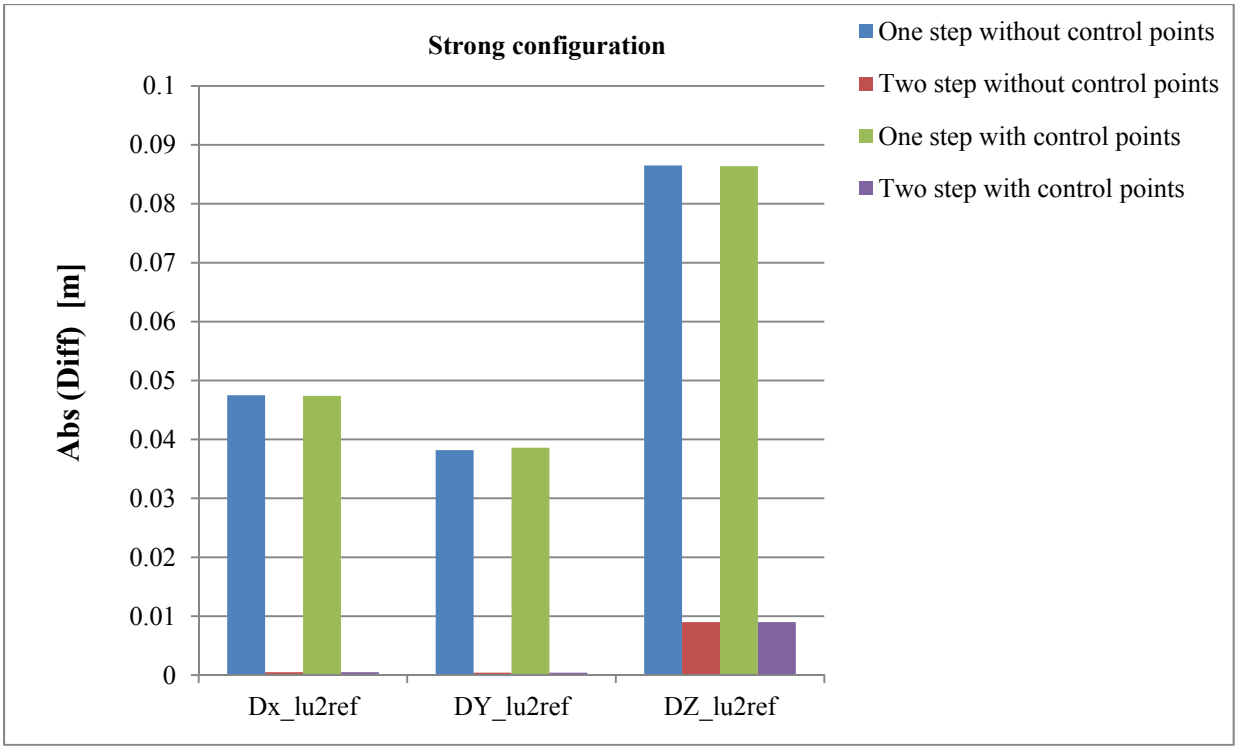

Figure 6.53. The difference between the estimated and true values of the lever arm offset relating scanner 1 and the reference scanner in experiment 2

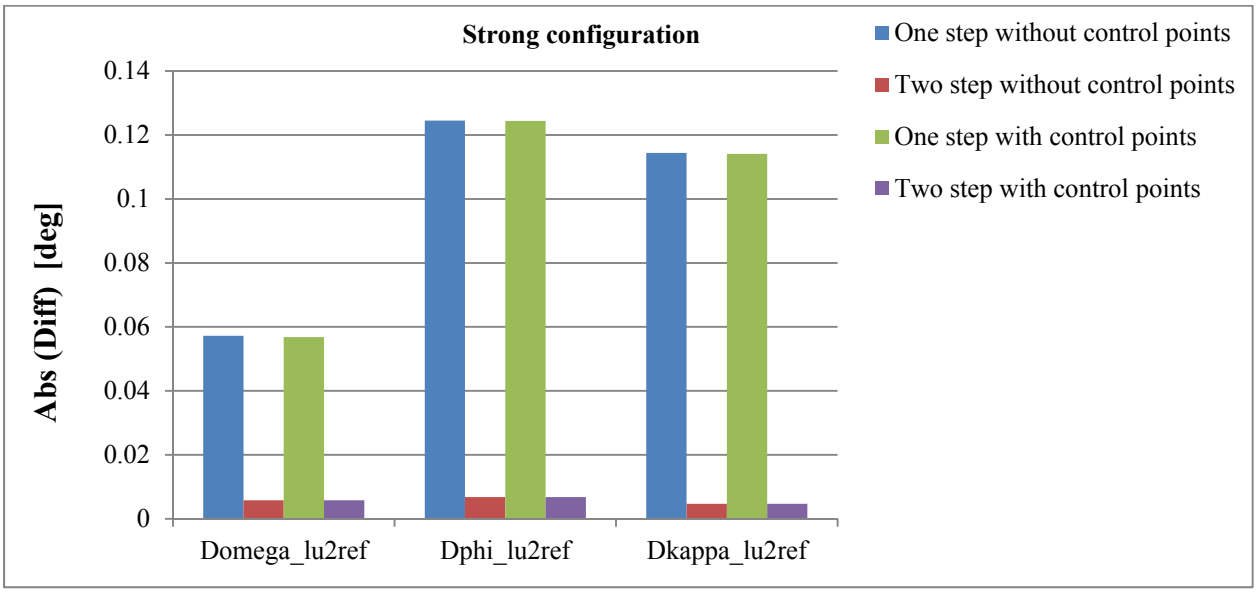

Figure 6.54 The difference between the estimated and true values of the rotation angles relating scanner 1 and the reference scanner coordinate systems in experiment 2

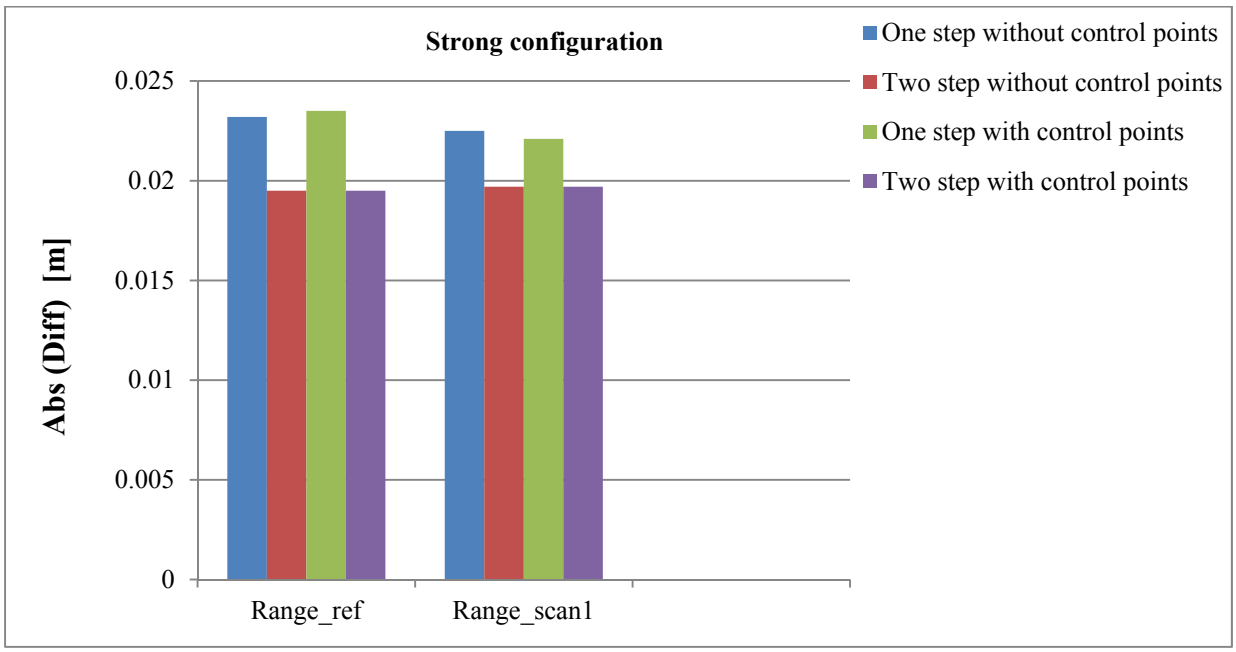

Figure 6.55. The difference between the estimated and true values of the range of the reference scanner and scanner 1 in experiment 2

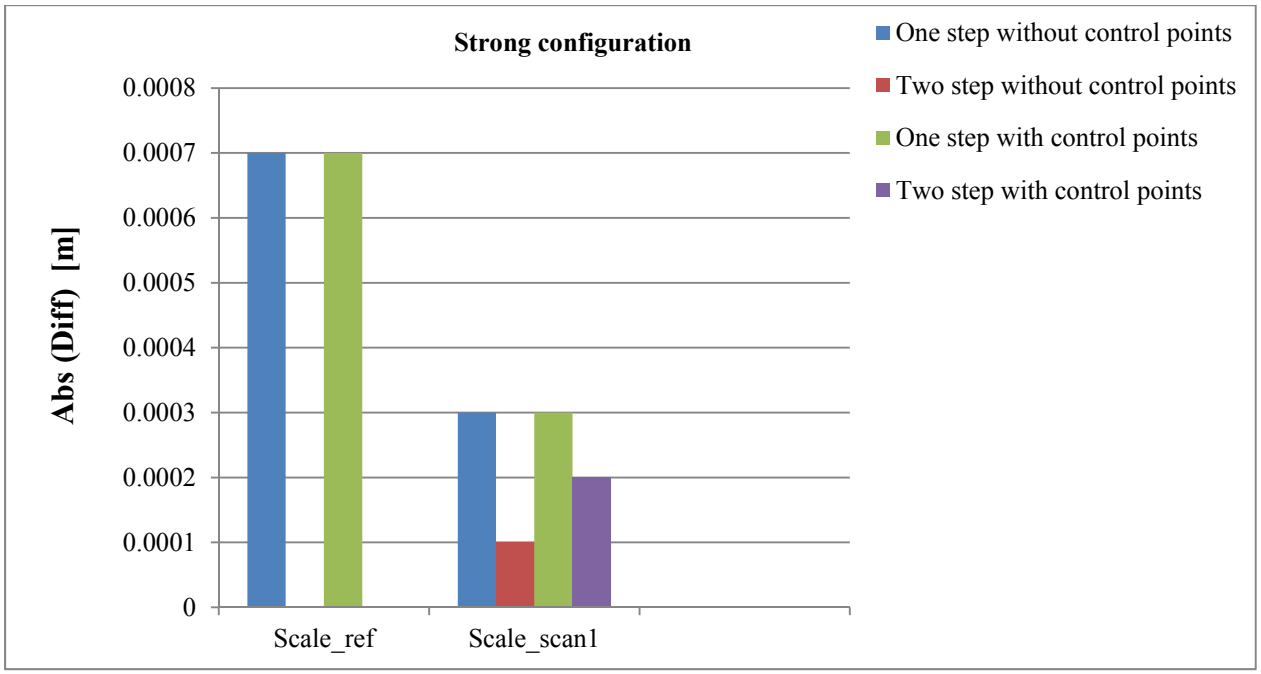

Figure 6.56. The difference between the estimated and true values of the scale of the mirror scanning angle β of the reference scanner and scanner 1 in experiment 2

6.5.4.4 Experiment "3"

In this experiment, one is interested in further evaluation of the impact of a severe deterioration in the quality of the integrated GPS/INS position and orientation information (i.e., worse than what is used in experiments 1 and 2) on the quality of the estimated system parameters from the one-step and two-step calibration procedures. The accuracy of the utilized GPS/INS and the introduced random errors used for this experiment are reported in Table 6.28.

Table 6.28. The accuracy of the utilized GPS/INS and the introduced random errors used for experiment "3"

Error type	**Value**
Accuracy (Noise level) of range in Velodyne HDL β 32E laser scanner	± 0.02 m
Accuracy (Noise level) of mirror scanning angle β in Velodyne HDL-32E laser scanner	± 0.001 deg
Accuracy (Noise level) of GPS	± 0.2 m
Accuracy (Noise level) of IMU Roll, Pitch Heading	 ± 0.02 deg ± 0.06 deg
The accuracy of the ground control point	± 0.05 m

In a similar fashion, the performed scenarios used in experiment "1" and "2" are used in this experiment. The results of the estimated system parameters from different scenarios using the one-step and two-step calibration procedures are reported in Tables 1.C-12.C (refer to Appendix C).

The absolute values of differences between the estimated and true values of the unknown system parameters using the weak configuration (as reported in Tables 1.C-4.C) are illustrated in figures 6.57-6.62.

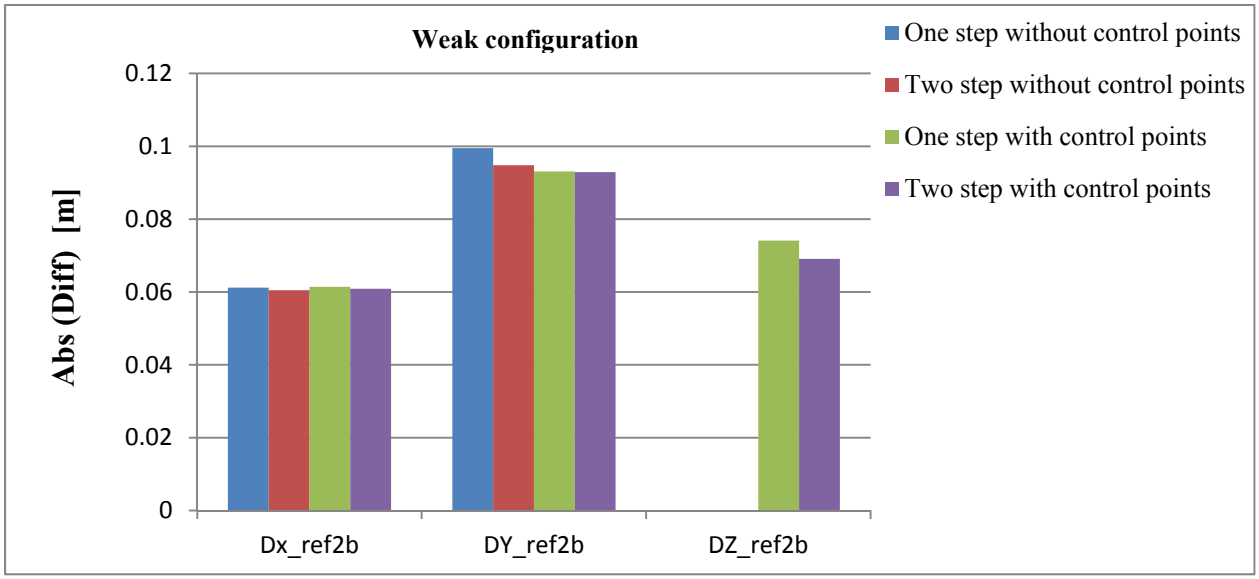

Figure 6.57. The difference between the estimated and true values of the lever arm offset relating the reference scanner and the IMU body frame in experiment 3

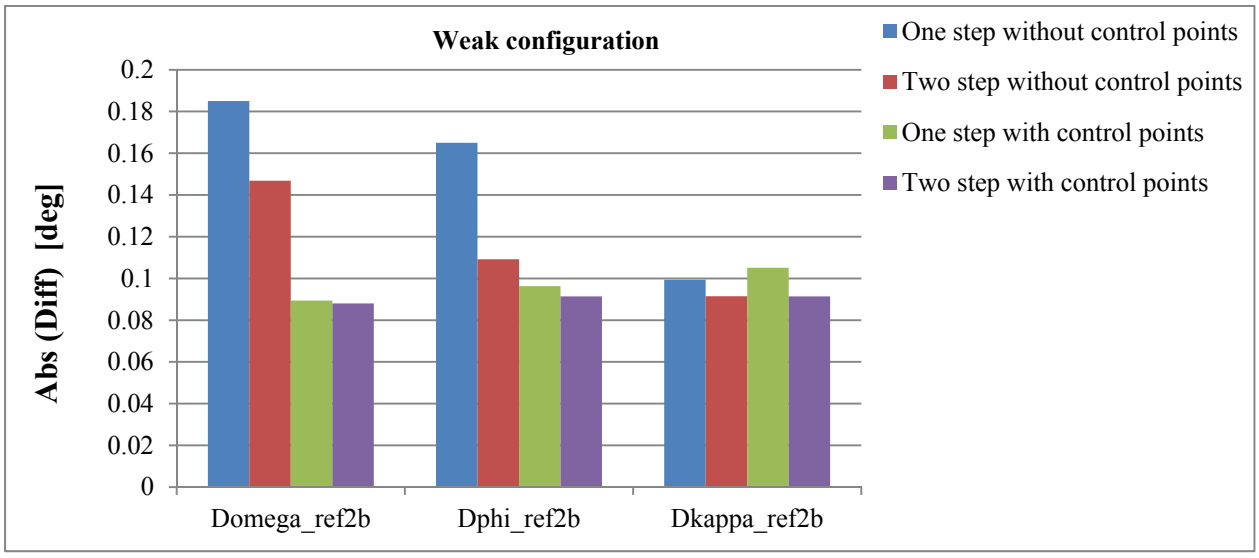

Figure 6.58. The difference between the estimated and true values of the rotation angles relating the reference scanner and the IMU body frame coordinate systems in experiment 3

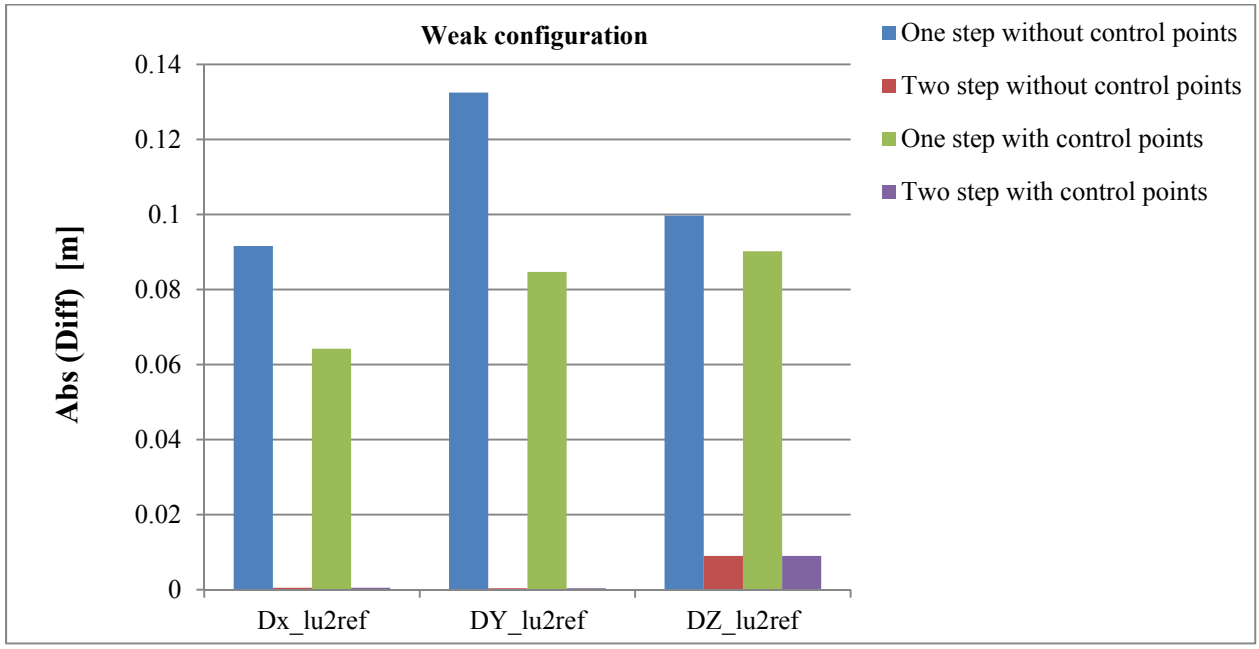

Figure 6.59. The difference between the estimated and true values of the lever arm offset relating scanner 1 and the reference scanner in experiment 3

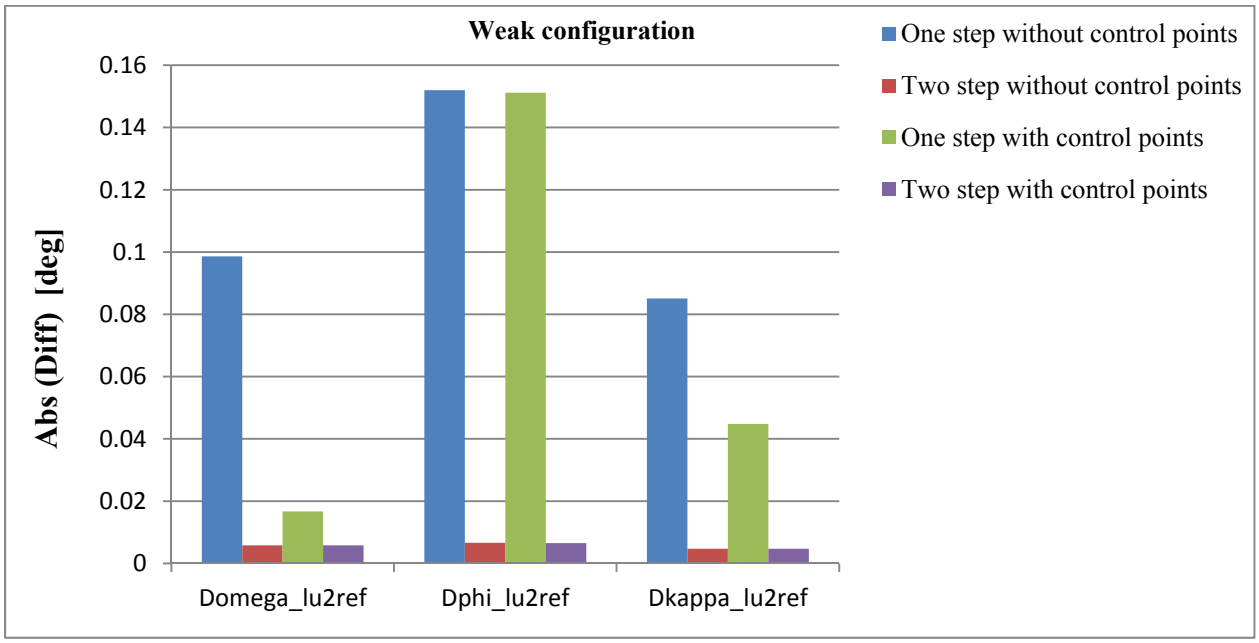

Figure 6.60. The difference between the estimated and true values of the rotation angles relating scanner 1 and the reference scanner coordinate systems in experiment 3

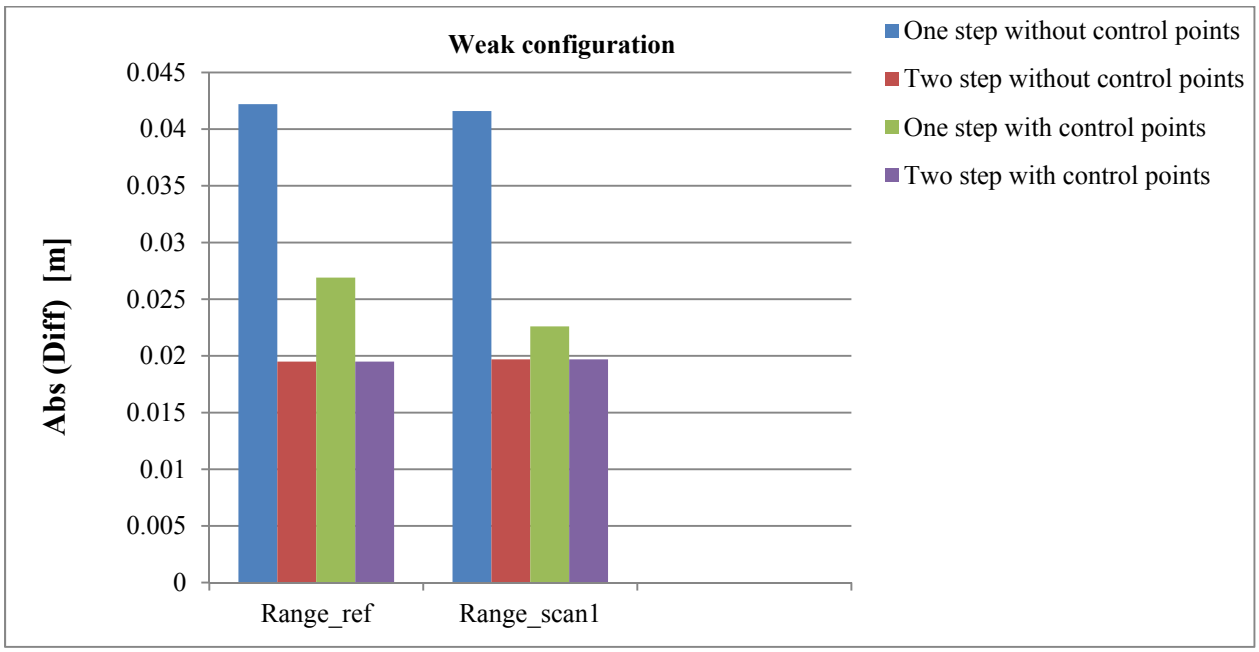

Figure 6.61. The difference between the estimated and true values of the range of the reference scanner and scanner 1 in experiment 3

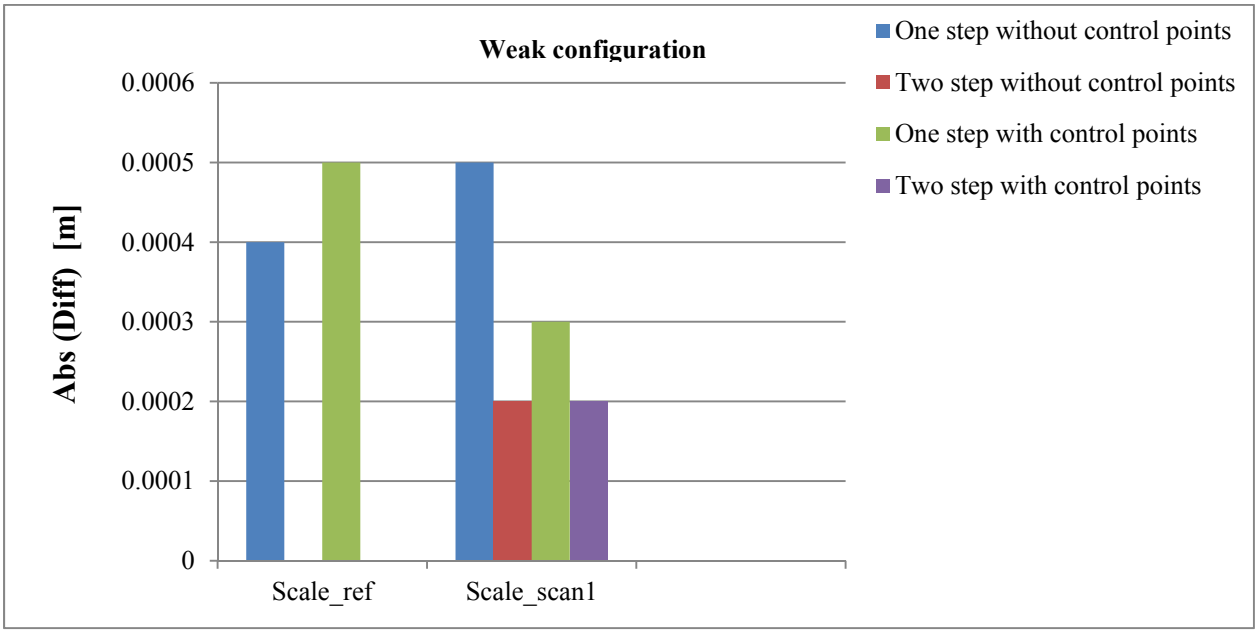

Figure 6.62. The difference between the estimated and true values of the scale of the mirror scanning angle β of the reference scanner and scanner 1 in experiment 3

The absolute values of differences between the estimated and true values of the unknown system parameters using the moderate configuration (as reported in Tables 5.C-8.C) are illustrated in figures 6.63-6.68.

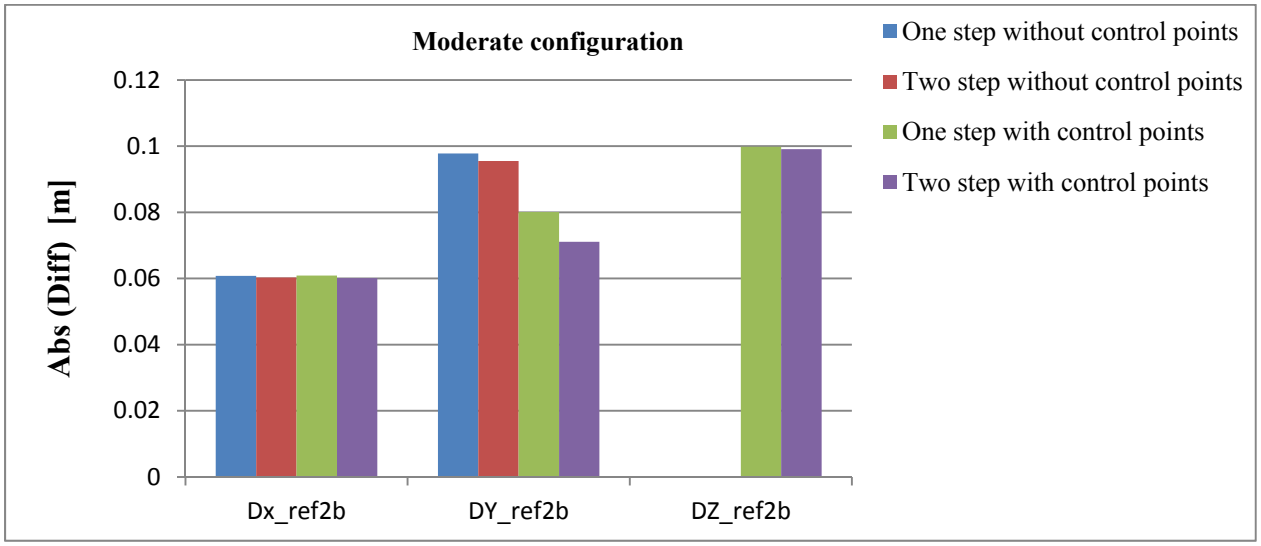

Figure 6.63. The difference between the estimated and true values of the lever arm offset relating the reference scanner and the IMU body frame in experiment 3

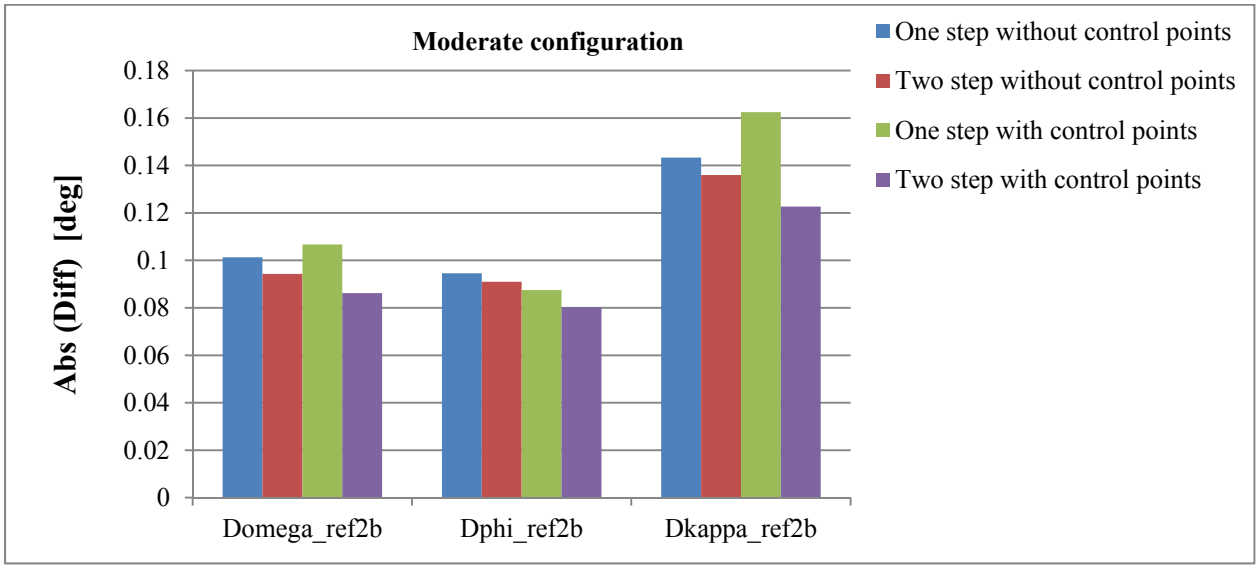

Figure 6.64. The difference between the estimated and true values of the rotation angles relating the reference scanner and the IMU body frame coordinate systems in experiment 3

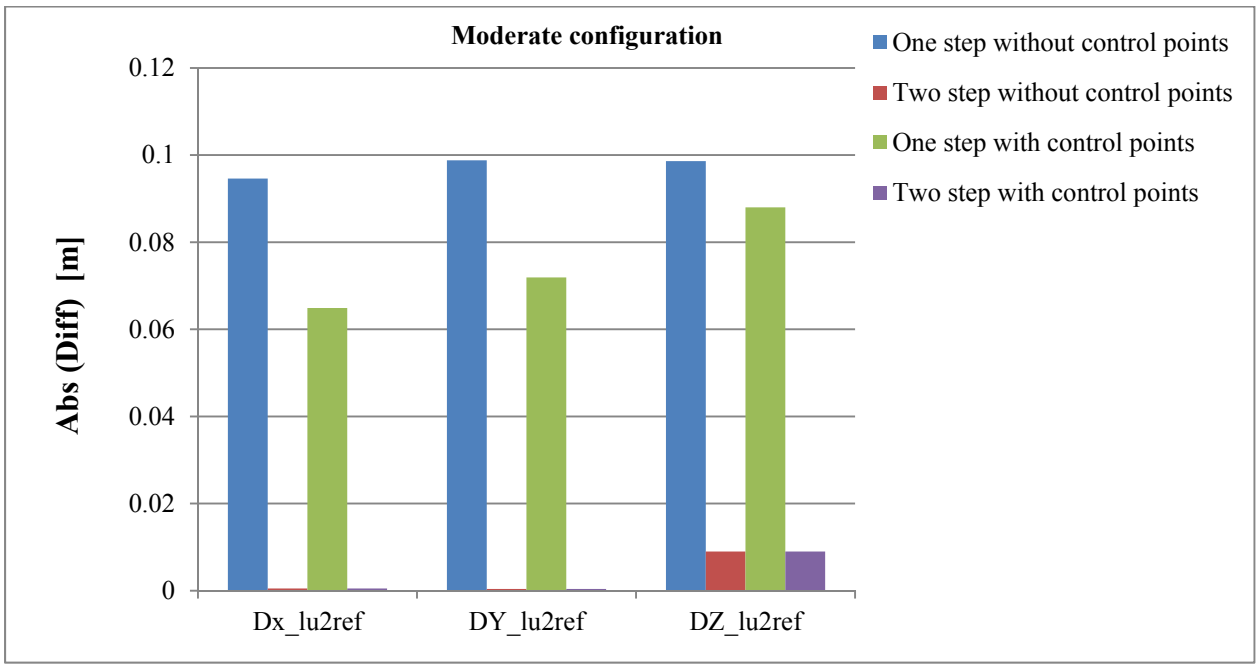

Figure 6.65. The difference between the estimated and true values of the lever arm offset relating scanner 1 and the reference scanner in experiment 3

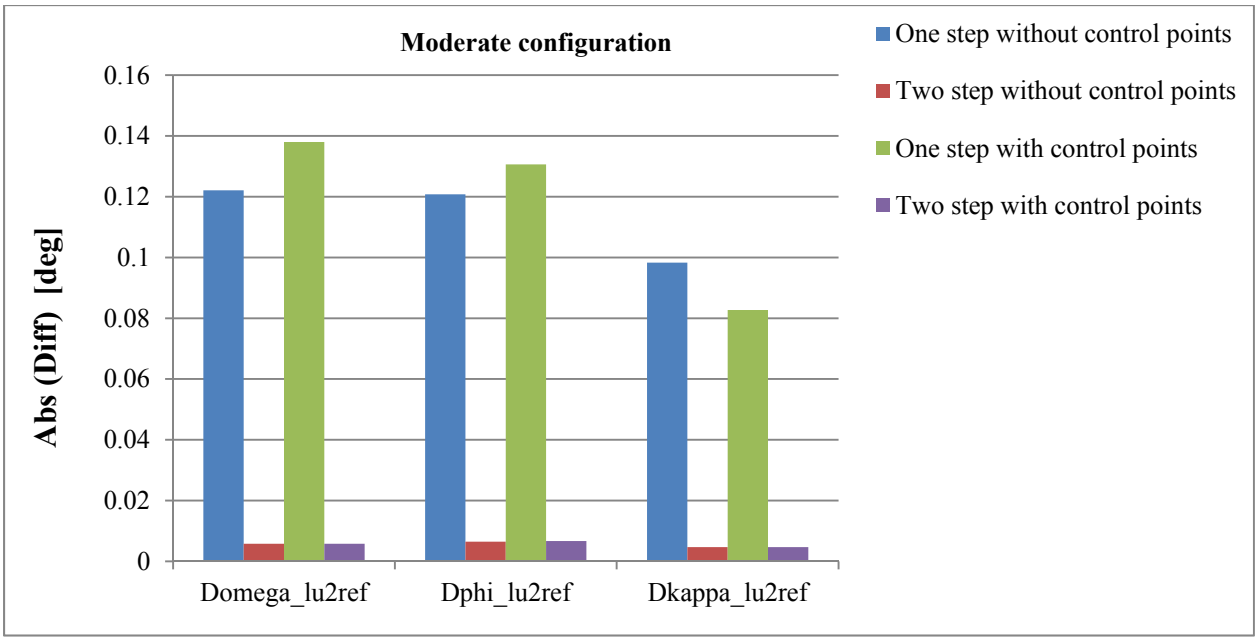

Figure 6.66. The difference between the estimated and true values of the rotation angles relating scanner 1 and the reference scanner coordinate systems in experiment 3

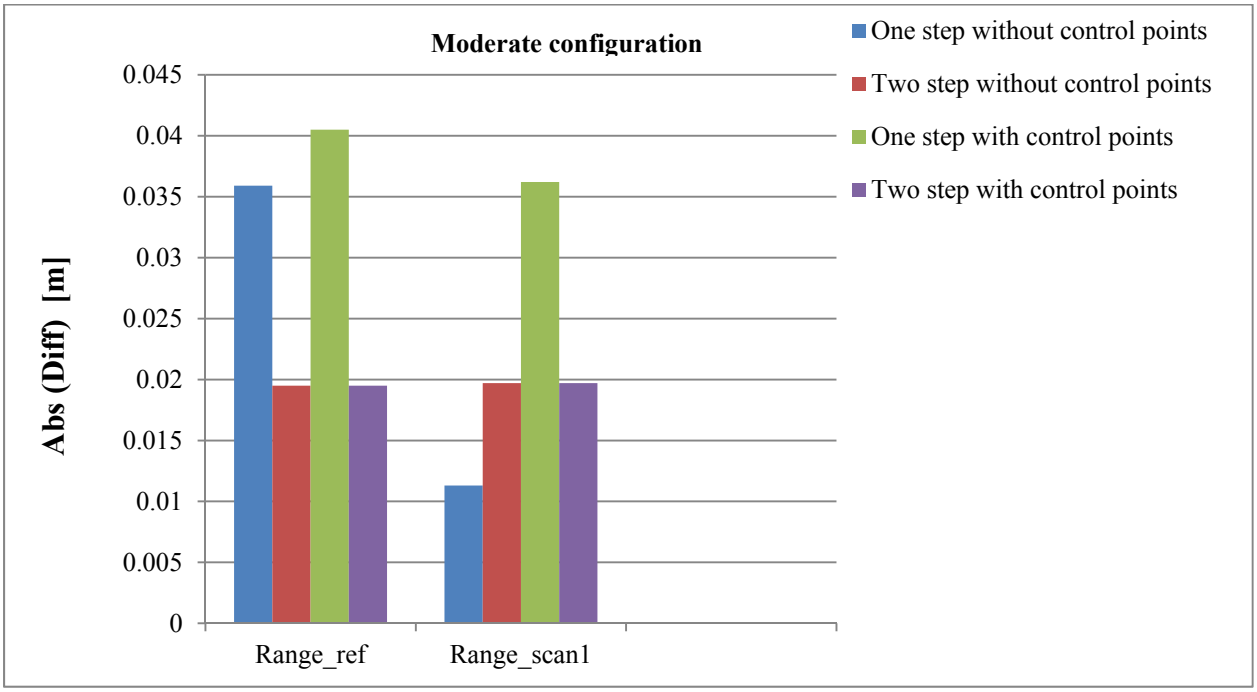

Figure 6.67. The difference between the estimated and true values of the range of the reference scanner and scanner 1 in experiment 3

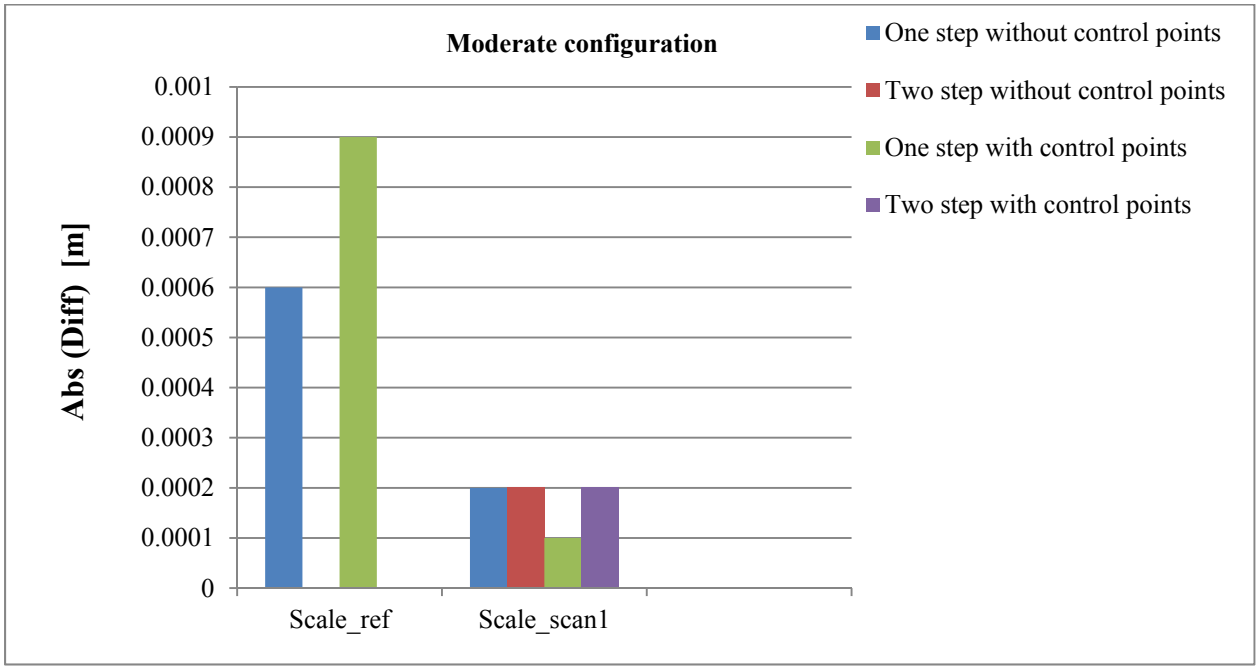

Figure 6.68. The difference between the estimated and true values of the scale of the mirror scanning angle β of the reference scanner and scanner 1 in experiment 3

The absolute values of differences between the estimated and true values of the unknown system parameters using the strong configuration (as reported in Tables 9.C- 12.C) are illustrated in figures 6.69-6.74.

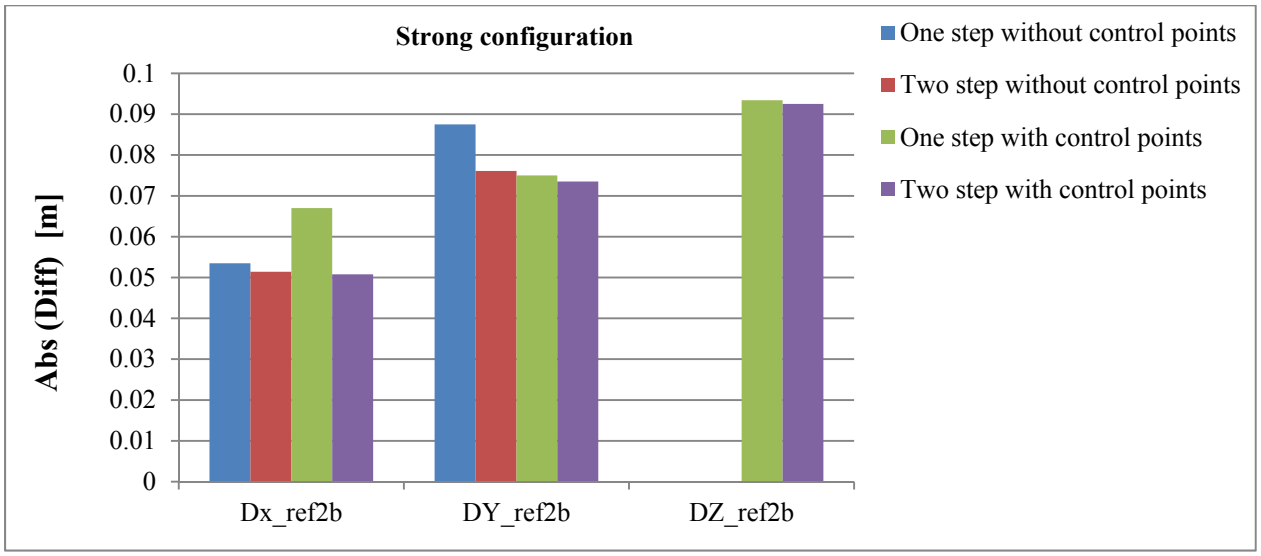

Figure 6.69. The difference between the estimated and true values of the lever arm offset relating the reference scanner and the IMU body frame in experiment 3

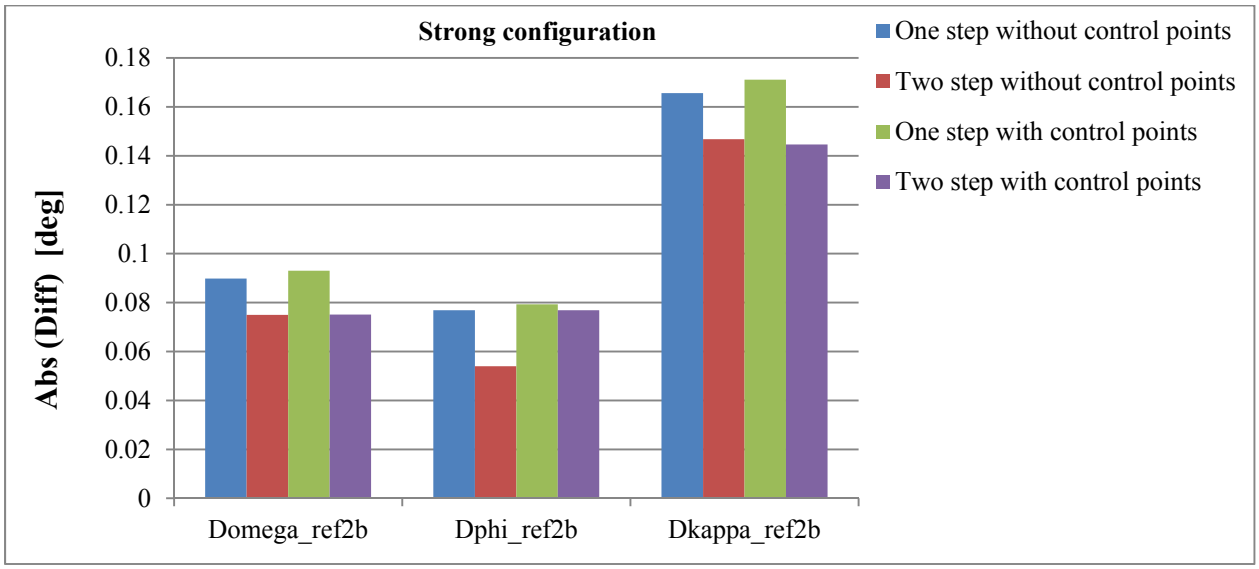

Figure 6.70. The difference between the estimated and true values of the rotation angles relating the reference scanner and the IMU body frame coordinate systems in experiment 3

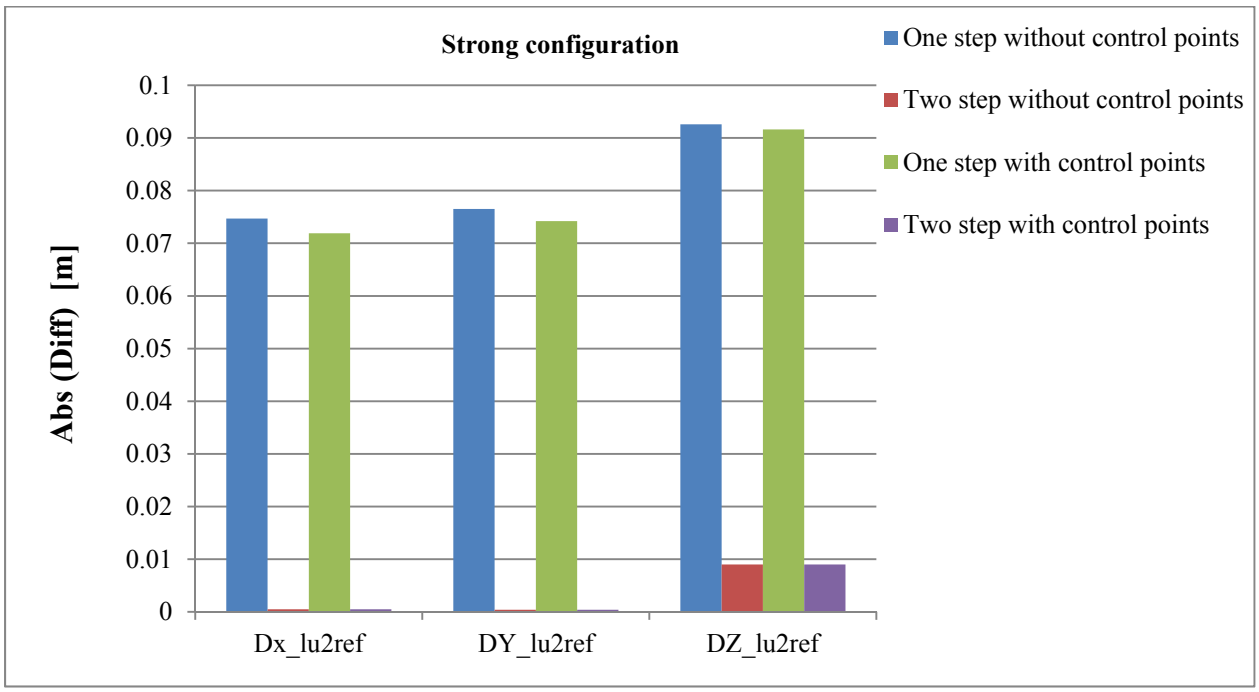

Figure 6.71. The difference between the estimated and true values of the lever arm offset relating scanner 1 and the reference scanner in experiment 3

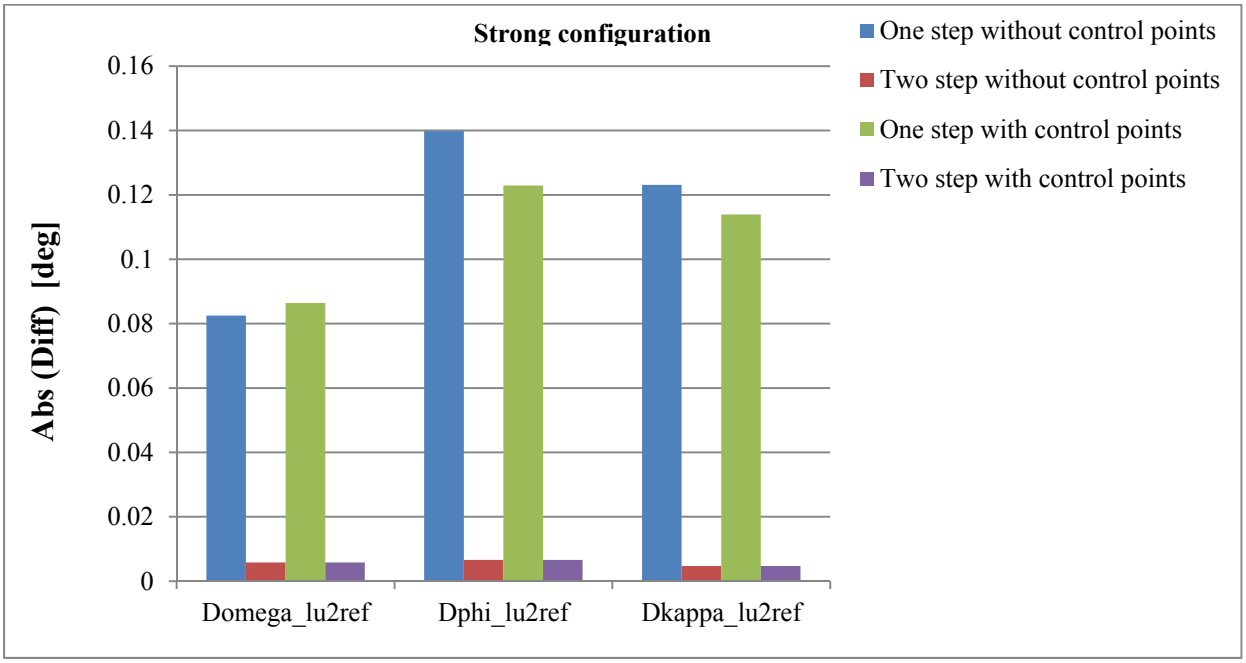

Figure 6.72. The difference between the estimated and true values of the rotation angles relating scanner 1 and the reference scanner coordinate systems in experiment 3

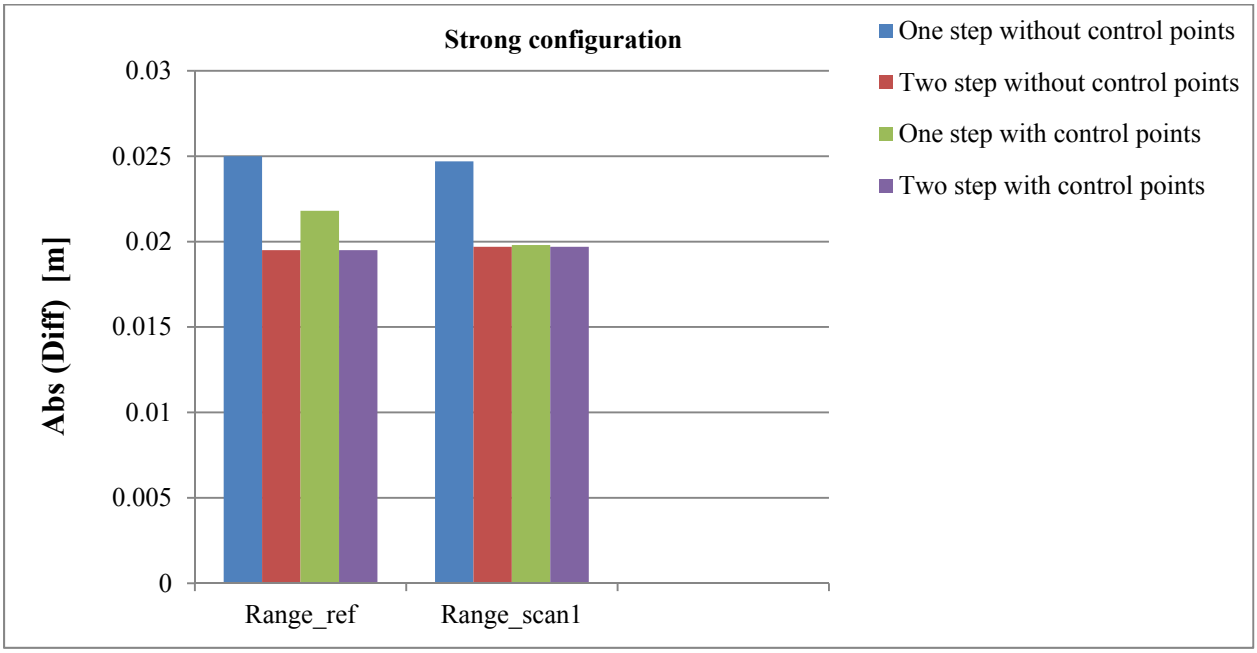

Figure 6.73. The difference between the estimated and true values of the range of the reference scanner and scanner 1 in experiment 3

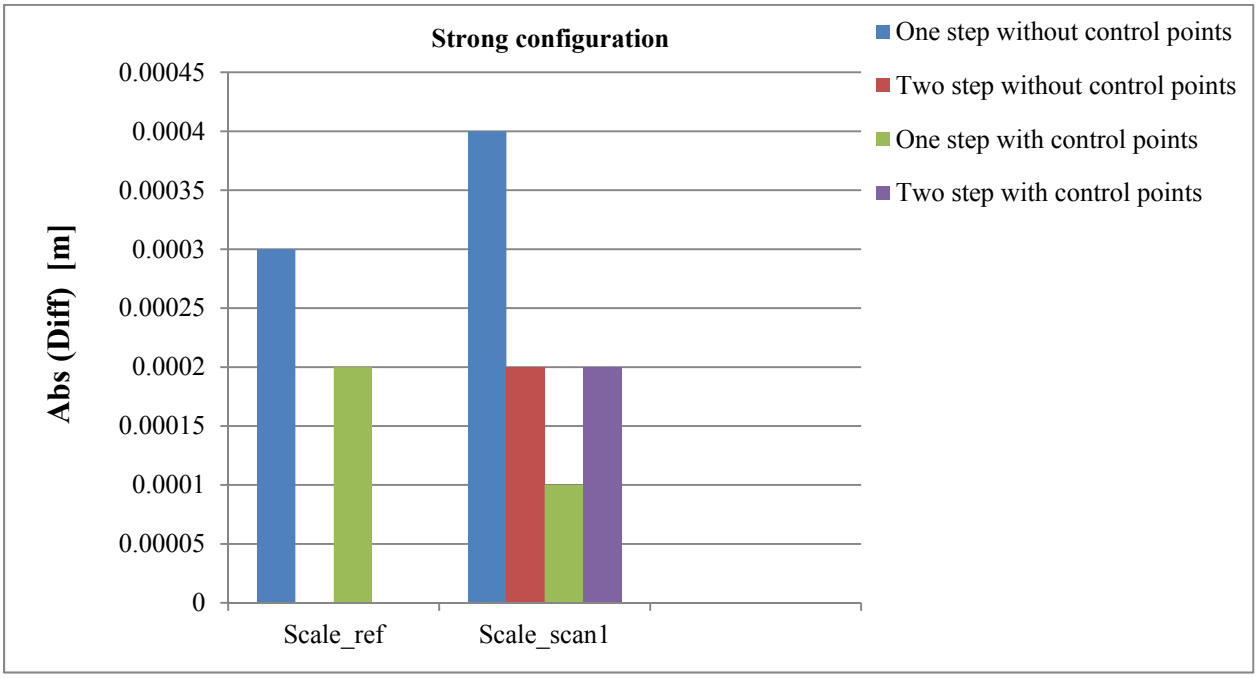

Figure 6.74. The difference between the estimated and true values of the scale of the mirror scanning angle β of the reference scanner and scanner 1 in experiment 3

From the performed experiments, one can note in scenarios I, II, V, VI, IX, and X, that the z-component of the lever arm offset "ΔZ_ref2b" relating the IMU body frame and the reference scanner is fixed. The ΔZ_ref2b cannot be estimated because there is no vertical discrepancy among the overlapping strip pairs, which are utilized in these experiments. Therefore, control points would be required for reliable estimation of the ΔZ_ref2b. Figure 6.75 shows the distribution of the control points used in scenarios III, IV, VII, VIII, XI, and XII.

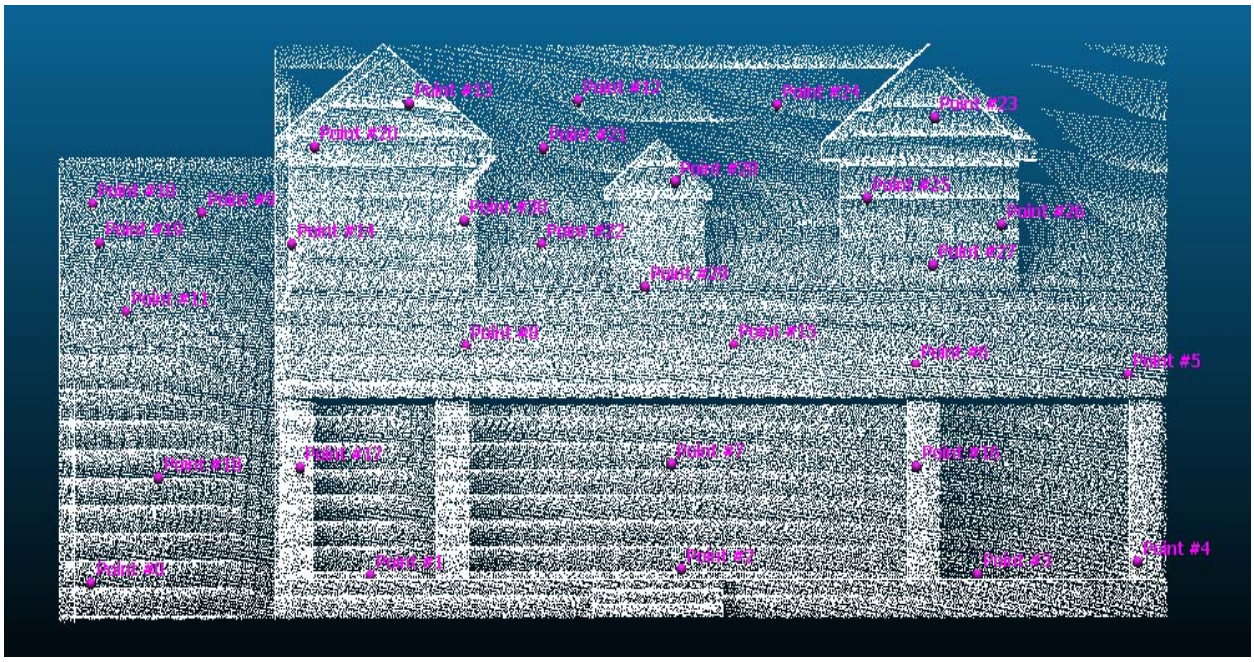

Figure 6.75. The distribution of the utilized ground control points (30 GCP) on the outdoor calibration site

From the performed experiments, the comparison the of differences between the estimated and true values of the unknown system parameters using the one-step and two-step calibration procedures are summarized in Tables 6.29-6.31

Table 6.29. The comparison of the differences between the true and estimated system parameters for experiment 1

Parameters	Improvement					
	Weak configuration		Moderate configuration		Strong configuration	
	Without control points	With control points	Without control points	With control points	Without control points	With control points
	One step/two step	One step/two step	One step/two step	One step/two step	One step/two step	One step/two step
The mounting parameters relating the reference scanner and the IMU body frame						
ΔX_ref2b [m]	0.0004/0.0003	0.0004 /0.0002	0.0004/0.0003	0.0003/0.0002	0.0002/0.0001	0.0001/0.0001
ΔY_ref2b [m]	0.0687/0.0588	0.0689/0.0582	0.0005/0.0004	0.0004/0.0003	0.0003/0.0002	0.0007/0.0005
ΔZ_ref2b [m]	Fixed	0.0781/0.0730	Fixed	0.0731/0.0703	Fixed	0.0750/0.0737
$\Delta\omega\_ref2b$ [deg]	0.0111/0.0101	0.0113/0.0063	0.0047/0.0032	0.0031/0.0010	0.0006/0.0003	0.0009/0.0002
$\Delta\varphi\_ref2b$ [deg]	0.0024/0.0022	0.0027/0.0021	0.0030/0.0010	0.0027/0.0016	0.0004/0.0002	0.0004/0.0001
$\Delta\kappa\_ref2b$ [deg]	0.0226/0.0097	0.0250/0.0097	0.0193/0.0147	0.0213/0.0147	0.0154/0.0138	0.0161/0.0136
The mounting parameters relating the scanner 1 and the reference scanner						
ΔX_lu2ref [m]	0.0055/0.0005	0.0056/0.0005	0.0007/0.0005	0.0007/0.0005	0.0006/0.0005	0.0005/0.0005
ΔY_lu2ref [m]	0.0676/0.0004	0.0678/0.0004	0.0008/0.0004	0.0008/0.0004	0.0006/0.0004	0.0007/0.0004
ΔZ_lu2ref [m]	0.0095/0.0090	0.0096/0.0090	0.0091/0.0089	0.0090/0.0089	0.0090/0.0088	0.0089/0.0088
$\Delta\omega\_lu2ref$ [deg]	0.0286/0.0057	0.0281/0.0057	0.0068/0.0054	0.0075/0.0054	0.0058/0.0055	0.0057/0.0054
$\Delta\varphi\_lu2ref$ [deg]	0.0075/0.0064	0.0069/0.0064	0.0071/0.0065	0.0069/0.0065	0.0070/0.0068	0.0073/0.0068
$\Delta\kappa\_lu2ref$ [deg]	0.0109/0.0047	0.0091/0.0047	0.0052/0.0047	0.0050/0.0047	0.0047/0.0047	0.0050/0.0047
Intrinsic parameters of reference scanner						
$\Delta\rho\_ref$ [m]	0.0242/0.0195	0.0306/0.0195	0.0212/0.0195	0.0249/0.0195	0.0196/0.0194	0.0224/0.0194
S_β_ref	0.0001/0.0000	0.0001/0.000	0.0001/0.0001	0.0001/0.0000	0.0001/0000	0.0001/0.0000
Intrinsic parameters of scanner 1						
$\Delta\rho\_lu_1$ [m]	0.0241/0.0197	0.0306/0.0197	0.0213/0.0197	0.0250/0.0197	0.0201/0.0198	0.0227/0.0198
$S_\beta\_lu_1$	0.0001/0.0001	0.0001/0.0001	0.0001/0.0001	0.0001/0.0001	0.0001/0.0001	0.0001/0.0001

Table 6.30. The comparison of the differences between the true and estimated system parameters or experiment 2

Parameters	Improvement					
	Weak configuration		Moderate configuration		Strong configuration	
	Without control points	With control points	Without control points	With control points	Without control points	With control points
	One step/two step	One step/two step	One step/two step	One step/two step	One step/two step	One step/two step
The mounting parameters relating the reference scanner and the IMU body frame						
ΔX_ref2b [m]	0.0549/0.0525	0.0531/0.0461	0.0375/0.0369	0.0380/0.0354	0.0289/0.0221	0.0387/0.0128
ΔY_ref2b [m]	0.0985/0.0928	0.0939/0.0919	0.0971/0.0878	0.0631/0.0606	0.0402/0.0310	0.0405/0.0329
ΔZ_ref2b [m]	Fixed	0.0680/0.0619	Fixed	0.0594/0.0554	Fixed	0.0527/0.0442
$\Delta\omega\_ref2b$ deg]	0.1040/0.1017	0.0853/0.0603	0.0968/0.0819	0.0866/0.0822	0.0682/0.0651	0.0870/0.0858
$\Delta\varphi\_ref2b$ [deg]	0.0949/0.0742	0.0912/0.0721	0.0923/0.0787	0.0826/0.0690	0.0530/0.0511	0.0840/0.0752
$\Delta\kappa\_ref2b$ [deg]	0.0977/0.0813	0.1016/0.0772	0.0855/0.0306	0.0121/0.0130	0.1340/0.0663	0.1367/0.0832
The mounting parameters relating the scanner 1 and the reference scanner						
ΔX_lu2ref [m]	0.0815/0.0005	0.0108/0.0005	0.0927/0.0005	0.0397/0.0005	0.0475/0.0005	0.0474/0.0005
ΔY_lu2ref [m]	0.1033/0.0004	0.1035/0.0004	0.0954/0.0004	0.0503/0.0004	0.0382/0.0004	0.0386/0.0004
ΔZ_lu2ref [m]	0.0991/0.009	0.0886/0.0090	0.0978/0.0090	0.0809/0.0090	0.0865/0.0090	0.0864/0.0090
$\Delta\omega\_lu2ref$ [deg]	0.0954/0.0058	0.0185/0.0058	0.1001/0.0058	0.1246/0.0058	0.0572/0.0058	0.0568/0.0058
$\Delta\varphi\_lu2ref$ deg]	0.1010/0.0067	0.1455/0.0067	0.1039/0.0066	0.1321/0.0066	0.1245/0.0068	0.1244/0.0068
$\Delta\kappa\_lu2ref$ [deg]	0.0849/0.0047	0.0519/0.0047	0.0960/0.0047	0.0784/0.0047	0.1144/0.0047	0.1141/0.0047
Intrinsic parameters of reference scanner						
$\Delta\rho\_ref$ [m]	0.0486/0.0195	0.0471/0.0195	0.0365/0.0195	0.0292/0.0195	0.0232/0.0195	0.0235/0.0195
S_β_ref	0.0002/0.0000	0.0002/0.0000	0.0003/0000	0.0002/0.0000	0.0007/0000	0.0007/0.0000
Intrinsic parameters of scanner 1						
$\Delta\rho\_lu_1$ [m]	0.0479/0.0197	0.0418/0.0197	0.0307/0.0197	0.0284/0.0197	0.0225/0.0197	0.0221/0.0197
$S_\beta\_lu_1$	0.0002/0.0002	0.0002/0.0002	0.0001/0.0001	0.0001/0.0002	0.0003/0.0001	0.0003/0.0002

Table 6.31. The comparison of the differences between the true and estimated system parameters for experiment 3

Parameters	Improvement					
	Weak configuration		Moderate configuration		Strong configuration	
	Without control points	With control points	Without control points	With control points	Without control points	With control points
	One step/two step	One step/two step	One step/two step	One step/two step	One step/two step	One step/two step
The mounting parameters relating the reference scanner and the IMU body frame						
ΔX_ref2b [m]	0.0612/0.0605	0.0614/0.0609	0.0608/0.0603	0.0609/0.0601	0.0535/0.0514	0.0670/0.0508
ΔY_ref2b [m]	0.0995/0.0948	0.0931/0.0929	0.0978/0.0955	0.0801/0.0711	0.0875/0.0761	0.0750/0.0735
ΔZ_ref2b [m]	Fixed	0.0741/0.0691	Fixed	0.0998/0.0991	Fixed	0.0934/0.0925
$\Delta\omega\_ref2b$ [deg]	0.1850/0.1468	0.0894/0.0880	0.1013/0.0943	0.1067/0.0862	0.0898/0.0750	0.0930/0.0751
$\Delta\varphi\_ref2b$ [deg]	0.1650/0.1092	0.0963/0.0914	0.0946/0.0910	0.0875/0.0802	0.0769/0.0540	0.0793/0.0769
$\Delta\kappa\_ref2b$ [deg]	0.0994/0.0915	0.1051/0.0914	0.1433/0.1360	0.1625/0.1227	0.1656/0.1468	0.1711/0.1446
The mounting parameters relating the scanner 1 and the reference scanner						
ΔX_lu2ref [m]	0.0916/0.0005	0.0642/0.0005	0.0946/0.0005	0.0649/0.0005	0.0747/0.0005	0.0719/0.0005
ΔY_lu2ref [m]	0.1325/0.0004	0.0847/0.0004	0.0988/0.0004	0.0719/0.0004	0.0765/0.0004	0.0742/0.0004
ΔZ_lu2ref [m]	0.0997/0.0090	0.0902/0.0090	0.0986/0.0090	0.0880/0.0090	0.0926/0.0090	0.0916/0.0090
$\Delta\omega\_lu2ref$ [deg]	0.0986/0.0058	0.0167/0.0058	0.1221/0.0058	0.1380/0.0058	0.0825/0.0058	0.0864/0.0058
$\Delta\varphi\_lu2ref$ [deg]	0.1520/0.0066	0.1512/0.0065	0.1208/0.0065	0.1306/0.0067	0.1398/0.0066	0.1229/0.0066
$\Delta\kappa\_lu2ref$ [deg]	0.0851/0.0047	0.0448/0.0047	0.0983/0.0047	0.0827/0.0047	0.1231/0.0047	0.1139/0.0047
Intrinsic parameters of reference scanner						
$\Delta\rho\_ref$ [m]	0.0422/0.0195	0.0269/0.0195	0.0359/0.0195	0.0405/0.0195	0.0250/0.0195	0.0218/0.0195
S_β_ref	0.0004/0.0000	0.0005/0.0000	0.0006/0.0000	0.0009/0.0000	0.0003/0.0000	0.0002/0.0000
Intrinsic parameters of scanner 1						
$\Delta\rho\_lu_1$ [m]	0.0416/0.0197	0.0226/0.0197	0.0113/0.0197	0.0362/0.0197	0.0247/0.0197	0.0198/0.0197
$S_\beta\_lu_1$	0.0005/0.0002	0.0003/0.0002	0.0002/0.0002	0.0001/0.0002	0.0004/0.0002	0.0001/0.0002

The findings from the performed experiments can be summarized as follows:

- Strong-configuration allows for better/closer estimation of the unknown system parameters (refer to the yellow highlighted cells in Table 6.29 in comparison with the cyan highlighted cells in Table 6.29),
- Two-step approach provides parameters that are closer to the true values of the unknown system parameters (refer to the green highlighted values in Table 6.29),
- The performance of the two-step approach is not as sensitive to the strength of the scanning configuration as the one-step approach (refer to the olive highlighted values in Table 6.30),
- Deterioration in the quality of the navigation data affects the quality of the estimated parameters (refer to the cyan highlighted cells in Table 6.29 in comparison with the grey highlighted cells in Table 6.31),
- Two-step approach is more robust than the one-step approach to deterioration in the quality of the navigation data (refer to the cyan highlighted values in Table 6.29 in comparison with the grey highlighted values in Table 6.31),
- For the one-step procedure, the weak configuration is more susceptible to deterioration in the quality of the navigation data (refer to the cyan highlighted cells in Table 6.29 in comparison with the grey highlighted cells in Table 6.31),
- Adding control points reduces the susceptibility to the deterioration in the quality of the navigation data (refer to the red highlighted values in Tables 6.29-6.31), and
- For the two-step procedure, the impact of adding control points is not significant as the impact on the results from the one-step procedures (refer to the orange highlighted values in Tables 6.29-6.31).

The qualitative analysis is performed by visual inspection of profiles generated before the two calibration procedure using the initial values for the unknown system parameters and after the one-step and two-step calibration procedures using the estimated values for the system parameters results in experiment "1" following the weak configuration (scenarios I and II). The objective of the visual inspection is to check any improvements in the quality of fit between overlapping strips (an illustration of one profile is shown in Figure 6.76). Through visual inspection of the profiles in Figure 6.76, slight improvement in the compatibility of the reconstructed point cloud using scenario I (after one-step approach) can be observed. While significant improvement in the compatibility of the reconstructed point cloud using scenario II (after two-step approach) can be noticed.

To quantitatively evaluate the performance of the proposed one-step and two-step calibration procedures, the discrepancies (i.e., three shifts (X_T,Y_T,Z_T) and three rotations (ω, φ, κ)) between conjugate surface elements in overlapping strips are calculated before the two calibration procedure using the initial values for the unknown parameters and after reconstructing the LiDAR point cloud using the estimated system parameters from experiment "1" using scenarios I, II, III and IV. Table 6.32 reports the estimated discrepancies before and after applying the one-step calibration procedure. From Table 6.32, one can observe large discrepancies among the overlapping strip pairs before the one-step calibration procedure (large shift in the X-axis, and Y-axis). A slight improvement after the one-step calibration procedure is noticeable (refer to the green highlighted values in Table 6.32). One can also note that there is a slight improvement in the compatibility of the overlapping strip pairs when adding the control information (refer to the yellow highlighted values in Table 6.32). Table 6.32 reports the estimated discrepancies before and after applying the two-step calibration procedure. A significant improvement after the two-

step calibration procedure is noticeable (refer to the grey highlighted values in Table 6.33). One can also note that there is almost no improvement in the compatibility of the overlapping strip pairs when adding the control information (refer to the violet highlighted values in Table 6.33).

Table 6.32. Discrepancies (i.e., three shifts and three rotations) between overlapping strips before and after the one-step calibration procedure

Before Calibration			**Proposed Calibration Overlapping Strips only (scenario I)**			**Proposed Calibration Overlapping Strips + Control points (scenario III)**		
X_T(m)	Y_T(m)	Z_T(m)	X_T(m)	Y_T(m)	Z_T(m)	X_T(m)	Y_T(m)	Z_T(m)
0.2027	-0.1991	-0.0349	0.1585	-0.1482	-0.0287	-0.1226	0.1117	-0.0275
ω(°)	φ(°)	κ(°)	ω(°)	φ(°)	κ(°)	ω(°)	φ(°)	κ(°)
0.1284	-0.0541	-0.0457	0.0981	0.0436	-0.0386	0.0966	0.0389	-0.0369

Table 6.33. Discrepancies (i.e., three shifts and three rotations) between overlapping strips before and after the two-step calibration procedure

Before Calibration			**Proposed Calibration Overlapping Strips only (scenario II)**			**Proposed Calibration Overlapping Strips + Control points (scenario IV)**		
X_T(m)	Y_T(m)	Z_T(m)	X_T(m)	Y_T(m)	Z_T(m)	X_T(m)	Y_T(m)	Z_T(m)
0.2027	-0.1991	-0.0349	0.0525	-0.0562	-0.0220	-0.0528	0.0565	-0.0218
ω(°)	φ(°)	κ(°)	ω(°)	φ(°)	κ(°)	ω(°)	φ(°)	κ(°)
0.1284	-0.0541	-0.0457	0.0821	0.0339	-0.0267	0.0836	0.0349	-0.0269

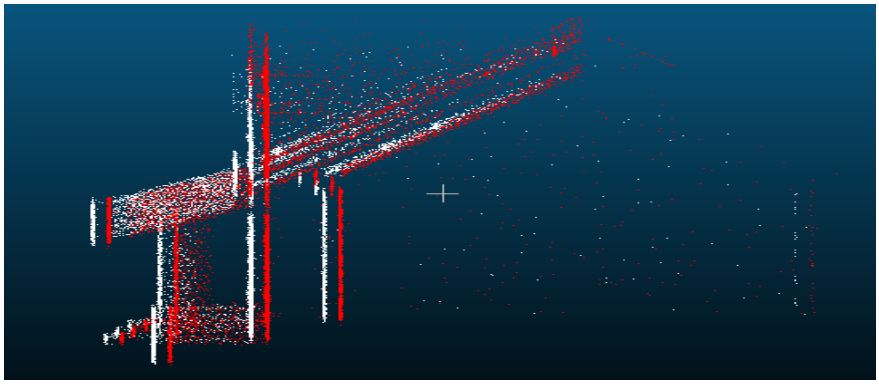

(a)

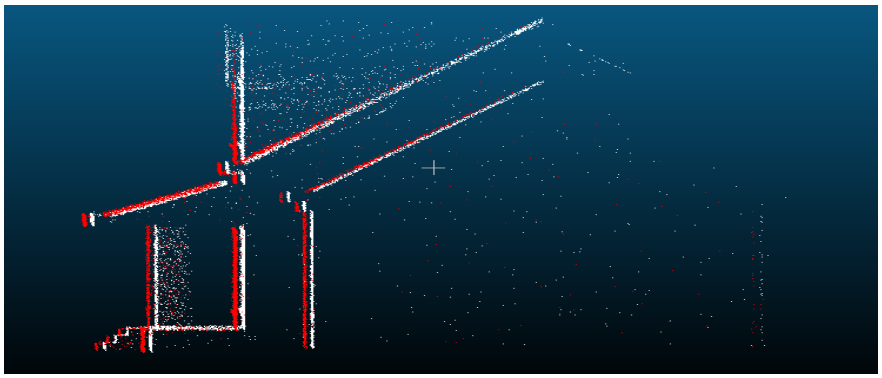

(b)

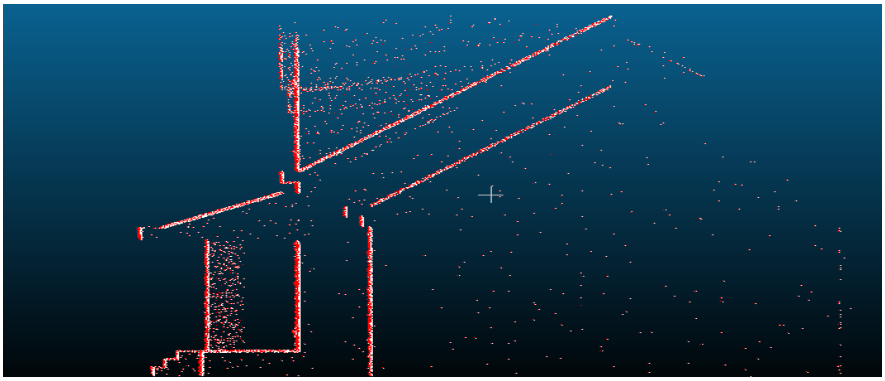

(c)

Figure 6.76. Profiles of the simulated surface before the two calibration procedures (a), after the one-step calibration procedure of scenario I (b), and after the two-step calibration procedure of scenario II (c)

Form the performed experiments in this section one can conclude that the two-step procedure is advantageous for the following reasons:

- More robust to the strength of the scanning configuration.
- More robust to the quality of the navigation data.
- More robust to the impact of having fewer/no ground control points.

Chapter Seven: **Conclusions and Recommendations for Future Work**

7.1 Conclusions

In the past few years, airborne laser scanning (ALS), static terrestrial laser scanning (TLS) and terrestrial mobile mapping (TMLS) systems have been developed as a leading technology for the acquisition of high density 3D spatial data. The ability of the laser scanning system to determine 3D points on the ground is the result of multiple components integrated to work together. For example, (i) the Global Positioning System (GPS) is used to provide the position of the sensor during the mission, (ii) an Inertial Navigation System (INS) is used to provide the sensor attitude, commonly referred to as roll, pitch, and heading, and (iii) the laser scanner records the scan angle relative to the sensor platform in addition to estimating the distance from the sensor to the ground point by measuring the time delay between a laser pulse transmission and its detection. The above information allows for the determination of the location of the points along the mapped surface. To ensure the geometric quality of the collected point cloud, ALS and TMLS systems should undergo a rigorous calibration procedure. The system calibration is a very crucial task to ensure the achievement of the expected accuracy. However, it is also the most complex task. Laser scanning system calibration includes individual sensor calibration (i.e., laser ranging and scanning unit) and mounting parameters calibration (i.e., lever arm offset and boresight angles) relating the system components such as the GPS, INS, and laser scanner. The system calibration requires the identification of common elements or primitives in overlapping LiDAR strips as well as control data.

In the last few years, extensive research efforts were carried out to develop approaches for the elimination of the impact of the systematic errors in the ALS system parameters on the derived

point cloud. The necessary flight and control configuration requirements have been discussed by few authors to perform the calibration of ALS systems. While the calibration of TMLS is introduced in few research work. The main contributions of this research can be summarized in the following sections.

7.1.1 Automatic Selection of Suitable Overlapping Strip Pairs/Regions

The current LiDAR system calibration procedure includes manual selection of overlapping strip pairs/regions among the overlapping LiDAR strips. Some problems could arise when using these manually-selected pairs/regions. In this research, a new methodology for automatic selection of appropriate overlapping strip pairs/regions is proposed. The main criteria for the selection of overlapping strip pairs/regions can be summarized as follows:

- Automatic selection of appropriate overlapping strip pairs, which should achieve the minimum optimal flight configuration that maximizes the impact of the discrepancies among conjugate surface elements in overlapping strips,
- Automatic selection of clustered regions within the suitable overlapping strip pairs. The main criteria for the selection of these clustered regions are as follows:
  - The candidate regions should have good variation in the topography (i.e., surfaces with varying slope and aspect values),
  - The candidate regions should be well-distributed within the overlapping area, and
  - The candidate regions should have a balance between their sizes.

The experimental results using real dataset are performed. The experimental results have shown that the quality of the estimated parameters using the automatic selection is quite similar to the estimated parameters using the manual selection while the processing time of automatic selection is 2 times faster than the manual selection.

The contributions of the proposed method can be summarized as follows:

- The proposed method is fully automated and does not depend on the operator, while the manual selection of overlapping pairs/regions relies on the experience of the operator, and
- Appropriate overlapping strip pairs which should achieve the minimum optimum flight configuration are automatically selected. Also, regions which represent suitable LiDAR surfaces (regions with varying slope, aspect, and distribution among the overlapping strips) to be used in the calibration procedure are automatically selected.

7.1.2 Calibration Technique of Airborne Multi-Laser Scanning System

Recently, in surveying and mapping applications, the development of airborne LiDAR systems is featured by the use of multiple laser scanners to carry out accurate and efficient method of capturing dense 3D data along ground and above ground features. In this research, new calibration procedure for dealing with airborne multi-laser scanning systems is introduced. The aim of the proposed calibration method is to estimate the system parameters (the mounting parameters relating the individual scanners to the IMU body frame and the intrinsic parameters of each laser scanner). The experiments are performed using the assumption that the real dataset are captured by 2 scanners involved the LiDAR system. The experimental results have shown

that accurate estimation of the calibration parameters of each laser scanner can be obtained using the proposed method. The contributions of the proposed method can be summarized as follows:

- The proposed method is fully automated and reliable for calibrating airborne LiDAR system characterized by the use of multiple laser scanners, and
- The proposed approach can be used to test the stability analysis of a single scanner data acquisition system and verify the quality of the navigation data within the data collection mission.

7.1.3 Indoor and Outdoor Calibration Technique of Terrestrial Mobile Multi-Laser Scanning Systems

Terrestrial Mobile laser scanning (TMLS) is the most recent LiDAR-based technology for fast and cost-effective acquisition of 3D spatial data. To reliably estimate the intrinsic and mounting parameters associated with TMLS systems, one needs to have good quality information regarding the position and orientation of the navigation frame. Such quality can be ensured by conducting the data collection for the calibration process in an open-sky environment where one has good accessibility to the GPS satellite constellation. However, such requirement will have a negative impact on the geometric distribution of the calibration features (in other words, one will not have access to calibrating surfaces with different slope and aspect values). This research presents an innovative method for circumventing such problem. The idea of the proposed calibration methodology is that the mounting parameters relating the different scanners to the reference frame of the navigation unit will be divided into two groups as follows (i) the mounting parameters relating the individual scanners to a reference scanner, and (ii) the mounting parameters relating the reference scanner to the reference frame of the navigation unit. The

advantage of this approach is that the first group of parameters can be determined through an indoor calibration test field, where one can have access to a favorable distribution of the calibration targets (e.g., good distribution of planar features with different slope and aspect values). The second group can be determined in an open-sky environment (outdoor calibration) to ensure reliable derivation of the position and orientation of the navigation frame while having an unfavorable distribution of the calibration targets. The proposed mathematical model of the indoor and outdoor calibration is introduced. In this research work, data simulation program is developed for generating 3D LiDAR data such as a Velodyne-based Mobile laser scanning system (HDL-32E). The experimental results are performed using a simulated dataset for investigating the indoor and outdoor LiDAR system calibration algorithms (two-step calibration process). As well, the experimental results are carried out for estimating the intrinsic parameters of each laser scanner and the mounting parameters relating the individual scanners to the reference scanner as well as estimating the mounting parameters relating the reference scanner to the reference frame of the navigation unit (IMU body frame) in a one-step calibration process. The experimental results have shown that the estimated parameters using the two-step calibration procedure are better than the estimated parameters derived from the one-step calibration procedure. The contributions of the proposed two-step calibration approach can be summarized as follows:

- The proposed two-step calibration approach is more robust than the one-step calibration approach to the strength of the scanning configuration,
- The proposed two-step calibration approach is more robust than the one-step calibration approach to the quality of the navigation data, and

- The proposed two-step calibration approach is more robust than the one-step calibration approach to the impact of having fewer/no ground control points.

7.2 Recommendations for Future Work

Recommendations/suggestions for future work related to the calibration of ALS and TMLS systems are as follows:

1. Test with real dataset captured from different sensors the proposed calibration procedure of airborne multi-laser scanning.

2. Further analysis of the multi-sensor airborne system calibration for studying the stability of the sensor parameters within the flight mission and/or using this approach to verify the quality of the navigation data within the mission.

3. Investigate the optimum flight and control configuration for airborne multi-laser scanning systems.

4. Test with real dataset the proposed methodology based on a two-step procedure for the calibration of terrestrial mobile multi-laser scanning systems.

5. For TMLS, the investigated intrinsic parameters included only range bias and mirror angle scale. Other systematic errors should be investigated.

6. Investigate the utilization of photogrammetric data in the calibration of airborne and terrestrial laser scanning systems and vice versa.

7. Study short and long term stability of ALS and TLMS systems as well as develop quantitative measures to describe the system stability.

8. Study the impact of the quality of the system calibration procedure on the quality of the derived products from laser scanning data processing (e.g., Digital terrain model (DTM), feature extraction, and object interpretation.

9. Develop standards and guide lines “best practices” for system calibration and stability analysis.

10. Investigate the possibility of integrating airborne and terrestrial laser scanning data for system calibration. This would include the utilized procedures for establishing the correspondences among the features in those scans as well as using such features for establishing the calibration similarity measure.

References

Ackermann, F., 1999. Airborne laser scanning - present status and future expectations, ISPRS Journal of Photogrammetry and Remote Sensing, Vol. 54, No. 2-3, pp. 64-67.

Atanacio-Jiménez, Gerardo, et al. "Lidar velodyne hdl-64e calibration using pattern planes." International Journal of Advanced Robotic Systems 8.5 (2011): 70-82.

Baltsavias, E.P., 1999a. Airborne laser scanning - basic relations and formulas, ISPRS Journal of Photogrammetry and Remote Sensing, Vol. 54, No. 2-3, pp. 199-214.

Bang, K., 2010. Alternative Methodologies for LiDAR System Calibration, Ph.D. dissertation, Department of Geomatics Engineering, University of Calgary, Canada, 160 p.

Bang, K.I., Habib, A.F., Kersting, A., 2010. Estimation of Biases in LiDAR System Calibration Parameters Using Overlapping Strips, The Canadian Journal of Remote Sensing, (accepted 2010).

Bossler, J. D., 2010. Manual of Geospatial Science and Technology, CRC Press, Boca Raton, US, pp. 440–463.

Bretar, F., A. Chauve, C. Mallet, and B. Jutzi, 2008. Managing full waveform Lidar data: A challenging task for the forthcoming years, The International Archives of the Photogrammetry, Remote Sensing and Spatial Information Sciences, 37(Part B1):415420.

Burman, H., 2000. Calibration and Orientation of Airborne Image and Laser Scanner Data Using GPS and INS, Ph.D. dissertation, Royal Institute of Technology, Stockholm, 125 p.

Chan, T. O., “Feature-based Boresight Self-Calibration of a Mobile Mapping System,” M.S. thesis, Dept. Geomatics Eng., Calgary, AB, p. 26, University of Calgary (2011).

Chow, J., A. Ebeling, and W. Teskey (2010). Low cost artificial planar target measurement techniques for terrestrial laser scanning. In FIG Congress 2010: Facing the Challenges - Building the Capacity, Sydney, Australia.

Clode, S., Kootsookos, P., and Rottensteiner, F., 2004. The automatic extraction of roads from LiDAR data, International Archives of Photogrammetry, Remote Sensing and Spatial Information Sciences, 35 (Part B3), pp. 231–236.

Crombaghs, M., E. De Min, and R. Bruegelmann, 2000. On the Adjustment of Overlapping Strips of Laser Altimeter Height Data, International Archives of Photogrammetry and Remote Sensing, 3(B3/1):230–237.

Csanyi, N., 2008. A Rigorous Approach to Comprehensive Performance Analysis of State-of-the-Art Airborne Mobile Mapping Systems, Ph.D. dissertation, The Ohio State University, 217 p.

El-Sheimy, N., Valeo, C., and Habib, A.F., 2005. Digital Terrain Modelling: Acquisition, Manipulation And Applications (1st Edition), Artech House, Norwood, US, 257p.

Eric Haines, "Point in Polygon Strategies" in Graphics Gems IV (1994).

Faro, 2007. www.faro.com. Homepage of the company FARO Technologies, Inc., accessed: June 2007.

Filin, S. and Csatho, B., "An Efficient algorithm for the Synthesis of Laser Altimetry Waveforms," BPRC Technical Report No. 2000-02, The Ohio State University, Columbus, OH, p.27 (2000).

Filin, S., 2001. Calibration of Space borne and Airborne Laser Altimeters Using Natural Surfaces, Ph.D. dissertation, Department of Civil and Environmental Engineering and Geodetic Science, the Ohio-State University, Columbus, OH, 129 p.

Filin S., and G. Vosselman, 2004. Adjustment of airborne laser altimetry strips, International Archives of Photogrammetry and Remote Sensing, 35(Part B3):285–289.

Filin, S., 2003a. Recovery of systematic biases in laser altimetry data using natural surfaces. Photogrammetric Engineering & Remote Sensing, 69(11), 1235–1242.

Filin, S., 2003b. Analysis and implementation of a laser strip adjustment model. International Archives of Photogrammetry and Remote Sensing, 34(3-W13), 65–70.

Friess, P., 2006. Toward a rigorous methodology for airborne laser mapping, Proceedings of EuroCOW, Castelldefels, Spain, unpaginated CD-ROM.

Fugro EarthData, Inc., LiDAR mapping fact sheet, white paper published in the company web-site, web-site, http://www.fugroearthdata.com/pdfs/FCT_Lidar-Educational_11-07.pdf (accessed Sep 2010).

Glennie, C. and D. D. Lichti (2010). Static calibration and analysis of the Velodyne HDL-64E S2 scanner for high accuracy mobile scanning. Remote Sensing 2 (6), 1610 - 1624.

Glennie, C. and D. D. Lichti (2011). Temporal stability of the Velodyne HDL-64E S2 scanner for high accuracy scanning applications. Remote Sensing 3 (3), 539 - 553.

Haala, N., Brenner, C., "Extraction of buildings and trees in urban environments," ISPRS Journal of Photogrammetry and Remote Sensing, Vol. 54, pp. 130-137 (1999).

Habib, A. F., Bang, K.I., Shin, S.W., and Mitishita, E., 2007. LiDAR system self-calibration using planar patches from photogrammetric data, The 5th International Symposium on Mobile Mapping Technology, [CD-ROM]. 28-31 May, Padua, Italy.

Habib, A., K. Bang, A. P. Kersting, and D. C. Lee, 2009. Error budget of LiDAR Systems and Quality Control of the Derived Data, Photogrammetric Engineering and Remote Sensing, 75(9):1093–1108.

Habib, A., A. P. Kersting, K. Bang, and D. C. Lee, 2010a. Alternative methodologies for the internal quality control of parallel LiDAR strips, IEEE Transactions on Geoscience and Remote Sensing, 48(1): 221–236.

Habib A., K. Bang, A. P. Kersting, and J. Chow, 2010b. Alternative Methodologies for LiDAR System Calibration, Remote Sensing, 2(3): 874–907.

Habib, A., Bang, K. I., and Kersting, A. P., 2010a. Lidar System Calibration: Impact on Plane Segmentation and photogrammetric Data Registration, ASPRS 2010 Annual Conference, San Diego, California, April 26 – May 30, 2010.

Habib, A. F., 2012. Advanced topic in photogrammetry (ENGO 667), Course Note of Department of Geomatics Eng., University of Calgary, Canada.

Harding, D. J., 2004. TerraPoint LiDAR mapping instrumentation and methodology, Documentation prepared by TerraPoint, LLC. 16 November. http:// denali.gsfc.nasa.gov/lidar/terrapoint/TerraPoint_System_Description. (accessed October 2009).

Huising, E. J., and L. M. G. Pereira, 1998. Errors and Accuracy Estimates of Laser Data Acquired by various Laser Scanning Systems for Topographic Applications, ISPRS Journal of Photogrammetry and Remote Sensing, 53(5): 245–261.

Kager, H., 2004. Discrepancies Between Overlapping Laser Scanning Strips-Simultaneous Fitting of Aerial Laser Scanner Strips, Proceedings of the International Society for Photogrammetry and Remote Sensing XXth Congress, Istanbul, 34(B/1):555–560.

Kager, H. and K. Kraus, 2001. Height Discrepancies between Overlapping Laser Scanner Strips, Optical 3-D Measurement Techniques V (A. Grün and H. Kahmen, editors), Vienna, Austria, pp.103–110.

Kersting, A. P., Habib, A., Bang, K. I., and Skaloud, J. Automated approach for rigorous light detection and ranging system calibration without preprocessing and strict terrain coverage requirements, Optical Engineering 51(7), 076201(July 2012).

Kersting, A. P., "Quality assurance of multi-sensor systems," PhD dissertation, Dept. Geomatics Eng., Calgary, AB, p. 265, University of Calgary (2011).

Kilian, J., N. Haala, and M. Englich, 1996. Capture and evaluation of airborne laser scanner data, International Archives of Photogrammetry and Remote Sensing, 31(PartB3): 383–388.

Koch, K. R., 1988. Parameter estimation and hypothesis testing in linear models, Springer-Verlag New York, Inc. New York, NY, USA, 378 p.

Kumari, P., W. Carter, and R. Shrestha (2011). Adjustment of systematic errors in ALS data through surface matching. Advances in Space Research 47 (10), 1851-1864.

Lari, Z., & Habib, A. (2013). New Approaches for Estimating the Local Point Density and its Impact on Lidar Data Segmentation. Photogrammetric engineering and remote sensing, 79(2), 195-207.

Lee, I., "Perceptual Organization of Surfaces," Ph.d. Dissertation, Dept. of Civil and Environmental Engineering, OH, USA (2002).

Lee, J., Yu, K., Kim, Y., and Habib, A.F., 2007. Adjustment of Discrepancies between LiDAR Data Strips Using Linear Features, IEEE Geoscience and Remote Sensing Letter, Vol. 4, No. 3, pp. 475-479.

Leica, 2007. www.leica-geosystems.com. Homepage of the company Leica Geosystems, accessed: August 2007.

Leslar, M. (2009). Extraction of geo-spatial information from LiDAR-based mobile mapping system for crowd control planning. In IEEE Toronto International Conference-Science and Technology for Humanity, Toronto, Canada, pp. 468-472.

Lindenthal, S.M.,V.R.Ussyshkin, J.G. Wang, M. Pokorny, 2011. Airborne lidar: a fully-automated self-calibration procedure, ISPRS Achieves, ISPRS Calgary 2011Workshop, 29-31 August 2011, Calgary, Canada,38 (5/W12),pp.73-78.

Maas H. G., 2002. Method for measuring height and planimetry discrepancies in airborne Laser scanner data, Photogrammetric Engineering and Remote Sensing, 68(9):933–940.

Mikhail, E. M., and F. Ackerman, 1976. Observations and Least Squares, New York: University Press of America, 497 p.

Morgan, D. (2009). Using mobile LiDAR to survey railway infrastructure. Lynx mobile mapper. In FIG Commissions 5, 6 and SSGA Workshop -Innovative Technologies for an Efficient Geospatial Management of Earth Resources, Lake Baikal, Russian Federation.

Morin, K. W., 2002. Calibration of Airborne Laser Scanners, M.S. thesis, University of Calgary, Department of Geomatics Engineering, Calgary, AB, 125 p. Optech, 2007.www.optech.ca. Homepage of the company Optech, accessed: June 2007.

Pack, R. T., Saunders, D., Fullmer, R., Budge, S., “The simulation of automatic ladar sensor control during flight operations using USU LadarSIM Software”, Proceedings of SPIE Vol. 6214, 62140L (2006).

Persson, Å., Holmgren, J. & U. Söderman, “Detecting and measuring individual trees using an airborne laser scanner,” Photogrammetric Engineering and Remote Sensing, 68, 925-932 (2002).

Petrie, G., & Toth, C. K. (2009). Introduction to laser ranging, profiling, and scanning. Topographic Laser Ranging and Scanning Principles and Processing, 1-27.

Rieger, P., N. Studnicka, et al. (2010). "Boresight alignment method for mobile laser scanning systems." Journal of Applied Geodesy 4(1): 13-21.

Riegl, 2007. www.riegl.com. Homepage of the company RIEGL Laser Measurement Systems GmbH, accessed: August 2007.

Rottensteiner, F., “Automatic generation of high-quality building models from Lidar data,” IEEE CG&A 23(6), pp. 42-51 (2003).

Schenk, T., 2001. Modelling and Analyzing Systematic Errors in Airborne Laser Scanners, Technical Notes in Photogrammetry, Vol. 19, The Ohio State University, Columbus, US.

Shan and C.K. Toth (Editors), Topographic Laser Ranging and Scanning: Principles and Processing. CRC Press, Taylor & Francis Group, Boca Raton, Florida, pp. 4-18.

Skaloud, J., and D. Lichti, 2006. Rigorous Approach to Bore-Sight Self-Calibration in Airborne Laser Scanning, ISPRS Journal of Photogrammetry and Remote Sensing, 61(6): 47–59.

Skaloud, J., J. Vallet, K. Keller, G. Veyssiere, and O. Koelbl, 2005. HELIMAP: Rapid large scale mapping using handheld LiDAR/CCD/GPS/INS sensors on helicopters, Proceedings ION GNSS 2005, Long Beach, CA, USA, 13–16 September, pp. 2461– 2467.

Skaloud, J., and D. Lichti, 2006. Rigorous Approach to Bore-Sight Self-Calibration in Airborne Laser Scanning, ISPRS Journal of Photogrammetry and Remote Sensing, 61(6): 47–59.

Song, J., Han, S., Yu, K., Kim, Y., 2002. Assessing the possibility of land-cover classification using LiDAR intensity data, International Archives of Photogrammetry, Remote Sensing and Spatial Information Sciences 34 (Part 3B), 9-13 September, Graz, Austria, pp. 259–262.

TopEye, 2007. www.blomasa.com. Homepage of the BLOM GROUP, accessed: Augsut 2007.

TopoSys, 2007. www.toposys.com. Homepage of the company TopoSys GmbH, accessed: June 2007.

Toth, C.K., 2002. Calibrating airborne lidar systems, Proceedings of ISPRS Commission II Symposium, Xi'an, China, pp. 475–480.

Vosselman, G., "Fusion of Laser Scanning Data, Maps and Aerial Photographs for Building Reconstruction," IEEE International Geoscience and Remote Sensing Symposium and the 24th Canadian Symposium on Remote Sensing, IGARSS'02, Toronto, Canada, June 24-28 (2002).

Vosselman, G., & Maas, H. G. (Eds.). (2010). Airborne and terrestrial laser scanning (Vol. 318). Dunbeath, UK: Whittles, pp. 16–18

Wang, M. and Tseng, Y. H., 2004. LiDAR data segmentation and classification based on octree structure, XXth International Society for Photogrammetry and Remote Sensing (ISPRS) Congress, Istanbul, Turkey.

Wehr, A., and Lohr, U., 1999. Airborne laser scanning - an introduction and overview, ISPRS Journal of Photogrammetry and Remote Sensing, 54(2-3): 68–82.

Zhu, L., J. Hyyppä, et al. (2011). "Photorealistic building reconstruction from mobile laser scanning data." Remote Sensing 3(7): 1406-1426.

3rdTech, 2007. www.3rdtech.com. Homepage of the company 3rdTech, accessed: June 2007.

Appendix A

Table 1.A. The results of estimated system parameters for scenario I in experiment 1

Parameters	True value	Initial value	Initial standard deviation	Estimated value	Estimated standard deviation	Abs (diff)
The mounting parameters relating the reference scanner and the IMU body frame						
$\Delta X\_ref2b\ [m]$	1.0	1.1	1.0e9	0.9996	0.0001	0.0004
$\Delta Y\_ref2b\ [m]$	1.0	0.9	1.0e9	0.9313	0.0004	0.0687
$\Delta Z\_ref2b\ [m]$	0.0	0.0	1.0e-9	Fixed		
$\Delta\omega\_ref2b\ [deg]$	5.0	5.1	1.0e9	5.0111	0.0016	0.0111
$\Delta\varphi\_ref2b\ [deg]$	-5.0	-5.1	1.0e9	-5.0024	0.0007	0.0024
$\Delta\kappa\_ref2b\ [deg]$	5.0	4.9	1.0e9	4.9774	0.0011	0.0226
The mounting parameters relating scanner 1 and the reference scanner						
$\Delta X\_lu_1 2ref\ [m]$	-1.0	-1.1	1.0e9	-0.9945	0.0001	0.0055
$\Delta Y\_lu_1 2ref\ [m]$	1.0	1.1	1.0e9	1.0676	0.0005	0.0676
$\Delta Z\_lu_1 2ref\ [m]$	0.0	-0.1	1.0e9	-0.0095	0.0003	0.0095
$\Delta\omega\_lu_1 2ref\ [deg]$	-5.0	-5.1	1.0e9	-5.0286	0.0023	0.0286
$\Delta\varphi\_lu_1 2ref\ [deg]$	5.0	4.9	1.0e9	5.0075	0.0011	0.0075
$\Delta\kappa\_lu_1 2ref\ [deg]$	-5.0	-4.9	1.0e9	-4.9891	0.0013	0.0109
Intrinsic parameters of the reference scanner						
$\Delta\rho\_ref\ [m]$	0.0	0.02	1.0e9	0.0242	0.0006	0.0242
S_β_ref	1.0	1.0001	1.0e9	1.0001	0.00001	0.0001
Intrinsic parameters of scanner 1						
$\Delta\rho\_lu_1\ [m]$	0.0	-0.02	1.0e9	0.0241	0.0006	0.0241
$S_\beta\_lu_1$	1.0	0.9999	1.0e9	1.0001	0.00001	0.0001

Table 2.A. The results of estimated system parameters for scenario II in experiment 1

Parameters	True value	Initial value	Initial standard deviation	Estimated value	Estimated standard deviation	Abs (diff)
The mounting parameters relating the reference scanner and the IMU body frame						
ΔX_ref2b [m]	1.0	1.1	1.0e9	0.9997	0.00001	0.0003
ΔY_ref2b [m]	1.0	0.9	1.0e9	0.9412	0.0002	0.0588
ΔZ_ref2b [m]	0.0	0.0	1.0e-9	Fixed		
$\Delta\omega\_ref2b$ [deg]	5.0	5.1	1.0e9	5.0101	0.0011	0.0101
$\Delta\varphi\_ref2b$ [deg]	-5.0	-5.1	1.0e9	-5.0022	0.0004	0.0022
$\Delta\kappa\_ref2b$ [deg]	5.0	4.9	1.0e9	4.9903	0.0008	0.0097
The mounting parameters relating scanner 1 and the reference scanner						
$\Delta X\_lu_1 2ref$ [m]	-1.0	-1.0005	0.00001	-1.0005	0.00001	0.0005
$\Delta Y\_lu_1 2ref$ [m]	1.0	0.9996	0.00001	0.9996	0.00001	0.0004
$\Delta Z\_lu_1 2ref$ [m]	0.0	-0.0090	0.0001	-0.0090	0.00001	0.0090
$\Delta\omega\_lu_1 2ref$ [deg]	-5.0	-4.9942	0.0007	-4.9943	0.0001	0.0057
$\Delta\varphi\_lu_1 2ref$ [deg]	5.0	4.9935	0.0008	4.9936	0.0002	0.0064
$\Delta\kappa\_lu_1 2ref$ [deg]	-5.0	-5.0047	0.0003	-5.0047	0.0001	0.0047
Intrinsic parameters of the reference scanner						
$\Delta\rho\_ref$ [m]	0.0	0.0195	0.0001	0.0195	0.00001	0.0195
S_β_ref	1.0	1.0000	0.00001	1.0000	0.00001	0.0000
Intrinsic parameters of scanner 1						
$\Delta\rho\_lu_1$ [m]	0.0	0.0197	0.0001	0.0197	0.00001	0.0197
$S_\beta\_lu_1$	1.0	0.9998	0.00001	0.9999	0.00001	0.0001

Table 3.A. The results of estimated system parameters for scenario III in experiment 1

Parameters	True value	Initial value	Initial standard deviation	Estimated value	Estimated standard deviation	Abs (diff)
The mounting parameters relating the reference scanner and the IMU body frame						
$\Delta X\_ref2b\ [m]$	1.0	1.1	1.0e9	0.9996	0.0001	0.0004
$\Delta Y\_ref2b\ [m]$	1.0	0.9	1.0e9	0.9311	0.0004	0.0689
$\Delta Z\_ref2b\ [m]$	0.0	0.1	1.0e9	0.0781	0.0015	0.0781
$\Delta\omega\_ref2b\ [deg]$	5.0	5.1	1.0e9	5.0113	0.0016	0.0113
$\Delta\varphi\_ref2b\ [deg]$	-5.0	-5.1	1.0e9	-5.0027	0.0007	0.0027
$\Delta\kappa\_ref2b\ [deg]$	5.0	4.9	1.0e9	4.9750	0.0010	0.0250
The mounting parameters relating scanner 1 and the reference scanner						
$\Delta X\_lu_1 2ref\ [m]$	-1.0	-1.1	1.0e9	-0.9944	0.0001	0.0056
$\Delta Y\_lu_1 2ref\ [m]$	1.0	1.1	1.0e9	1.0678	0.0005	0.0678
$\Delta Z\_lu_1 2ref\ [m]$	0.0	-0.1	1.0e9	-0.0096	0.0004	0.0096
$\Delta\omega\_lu_1 2ref\ [deg]$	-5.0	-5.1	1.0e9	-5.0281	0.0023	0.0281
$\Delta\varphi\_lu_1 2ref\ [deg]$	5.0	4.9	1.0e9	5.0069	0.0011	0.0069
$\Delta\kappa\_lu_1 2ref\ [deg]$	-5.0	-4.9	1.0e9	-4.9909	0.0013	0.0091
Intrinsic parameters of the reference scanner						
$\Delta\rho\_ref\ [m]$	0.0	0.02	1.0e9	0.0306	0.0006	0.0306
S_β_ref	1.0	1.0001	1.0e9	1.0001	0.00001	0.0001
Intrinsic parameters of scanner 1						
$\Delta\rho\_lu_1\ [m]$	0.0	-0.02	1.0e9	0.0306	0.0006	0.0306
$S_\beta\_lu_1$	1.0	0.9999	1.0e9	1.0001	0.00001	0.0001

Table 4.A. The results of estimated system parameters for scenario IV in experiment 1

Parameters	True value	Initial value	Initial standard deviation	Estimated value	Estimated standard deviation	Abs (diff)
The mounting parameters relating the reference scanner and the IMU body frame						
ΔX_ref2b [m]	1.0	1.1	1.0e9	0.9998	0.00001	0.0002
ΔY_ref2b [m]	1.0	0.9	1.0e9	0.9418	0.0002	0.0582
ΔZ_ref2b [m]	0.0	0.1	1.0e9	0.0730	0.0014	0.0730
$\Delta\omega\_ref2b$ [deg]	5.0	5.1	1.0e9	5.0063	0.0011	0.0063
$\Delta\varphi\_ref2b$ [deg]	-5.0	-5.1	1.0e9	-5.0021	0.0004	0.0021
$\Delta\kappa\_ref2b$ [deg]	5.0	4.9	1.0e9	4.9903	0.0008	0.0097
The mounting parameters relating scanner 1 and the reference scanner						
$\Delta X\_lu_1 2ref$ [m]	-1.0	-1.0005	0.00001	-1.0005	0.00001	0.0005
$\Delta Y\_lu_1 2ref$ [m]	1.0	0.9996	0.00001	0.9996	0.00001	0.0004
$\Delta Z\_lu_1 2ref$ [m]	0.0	-0.0090	0.0001	-0.0090	0.00001	0.0090
$\Delta\omega\_lu_1 2ref$ [deg]	-5.0	-4.9942	0.0007	-4.9943	0.0001	0.0057
$\Delta\varphi\_lu_1 2ref$ [deg]	5.0	4.9935	0.0008	4.9936	0.0002	0.0064
$\Delta\kappa\_lu_1 2ref$ [deg]	-5.0	-5.0047	0.0003	-5.0047	0.0001	0.0047
Intrinsic parameters of the reference scanner						
$\Delta\rho\_ref$ [m]	0.0	0.0195	0.0001	0.0195	0.00001	0.0195
S_β_ref	1.0	1.0000	0.00001	1.0000	0.00001	0.0000
Intrinsic parameters of scanner 1						
$\Delta\rho\_lu_1$ [m]	0.0	0.0197	0.0001	0.0197	0.00001	0.0197
$S_\beta\_lu_1$	1.0	0.9998	0.00001	0.9999	0.00001	0.0001

Table 5.A. The results of estimated system parameters for scenario V in experiment 1

Parameters	True value	Initial value	Initial standard deviation	Estimated value	Estimated standard deviation	Abs (diff)
The mounting parameters relating the reference scanner and the IMU body frame						
$\Delta X\_ref2b\ [m]$	1.0	1.1	1.0e9	0.9996	0.0001	0.0004
$\Delta Y\_ref2b\ [m]$	1.0	0.9	1.0e9	0.9995	0.0001	0.0005
$\Delta Z\_ref2b\ [m]$	0.0	0.0	1.0e-9	Fixed		
$\Delta\omega\_ref2b\ [deg]$	5.0	5.1	1.0e9	5.0047	0.0008	0.0047
$\Delta\varphi\_ref2b\ [deg]$	-5.0	-5.1	1.0e9	-4.9970	0.0004	0.0030
$\Delta\kappa\_ref2b\ [deg]$	5.0	4.9	1.0e9	4.9807	0.0007	0.0193
The mounting parameters relating scanner 1 and the reference scanner						
$\Delta X\_lu_1 2ref\ [m]$	-1.0	-1.1	1.0e9	-1.0007	0.0001	0.0007
$\Delta Y\_lu_1 2ref\ [m]$	1.0	1.1	1.0e9	0.9992	0.0002	0.0008
$\Delta Z\_lu_1 2ref\ [m]$	0.0	-0.1	1.0e9	-0.0091	0.0002	0.0091
$\Delta\omega\_lu_1 2ref\ [deg]$	-5.0	-5.1	1.0e9	-5.0068	0.0010	0.0068
$\Delta\varphi\_lu_1 2ref\ [deg]$	5.0	4.9	1.0e9	4.9929	0.0006	0.0071
$\Delta\kappa\_lu_1 2ref\ [deg]$	-5.0	-4.9	1.0e9	-4.9948	0.0007	0.0052
Intrinsic parameters of the reference scanner						
$\Delta\rho\_ref\ [m]$	0.0	0.02	1.0e9	0.0212	0.0004	0.0212
S_β_ref	1.0	1.0001	1.0e9	1.0001	0.00001	0.0001
Intrinsic parameters of scanner 1						
$\Delta\rho\_lu_1\ [m]$	0.0	-0.02	1.0e9	0.0213	0.0004	0.0213
$S_\beta\_lu_1$	1.0	0.9999	1.0e9	1.0001	0.00001	0.0001

Table 6.A. The results of estimated system parameters for scenario VI in experiment 1

Parameters	True value	Initial value	Initial standard deviation	Estimated value	Estimated standard deviation	Abs (diff)
The mounting parameters relating the reference scanner and the IMU body frame						
ΔX_ref2b [m]	1.0	1.1	1.0e9	0.9997	0.0000	0.0003
ΔY_ref2b [m]	1.0	0.9	1.0e9	0.9996	0.0001	0.0004
ΔZ_ref2b [m]	0.0	0.0	1.0e-9	Fixed		
$\Delta\omega\_ref2b$ [deg]	5.0	5.1	1.0e9	5.0032	0.0004	0.0032
$\Delta\varphi\_ref2b$ [deg]	-5.0	-5.1	1.0e9	-4.9990	0.0003	0.0010
$\Delta\kappa\_ref2b$ [deg]	5.0	4.9	1.0e9	4.9853	0.0005	0.0147
The mounting parameters relating scanner 1 and the reference scanner						
$\Delta X\_lu_1 2ref$ [m]	-1.0	-1.0005	0.00001	-1.0005	0.00001	0.0005
$\Delta Y\_lu_1 2ref$ [m]	1.0	0.9996	0.00001	0.9996	0.00001	0.0004
$\Delta Z\_lu_1 2ref$ [m]	0.0	-0.0090	0.0001	-0.0089	0.00001	0.0089
$\Delta\omega\_lu_1 2ref$ [deg]	-5.0	-4.9942	0.0007	-4.9946	0.0001	0.0054
$\Delta\varphi\_lu_1 2ref$ [deg]	5.0	4.9935	0.0008	4.9935	0.0001	0.0065
$\Delta\kappa\_lu_1 2ref$ [deg]	-5.0	-5.0047	0.0003	-5.0047	0.0001	0.0047
Intrinsic parameters of the reference scanner						
$\Delta\rho\_ref$ [m]	0.0	0.0195	0.0001	0.0195	0.00001	0.0195
S_β_ref	1.0	1.0000	0.00001	1.0001	0.00001	0.0001
Intrinsic parameters of scanner 1						
$\Delta\rho\_lu_1$ [m]	0.0	0.0197	0.0001	0.0197	0.00001	0.0197
$S_\beta\_lu_1$	1.0	0.9998	0.00001	0.9999	0.00001	0.0001

Table 7.A. The results of estimated system parameters for scenario VII in experiment 1

Parameters	True value	Initial value	Initial standard deviation	Estimated value	Estimated standard deviation	Abs (diff)
The mounting parameters relating the reference scanner and the IMU body frame						
$\Delta X\_ref2b\ [m]$	1.0	1.1	1.0e9	0.9997	0.0001	0.0003
$\Delta Y\_ref2b\ [m]$	1.0	0.9	1.0e9	0.9996	0.0001	0.0004
$\Delta Z\_ref2b\ [m]$	0.0	0.1	1.0e9	0.0731	0.0011	0.0731
$\Delta\omega\_ref2b\ [deg]$	5.0	5.1	1.0e9	5.0031	0.0008	0.0031
$\Delta\varphi\_ref2b\ [deg]$	-5.0	-5.1	1.0e9	-4.9973	0.0005	0.0027
$\Delta\kappa\_ref2b\ [deg]$	5.0	4.9	1.0e9	4.9787	0.0007	0.0213
The mounting parameters relating scanner 1 and the reference scanner						
$\Delta X\_lu_1 2ref\ [m]$	-1.0	-1.1	1.0e9	-0.9993	0.0001	0.0007
$\Delta Y\_lu_1 2ref\ [m]$	1.0	1.1	1.0e9	0.9992	0.0002	0.0008
$\Delta Z\_lu_1 2ref\ [m]$	0.0	-0.1	1.0e9	-0.0090	0.0002	0.0090
$\Delta\omega\_lu_1 2ref\ [deg]$	-5.0	-5.1	1.0e9	-5.0075	0.0011	0.0075
$\Delta\varphi\_lu_1 2ref\ [deg]$	5.0	4.9	1.0e9	4.9931	0.0007	0.0069
$\Delta\kappa\_lu_1 2ref\ [deg]$	-5.0	-4.9	1.0e9	-4.9950	0.0008	0.0050
Intrinsic parameters of the reference scanner						
$\Delta\rho\_ref\ [m]$	0.0	0.02	1.0e9	0.0249	0.0004	0.0249
S_β_ref	1.0	1.0001	1.0e9	1.0001	0.00001	0.0001
Intrinsic parameters of scanner 1						
$\Delta\rho\_lu_1\ [m]$	0.0	-0.02	1.0e9	0.0250	0.0004	0.0250
$S_\beta\_lu_1$	1.0	0.9999	1.0e9	1.0001	0.00001	0.0001

Table 8.A. The results of estimated system parameters for scenario VIII in experiment 1

Parameters	True value	Initial value	Initial standard deviation	Estimated value	Estimated standard deviation	Abs (diff)
The mounting parameters relating the reference scanner and the IMU body frame						
$\Delta X\_ref2b\ [m]$	1.0	1.1	1.0e9	0.9998	0.00001	0.0002
$\Delta Y\_ref2b\ [m]$	1.0	0.9	1.0e9	0.9997	0.0001	0.0003
$\Delta Z\_ref2b\ [m]$	0.0	0.1	1.0e9	0.0703	0.0010	0.0703
$\Delta\omega\_ref2b\ [deg]$	5.0	5.1	1.0e9	5.0010	0.0004	0.0010
$\Delta\varphi\_ref2b\ [deg]$	-5.0	-5.1	1.0e9	-5.0016	0.0003	0.0016
$\Delta\kappa\_ref2b\ [deg]$	5.0	4.9	1.0e9	4.9853	0.0005	0.0147
The mounting parameters relating scanner 1 and the reference scanner						
$\Delta X\_lu_1 2ref\ [m]$	-1.0	-1.0005	0.00001	-1.0005	0.00001	0.0005
$\Delta Y\_lu_1 2ref\ [m]$	1.0	0.9996	0.00001	0.9996	0.00001	0.0004
$\Delta Z\_lu_1 2ref\ [m]$	0.0	-0.0090	0.0001	-0.0089	0.00001	0.0089
$\Delta\omega\_lu_1 2ref\ [deg]$	-5.0	-4.9942	0.0007	-4.9946	0.0001	0.0054
$\Delta\varphi\_lu_1 2ref\ [deg]$	5.0	4.9935	0.0008	4.9935	0.0001	0.0065
$\Delta\kappa\_lu_1 2ref\ [deg]$	-5.0	-5.0047	0.0003	-5.0047	0.0001	0.0047
Intrinsic parameters of the reference scanner						
$\Delta\rho\_ref\ [m]$	0.0	0.0195	0.0001	0.0195	0.00001	0.0195
S_β_ref	1.0	1.0000	0.00001	1.0000	0.00001	0.0000
Intrinsic parameters of scanner 1						
$\Delta\rho\_lu_1\ [m]$	0.0	0.0197	0.0001	0.0197	0.00001	0.0197
$S_\beta\_lu_1$	1.0	0.9998	0.00001	0.9999	0.00001	0.0001

Table 9.A. The results of estimated system parameters for scenario IX in experiment 1

Parameters	True value	Initial value	Initial standard deviation	Estimated value	Estimated standard deviation	Abs (diff)
The mounting parameters relating the reference scanner and the IMU body frame						
ΔX_ref2b [m]	1.0	1.1	1.0e9	0.9998	0.00001	0.0002
ΔY_ref2b [m]	1.0	0.9	1.0e9	0.9997	0.0001	0.0003
ΔZ_ref2b [m]	0.0	0.0	1.0e-9	Fixed		
$\Delta\omega\_ref2b$ [deg]	5.0	5.1	1.0e9	5.0006	0.0005	0.0006
$\Delta\varphi\_ref2b$ [deg]	-5.0	-5.1	1.0e9	-5.0004	0.0004	0.0004
$\Delta\kappa\_ref2b$ [deg]	5.0	4.9	1.0e9	4.9846	0.0005	0.0154
The mounting parameters relating scanner 1 and the reference scanner						
$\Delta X\_lu_1 2ref$ [m]	-1.0	-1.1	1.0e9	-1.0006	0.0001	0.0006
$\Delta Y\_lu_1 2ref$ [m]	1.0	1.1	1.0e9	0.9994	0.0001	0.0006
$\Delta Z\_lu_1 2ref$ [m]	0.0	-0.1	1.0e9	-0.0090	0.0001	0.0090
$\Delta\omega\_lu_1 2ref$ [deg]	-5.0	-5.1	1.0e9	-5.0058	0.0007	0.0058
$\Delta\varphi\_lu_1 2ref$ [deg]	5.0	4.9	1.0e9	5.0070	0.0006	0.0070
$\Delta\kappa\_lu_1 2ref$ [deg]	-5.0	-4.9	1.0e9	-4.9953	0.0006	0.0047
Intrinsic parameters of the reference scanner						
$\Delta\rho\_ref$ [m]	0.0	0.02	1.0e9	0.0196	0.0003	0.0196
S_β_ref	1.0	1.0001	1.0e9	1.0001	0.00001	0.0001
Intrinsic parameters of scanner 1						
$\Delta\rho\_lu_1$ [m]	0.0	-0.02	1.0e9	0.0201	0.0003	0.0201
$S_\beta\_lu_1$	1.0	0.9999	1.0e9	1.0001	0.00001	0.0001

Table 10.A. The results of estimated system parameters for scenario X in experiment 1

Parameters	True value	Initial value	Initial standard deviation	Estimated value	Estimated standard deviation	Abs (diff)
The mounting parameters relating the reference scanner and the IMU body frame						
$\Delta X\_ref2b\ [m]$	1.0	1.1	1.0e9	0.9999	0.00001	0.0001
$\Delta Y\_ref2b\ [m]$	1.0	0.9	1.0e9	0.9998	0.00001	0.0002
$\Delta Z\_ref2b\ [m]$	0.0	0.0	1.0e-9	Fixed		
$\Delta\omega\_ref2b\ [deg]$	5.0	5.1	1.0e9	5.0003	0.0003	0.0003
$\Delta\varphi\_ref2b\ [deg]$	-5.0	-5.1	1.0e9	-5.0002	0.0002	0.0002
$\Delta\kappa\_ref2b\ [deg]$	5.0	4.9	1.0e9	4.9862	0.0004	0.0138
The mounting parameters relating scanner 1 and the reference scanner						
$\Delta X\_lu_1 2ref\ [m]$	-1.0	-1.0005	0.00001	-1.0005	0.00001	0.0005
$\Delta Y\_lu_1 2ref\ [m]$	1.0	0.9996	0.00001	0.9996	0.00001	0.0004
$\Delta Z\_lu_1 2ref\ [m]$	0.0	-0.0090	0.0001	-0.0088	0.00001	0.0088
$\Delta\omega\_lu_1 2ref\ [deg]$	-5.0	-4.9942	0.0007	-4.9945	0.0001	0.0055
$\Delta\varphi\_lu_1 2ref\ [deg]$	5.0	4.9935	0.0008	4.9932	0.0002	0.0068
$\Delta\kappa\_lu_1 2ref\ [deg]$	-5.0	-5.0047	0.0003	-5.0047	0.0001	0.0047
Intrinsic parameters of the reference scanner						
$\Delta\rho\_ref\ [m]$	0.0	0.0195	0.0001	0.0194	0.00001	0.0194
S_β_ref	1.0	1.0000	0.00001	1.0000	0.00001	0.0000
Intrinsic parameters of scanner 1						
$\Delta\rho\_lu_1\ [m]$	0.0	0.0197	0.0001	0.0198	0.00001	0.0198
$S_\beta\_lu_1$	1.0	0.9998	0.00001	0.9999	0.00001	0.0001

Table 34.A. The results of estimated system parameters for scenario XI in experiment 1

Parameters	True value	Initial value	Initial standard deviation	Estimated value	Estimated standard deviation	Abs (diff)
The mounting parameters relating the reference scanner and the IMU body frame						
$\Delta X\_ref2b\ [m]$	1.0	1.1	1.0e9	0.9999	0.00001	0.0001
$\Delta Y\_ref2b\ [m]$	1.0	0.9	1.0e9	0.9993	0.0001	0.0007
$\Delta Z\_ref2b\ [m]$	0.0	0.1	1.0e9	0.0750	0.0008	0.0750
$\Delta\omega\_ref2b\ [deg]$	5.0	5.1	1.0e9	5.0009	0.0005	0.0009
$\Delta\varphi\_ref2b\ [deg]$	-5.0	-5.1	1.0e9	-5.0004	0.0004	0.0004
$\Delta\kappa\_ref2b\ [deg]$	5.0	4.9	1.0e9	4.9839	0.0005	0.0161
The mounting parameters relating scanner 1 and the reference scanner						
$\Delta X\_lu_1 2ref\ [m]$	-1.0	-1.1	1.0e9	-1.0005	0.0001	0.0005
$\Delta Y\_lu_1 2ref\ [m]$	1.0	1.1	1.0e9	0.9993	0.0001	0.0007
$\Delta Z\_lu_1 2ref\ [m]$	0.0	-0.1	1.0e9	-0.0089	0.0001	0.0089
$\Delta\omega\_lu_1 2ref\ [deg]$	-5.0	-5.1	1.0e9	-5.0057	0.0007	0.0057
$\Delta\varphi\_lu_1 2ref\ [deg]$	5.0	4.9	1.0e9	5.0073	0.0006	0.0073
$\Delta\kappa\_lu_1 2ref\ [deg]$	-5.0	-4.9	1.0e9	-4.9950	0.0006	0.0050
Intrinsic parameters of the reference scanner						
$\Delta\rho\_ref\ [m]$	0.0	0.02	1.0e9	0.0224	0.0003	0.0224
S_β_ref	1.0	1.0001	1.0e9	1.0001	0.00001	0.0001
Intrinsic parameters of scanner 1						
$\Delta\rho\_lu_1\ [m]$	0.0	-0.02	1.0e9	0.0227	0.0003	0.0227
$S_\beta\_lu_1$	1.0	0.9999	1.0e9	1.0001	0.00001	0.0001

Table 12.A. The results of estimated system parameters for scenario XII in experiment 1

Parameters	True value	Initial value	Initial standard deviation	Estimated value	Estimated standard deviation	Abs (diff)
The mounting parameters relating the reference scanner and the IMU body frame						
ΔX_ref2b [m]	1.0	1.1	1.0e9	0.9999	0.00001	0.0001
ΔY_ref2b [m]	1.0	0.9	1.0e9	0.9995	0.00001	0.0005
ΔZ_ref2b [m]	0.0	0.1	1.0e9	0.0737	0.0008	0.0737
$\Delta\omega\_ref2b$ [deg]	5.0	5.1	1.0e9	5.0002	0.0003	0.0002
$\Delta\varphi\_ref2b$ [deg]	-5.0	-5.1	1.0e9	-5.0001	0.0002	0.0001
$\Delta\kappa\_ref2b$ [deg]	5.0	4.9	1.0e9	4.9864	0.0004	0.0136
The mounting parameters relating scanner 1 and the reference scanner						
$\Delta X\_lu_1 2ref$ [m]	-1.0	-1.0005	0.00001	-1.0005	0.00001	0.0005
$\Delta Y\_lu_1 2ref$ [m]	1.0	0.9996	0.00001	0.9996	0.00001	0.0004
$\Delta Z\_lu_1 2ref$ [m]	0.0	-0.0090	0.0001	-0.0088	0.00001	0.0088
$\Delta\omega\_lu_1 2ref$ [deg]	-5.0	-4.9942	0.0007	-4.9946	0.0001	0.0054
$\Delta\varphi\_lu_1 2ref$ [deg]	5.0	4.9935	0.0008	4.9932	0.0002	0.0068
$\Delta\kappa\_lu_1 2ref$ [deg]	-5.0	-5.0047	0.0003	-5.0047	0.0001	0.0047
Intrinsic parameters of the reference scanner						
$\Delta\rho\_ref$ [m]	0.0	0.0195	0.0001	0.0194	0.00001	0.0194
S_β_ref	1.0	1.0000	0.00001	1.0000	0.00001	0.0000
Intrinsic parameters of scanner 1						
$\Delta\rho\_lu_1$ [m]	0.0	0.0197	0.0001	0.0198	0.00001	0.0198
$S_\beta\_lu_1$	1.0	0.9998	0.00001	0.9999	0.00001	0.0001

Appendix B

Table 1.B. The results of estimated system parameters for scenario I in experiment 2

Parameters	True value	Initial value	Initial standard deviation	Estimated value	Estimated standard deviation	Abs (diff)
The mounting parameters relating the reference scanner and the IMU body frame						
ΔX_ref2b *[m]*	1.0	1.1	1.0e9	1.0549	0.0004	0.0549
ΔY_ref2b *[m]*	1.0	0.9	1.0e9	0.9015	0.0008	0.0985
ΔZ_ref2b *[m]*	0.0	0.0	1.0e-9	Fixed		
$\Delta\omega\_ref2b$ *[deg]*	5.0	5.1	1.0e9	5.1040	0.0035	0.1040
$\Delta\varphi\_ref2b$ *[deg]*	-5.0	-5.1	1.0e9	-5.0949	0.0018	0.0949
$\Delta\kappa\_ref2b$ *[deg]*	5.0	4.9	1.0e9	4.9023	0.0035	0.0977
The mounting parameters relating scanner 1 and the reference scanner						
$\Delta X\_lu_1 2ref$ *[m]*	-1.0	-1.1	1.0e9	-1.0815	0.0005	0.0815
$\Delta Y\_lu_1 2ref$ *[m]*	1.0	1.1	1.0e9	1.1033	0.0010	0.1033
$\Delta Z\_lu_1 2ref$ *[m]*	0.0	-0.1	1.0e9	-0.0991	0.0008	0.0991
$\Delta\omega\_lu_1 2ref$ *[deg]*	-5.0	-5.1	1.0e9	-5.0954	0.0046	0.0954
$\Delta\varphi\_lu_1 2ref$ *[deg]*	5.0	4.9	1.0e9	4.8990	0.0024	0.1010
$\Delta\kappa\_lu_1 2ref$ *[deg]*	-5.0	-4.9	1.0e9	-4.9151	0.0030	0.0849
Intrinsic parameters of the reference scanner						
$\Delta\rho\_ref$ *[m]*	0.0	0.02	1.0e9	0.0486	0.0010	0.0486
S_β_ref	1.0	1.0001	1.0e9	1.0002	0.00001	0.0002
Intrinsic parameters of scanner 1						
$\Delta\rho\_lu_1$ *[m]*	0.0	-0.02	1.0e9	-0.0479	0.0009	0.0479
$S_\beta\_lu_1$	1.0	0.9999	1.0e9	1.0002	0.00001	0.0002

Table 2.B. The results of estimated system parameters for scenario II in experiment 2

Parameters	True value	Initial value	Initial standard deviation	Estimated value	Estimated standard deviation	Abs (diff)
The mounting parameters relating the reference scanner and the IMU body frame						
ΔX_ref2b [m]	1.0	1.1	1.0e9	1.0525	0.0002	0.0525
ΔY_ref2b [m]	1.0	0.9	1.0e9	0.9072	0.0002	0.0928
ΔZ_ref2b [m]	0.0	0.0	1.0e-9	Fixed		
$\Delta\omega\_ref2b$ [deg]	5.0	5.1	1.0e9	5.1017	0.0019	0.1017
$\Delta\varphi\_ref2b$ [deg]	-5.0	-5.1	1.0e9	-5.0742	0.0008	0.0742
$\Delta\kappa\_ref2b$ [deg]	5.0	4.9	1.0e9	4.9187	0.0025	0.0813
The mounting parameters relating scanner 1 and the reference scanner						
$\Delta X\_lu_1 2ref$ [m]	-1.0	-1.0005	0.00001	-1.0005	0.00001	0.0005
$\Delta Y\_lu_1 2ref$ [m]	1.0	0.9996	0.00001	0.9996	0.00001	0.0004
$\Delta Z\_lu_1 2ref$ [m]	0.0	-0.0090	0.0001	-0.0090	0.00001	0.0090
$\Delta\omega\_lu_1 2ref$ [deg]	-5.0	-4.9942	0.0007	-4.9942	0.0003	0.0058
$\Delta\varphi\_lu_1 2ref$ [deg]	5.0	4.9935	0.0008	4.9933	0.0003	0.0067
$\Delta\kappa\_lu_1 2ref$ [deg]	-5.0	-5.0047	0.0003	-5.0047	0.0001	0.0047
Intrinsic parameters of the reference scanner						
$\Delta\rho\_ref$ [m]	0.0	0.0195	0.0001	0.0195	0.00001	0.0195
S_β_ref	1.0	1.0	0.00001	1.0000	0.00001	0.0000
Intrinsic parameters of scanner 1						
$\Delta\rho\_lu_1$ [m]	0.0	0.0197	0.0001	0.0197	0.00001	0.0197
$S_\beta\_lu_1$	1.0	0.9998	0.00001	0.9998	0.00001	0.0002

Table 3.B. The results of estimated system parameters for scenario III in experiment 2

Parameters	True value	Initial value	Initial standard deviation	Estimated value	Estimated standard deviation	Abs (diff)
The mounting parameters relating the reference scanner and the IMU body frame						
$\Delta X\_ref2b\ [m]$	1.0	1.1	1.0e9	1.0531	0.0003	0.0531
$\Delta Y\_ref2b\ [m]$	1.0	0.9	1.0e9	0.9061	0.0006	0.0939
$\Delta Z\_ref2b\ [m]$	0.0	0.1	1.0e9	0.0680	0.0066	0.0680
$\Delta\omega\_ref2b\ [deg]$	5.0	5.1	1.0e9	5.0853	0.0028	0.0853
$\Delta\varphi\_ref2b\ [deg]$	-5.0	-5.1	1.0e9	-5.0912	0.0013	0.0912
$\Delta\kappa\_ref2b\ [deg]$	5.0	4.9	1.0e9	4.8984	0.0028	0.1016
The mounting parameters relating scanner 1 and the reference scanner						
$\Delta X\_lu_1 2ref\ [m]$	-1.0	-1.1	1.0e9	-1.0108	0.0004	0.0108
$\Delta Y\_lu_1 2ref\ [m]$	1.0	1.1	1.0e9	1.1035	0.0008	0.1035
$\Delta Z\_lu_1 2ref\ [m]$	0.0	-0.1	1.0e9	-0.0886	0.0007	0.0886
$\Delta\omega\_lu_1 2ref\ [deg]$	-5.0	-5.1	1.0e9	-5.0185	0.0039	0.0185
$\Delta\varphi\_lu_1 2ref\ [deg]$	5.0	4.9	1.0e9	4.8545	0.0020	0.1455
$\Delta\kappa\_lu_1 2ref\ [deg]$	-5.0	-4.9	1.0e9	-4.9481	0.0026	0.0519
Intrinsic parameters of the reference scanner						
$\Delta\rho\_ref\ [m]$	0.0	0.02	1.0e9	0.0471	0.0008	0.0471
S_β_ref	1.0	1.0001	1.0e9	1.0002	0.00001	0.0002
Intrinsic parameters of scanner 1						
$\Delta\rho\_lu_1\ [m]$	0.0	-0.02	1.0e9	0.0418	0.0008	0.0418
$S_\beta\_lu_1$	1.0	0.9999	1.0e9	0.9998	0.00001	0.0002

Table 4.B. The results of estimated system parameters for scenario IV in experiment 2

Parameters	True value	Initial value	Initial standard deviation	Estimated value	Estimated standard deviation	Abs (diff)
The mounting parameters relating the reference scanner and the IMU body frame						
ΔX_ref2b [m]	1.0	1.1	1.0e9	1.0461	0.0002	0.0461
ΔY_ref2b [m]	1.0	0.9	1.0e9	0.9081	0.0002	0.0919
ΔZ_ref2b [m]	0.0	0.1	1.0e9	0.0619	0.0027	0.0619
$\Delta\omega\_ref2b$ [deg]	5.0	5.1	1.0e9	5.0603	0.0019	0.0603
$\Delta\varphi\_ref2b$ [deg]	-5.0	-5.1	1.0e9	-5.0721	0.0008	0.0721
$\Delta\kappa\_ref2b$ [deg]	5.0	4.9	1.0e9	4.9228	0.0024	0.0772
The mounting parameters relating scanner 1 and the reference scanner						
$\Delta X\_lu_1 2ref$ [m]	-1.0	-1.0005	0.00001	-1.0005	0.00001	0.0005
$\Delta Y\_lu_1 2ref$ [m]	1.0	0.9996	0.00001	0.9996	0.00001	0.0004
$\Delta Z\_lu_1 2ref$ [m]	0.0	-0.0090	0.0001	-0.0090	0.00001	0.0090
$\Delta\omega\_lu_1 2ref$ [deg]	-5.0	-4.9942	0.0007	-4.9942	0.0003	0.0058
$\Delta\varphi\_lu_1 2ref$ [deg]	5.0	4.9935	0.0008	4.9933	0.0003	0.0067
$\Delta\kappa\_lu_1 2ref$ [deg]	-5.0	-5.0047	0.0003	-5.0047	0.0001	0.0047
Intrinsic parameters of the reference scanner						
$\Delta\rho\_ref$ [m]	0.0	0.0195	0.0001	0.0195	0.00001	0.0195
S_β_ref	1.0	1.0	0.00001	1.0000	0.00001	0.0000
Intrinsic parameters of scanner 1						
$\Delta\rho\_lu_1$ [m]	0.0	0.0197	0.0001	0.0197	0.00001	0.0197
$S_\beta\_lu_1$	1.0	0.9998	0.00001	0.9998	0.00001	0.0002

Table 5.B. The results of estimated system parameters for scenario V in experiment 2

Parameters	True value	Initial value	Initial standard deviation	Estimated value	Estimated standard deviation	Abs (diff)
The mounting parameters relating the reference scanner and the IMU body frame						
$\Delta X\_ref2b\ [m]$	1.0	1.1	1.0e9	1.0375	0.0002	0.0375
$\Delta Y\_ref2b\ [m]$	1.0	0.9	1.0e9	0.9029	0.0004	0.0971
$\Delta Z\_ref2b\ [m]$	0.0	0.0	1.0e-9	Fixed		
$\Delta\omega\_ref2b\ [deg]$	5.0	5.1	1.0e9	5.0968	0.0017	0.0968
$\Delta\varphi\_ref2b\ [deg]$	-5.0	-5.1	1.0e9	-5.0923	0.0011	0.0923
$\Delta\kappa\_ref2b\ [deg]$	5.0	4.9	1.0e9	4.9145	0.0019	0.0855
The mounting parameters relating scanner 1 and the reference scanner						
$\Delta X\_lu_1 2ref\ [m]$	-1.0	-1.1	1.0e9	-1.0927	0.0003	0.0927
$\Delta Y\_lu_1 2ref\ [m]$	1.0	1.1	1.0e9	1.0954	0.0005	0.0954
$\Delta Z\_lu_1 2ref\ [m]$	0.0	-0.1	1.0e9	-0.0978	0.0004	0.0978
$\Delta\omega\_lu_1 2ref\ [deg]$	-5.0	-5.1	1.0e9	-5.1001	0.0022	0.1001
$\Delta\varphi\_lu_1 2ref\ [deg]$	5.0	4.9	1.0e9	4.8961	0.0014	0.1039
$\Delta\kappa\_lu_1 2ref\ [deg]$	-5.0	-4.9	1.0e9	-4.9060	0.0014	0.0960
Intrinsic parameters of the reference scanner						
$\Delta\rho\_ref\ [m]$	0.0	0.02	1.0e9	0.0365	0.0006	0.0365
S_β_ref	1.0	1.0001	1.0e9	1.0003	0.00001	0.0003
Intrinsic parameters of scanner 1						
$\Delta\rho\_lu_1\ [m]$	0.0	-0.02	1.0e9	-0.0307	0.0006	0.0307
$S_\beta\_lu_1$	1.0	0.9999	1.0e9	0.9999	0.00001	0.0001

Table 6.B. The results of estimated system parameters for scenario VI in experiment 2

Parameters	True value	Initial value	Initial Standard deviation	Estimated value	Estimated Standard deviation	Abs (diff)
The mounting parameters relating the reference scanner and the IMU body frame						
ΔX_ref2b [m]	1.0	1.1	1.0e9	1.0369	0.0001	0.0369
ΔY_ref2b [m]	1.0	0.9	1.0e9	0.9122	0.0001	0.0878
ΔZ_ref2b [m]	0.0	0.0	1.0e-9	Fixed		
$\Delta\omega\_ref2b$ [deg]	5.0	5.1	1.0e9	5.0819	0.0009	0.0819
$\Delta\varphi\_ref2b$ [deg]	-5.0	-5.1	1.0e9	-5.0787	0.0007	0.0787
$\Delta\kappa\_ref2b$ [deg]	5.0	4.9	1.0e9	4.9694	0.0017	0.0306
The mounting parameters relating scanner 1 and the reference scanner						
$\Delta X\_lu_1 2ref$ [m]	-1.0	-1.0005	0.00001	-1.0005	0.00001	0.0005
$\Delta Y\_lu_1 2ref$ [m]	1.0	0.9996	0.00001	0.9996	0.00001	0.0004
$\Delta Z\_lu_1 2ref$ [m]	0.0	-0.0090	0.0001	-0.0090	0.00001	0.0090
$\Delta\omega\_lu_1 2ref$ [deg]	-5.0	-4.9942	0.0007	-4.9942	0.0003	0.0058
$\Delta\varphi\_lu_1 2ref$ [deg]	5.0	4.9935	0.0008	4.9934	0.0003	0.0066
$\Delta\kappa\_lu_1 2ref$ [deg]	-5.0	-5.0047	0.0003	-5.0047	0.0001	0.0047
Intrinsic parameters of the reference scanner						
$\Delta\rho\_ref$ [m]	0.0	0.0195	0.0001	0.0195	0.00001	0.0195
S_β_ref	1.0	1.0	0.00001	1.0000	0.00001	0.0000
Intrinsic parameters of scanner 1						
$\Delta\rho\_lu_1$ [m]	0.0	0.0197	0.0001	0.0197	0.00001	0.0197
$S_\beta\_lu_1$	1.0	0.9998	0.00001	0.9999	0.00001	0.0001

Table 7.B. The results of estimated system parameters for scenario VII in experiment 2

Parameters	True value	Initial value	Initial standard deviation	Estimated value	Estimated standard deviation	Abs (diff)
The mounting parameters relating the reference scanner and the IMU body frame						
$\Delta X\_ref2b\ [m]$	1.0	1.1	1.0e9	1.0380	0.0002	0.0380
$\Delta Y\_ref2b\ [m]$	1.0	0.9	1.0e9	0.9369	0.0003	0.0631
$\Delta Z\_ref2b\ [m]$	0.0	0.1	1.0e9	0.0594	0.0016	0.0594
$\Delta\omega\_ref2b\ [deg]$	5.0	5.1	1.0e9	5.0866	0.0014	0.0866
$\Delta\varphi\_ref2b\ [deg]$	-5.0	-5.1	1.0e9	-5.0826	0.0009	0.0826
$\Delta\kappa\_ref2b\ [deg]$	5.0	4.9	1.0e9	4.9879	0.0017	0.0121
The mounting parameters relating scanner 1 and the reference scanner						
$\Delta X\_lu_1 2ref\ [m]$	-1.0	-1.1	1.0e9	-1.0397	0.0003	0.0397
$\Delta Y\_lu_1 2ref\ [m]$	1.0	1.1	1.0e9	1.0503	0.0004	0.0503
$\Delta Z\_lu_1 2ref\ [m]$	0.0	-0.1	1.0e9	-0.0809	0.0004	0.0809
$\Delta\omega\_lu_1 2ref\ [deg]$	-5.0	-5.1	1.0e9	-5.1246	0.0020	0.1246
$\Delta\varphi\_lu_1 2ref\ [deg]$	5.0	4.9	1.0e9	4.8679	0.0012	0.1321
$\Delta\kappa\_lu_1 2ref\ [deg]$	-5.0	-4.9	1.0e9	-4.9216	0.0014	0.0784
Intrinsic parameters of the reference scanner						
$\Delta\rho\_ref\ [m]$	0.0	0.02	1.0e9	0.0292	0.0006	0.0292
S_β_ref	1.0	1.0001	1.0e9	1.0002	0.00001	0.0002
Intrinsic parameters of scanner 1						
$\Delta\rho\_lu_1\ [m]$	0.0	-0.02	1.0e9	0.0285	0.0006	0.0284
$S_\beta\_lu_1$	1.0	0.9999	1.0e9	1.0001	0.00001	0.0001

Table 8.B. The results of estimated system parameters for scenario VIII in experiment 2

Parameters	True value	Initial value	Initial standard deviation	Estimated value	Estimated standard deviation	Abs (diff)
The mounting parameters relating the reference scanner and the IMU body frame						
ΔX_ref2b [m]	1.0	1.1	1.0e9	1.0354	0.0001	0.0354
ΔY_ref2b [m]	1.0	0.9	1.0e9	0.9394	0.0001	0.0606
ΔZ_ref2b [m]	0.0	0.1	1.0e9	0.0554	0.0018	0.0554
$\Delta\omega\_ref2b$ [deg]	5.0	5.1	1.0e9	5.0822	0.0009	0.0822
$\Delta\varphi\_ref2b$ [deg]	-5.0	-5.1	1.0e9	-5.0690	0.0007	0.0690
$\Delta\kappa\_ref2b$ [deg]	5.0	4.9	1.0e9	4.9870	0.0017	0.0130
The mounting parameters relating scanner 1 and the reference scanner						
$\Delta X\_lu_1 2ref$ [m]	-1.0	-1.0005	0.00001	-1.0005	0.00001	0.0005
$\Delta Y\_lu_1 2ref$ [m]	1.0	0.9996	0.00001	0.9996	0.00001	0.0004
$\Delta Z\_lu_1 2ref$ [m]	0.0	-0.0090	0.0001	-0.0090	0.00001	0.0090
$\Delta\omega\_lu_1 2ref$ [deg]	-5.0	-4.9942	0.0007	-4.9942	0.0003	0.0058
$\Delta\varphi\_lu_1 2ref$ [deg]	5.0	4.9935	0.0008	4.9934	0.0003	0.0066
$\Delta\kappa\_lu_1 2ref$ [deg]	-5.0	-5.0047	0.0003	-5.0047	0.0001	0.0047
Intrinsic parameters of the reference scanner						
$\Delta\rho\_ref$ [m]	0.0	0.0195	0.0001	0.0195	0.00001	0.0195
S_β_ref	1.0	1.0	0.00001	1.0000	0.00001	0.0000
Intrinsic parameters of scanner 1						
$\Delta\rho\_lu_1$ [m]	0.0	0.0197	0.0001	0.0197	0.00001	0.0197
$S_\beta\_lu_1$	1.0	0.9998	0.00001	0.9998	0.00001	0.0002

Table 9.B. The results of estimated system parameters for scenario IX in experiment 2

Parameters	True value	Initial value	Initial standard deviation	Estimated value	Estimated standard deviation	Abs (diff)
The mounting parameters relating the reference scanner and the IMU body frame						
ΔX_ref2b [m]	1.0	1.1	1.0e9	1.0289	0.0001	0.0289
ΔY_ref2b [m]	1.0	0.9	1.0e9	0.9598	0.0002	0.0402
ΔZ_ref2b [m]	0.0	0.0	1.0e-9	Fixed		
$\Delta\omega\_ref2b$ [deg]	5.0	5.1	1.0e9	5.0682	0.0010	0.0682
$\Delta\varphi\_ref2b$ [deg]	-5.0	-5.1	1.0e9	-5.0530	0.0007	0.0530
$\Delta\kappa\_ref2b$ [deg]	5.0	4.9	1.0e9	4.8660	0.0014	0.1340
The mounting parameters relating scanner 1 and the reference scanner						
$\Delta X\_lu_1 2ref$ [m]	-1.0	-1.1	1.0e9	-1.0475	0.0002	0.0475
$\Delta Y\_lu_1 2ref$ [m]	1.0	1.1	1.0e9	1.0382	0.0003	0.0382
$\Delta Z\_lu_1 2ref$ [m]	0.0	-0.1	1.0e9	-0.0865	0.0003	0.0865
$\Delta\omega\_lu_1 2ref$ [deg]	-5.0	-5.1	1.0e9	-5.0572	0.0014	0.0572
$\Delta\varphi\_lu_1 2ref$ [deg]	5.0	4.9	1.0e9	4.8755	0.0011	0.1245
$\Delta\kappa\_lu_1 2ref$ [deg]	-5.0	-4.9	1.0e9	-4.8856	0.0011	0.1144
Intrinsic parameters of the reference scanner						
$\Delta\rho\_ref$ [m]	0.0	0.02	1.0e9	0.0232	0.0005	0.0232
S_β_ref	1.0	1.0001	1.0e9	1.0007	0.00001	0.0007
Intrinsic parameters of scanner 1						
$\Delta\rho\_lu_1$ [m]	0.0	-0.02	1.0e9	0.0225	0.0005	0.0225
$S_\beta\_lu_1$	1.0	0.9999	1.0e9	1.0003	0.00001	0.0003

Table 10.B. The results of estimated system parameters for scenario X in experiment 2

Parameters	True value	Initial value	Initial standard deviation	Estimated value	Estimated standard deviation	Abs (diff)
The mounting parameters relating the reference scanner and the IMU body frame						
ΔX_ref2b [m]	1.0	1.1	1.0e9	1.0221	0.0001	0.0221
ΔY_ref2b [m]	1.0	0.9	1.0e9	0.9690	0.0001	0.0310
ΔZ_ref2b [m]	0.0	0.0	1.0e-9	Fixed		
$\Delta\omega\_ref2b$ [deg]	5.0	5.1	1.0e9	5.0651	0.0008	0.0651
$\Delta\varphi\_ref2b$ [deg]	-5.0	-5.1	1.0e9	-5.0511	0.0006	0.0511
$\Delta\kappa\_ref2b$ [deg]	5.0	4.9	1.0e9	4.9337	0.0016	0.0663
The mounting parameters relating scanner 1 and the reference scanner						
$\Delta X\_lu_1 2ref$ [m]	-1.0	-1.0005	0.00001	-1.0005	0.00001	0.0005
$\Delta Y\_lu_1 2ref$ [m]	1.0	0.9996	0.00001	0.9996	0.00001	0.0004
$\Delta Z\_lu_1 2ref$ [m]	0.0	-0.0090	0.0001	-0.0090	0.00001	0.0090
$\Delta\omega\_lu_1 2ref$ [deg]	-5.0	-4.9942	0.0007	-4.9942	0.0003	0.0058
$\Delta\varphi\_lu_1 2ref$ [deg]	5.0	4.9935	0.0008	4.9936	0.0003	0.0068
$\Delta\kappa\_lu_1 2ref$ [deg]	-5.0	-5.0047	0.0003	-5.0047	0.0001	0.0047
Intrinsic parameters of the reference scanner						
$\Delta\rho\_ref$ [m]	0.0	0.0195	0.0001	0.0195	0.00001	0.0195
S_β_ref	1.0	1.0	0.00001	1.0000	0.00001	0.0000
Intrinsic parameters of scanner 1						
$\Delta\rho\_lu_1$ [m]	0.0	0.0197	0.0001	0.0197	0.00001	0.0197
$S_\beta\_lu_1$	1.0	0.9998	0.00001	0.9999	0.00001	0.0001

Table 11.B. The results of estimated system parameters for scenario XI in experiment 2

Parameters	True value	Initial value	Initial standard deviation	Estimated value	Estimated standard deviation	Abs (diff)
The mounting parameters relating the reference scanner and the IMU body frame						
ΔX_ref2b *[m]*	1.0	1.1	1.0e9	1.0387	0.0002	0.0387
ΔY_ref2b *[m]*	1.0	0.9	1.0e9	0.9595	0.0003	0.0405
ΔZ_ref2b *[m]*	0.0	0.1	1.0e9	0.0527	0.0016	0.0527
$\Delta\omega\_ref2b$ *[deg]*	5.0	5.1	1.0e9	5.0870	0.0010	0.0870
$\Delta\varphi\_ref2b$ *[deg]*	-5.0	-5.1	1.0e9	-5.0840	0.0007	0.0840
$\Delta\kappa\_ref2b$ *[deg]*	5.0	4.9	1.0e9	4.8633	0.0015	0.1367
The mounting parameters relating scanner 1 and the reference scanner						
$\Delta X\_lu_1 2ref$ *[m]*	-1.0	-1.1	1.0e9	-1.0474	0.0002	0.0474
$\Delta Y\_lu_1 2ref$ *[m]*	1.0	1.1	1.0e9	1.0386	0.0003	0.0386
$\Delta Z\_lu_1 2ref$ *[m]*	0.0	-0.1	1.0e9	-0.0864	0.0003	0.0864
$\Delta\omega\_lu_1 2ref$ *[deg]*	-5.0	-5.1	1.0e9	-5.0568	0.0014	0.0568
$\Delta\varphi\_lu_1 2ref$ *[deg]*	5.0	4.9	1.0e9	4.8756	0.0011	0.1244
$\Delta\kappa\_lu_1 2ref$ *[deg]*	-5.0	-4.9	1.0e9	-4.8859	0.0011	0.1141
Intrinsic parameters of the reference scanner						
$\Delta\rho\_ref$ *[m]*	0.0	0.02	1.0e9	0.0235	0.0005	0.0235
S_β_ref	1.0	1.0001	1.0e9	1.0007	0.00001	0.0007
Intrinsic parameters of scanner 1						
$\Delta\rho\_lu_1$ *[m]*	0.0	-0.02	1.0e9	-0.0221	0.0005	0.0221
$S_\beta\_lu_1$	1.0	0.9999	1.0e9	1.0003	0.00001	0.0003

Table 12.B. The results of estimated system parameters for scenario XII in experiment 2

Parameters	True value	Initial value	Initial standard deviation	Estimated value	Estimated standard deviation	Abs (diff)
The mounting parameters relating the reference scanner and the IMU body frame						
$\Delta X\_ref2b\ [m]$	1.0	1.1	1.0e9	1.0128	0.0001	0.0128
$\Delta Y\_ref2b\ [m]$	1.0	0.9	1.0e9	0.9671	0.0001	0.0329
$\Delta Z\_ref2b\ [m]$	0.0	0.1	1.0e9	0.0442	0.0017	0.0442
$\Delta\omega\_ref2b\ [deg]$	5.0	5.1	1.0e9	5.0858	0.0008	0.0858
$\Delta\varphi\_ref2b\ [deg]$	-5.0	-5.1	1.0e9	-5.0752	0.0006	0.0752
$\Delta\kappa\_ref2b\ [deg]$	5.0	4.9	1.0e9	4.9168	0.0017	0.0832
The mounting parameters relating scanner 1 and the reference scanner						
$\Delta X\_lu_1 2ref\ [m]$	-1.0	-1.0005	0.00001	-1.0005	0.00001	0.0005
$\Delta Y\_lu_1 2ref\ [m]$	1.0	0.9996	0.00001	0.9996	0.00001	0.0004
$\Delta Z\_lu_1 2ref\ [m]$	0.0	-0.0090	0.0001	-0.0090	0.00001	0.0090
$\Delta\omega\_lu_1 2ref\ [deg]$	-5.0	-4.9942	0.0007	-4.9942	0.0003	0.0058
$\Delta\varphi\_lu_1 2ref\ [deg]$	5.0	4.9935	0.0008	4.9932	0.0003	0.0068
$\Delta\kappa\_lu_1 2ref\ [deg]$	-5.0	-5.0047	0.0003	-5.0047	0.0001	0.0047
Intrinsic parameters of the reference scanner						
$\Delta\rho\_ref\ [m]$	0.0	0.0195	0.0001	0.0195	0.00001	0.0195
S_β_ref	1.0	1.0	0.00001	1.0000	0.00001	0.0000
Intrinsic parameters of scanner 1						
$\Delta\rho\_lu_1\ [m]$	0.0	0.0197	0.0001	0.0197	0.00001	0.0197
$S_\beta\_lu_1$	1.0	0.9998	0.00001	0.9998	0.00001	0.0002

Appendix C

Table 1.C. The results of estimated system parameters for scenario I in experiment 3

Parameters	True value	Initial value	Initial standard deviation	Estimated value	Estimated standard deviation	Abs (diff)
The mounting parameters relating the reference scanner and the IMU body frame						
ΔX_ref2b [m]	1.0	1.1	1.0e9	1.0612	0.0003	0.0612
ΔY_ref2b [m]	1.0	0.9	1.0e9	0.9005	0.0006	0.0995
ΔZ_ref2b [m]	0.0	0.0	1.0e-9	Fixed		
$\Delta\omega\_ref2b$ [deg]	5.0	5.1	1.0e9	5.1850	0.0027	0.1850
$\Delta\varphi\_ref2b$ [deg]	-5.0	-5.1	1.0e9	-5.1650	0.0013	0.1650
$\Delta\kappa\_ref2b$ [deg]	5.0	4.9	1.0e9	4.9006	0.0030	0.0994
The mounting parameters relating scanner 1 and the reference scanner						
$\Delta X\_lu_1 2ref$ [m]	-1.0	-1.1	1.0e9	-1.0916	0.0005	0.0916
$\Delta Y\_lu_1 2ref$ [m]	1.0	1.1	1.0e9	1.1325	0.0009	0.1325
$\Delta Z\_lu_1 2ref$ [m]	0.0	-0.1	1.0e9	-0.0997	0.0007	0.0997
$\Delta\omega\_lu_1 2ref$ [deg]	-5.0	-5.1	1.0e9	-5.0986	0.0039	0.0986
$\Delta\varphi\_lu_1 2ref$ [deg]	5.0	4.9	1.0e9	4.8480	0.0023	0.1520
$\Delta\kappa\_lu_1 2ref$ [deg]	-5.0	-4.9	1.0e9	-4.9149	0.0027	0.0851
Intrinsic parameters of the reference scanner						
$\Delta\rho\_ref$ [m]	0.0	0.02	1.0e9	0.0422	0.0008	0.0422
S_β_ref	1.0	1.0001	1.0e9	1.0004	0.00001	0.0004
Intrinsic parameters of scanner 1						
$\Delta\rho\_lu_1$ [m]	0.0	-0.02	1.0e9	-0.0416	0.0008	0.0416
$S_\beta\_lu_1$	1.0	0.9999	1.0e9	0.9995	0.00001	0.0005

Table 2.C. The results of estimated system parameters for scenario II in experiment 3

Parameters	True value	Initial value	Initial standard deviation	Estimated value	Estimated standard deviation	Abs (diff)
The mounting parameters relating the reference scanner and the IMU body frame						
ΔX_ref2b [m]	1.0	1.1	1.0e9	1.0605	0.0002	0.0605
ΔY_ref2b [m]	1.0	0.9	1.0e9	0.9052	0.0002	0.0948
ΔZ_ref2b [m]	0.0	0.0	1.0e-9	Fixed		
$\Delta\omega\_ref2b$ [deg]	5.0	5.1	1.0e9	5.1468	0.0020	0.1468
$\Delta\varphi\_ref2b$ [deg]	-5.0	-5.1	1.0e9	-5.1092	0.0009	0.1092
$\Delta\kappa\_ref2b$ [deg]	5.0	4.9	1.0e9	4.9085	0.0029	0.0915
The mounting parameters relating scanner 1 and the reference scanner						
$\Delta X\_lu_1 2ref$ [m]	-1.0	-1.0005	0.00001	-1.0005	0.00001	0.0005
$\Delta Y\_lu_1 2ref$ [m]	1.0	0.9996	0.00001	0.9996	0.00001	0.0004
$\Delta Z\_lu_1 2ref$ [m]	0.0	-0.0090	0.0001	-0.0090	0.00001	0.0090
$\Delta\omega\_lu_1 2ref$ [deg]	-5.0	-4.9942	0.0007	-4.9942	0.0003	0.0058
$\Delta\varphi\_lu_1 2ref$ [deg]	5.0	4.9935	0.0008	4.9934	0.0003	0.0066
$\Delta\kappa\_lu_1 2ref$ [deg]	-5.0	-5.0047	0.0003	-5.0047	0.0001	0.0047
Intrinsic parameters of the reference scanner						
$\Delta\rho\_ref$ [m]	0.0	0.0195	0.0001	0.0195	0.00001	0.0195
S_β_ref	1.0	1.0	0.00001	1.0000	0.00001	0.0000
Intrinsic parameters of scanner 1						
$\Delta\rho\_lu_1$ [m]	0.0	0.0197	0.0001	0.0197	0.00001	0.0197
$S_\beta\_lu_1$	1.0	0.9998	0.00001	0.9998	0.00001	0.0002

Table 3.C. The results of estimated system parameters for scenario III in experiment 3

Parameters	True value	Initial value	Initial standard deviation	Estimated value	Estimated standard deviation	Abs (diff)
The mounting parameters relating the reference scanner and the IMU body frame						
ΔX_ref2b [m]	1.0	1.1	1.0e9	1.0614	0.0003	0.0614
ΔY_ref2b [m]	1.0	0.9	1.0e9	0.9069	0.0007	0.0931
ΔZ_ref2b [m]	0.0	0.1	1.0e9	0.0741	0.0028	0.0741
$\Delta\omega\_ref2b$ [deg]	5.0	5.1	1.0e9	5.0894	0.0028	0.0894
$\Delta\varphi\_ref2b$ [deg]	-5.0	-5.1	1.0e9	-5.0963	0.0013	0.0963
$\Delta\kappa\_ref2b$ [deg]	5.0	4.9	1.0e9	4.8949	0.0030	0.1051
The mounting parameters relating scanner 1 and the reference scanner						
$\Delta X\_lu_1 2ref$ [m]	-1.0	-1.1	1.0e9	-1.0642	0.0005	0.0642
$\Delta Y\_lu_1 2ref$ [m]	1.0	1.1	1.0e9	1.0847	0.0009	0.0847
$\Delta Z\_lu_1 2ref$ [m]	0.0	-0.1	1.0e9	-0.0902	0.0007	0.0902
$\Delta\omega\_lu_1 2ref$ [deg]	-5.0	-5.1	1.0e9	-4.9833	0.0039	0.0167
$\Delta\varphi\_lu_1 2ref$ [deg]	5.0	4.9	1.0e9	4.8488	0.0020	0.1512
$\Delta\kappa\_lu_1 2ref$ [deg]	-5.0	-4.9	1.0e9	-4.9552	0.0026	0.0448
Intrinsic parameters of the reference scanner						
$\Delta\rho\_ref$ [m]	0.0	0.02	1.0e9	0.0269	0.0008	0.0269
S_β_ref	1.0	1.0001	1.0e9	1.0005	0.00001	0.0005
Intrinsic parameters of scanner 1						
$\Delta\rho\_lu_1$ [m]	0.0	-0.02	1.0e9	-0.0226	0.0008	0.0226
$S_\beta\_lu_1$	1.0	0.9999	1.0e9	1.0003	0.00001	0.0003

Table 4.C. The results of estimated system parameters for scenario IV in experiment 3

Parameters	True value	Initial value	Initial standard deviation	Estimated value	Estimated standard deviation	Abs (diff)
The mounting parameters relating the reference scanner and the IMU body frame						
ΔX_ref2b [m]	1.0	1.1	1.0e9	1.0609	0.0002	0.0609
ΔY_ref2b [m]	1.0	0.9	1.0e9	0.9071	0.0002	0.0929
ΔZ_ref2b [m]	0.0	0.1	1.0e9	0.0691	0.0028	0.0691
$\Delta\omega\_ref2b$ [deg]	5.0	5.1	1.0e9	5.0880	0.0020	0.0880
$\Delta\varphi\_ref2b$ [deg]	-5.0	-5.1	1.0e9	-5.0914	0.0009	0.0914
$\Delta\kappa\_ref2b$ [deg]	5.0	4.9	1.0e9	4.9086	0.0028	0.0914
The mounting parameters relating scanner 1 and the reference scanner						
$\Delta X\_lu_1 2ref$ [m]	-1.0	-1.0005	0.00001	-1.0005	0.00001	0.0005
$\Delta Y\_lu_1 2ref$ [m]	1.0	0.9996	0.00001	0.9996	0.00001	0.0004
$\Delta Z\_lu_1 2ref$ [m]	0.0	-0.0090	0.0001	-0.0090	0.00001	0.0090
$\Delta\omega\_lu_1 2ref$ [deg]	-5.0	-4.9942	0.0007	-4.9942	0.0003	0.0058
$\Delta\varphi\_lu_1 2ref$ [deg]	5.0	4.9935	0.0008	4.9935	0.0003	0.0065
$\Delta\kappa\_lu_1 2ref$ [deg]	-5.0	-5.0047	0.0003	-5.0047	0.0001	0.0047
Intrinsic parameters of the reference scanner						
$\Delta\rho\_ref$ [m]	0.0	0.0195	0.0001	0.0195	0.00001	0.0195
S_β_ref	1.0	1.0	0.00001	1.0000	0.00001	0.0000
Intrinsic parameters of scanner 1						
$\Delta\rho\_lu_1$ [m]	0.0	0.0197	0.0001	0.0197	0.00001	0.0197
$S_\beta\_lu_1$	1.0	0.9998	0.00001	0.9998	0.00001	0.0002

Table 5.C. The results of estimated system parameters for scenario V in experiment 3

Parameters	True value	Initial value	Initial Standard deviation	Estimated value	Estimated Standard deviation	Abs (diff)
The mounting parameters relating the reference scanner and the IMU body frame						
ΔX_ref2b [m]	1.0	1.1	1.0e9	1.0608	0.0002	0.0608
ΔY_ref2b [m]	1.0	0.9	1.0e9	0.9022	0.0003	0.0978
ΔZ_ref2b [m]	0.0	0.0	1.0e-9	Fixed		
$\Delta\omega\_ref2b$ [deg]	5.0	5.1	1.0e9	5.1013	0.0015	0.1013
$\Delta\varphi\_ref2b$ [deg]	-5.0	-5.1	1.0e9	-5.0946	0.0009	0.0946
$\Delta\kappa\_ref2b$ [deg]	5.0	4.9	1.0e9	4.8567	0.0018	0.1433
The mounting parameters relating scanner 1 and the reference scanner						
$\Delta X\_lu_1 2ref$ [m]	-1.0	-1.1	1.0e9	-1.0946	0.0003	0.0946
$\Delta Y\_lu_1 2ref$ [m]	1.0	1.1	1.0e9	1.0988	0.0005	0.0988
$\Delta Z\_lu_1 2ref$ [m]	0.0	-0.1	1.0e9	-0.0986	0.0004	0.0986
$\Delta\omega\_lu_1 2ref$ [deg]	-5.0	-5.1	1.0e9	-5.1221	0.0020	0.1221
$\Delta\varphi\_lu_1 2ref$ [deg]	5.0	4.9	1.0e9	4.8792	0.0012	0.1208
$\Delta\kappa\_lu_1 2ref$ [deg]	-5.0	-4.9	1.0e9	-4.9083	0.0014	0.0983
Intrinsic parameters of the reference scanner						
$\Delta\rho\_ref$ [m]	0.0	0.02	1.0e9	0.0359	0.0005	0.0359
S_β_ref	1.0	1.0001	1.0e9	1.0006	0.00001	0.0006
Intrinsic parameters of scanner 1						
$\Delta\rho\_lu_1$ [m]	0.0	-0.02	1.0e9	-0.0113	0.0006	0.0113
$S_\beta\_lu_1$	1.0	0.9999	1.0e9	0.9998	0.00001	0.0002

Table 6.C. The results of estimated system parameters for scenario VI in experiment 3

Parameters	True value	Initial value	Initial Standard deviation	Estimated value	Estimated Standard deviation	Abs (diff)
The mounting parameters relating the reference scanner and the IMU body frame						
ΔX_ref2b [m]	1.0	1.1	1.0e9	1.0603	0.0001	0.0603
ΔY_ref2b [m]	1.0	0.9	1.0e9	0.9045	0.0001	0.0955
ΔZ_ref2b [m]	0.0	0.0	1.0e-9	Fixed		
$\Delta\omega\_ref2b$ [deg]	5.0	5.1	1.0e9	5.0943	0.0009	0.0943
$\Delta\varphi\_ref2b$ [deg]	-5.0	-5.1	1.0e9	-5.0910	0.0006	0.0910
$\Delta\kappa\_ref2b$ [deg]	5.0	4.9	1.0e9	4.8640	0.0017	0.1360
The mounting parameters relating scanner 1 and the reference scanner						
$\Delta X\_lu_1 2ref$ [m]	-1.0	-1.0005	0.00001	-1.0005	0.00001	0.0005
$\Delta Y\_lu_1 2ref$ [m]	1.0	0.9996	0.00001	0.9996	0.00001	0.0004
$\Delta Z\_lu_1 2ref$ [m]	0.0	-0.0090	0.0001	-0.0090	0.00001	0.0090
$\Delta\omega\_lu_1 2ref$ [deg]	-5.0	-4.9942	0.0007	-4.9942	0.0003	0.0058
$\Delta\varphi\_lu_1 2ref$ [deg]	5.0	4.9935	0.0008	4.9934	0.0003	0.0065
$\Delta\kappa\_lu_1 2ref$ [deg]	-5.0	-5.0047	0.0003	-5.0047	0.0001	0.0047
Intrinsic parameters of the reference scanner						
$\Delta\rho\_ref$ [m]	0.0	0.0195	0.0001	0.0195	0.00001	0.0195
S_β_ref	1.0	1.0	0.00001	1.0000	0.00001	0.0000
Intrinsic parameters of scanner 1						
$\Delta\rho\_lu_1$ [m]	0.0	0.0197	0.0001	0.0197	0.00001	0.0197
$S_\beta\_lu_1$	1.0	0.9998	0.00001	0.9998	0.00001	0.0002

Table 7.C. The results of estimated system parameters for scenario VII in experiment 3

Parameters	True value	Initial value	Initial standard deviation	Estimated value	Estimated standard deviation	Abs (diff)
The mounting parameters relating the reference scanner and the IMU body frame						
ΔX_ref2b *[m]*	1.0	1.1	1.0e9	1.0609	0.0002	0.0609
ΔY_ref2b *[m]*	1.0	0.9	1.0e9	0.9199	0.0003	0.0801
ΔZ_ref2b *[m]*	0.0	0.1	1.0e9	0.0998	0.0016	0.0998
$\Delta\omega\_ref2b$ *[deg]*	5.0	5.1	1.0e9	5.1067	0.0014	0.1067
$\Delta\varphi\_ref2b$ *[deg]*	-5.0	-5.1	1.0e9	-5.0875	0.0009	0.0875
$\Delta\kappa\_ref2b$ *[deg]*	5.0	4.9	1.0e9	4.8375	0.0017	0.1625
The mounting parameters relating scanner 1 and the reference scanner						
$\Delta X\_lu_1 2ref$ *[m]*	-1.0	-1.1	1.0e9	-1.0649	0.0003	0.0649
$\Delta Y\_lu_1 2ref$ *[m]*	1.0	1.1	1.0e9	1.0719	0.0004	0.0719
$\Delta Z\_lu_1 2ref$ *[m]*	0.0	-0.1	1.0e9	-0.0880	0.0004	0.0880
$\Delta\omega\_lu_1 2ref$ *[deg]*	-5.0	-5.1	1.0e9	-5.1380	0.0019	0.1380
$\Delta\varphi\_lu_1 2ref$ *[deg]*	5.0	4.9	1.0e9	4.8694	0.0012	0.1306
$\Delta\kappa\_lu_1 2ref$ *[deg]*	-5.0	-4.9	1.0e9	-4.9173	0.0013	0.0827
Intrinsic parameters of the reference scanner						
$\Delta\rho\_ref$ *[m]*	0.0	0.02	1.0e9	0.0405	0.0005	0.0405
S_β_ref	1.0	1.0001	1.0e9	1.0009	0.00001	0.0009
Intrinsic parameters of scanner 1						
$\Delta\rho\_lu_1$ *[m]*	0.0	-0.02	1.0e9	-0.0362	0.0005	0.0362
$S_\beta\_lu_1$	1.0	0.9999	1.0e9	0.9999	0.00001	0.0001

Table 8.C. The results of estimated system parameters for scenario VIII in experiment 3

Parameters	True value	Initial value	Initial standard deviation	Estimated value	Estimated standard deviation	Abs (diff)
The mounting parameters relating the reference scanner and the IMU body frame						
ΔX_ref2b [m]	1.0	1.1	1.0e9	1.0601	0.0001	0.0601
ΔY_ref2b [m]	1.0	0.9	1.0e9	0.9289	0.0001	0.0711
ΔZ_ref2b [m]	0.0	0.1	1.0e9	0.0991	0.0017	0.0991
$\Delta\omega\_ref2b$ [deg]	5.0	5.1	1.0e9	5.0862	0.0009	0.0862
$\Delta\varphi\_ref2b$ [deg]	-5.0	-5.1	1.0e9	-5.0802	0.0006	0.0802
$\Delta\kappa\_ref2b$ [deg]	5.0	4.9	1.0e9	4.8773	0.0017	0.1227
The mounting parameters relating scanner 1 and the reference scanner						
$\Delta X\_lu_1 2ref$ [m]	-1.0	-1.0005	0.00001	-1.0005	0.00001	0.0005
$\Delta Y\_lu_1 2ref$ [m]	1.0	0.9996	0.00001	0.9996	0.00001	0.0004
$\Delta Z\_lu_1 2ref$ [m]	0.0	-0.0090	0.0001	-0.0090	0.00001	0.0090
$\Delta\omega\_lu_1 2ref$ [deg]	-5.0	-4.9942	0.0007	-4.9942	0.0003	0.0058
$\Delta\varphi\_lu_1 2ref$ [deg]	5.0	4.9935	0.0008	4.9933	0.0003	0.0067
$\Delta\kappa\_lu_1 2ref$ [deg]	-5.0	-5.0047	0.0003	-5.0047	0.0001	0.0047
Intrinsic parameters of the reference scanner						
$\Delta\rho\_ref$ [m]	0.0	0.0195	0.0001	0.0195	0.00001	0.0195
S_β_ref	1.0	1.0	0.00001	1.0000	0.00001	0.0000
Intrinsic parameters of scanner 1						
$\Delta\rho\_lu_1$ [m]	0.0	0.0197	0.0001	0.0197	0.00001	0.0197
$S_\beta\_lu_1$	1.0	0.9998	0.00001	0.9998	0.00001	0.0002

Table 9.C. The results of estimated system parameters for scenario IX in experiment 3

Parameters	True value	Initial value	Initial standard deviation	Estimated value	Estimated standard deviation	Abs (diff)
The mounting parameters relating the reference scanner and the IMU body frame						
ΔX_ref2b [m]	1.0	1.1	1.0e9	1.0535	0.0002	0.0535
ΔY_ref2b [m]	1.0	0.9	1.0e9	0.9125	0.0002	0.0875
ΔZ_ref2b [m]	0.0	0.0	1.0e-9	Fixed		
$\Delta\omega\_ref2b$ [deg]	5.0	5.1	1.0e9	5.0898	0.0010	0.0898
$\Delta\varphi\_ref2b$ [deg]	-5.0	-5.1	1.0e9	-5.0769	0.0007	0.0769
$\Delta\kappa\_ref2b$ [deg]	5.0	4.9	1.0e9	4.8344	0.0014	0.1656
The mounting parameters relating scanner 1 and the reference scanner						
$\Delta X\_lu_1 2ref$ [m]	-1.0	-1.1	1.0e9	-1.0747	0.0002	0.0747
$\Delta Y\_lu_1 2ref$ [m]	1.0	1.1	1.0e9	1.0765	0.0003	0.0765
$\Delta Z\_lu_1 2ref$ [m]	0.0	-0.1	1.0e9	-0.0926	0.0003	0.0926
$\Delta\omega\_lu_1 2ref$ [deg]	-5.0	-5.1	1.0e9	-5.0825	0.0014	0.0825
$\Delta\varphi\_lu_1 2ref$ [deg]	5.0	4.9	1.0e9	4.8602	0.0011	0.1398
$\Delta\kappa\_lu_1 2ref$ [deg]	-5.0	-4.9	1.0e9	-4.8769	0.0010	0.1231
Intrinsic parameters of the reference scanner						
$\Delta\rho\_ref$ [m]	0.0	0.02	1.0e9	0.0250	0.0005	0.0250
S_β_ref	1.0	1.0001	1.0e9	1.0003	0.00001	0.0003
Intrinsic parameters of scanner 1						
$\Delta\rho\_lu_1$ [m]	0.0	-0.02	1.0e9	-0.0247	0.0005	0.0247
$S_\beta\_lu_1$	1.0	0.9999	1.0e9	1.0004	0.00001	0.0004

Table 10.C. The results of estimated system parameters for scenario X in experiment 3

Parameters	True value	Initial value	Initial standard deviation	Estimated value	Estimated standard deviation	Abs (diff)
The mounting parameters relating the reference scanner and the IMU body frame						
ΔX_ref2b *[m]*	1.0	1.1	1.0e9	1.0514	0.0001	0.0514
ΔY_ref2b *[m]*	1.0	0.9	1.0e9	0.9239	0.0001	0.0761
ΔZ_ref2b *[m]*	0.0	0.0	1.0e-9	Fixed		
$\Delta\omega\_ref2b$ *[deg]*	5.0	5.1	1.0e9	5.0750	0.0006	0.0750
$\Delta\varphi\_ref2b$ *[deg]*	-5.0	-5.1	1.0e9	-5.0540	0.0005	0.0540
$\Delta\kappa\_ref2b$ *[deg]*	5.0	4.9	1.0e9	4.8532	0.0014	0.1468
The mounting parameters relating scanner 1 and the reference scanner						
$\Delta X\_lu_1 2ref$ *[m]*	-1.0	-1.0005	0.00001	-1.0005	0.00001	0.0005
$\Delta Y\_lu_1 2ref$ *[m]*	1.0	0.9996	0.00001	0.9996	0.00001	0.0004
$\Delta Z\_lu_1 2ref$ *[m]*	0.0	-0.0090	0.0001	-0.0090	0.00001	0.0090
$\Delta\omega\_lu_1 2ref$ *[deg]*	-5.0	-4.9942	0.0007	-4.9942	0.0002	0.0058
$\Delta\varphi\_lu_1 2ref$ *[deg]*	5.0	4.9935	0.0008	4.9934	0.0003	0.0066
$\Delta\kappa\_lu_1 2ref$ *[deg]*	-5.0	-5.0047	0.0003	-5.0047	0.0001	0.0047
Intrinsic parameters of the reference scanner						
$\Delta\rho\_ref$ *[m]*	0.0	0.0195	0.0001	0.0195	0.00001	0.0195
S_β_ref	1.0	1.0	0.00001	1.0000	0.00001	0.0000
Intrinsic parameters of scanner 1						
$\Delta\rho\_lu_1$ *[m]*	0.0	0.0197	0.0001	0.0197	0.00001	0.0197
$S_\beta\_lu_1$	1.0	0.9998	0.00001	0.9998	0.00001	0.0002

Table 11.C. The results of estimated system parameters for scenario XI in experiment 3

Parameters	True value	Initial value	Initial standard deviation	Estimated value	Estimated standard deviation	Abs (diff)
The mounting parameters relating the reference scanner and the IMU body frame						
ΔX_ref2b [m]	1.0	1.1	1.0e9	1.0670	0.0002	0.0670
ΔY_ref2b [m]	1.0	0.9	1.0e9	0.9250	0.0002	0.0750
ΔZ_ref2b [m]	0.0	0.1	1.0e9	0.0934	0.0014	0.0934
$\Delta\omega\_ref2b$ [deg]	5.0	5.1	1.0e9	5.0930	0.0010	0.0930
$\Delta\varphi\_ref2b$ [deg]	-5.0	-5.1	1.0e9	-5.0793	0.0008	0.0793
$\Delta\kappa\_ref2b$ [deg]	5.0	4.9	1.0e9	4.8289	0.0014	0.1711
The mounting parameters relating scanner 1 and the reference scanner						
$\Delta X\_lu_1 2ref$ [m]	-1.0	-1.1	1.0e9	-1.0719	0.0002	0.0719
$\Delta Y\_lu_1 2ref$ [m]	1.0	1.1	1.0e9	1.0742	0.0003	0.0742
$\Delta Z\_lu_1 2ref$ [m]	0.0	-0.1	1.0e9	-0.0916	0.0003	0.0916
$\Delta\omega\_lu_1 2ref$ [deg]	-5.0	-5.1	1.0e9	-5.0864	0.0014	0.0864
$\Delta\varphi\_lu_1 2ref$ [deg]	5.0	4.9	1.0e9	4.8771	0.0011	0.1229
$\Delta\kappa\_lu_1 2ref$ [deg]	-5.0	-4.9	1.0e9	-4.8861	0.0010	0.1139
Intrinsic parameters of the reference scanner						
$\Delta\rho\_ref$ [m]	0.0	0.02	1.0e9	0.0218	0.0004	0.0218
S_β_ref	1.0	1.0001	1.0e9	1.0002	0.00001	0.0002
Intrinsic parameters of scanner 1						
$\Delta\rho\_lu_1$ [m]	0.0	-0.02	1.0e9	-0.0198	0.0004	0.0198
$S_\beta\_lu_1$	1.0	0.9999	1.0e9	0.9999	0.00001	0.0001

Table 12.C. The results of estimated system parameters for scenario XII in experiment 3

Parameters	True value	Initial value	Initial standard deviation	Estimated value	Estimated standard deviation	Abs (diff)
The mounting parameters relating the reference scanner and the IMU body frame						
$\Delta X\_ref2b\ [m]$	1.0	1.1	1.0e9	1.0508	0.0001	0.0508
$\Delta Y\_ref2b\ [m]$	1.0	0.9	1.0e9	0.9265	0.0001	0.0735
$\Delta Z\_ref2b\ [m]$	0.0	0.1	1.0e9	0.0925	0.0015	0.0925
$\Delta\omega\_ref2b\ [deg]$	5.0	5.1	1.0e9	5.0751	0.0006	0.0751
$\Delta\varphi\_ref2b\ [deg]$	-5.0	-5.1	1.0e9	-5.0769	0.0005	0.0769
$\Delta\kappa\_ref2b\ [deg]$	5.0	4.9	1.0e9	4.8554	0.0014	0.1446
The mounting parameters relating scanner 1 and the reference scanner						
$\Delta X\_lu_1 2ref\ [m]$	-1.0	-1.0005	0.00001	-1.0005	0.00001	0.0005
$\Delta Y\_lu_1 2ref\ [m]$	1.0	0.9996	0.00001	0.9996	0.00001	0.0004
$\Delta Z\_lu_1 2ref\ [m]$	0.0	-0.0090	0.0001	-0.0090	0.00001	0.0090
$\Delta\omega\_lu_1 2ref\ [deg]$	-5.0	-4.9942	0.0007	-4.9942	0.0003	0.0058
$\Delta\varphi\_lu_1 2ref\ [deg]$	5.0	4.9935	0.0008	4.9934	0.0003	0.0066
$\Delta\kappa\_lu_1 2ref\ [deg]$	-5.0	-5.0047	0.0003	-5.0047	0.0001	0.0047
Intrinsic parameters of the reference scanner						
$\Delta\rho\_ref\ [m]$	0.0	0.0195	0.0001	0.0195	0.00001	0.0195
S_β_ref	1.0	1.0	0.00001	1.0000	0.00001	0.0000
Intrinsic parameters of scanner 1						
$\Delta\rho\_lu_1\ [m]$	0.0	0.0197	0.0001	0.0197	0.00001	0.0197
$S_\beta\_lu_1$	1.0	0.9998	0.00001	0.9998	0.00001	0.0002